Etude d'un auto-oscillateur non-isochrone : Application à la dynamique non-linéaire de l'aimantation induite par transfert de spin

Michaël Quinsat

▶ **To cite this version:**

Michaël Quinsat. Etude d'un auto-oscillateur non-isochrone : Application à la dynamique non-linéaire de l'aimantation induite par transfert de spin. Autre. Université de Grenoble, 2012. Français. NNT : 2012GRENY083 . tel-00846484

HAL Id: tel-00846484

https://theses.hal.science/tel-00846484

Submitted on 19 Jul 2013

HAL is a multi-disciplinary open access archive for the deposit and dissemination of scientific research documents, whether they are published or not. The documents may come from teaching and research institutions in France or abroad, or from public or private research centers.

L'archive ouverte pluridisciplinaire **HAL**, est destinée au dépôt et à la diffusion de documents scientifiques de niveau recherche, publiés ou non, émanant des établissements d'enseignement et de recherche français ou étrangers, des laboratoires publics ou privés.

UNIVERSITÉ DE GRENOBLE

THÈSE

pour obtenir le grade de

DOCTEUR DE L'UNIVERSITÉ DE GRENOBLE

Spécialité: Physique

Arrêté ministériel : 7 août 2006

Présentée par

Michaël QUINSAT

Thèse dirigée par **Ursula EBELS** et

co-encadrée par **Marie-Claire CYRILLE**

préparée au sein du

CEA-LETI

dans l'**École Doctorale**:**Physique**

Étude d'un auto-oscillateur non-isochrone : Application à la dynamique non-linéaire de l'aimantation induite par transfert de spin

Thèse soutenue publiquement le **28 Septembre 2012**,

devant le jury composé de:

Monsieur Daniel BÜRGLER

Privatdozent au Peter Grünberg Institut de Jülich, Rapporteur

Monsieur Vincent CROS

Chercheur au CNRS/Thales, Rapporteur

Madame Marie-Claire CYRILLE

Ingénieur au CEA, Co-Encadrante

Madame Ursula EBELS

Ingénieur au CEA, Directrice de thèse

Monsieur Joo-Von KIM

Chercheur au CNRS/IEF, Membre

Monsieur Andrei SLAVIN

Professeur de l'Université d'Oakland, Membre

Monsieur Pascal XAVIER

Professeur de l'Université de Grenoble, Président du Jury

Abstract

Spin Torque Oscillators (STO) are nano-sized Radio-Frequency oscillators whose frequency can be tuned by an order of magnitude. This tuning originates from the nonlinear properties of the underlying magnetization dynamics that is induced by spin transfer torque (STT) in multilayered magnetic nanostructures.

Being highly tunable in frequency has the inconvenience of creating a very strong sensitivity to noise. As a result the spectral purity of STOs is far below the one required (for applications for instance in telecommunications).

The magnetization dynamics induced by STT has been described theoretically in the frame of nonlinear spin wave theory that makes the essential features of the underlying properties very transparent. However important information on the excitation mode are "buried" in phenomenological parameters such as, ν the amplitude-phase coupling, and Γ_p, the amplitude relaxation rate. Determining these parameters with accuracy from experiments is thus an important issue.

This thesis describes several experimental methods to extract these parameters. The first involves time domain noise spectroscopy which permits the power spectral density of phase and amplitude noise to be extracted. The analysis of such noise in light of theoretical models allows not only direct extraction of the nonlinear parameters, but also to quantify the technological relevant phase noise. This is demonstrated for magnetic tunnel junction devices.

A second method involves the analysis of higher harmonic linewidths, where it is shown that due to the non-isochronous property of STOs, the relationship between Δf_n and Δf_1 is nontrivial and allows ν and Γ_p to be determined.

We then apply the information gathered on the autonomous dynamics of STOs to understand the non-autonomous dynamics of STOs that are a prerequisite for the use of STOs in complex RF architectures. It is shown experimentally how the nonlinear parameters influence this non-autonomous behavior.

Keywords: - Spintronics, nanomagnetism, oscillators, nonlinear dynamics, autonomous dynamics.

Remerciements

Je tiens à remercier les personnes qui, par leur attention, aide et gentillesse m'ont permis de partager de bons moments au labo et ailleurs pendant ces trois années.

Tout d'abord, mes encadrantes (les personnes qui m'ont encadrées) qui ont toujours assumé leurs rôles et même au-delà en s'assurant ainsi que leurs thésards s'épanouissent. Ursula donc, pour son encadrement au quotidien et son sens du perfectionnisme qui me permet aujourd'hui d'envisager sereinement l'avenir. Marie-Claire pour ses conseils de manager et son constant optimisme pour les problèmes quotidiens et les tâches à venir. JP pour m'avoir tout appris sur les manips RF et autres détails qui ont fait de ma thèse une réussite. Daria, Liliana, Ioana et Helga pour leurs simu incroyables et leurs connaissances en maths. Mair pour ses aides indispensables permettant la compréhension de tout un tas de trucs allant de la théorie de STT et du transport aux Pink Floyds. Bernard Dieny et Viala pour leurs conseils et leur confiance quotidienne. Il me faut aussi remercier les personnes avec qui j'ai pu collaborer et qui m'ont apporté une autre vision à mon sujet d'étude; Michel Prigent, Raphaël Sommet, Jean-christophe Nallatamby, Vasyl Tiberkevich, Andrei Slavin, Mark Keller, Laurence Bianchini, Micha et Patrick.

Les compagnons d'études ensuite, c-à-d le groupe RF de Spintec. Dimitri dont j'ai hérité les manips et qui m'a permis d'être à l'aise avec le sujet après son départ. Juan et son expertise en FMR, ses conseils avisés et son goût prononcé pour l'épistémiologie. Felipe, grâce à qui la partie théorique de ma thèse à trouver un contexte général plutôt qu'un enchevêtrement de formules sans queue ni tête. Les "process people", qui doivent assumer le rôle le plus important et pourtant le moins glorifiant des projets en fournissant moults échantillons, Karin et Jiafeng. Les autres thèsards avec qui les échanges réciproques m'ont permis d'avancer dans diverses directions, Adrien, Abhijit, Elmer, Sylvain, Bertrand, Christophe. Enfin au petit nouveau, Alex, qui m'a pas mal aidé pour l'anglais et dont les derniers résultats expérimentaux m'ont redonné espoirs dans l'étude des STOs! Les gens de passages, Noël, Guillaume, Amine, SeoWon,... : on se reverra surement un jour!

Viens ensuite les gens du labo, Emeline, Gor, Adrien et Julien (qui ont rendu le bureau bruyant mais plein de vie). Julien aussi, pour les coups salvateurs du Jeudi soir, partagés avec Lucien et Jerem, les "crocus guy" toujours OK pour rendre service et donner des conseils - bien utiles - de seniors. Le cynisme appréciable de Sébastien, la gentillesse de Maria et Lavinia. L'humour de Hongxin qui a toujours gardé le sourire! Lara, Abdel et brahim, les post-docs de l'autre bureau.

Les secrétaires de Spintec, Cat et Rachel et celles du Leti Béa et Christine, qui aident au quotidien pour que tout soit plus "lisse". Vient enfin les indénombrables amis de la cafèt de Spintec (Marité, Claire, Emilie, les nouveaux thésards (trop nombreux pour les citer tous!), Vincent, Gilles, Isabelles, les Stéphanes et les autres...), qui ont fait que

l'heure (ou les deux heures...) du break de midi était toujours appréciable, sans pour autant oublier nos amis du LETI (Anaïs, Bertrand, Hélène, Simon...).

Je tiens aussi à remercier mon jury de thèse pour leur disponibilité et leur lecture attentive de mon manuscrit, le président du jury Pascal Xavier, les rapporteurs Daniel Burgler et Vincent Cros, Joo-von Kim pour sa relecture attentive et ses corrections, et Andrei Slavin pour son soutient aussi.

Finalement, ma famille et surtout ma femme, Moé, pour m'avoir supporté (et épousé!) pendant cette thèse.

Merci.

A ma femme
et à ma famille

Contents

I Introduction **1**

1 Context - Spin Transfer in Ferromagnetic materials **5**
1.1 Ferromagnetism and Spin dependent transport 5
1.1.1 Origin of Ferromagnetism in 3d transition metals 5
1.1.2 Spin dependent Tunneling processes 9
1.1.2.1 Tunneling effect from the free electron models 9
1.1.2.2 Coherent Tunneling Effects 10
1.2 From STT to Spin Torque Oscillator 12
1.2.1 Magnetization Dynamics under STT 12
1.2.1.1 The LLG equation 12
1.2.1.2 The Spin Transfer Torques 14
1.2.2 State Diagram of in-plane magnetized magneto-resistive devices . 17
1.2.3 State diagram with temperature 18
1.2.3.1 Effects on the Switching Process 18
1.2.3.2 Effects on the Stable Dynamical States 20
1.2.3.3 Spin Transfer Oscillator in presence of noise 21

2 Context - Spin Torque Oscillator **25**
2.1 Oscillators: an introduction 25
2.1.1 Damped oscillator, resonator and quality factor 26
2.1.2 Notion of self-sustained oscillator 28
2.1.2.1 Amplitude in self-sustained oscillator 30
2.1.2.2 Phase in self-sustained oscillator 31
2.1.2.3 Noise in self-sustained oscillator 32
2.1.2.4 Conclusion on self-sustained oscillators 33
2.2 Spin Transfer Oscillators 33
2.2.1 Magnetism and damped oscillator: FMR 34
2.2.2 KTS Model 35
2.2.2.1 From the LLGS equation to an autonomous auto-oscillator equation 35
2.2.2.2 KTS model in literature 38
2.2.3 The thermal noise model in the KTS theory 43
2.2.3.1 Diffusion constant from The Fokker-Planck formalism . . 44
2.2.3.2 Amplitude noise in autonomous STOs 45
2.2.3.3 Amplitude noise relaxation and its link to the phase noise 46
2.3 Summary 51

II Experimental techniques and autonomous regime under noise 53

3 Experimental techniques 57
3.1 Specifics of RF measurements . . . 58
3.1.1 Transmission line theory . . . 59
3.1.2 Impedance matching . . . 60
3.1.3 Microwave Network analysis . . . 61
3.1.4 Gain correction and de-embedding . . . 62
3.1.5 Measurement of the voltage PSD . . . 64
3.2 The time-frequency measurement . . . 67
3.2.1 Introduction to signal analysis . . . 67
3.2.2 Phase noise from frequency domain measurement . . . 76
3.2.2.1 Phase noise measurement with a commercial signal analyzer 76
3.2.2.2 Amplitude Noise measurement . . . 78
3.2.3 Phase and Amplitude noise Measurement from a Time signal . . . 79
3.2.3.1 Signal analysis of a noisy oscillator output signal . . . 79
3.2.3.2 Experimental extraction of Phase and Amplitude . . . 82
3.3 Presentation of the tunnel junction devices . . . 90
3.4 Conclusion . . . 96

4 Amplitude and phase noise of STO 99
4.1 $I < I_c$: Damped Harmonic Oscillator . . . 99
4.1.1 Model description . . . 100
4.1.2 Experiments of subcritical regime and comparison to the KTS model 101
4.1.3 The damped harmonic oscillator: towards the nonlinear regime driven by temperature . . . 106
4.2 $I > I_c$: Non-isochronous Auto-Oscillator . . . 110
4.2.1 Power Distribution in the Above-Threshold Regime . . . 113
4.2.2 Amplitude Noise Relaxation . . . 117
4.2.2.1 Extraction of Γ_p . . . 118
4.2.2.2 Influence of thermal Johnson-Nyquist noise in Amplitude noise measurements . . . 121
4.2.2.3 Extraction of Δf_0 from amplitude noise . . . 121
4.2.3 Phase Noise of the Free Running STO . . . 123
4.2.4 FWHM in the case of non-isochronous auto-oscillator . . . 126
4.2.4.1 Analytical expression of the FWHM . . . 126
4.2.4.2 Signal FWHM Δf and linear HWHM Δf_0 . . . 128
4.2.4.3 Discussion on Δf_0 parameter . . . 129
4.3 Conclusion on the systematic comparison of KTS theory to experiments . 130
4.4 Study of Δf of higher harmonics . . . 132
4.4.1 Model description . . . 132
4.4.2 Extraction of nonlinear parameters through harmonic linewidth analysis . . . 137
4.5 Temperature dependence, noise origin and nonlinear parameters . . . 142
4.6 Flicker noise in degraded junctions . . . 145

III Non-autonomous regime of non-isochronous STOs 151

5 Modulation experiments 155
5.1 Modulation in the KTS model . . . 155
5.1.1 Physical picture of the modulation in the frame of an auto-oscillator 156
5.1.2 Sinusoid modulation of the anti-damping dissipation in STOs . . 158
5.2 Experimental protocol . . . 160
5.3 Modulation Experiments . . . 162
5.3.1 STO Spectrogram under low frequency modulation . . . 164
5.3.2 Frequency response roll-off . . . 167
5.3.3 Nonlinear damping Q extracted from modulation experiments . . 168
5.3.4 Conclusion on modulation experiments . . . 169
5.4 Perspective: noise in current and cyclostationary processes . . . 170
5.5 Perspective: PLLs . . . 172

6 Synchronization 175
6.1 Macrospin description of the fractional synchronization for the IPP mode 176
6.1.1 Symmetry of the "microwave" STT term . . . 176
6.1.2 Ellipticity dependent fractional synchronization . . . 178
6.2 Experimental verification . . . 180
6.2.1 HTMR devices . . . 180
6.2.2 LTMR devices . . . 182
6.3 Synchronization in auto-oscillators . . . 184
6.3.1 Macrospin simulations . . . 184
6.3.2 Phase synchronization phenomenon in quasi-linear oscillators . . . 186
6.3.3 Synchronization of a macrospin mode and a LTMR device; Phase Slips . . . 189
6.3.4 Non-Adlerian dynamics and its consequence on the emitted spectrum 192
6.3.4.1 Mathematical description . . . 192
6.3.4.2 Sideband appearance in the emitted spectrum . . . 193
6.3.4.3 Effect on the low frequency noise of STOs . . . 194
6.3.4.4 Stabilization of the MR signal under synchronization . . 195
6.3.4.5 Conclusion . . . 197
6.4 Perspectives of synchronization in STOs . . . 199
6.4.1 Perspective: Oscillator Formalism toward Applications . . . 199
6.4.2 Perspective: Mutual phase locking and RF-devices . . . 202

IV Conclusion 203

Part I

Introduction

Over the past decades, miniaturization was expected to shrink all electronics products such that it opened new unprecedented and unforeseeable possibilities to respond to human needs. For example, the “need” to “telecommunicate” in the late 1990’s was so huge, that as a consequence there was a telecommunication bubble (early 2000), due to the inability to scale the telecommunication offer to its real demand. Nowadays the global telecommunication market represents 3 trillions of US dollars (as in 2010), equivalent to the total German GDP. Today, there are probably more people owning a cell phone than people owning a toothbrush: 75% of the world population owns a cell phone. In 2004, the miniaturization technologies in electronics, i.e. the semiconductor industries and its market represented only 200 billions dollars and enabled about 10% of the world GDP.

Recent technological progresses are much linked to miniaturization, pushing forward research in nano-science and nano-technologies. Advances in thin film deposition and nano-structuration have led to a new field of nano-electronics called the spin electronics or spintronics. The beginning of spintronics was in 1988 with the discovery of the giant magnetoresistance effect (GMR). This effect was successfully used to enable higher density Hard Disk Drives in less than 5 years of R&D. This is due to the fact that the magnetization state corresponding to a bit of information can be measured electrically with a great accuracy using the MR effects in nanoscale devices. Thereafter in 1996, the discovery of the Spin Transfer Torque (STT) allowed to control the magnetization state electrically, through a spin polarized current. Combining electrical ”reading” and ”writing” of the magnetization will have direct applications for the development of Magnetic Random Access Memory (called STT-MRAM) that is a promising candidate for a ”universal” RAM (fast, low consumption, non-volatile) that could replace SRAMs to DRAMs in the 2X nanometre technological node.

In the research presented in this dissertation we have used the MR effect and STT for a different application. Notably, a spin polarized current can drive the magnetization into large angle steady state oscillation, where the magnetization response is very non-linear. The MR effect then converts these oscillations into an oscillatory output signal at frequencies that can range from 100 MHz to several tens of gigahertz. These effects, when realized in nanoscale devices, have potential applications as miniaturized tunable Radio-Frequency sources that could address issues of wireless communication such as cognitive RF and low consumption. After the first demonstration by Kiselev et al. of the Spin Transfer Oscillator (STO), it has rapidly become clear that steady-state auto-oscillations in the microwave range were generated whose frequency depends on the applied current or external magnetic field. This frequency tuning property of auto-oscillator is very desirable for RF sources and are called Voltage Controlled Oscillators (VCO).

Prior to the start of my thesis, studies in this field was very much focused on demonstrating the auto-oscillations for a large variety of different nano-device configurations as well as on analyzing and understanding the corresponding excitation spectra that were then compared to theoretical simulations. With the introduction of Magnetic Tunnel Junction (MTJ) devices by the end of 2007, the STO output power, one of the key parameters for applications, could be improved from the pico-Watt to the micro-Watt. This allowed addressing a number of other issues important for application but also for the development of the underlying theoretical models.

This thesis is focused on the problem of measuring the effect of the noise on the

auto-oscillation emitted from STO. This involves both theoretical and phenomenological arguments to model the effects of noise in the non-linear magnetization dynamics. Indeed, it has been shown that the noise performance of STO emission is determined by the strong nonlinearities of the magnetization dynamics. The real interest of this thesis is thus to relate the noise properties of STOs, to the non-linear parameters from theoretical models that govern the magnetization dynamics.

Part I presents the context of this thesis. Chapter 1 helps the reader to understand the basic concepts of the devices we study. From the origin of ferromagnetism in $3d$ transition metal to spin dependent tunneling process, we familiarize the reader with concepts such as magnetization and magnetoresistance effects. These two cannot be dissociated from the transfer of spin angular momentum that is investigated from a classical picture to understand its main effect on the magnetization dynamics in MTJs. Chapter 2 introduces the STO as an auto-oscillator using a recent approach to solve the problem of the magnetization dynamics in the non-linear regime in presence of STT. This phenomenological approach described in literature, the KTS model, is reviewed and it is shown how it will help us to address the problem of noise modeling in STOs when using a Fokker-Plank equation to describe the diffusion by the noise of the STOs oscillation characteristics.

Part II presents the main achievements of this work that is the measurement of the phase and amplitude noise of STOs, which are basic quantities used to characterize noise properties of oscillators such as VCOs for applications. Chapter 3 is dedicated to specific frequency and time domain measurement techniques that I developed and applied to STOs. The relatively low power and the large noise acting on STOs require developing specific tools using time domain spectroscopy. The noise measurements of STOs are then compared to theoretical predictions in Chapter 4 for MTJ devices. It is shown how key parameters of the KTS model are extracted from the nonlinear magnetization dynamics we measure. The results fits well with the KTS model, which allows for the capabilities of STOs to be quantified more explicitly, in contrast to previous models. Minor discrepancies found between experimental results and the models of magnetization dynamics will be discussed as a perspective for further theoretical investigations in the field of non-linear magnetization dynamics interacting with a thermal bath.

Part III is dedicated to understanding further the role of these key parameters in the non-autonomous regime of the STOs, which is of main importance for applications. Chapter 5 is dedicated to modulation experiments in order to quantify the agility of STOs that is of primary interest for RF applications, such stable RF sources and fast dynamical field sensors. Modulation experiments are also used to confirm the results obtained in Part II and to explore new paths for the study of STOs for both fundamental and applicative aspects. Chapter 6 details synchronization experiments on STOs in presence of noise. Preliminary results of an STO synchronized to an external microwave source are presented in order to describe certain dynamical features of this phase locked state.

Chapter 1

Context - Spin Transfer in Ferromagnetic materials

This chapter gives key notions to better understand the context and the results of this thesis. It includes basic models of the origin of ferromagnetism and spin dependent phenomena, such as spin dependent tunneling effects. The transfer of angular spin momentum to a ferromagnetic material by a spin polarized current is also reviewed. Finally, the dynamics of the magnetization of a ferromagnetic thin film in a voltage biased magnetic tunnel junction is described. This is the basis of a spin transfer oscillator.

1.1 Ferromagnetism and Spin dependent transport

In this part we introduce the origin of ferromagnetism in $3d$ transition metals which is relevant for the devices we are going to study. This will be followed by an introduction to spin dependent transport phenomena, with a focus on tunneling transport and the corresponding tunnel transport models.

1.1.1 Origin of Ferromagnetism in 3d transition metals

In a classical picture[1], an atom is made of a positively charged core around which revolve negatively charged electrons. When the electron trajectory is considered circular with radius r and a velocity v around the core (see Fig. 1.1), the trajectory described by the electron is then inducing a current of intensity I. This gives a magnetic moment, the so-called orbital moment $\vec{m}_0$, such that:

$$\vec{m}_0 = IS \cdot \vec{r} \times \vec{v}.$$

Here S is the area of the disk formed by the electron trajectory. The time taken for the electron to make one revolution being $\tau = 2\pi r/v$, it follows that $I = -ev/2\pi r$, which leads to the magnetic moment:

$$\vec{m}_0 = -\frac{e}{2}\vec{r} \times \vec{v} = -\frac{e}{2m_e}\vec{l}_0 \ ,$$

[1]Interested readers may find more details in Ref. [1].

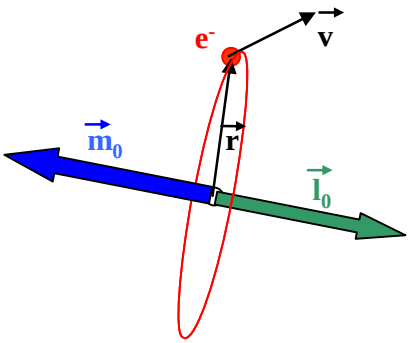

Fig. 1.1: The electron (in red) has a circular trajectory of radius r and a velocity v around the core, resulting in a magnetic moment $\vec{m}_0$ (classical picture).

where m_e is the electron mass and $\vec{l_0}$ is orbital moment. In quantum mechanics, the orbital moment (that corresponds to the orbital trajectory in the previous classical model) is quantified by the vectorial operator ℓ such that $\vec{l_0} = \hbar\vec{\ell}$. The moment $\vec{\ell}$ is defined by quantum numbers l and m that respectively represents the orbital number (that are s, p, d orbitals for $l = 0, 1, 2...$) and the magnetic number that gives the (discrete) "shape" of the orbital (for example p_x, p_y, p_z ...). Finally, we write $\vec{m}_0 = -\mu_B\vec{\ell}$ with $\mu_B = \hbar e/2m_e$ the Bohr magneton, the base unit of magnetic moment.

In fact, experimental observations have shown differences between the orbital magnetic moment and the measured magnetic moment. Stern and Gerlach experimentally showed the existence of an intrinsic momentum due to the electron that is the the spin momentum, with:

$$\vec{l_s} = \hbar\vec{\boldsymbol{s}}.$$

In a similar way to the vectorial operator ℓ, which is called orbital momentum, $\boldsymbol{s}$ is called spin angular momentum. Its projection on the quantization axis is the spin quantum number $\sigma = \pm 1/2$. By analogy with orbital magnetic moments, a spin magnetic moment exists $\vec{m}_s$:

$$\vec{m}_s = -2\mu_B \cdot \boldsymbol{s}.$$

Finally, the total magnetic moment for a single electron is $\vec{m}_t = \vec{m}_0 + \vec{m}_s$. This demonstration allows first insights and an introduction to the origin of magnetism that is evidently more complex with a large number of electrons and atoms in bulk materials. Since inner-shell electrons are paired such that their contribution to the atom's magnetic moment is zero, the magnetism finds its origin in non-saturated electronic shells.

This model implies that electrons responsible for the total magnetic moment are localized. The application of this model is thus limited to the case of bulk $3d$ transition metals. Indeed, as shown in Fig. 1.2, electrons responsible for magnetism can move along the atoms since their probability to be at the inter-atomic distance is non-zero: electrons responsible for magnetism are delocalized. Contrary to $4f$ electrons, $3d$ electrons have a spatial extension that allows the delocalization for the electrons responsible for magnetism. Therefore, when considering the continuum of energy states available for $3d$

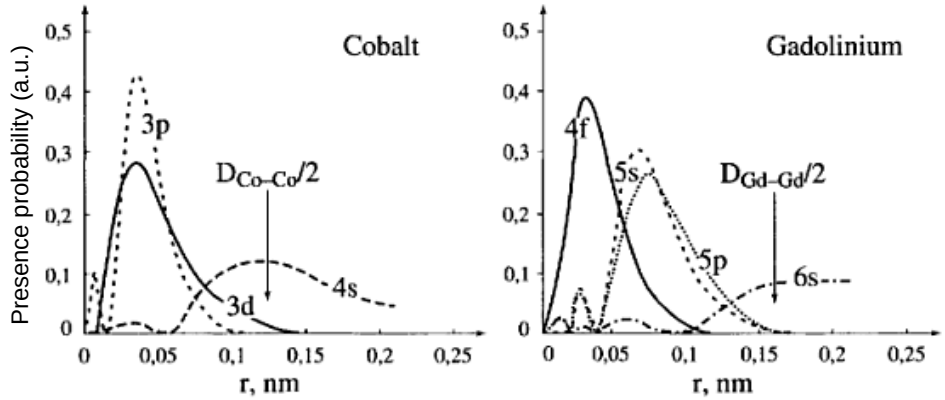

Fig. 1.2: Electron occupation probability versus the distance from the core for different electronic shells for cobalt and gadolinium. $3d$ electrons, responsible for magnetism in Co, are delocalized while in Ga, $4f$ electrons (responsible for magnetism) are localized. From [1].

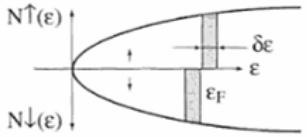

Fig. 1.3: Displacement between minority electrons and majority electrons. From [1].

electrons, it is no longer possible to distinguish a magnetic state for those electrons, i.e. the band structure should be the same for each spin population. The use of the itinerant electron model from Stoner is then a better description to explain the ferromagnetism in $3d$ transition metals.

Pauli's exclusion principle and Hund's filling rule (lowest energy states are first filled), imply that spins paired with opposite spin sign share one orbital. This would preclude the possibility to obtain different density of states for the spin populations $\uparrow$ and $\downarrow$ inside a material. These principles do not exclude the probability of finding two electrons of opposite sign at the same place. Therefore, two electrons of opposite spin sign will repel on average more than two electrons of same spin sign in the bulk. Stoner introduced a model for which repulsive forces between two electrons of opposite spins is stronger, by a quantity I, than between two electrons of the same spin. A potential interaction energy is introduced of the form $E_p = IN_\uparrow N_\downarrow$, where $N_\uparrow$ and $N_\downarrow$ are the electron densities of each spin.

We first assume two equal populations of spin $N_\uparrow = N_\downarrow = N/2$. We then transfer $N(\varepsilon_f)\delta\varepsilon$ electrons from $\downarrow$ state to $\uparrow$ state as shown in Fig. 1.3. The kinetic energy increases by $\Delta E_c = N(\varepsilon_F)(\delta\varepsilon)^2$ while the variation of the interaction energy discussed above is:

$$I\left[\frac{N}{2} + N(\varepsilon_F)\delta\varepsilon\right]\left[\frac{N}{2} - N(\varepsilon_F)\delta\varepsilon\right] - I\left[\frac{N}{2}\right]^2 = -IN^2(\varepsilon_F)(\delta\varepsilon)^2 \,,$$

and the total energy variation between equal populations of the ferromagnetic is:

$$\Delta E = N(\varepsilon_F)(\delta\varepsilon)^2\left[1 - IN(\varepsilon_F)\right].$$

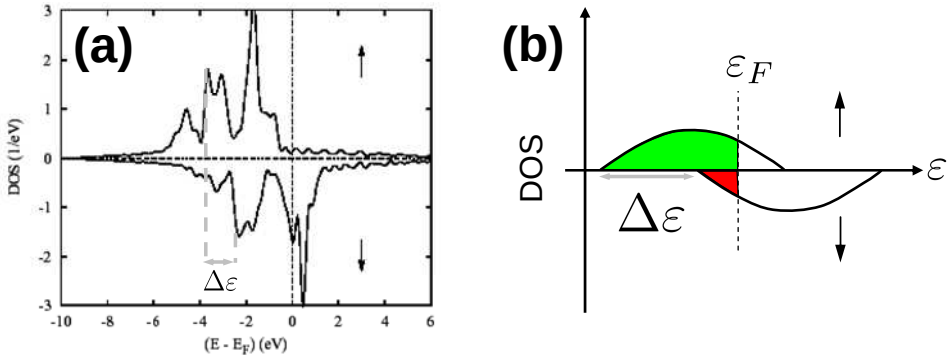

Fig. 1.4: (a) Density of States (DOS) of Cobalt from *ab-initio* calculations, from [2]. (b) Schematic of DOS in a ferromagnetic $3d$ transition metal, where similar shaped-bands are effectively shifted by the Stoner potential $\Delta\varepsilon$.

From this it follows that the non-magnetic state is stable if $IN(\epsilon_F) < 1$. In the case of $IN(\varepsilon_F) > 1$, a minimum of energy exists when $N_\uparrow$ and $N_\downarrow$ are different, leading to a ferromagnetic order. This criterion is called the Stoner criterion. For all practical purposes, however, I is difficult to evaluate. While this model has many limitations, it is helpful to qualitatively explain the ferromagnetism of cobalt, nickel and iron that have large densities of state at the Fermi level (therefore the repulsive interaction $IN(\varepsilon_F)$ is greater). Indeed, it has been shown that transition metals have a narrow band (about 5 or 10eV) as shown by the example of bcc-cobalt in Fig. 1.4. This description of ferromagnetism will be enough to explain qualitatively other effects that are described later. Indeed, spin dependent transport in Magnetic Tunnel Junction (MTJ) and spin transfer torque effects can be linked to the Stoner model. For this, let us introduce an empirical parameter, the Stoner energy gap $\Delta\varepsilon$. As shown in Fig. 1.4, the Stoner criterion corresponds to a shift of $+\Delta\varepsilon$ in energy for the minority electrons in the DOS of bulk bcc-Cobalt compared to majority electrons, i.e. the band structures are different for each spin population. As we will see, this potential $e\Delta\varepsilon$ is also at the origin of spin dependent transport and spin transfer torque (based on the free electron model) in MTJs. In the next section the basics of spin dependent tunneling processes found in MTJs are presented with emphasis on MgO-based MTJs.

1.1.2 Spin dependent Tunneling processes

In this section, we review models of the spin dependent tunneling effect. The objective is to introduce the basic vocabulary and the limitations of the models presented.

The Stoner potential $e\Delta\varepsilon$ allows one to use the free-electron model to express the tunneling probability for electrons of different spin signs. It serves to define the magneto-resistance (MR) and its approximate evolution with the applied voltage for example. We also introduce the coherent tunneling effect in crystalline magnetic tunnel junctions (MTJ) where the free electron model is of limited use. The coherent tunneling effect is only investigated for the sake of presenting the recent trends in MTJs.

1.1.2.1 Tunneling effect from the free electron models

A magnetic tunnel junction consists of two ferromagnetic electrodes separated by a thin insulating layer. By applying a bias voltage to the structure, electrons will pass through the insulating barrier by an effect known as tunneling. The resulting current that flows inside the barrier is proportional to the density of states close to the Fermi level of each electrode. However, as explained previously, the density of states in ferromagnetic materials are different according to the spin orientation considered. Therefore, for a similar voltage, the parallel (anti-parallel) magnetization configuration, the current density J_P (J_{AP}) is:

$$\begin{cases} J_P \propto N_1^{\uparrow} N_2^{\uparrow} + N_1^{\downarrow} N_2^{\downarrow} \\ \\ J_{AP} \propto N_1^{\uparrow} N_2^{\downarrow} + N_1^{\downarrow} N_2^{\uparrow} \end{cases} , \tag{1.1}$$

where N_i^{σ} are the density of states at the electrode i for the spin direction σ at the Fermi level. Here, we consider that the DOSs remain constant close to ε_F for small applied voltage.

In fact, this model assumes that there are two independent conduction channels for majority and minority spins. In Fig. 1.5, this model is schematically shown. In the parallel case, the majority spins of electrode 1 are also majority spins of electrode 2. On the contrary, for the anti-parallel configuration the majority spins of electrode 1 are the minority spins in electrode 2. The schematics on the right in Fig. 1.5 represent the equivalent electrical circuit of this two channel model in both configurations.

Eq. 1.1 leads to the expression of the Tunnel Magneto-Resistance (TMR) ratio given by Julière in 1975 [3]:

$$\mathrm{TMR}(\%) = \frac{J_P - J_{AP}}{J_P} = \frac{2P_1P_2}{1 - P_1P_2} \quad \text{with} \quad P_i = \frac{N_i^{\uparrow} - N_i^{\downarrow}}{N_i^{\uparrow} + N_i^{\downarrow}} , \tag{1.2}$$

where P_i is the polarization of the i electrode.

Slonczewski [4] then expressed Eq. 1.2 by writing the transmission coefficient for each spin when taking into account the *effective* polarization of the DOS at each Ferromagnetic/Insulator interface:

$$P_i = \frac{(k_{\uparrow} - k_{\downarrow})(\kappa^2 - k_{\uparrow}k_{\downarrow})}{(k_{\uparrow} + k_{\downarrow})(\kappa^2 + k_{\uparrow}k_{\downarrow})} , \tag{1.3}$$

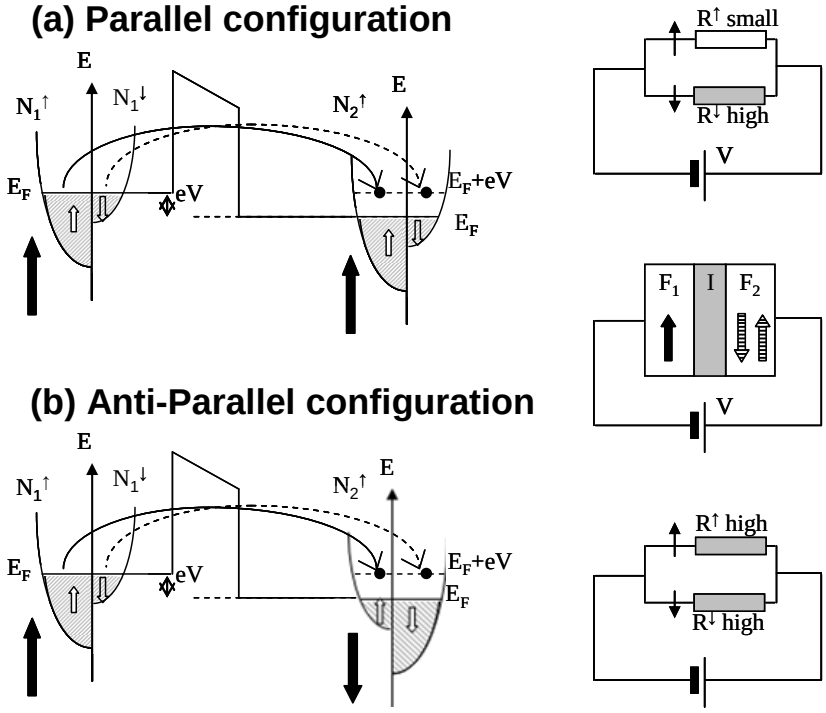

Fig. 1.5: Schematic representation of the golden Fermi rule Eq. 1.1 in (a) the parallel configuration and (b) the anti-parallel configuration of the two electrodes. This two band model supposes the existence of a Stoner potential.

where k_σ depends on the Stoner energy, $\kappa^2 = 2m_e(U_0 - \varepsilon_F)/\hbar^2$ is the effective barrier height and U_0 the total barrier height. Using this formalism, the angular dependence of the conductance $G = I/V$ through an insulating barrier of width d, in the low voltage limit, is given by:

$$G(\theta) = G_0[1 + P_1 P_2 \cos(\theta)] \text{ with } G_0 \propto e^{-2\kappa d} . \tag{1.4}$$

When κ is large, the Slonczewski model (Eq. 1.3) is equivalent to the Julière model for infinite barrier height (U_0 is large). Because this free electron model takes into account the parabolic band structures of each spin direction, it is also possible to derive analytically the expression of the conductance versus the applied voltage similar to the case for non-magnetic tunnel junctions [5, 6] (See for example Ref. [7]).

1.1.2.2 Coherent Tunneling Effects

Since our devices are based on CoFeB / MgO / CoFeB stacks, it will be important to introduce the coherent tunneling effect that is not explained by the free electron model. Indeed, it appears that in crystalline tunnel junctions such as in bcc-Fe/Rock Salt-MgO/bcc-Fe, the electrons propagate or tunnel within specific electronic Bloch states. In the case of bcc-Fe(001), there are four electronic bands, also present in the rock salt MgO structure. In particular, the Δ_1 band is occupied at the Fermi level for the majority spins and has the slowest decay rate in MgO. Indeed at the crystalline Fe/MgO interface, the Bloch vector is assumed to be $k_z = q + ip$ and therefore decays with p

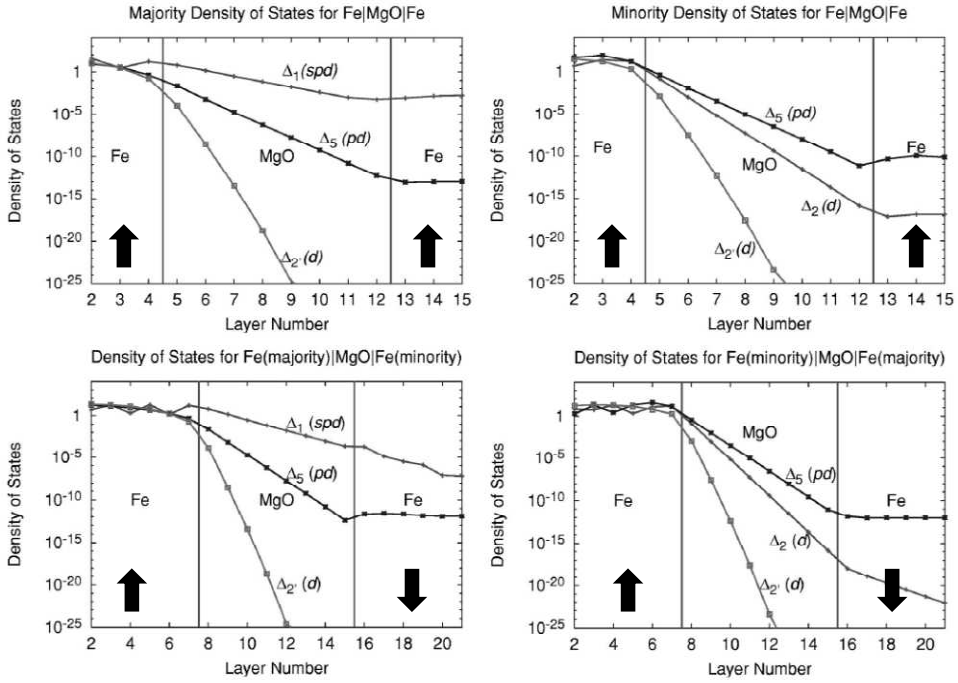

Fig. 1.6: Tunneling-DOS ($\Psi\Psi^*$) for $k_{||} = 0$ in a Fe(001)/MgO(001)/Fe(001) junction in the P state (top figures) and the AP state (bottom figures). The Δ_1 band has the slowest decay rate in the P state (top-left) compared to the other symmetry bands. The Δ_1 band does not exist inside the right Fe electrode for minority spins in the P state (see top-right) and the AP state (see bottom-right). In the AP state, Δ_1 band also decays in the right Fe electrode. Adapted from [9].

which depends on the band considered[2]. This implies that in the parallel configuration, transport will occur through the Δ_1 band. The slow decay rate of the Δ_1 band and the relatively low electron probability in the AP state are illustrated in Fig. 1.6 that shows the density of state for each electronic band in the P and the AP state for an epitaxial Fe/MgO/Fe junction.

The calculations given in Ref. [9] reported a TMR ratio higher than 1000% in Fe(001) / MgO / Fe(001) crystalline junctions. Even higher TMR ratios were reported from calculations for FeCo / MgO / FeCo crystalline junctions [10]. In real structures with defects it is still unlikely to reach such predicted values, for instance a TMR of 1000% at 5 K has been reached by Ikeda et al. [11] after a careful stack engineering with CoFeB electrodes. The advantage of CoFeB electrodes is that after deposition, the CoFeB / MgO / CoFeB stack is amorphous. After annealing, the MgO imposes its crystalline structure onto the CoFeB electrodes that forms an epitaxial FeCo(001) / MgO(001) / FeCo(001) heterostructure (the boron is diffused to the grain boundaries).

[2]For a lattice parameter a, Bloch conditions impose that the Bloch wavefunction satisfies $\Psi_k(r+a) = (\exp ik_z \cdot a)\Psi_k(r)$ [8].

1.2 From STT to Spin Torque Oscillator

While the giant magneto-resistance (GMR) effect discovered in 1988 [12, 13] found direct application for read-head sensors in 1995, the reverse associated effect known as Spin Transfer Torque (STT) was theoretically described by Slonczewski [14] and Berger [15] only in 1996. Two years after these predictions, Tsoi et al. [16] experimentally observed the first excitations in magnetic spin-valves due to spin polarized current. A year later, magnetic switching in metallic magnetic spin valves was observed by Myers et al. [17] and Katine et al. [18]. The first observations of magnetic switching/excitations in MTJ devices based on an alumina oxide barrier have been done by Fuchs et al. [19]. Soon after, first studies reported STT effect in crystalline MgO based MTJ. This was shown on a 4kbit memory STT-MRAM chip presented by Hosomi et al. [20] from Sony Corporation. While alumina-based MTJ were already of use for practical applications even with a TMR of 70% [21], the combination of STT and large TMR ratio due to MgO coherent tunneling effect leads to a very important perspective of STT-MRAM as a future integrable non-volatile memory. Indeed the ITRS roadmap starts to include the MRAM development as a key memory for future electronics applications [22].

In this section, we introduce for the specific case of MTJs the effect of STT on the local magnetization of the ferromagnetic electrodes using the Landau-Lifshitz-Gilbert-Slonczewski equation. This equation describes the switching of the magnetization in STT-MRAM as well as the magnetization dynamics. After a short introduction of this LLGS equation we summarize the dynamic magnetization states induced by the STT and indicate the influence of the thermal fluctuations on the switching in precessional dynamics.

1.2.1 Magnetization Dynamics under STT

The equation that governs the dynamics of ferromagnetic materials under STT is the Landau-Lifshitz-Gilbert-Slonczewski (LLGS) equation. To understand this equation, we subsequently introduce each of its terms. We first introduce the LLG equation, which describes the magnetization dynamics with damping only. We then introduce the origin of the STT terms and their impact on the magnetization dynamics. It will allow us to give the magnetization state diagram in presence of STT section 1.2.2.

1.2.1.1 The LLG equation

The evolution of the magnetization $\vec{M}$ under the torque $\vec{T}$ exerted by a magnetic field $\vec{H}$ is given by:

$$\frac{d\vec{M}}{dt} = -\gamma\vec{T} = -\gamma\vec{M} \times \vec{H} \ , \tag{1.5}$$

where γ is the gyromagnetic ratio. The potential energy U_e of the magnetization $\vec{M}$ in a magnetic field $\vec{H}_e$ can be written:

$$U_e = -\mu_0\vec{M} \cdot \vec{H}_e \ , \tag{1.6}$$

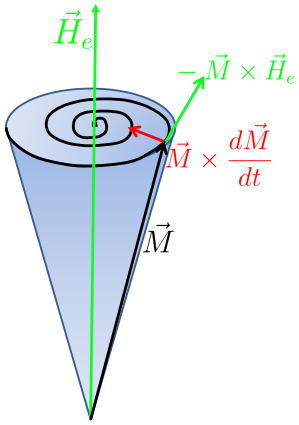

Fig. 1.7: Schematics of the precessional torque $-\vec{M} \times \vec{H}_e$ and damping torque $\vec{M} \times \frac{d\vec{M}}{dt}$. The black spiral represents the magnetization trajectory.

with μ_0 the magnetic permeability. It is possible to find $\vec{H}_e$ for any conservative magnetic interaction (i.e. magnetic energy), so that the total potential energy U_e is the sum of all potential energies U_i resulting from any fields $\vec{H}_i$ acting on the magnetization $\vec{M}$. If we now consider the equilibrium position to be $\frac{d\vec{M}}{dt} = 0$ from Eq. 1.5, for a given applied field (i.e. magnetic energy), it implies that:

$$\vec{H}_e = -\frac{\partial U_e}{\delta \vec{M}} \, .$$

It is important to note that the field $\vec{H}_e$ in Eq. 1.5 is an *effective field* since it results from the sum of all interactions acting on the magnetic moment. We list in the following some of the different magnetic interactions that can be found in our devices. The Zeeman interaction that originates from an external applied field to the magnetization, the demagnetizing interactions that include dipolar field and shape anisotropies (that are self-fields of the magnetization), the magneto-crystalline anisotropy, which can have many forms and symmetries. In our study, we will consider the "Macrospin" approach, that is to consider the exchange energy (interaction) is so large that all spins are parallel and act as one single "macro" spin. There exist other types of magnetic interactions that have to be considered for specific studies, such as interlayer exchange bias interaction that occurs at the interface between a ferromagnetic layer and an antiferromagnetic layer, or the interlayer exchange interaction across nonmagnetic layer NM in FM/NM/FM structures called the RKKY interaction.

According to Eq. 1.5, the magnetization only precesses around the effective field on a closed loop trajectory, i.e. at constant magnetic energy U_e. In reality, the magnetization is damped such that the magnetization aligns towards the effective field ($\vec{M} \times \vec{H}_e = \vec{0}$). While the detailed mechanisms contributing to magnetization damping are not yet fully elucidated, Gilbert introduced a phenomenological damping torque to Eq. 1.5 to obtain the LLG equation:

$$\frac{d\vec{M}}{dt} = -\gamma \vec{M} \times \vec{H} + \gamma \frac{\alpha}{M_s} \vec{M} \times \frac{d\vec{M}}{dt} \, , \tag{1.7}$$

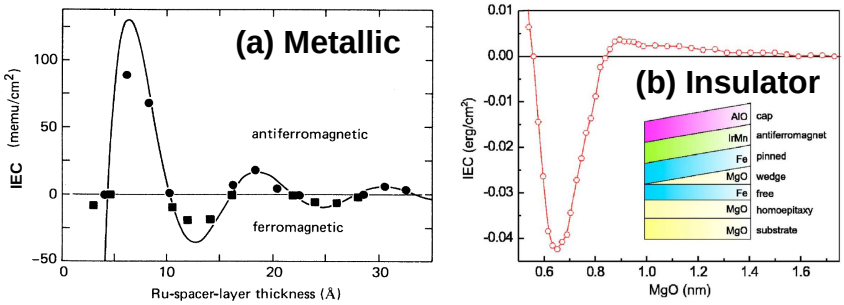

Fig. 1.8: Measured strength of the IEC energy for (a) a Py/Ru(t)/Py stack [24] and (b) Fe/MgO(t)/Fe MTJ [25].

with M_s the magnetization at saturation and α the Gilbert damping constant. Typically, $\alpha \approx 0.01$ in normal ferromagnetic metals. From any initial position, the damping makes the magnetization to relax towards the effective field on a timescale given by αM_s. The effect of damping on the overall trajectory is shown in Fig. 1.7.

The damping term originates from energy exchanges between magnetization and the thermal bath. Both *intrinsic* and *extrinsic* damping contributions can exist in a given material. The intrinsic damping term is still subject to discussions and it depends on the material considered. For metals recent theories aimed to predict its value from *ab-initio* calculations. The *extrinsic* term is given by the environment of the ferromagnetic material. Magnons can interact/scatter in such a way that they contribute to the observed damping. Also, spin pumping can contribute to the damping term. The spin pumping effect considers that due to the precession spins are pumped out of the volume. If these spins are scattered before they return to the precessing volume then damping is enhanced. See Ref. [23] for more details.

In the next part, we introduce the spin transfer torques that induce both a novel magnetic (conservative) interaction, and a novel *extrinsic* damping term. In addition, we will see that the damping contribution of STT can be negative, i.e. can compensate the intrinsic damping. This allows one to study the magnetization dynamics in the nonlinear regime. We introduce in the following both the origins and the effects of the STTs on the magnetization dynamics, with a focus on the "free" layer of a MTJ.

1.2.1.2 The Spin Transfer Torques

In a MTJ - we only consider the dynamics of one layer - called the Free Layer - with respect to the other one - called fixed layer - which is pinned by a large exchange field. In the standard notation $FM_1/MgO/FM_2$ for an MTJ, we consider FM_1 (FM_2) as the fixed (free) layer with a magnetization $\vec{M}_1$ ($\vec{M}_2$). In addition to usual magnetic interactions acting on a simple magnetic particle in the macrospin approach, it is possible that a magnetic interaction occurs because of the proximity of another magnetic moment.

The RKKY coupling mediated by conduction electrons between two ferromagnetic layers separated by a thin metallic film is an example of this. From the coupling energy $E_{RKKY} = J\vec{M}_1 \cdot \vec{M}_2$, a field $H^i_{RKKY} = \partial E_{RKKY}/\partial \vec{M}_i$ acts upon FM_i and therefore exerts a torque on FM_i.

A similar interlayer exchange coupling (IEC) happens in MTJs, where "the RKKY

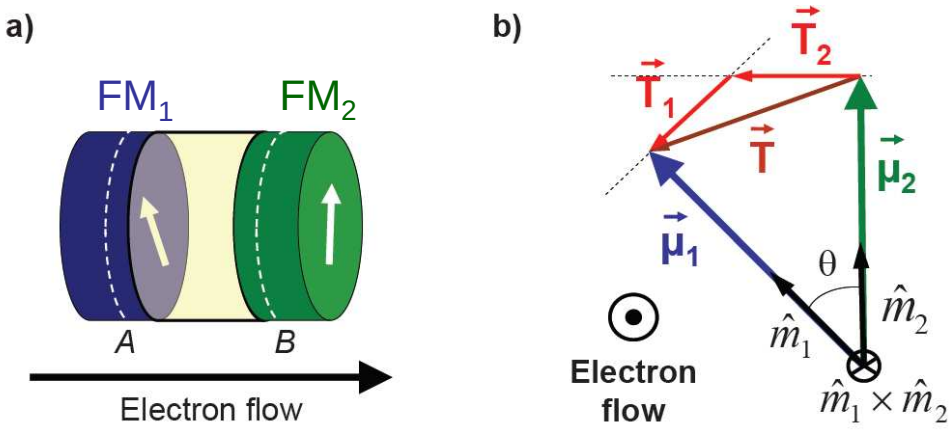

Fig. 1.9: (a) Schematic of the MTJ with FM_1 and FM_2. (b) Schematic of torques involved. To change its angular momentum from $\vec{\mu}_1$ to $\vec{\mu}_2$, "one" electron has to lose the torque $-\vec{T}$. This torque is subdivided in $\vec{T}_1$ and $\vec{T}_2$ that respectively acts on $\vec{M}_1$ and $\vec{M}_2$. From [26].

coupling" is now mediated by the evanescent states rather than conduction electrons [4, 26]. In Fig. 1.8 experimental measurements of this IEC strength in metallic and insulator based heterostructures is shown as a function of interlayer thickness. The physical origin of these torques is that the number of electrons that flow from the left to the right electrodes and from the right to the left electrodes are equal such that there is no net current charge but a non-zero spin current, even at zero voltage bias. This results in an equal transverse torque on each electrodes. When applying a voltage bias to the MTJ, there is now an additional contribution to this torque due to the net charge current. Finally, the total torque acting on $\vec{M}_2$ can be written as:

$$\vec{T}_\perp = \vec{T}_\perp^0 + b_j \vec{M}_2 \times \vec{p}\,, \tag{1.8}$$

where $\vec{T}_\perp^0$ is the zero voltage bias torque, b_j depends on the net charge current and $\vec{p}$ is the orientation of the fixed magnetic moment ($\vec{M}_1$). The transverse torque due to the b_j term is similar to the torque exerted by a magnetic field, that is why this term is referred as "field-like term".

Finally, we introduce the term known as *Spin Transfer Torque* in MTJ which is responsible for inducing steady state oscillations of the magnetization or its switching. We consider the MTJ with $\vec{M}_1$ and $\vec{M}_2$ that are misaligned with an angle θ and an electron flow from the left to the right electrode (see Fig. 1.9). Electrons flowing in FM_1 are spin polarized along $\vec{M}_1$ and carry an angular spin momentum $\vec{\mu}_1$, once they have passed through FM_2 their angular spin momentum is $\vec{\mu}_2$. Hence, a momentum $\vec{T}$ is given to the system in the process (the electron flow in the MTJ). Since the magnetizations $\vec{M}_1$ and $\vec{M}_2$ "give" their spin orientation to the electron flow, it is natural that spin polarized electrons "give back" their momenta to the magnetization $\vec{M}_1$ and $\vec{M}_2$. However, the magnetization norm $\vec{M}_1$ and $\vec{M}_2$ are constant:

$$\frac{d\left|\vec{M}\right|^2}{dt} = 2\vec{M} \cdot \frac{d\vec{M}}{dt} = 0\,. \tag{1.9}$$

It results that any variation $\frac{d\vec{M}}{dt}$ is necessarily transverse to the magnetization $\vec{M}$. $\vec{T}$ is then written as a sum of two moments $\vec{T}_1$ and $\vec{T}_2$ acting respectively on $\vec{M}_1$ and $\vec{M}_2$. In practice, FM_1 is designed to be "*fixed*" with the direction $\vec{p}$, so as to make FM_1 insensitive to $\vec{T}_1$, for example by using a Synthetic Anti-Ferromagnetic (SAF) structures or a thick electrode FM_1. Similarly to the b_j term in Eq. 1.8, $\vec{p}$ is used such that the torque acting on FM_2 can be written:

$$\vec{T}_2 = \vec{T}_{\parallel} = \frac{a_j}{M_s}\vec{M}_2 \times \left(\vec{M}_2 \times \vec{p}\right) \ , \tag{1.10}$$

where a_j depends on both current amplitude and orientation. The direction of this torque $\vec{T}_{\parallel}$ can have a component in the same direction as the aforementioned damping term. Indeed, the vector $\frac{d\vec{M}_2}{dt}$ is orthogonal to $\vec{M}_2$ and so is $\vec{M}_2 \times \vec{p}$. However, the a_j term sign is linear with the current flow and therefore, the orientation of $\vec{T}_{\parallel}$ depends on the current orientation. As a consequence, the STT can either increase the Gilbert damping, reduce it or even fully compensate it. Based on this idea, Slonczewski [14] and Berger [15] predicted steady state oscillations and switching of the magnetic moment under the influence of current flow in a multilayer magnetic structure.

Recent works on STT in MTJ are about to determine exactly the voltage (or current) dependence of parallel and perpendicular torques. The present consensus is that a_j and b_j terms depend on the MTJ stack composition. Indeed, those terms are very related to the Stoner potential in $3d$ transition metals [26]; experiments and theories agree that a_j is mostly linear with current and b_j mostly quadratic (at low bias) [27, 28].

The exact determination of those terms is not only of fundamental interest but also of main importance for application purposes since STT effects are expected to be used in high density RAM. For example, it has been shown that "back switching" processes occur at high bias voltage due to the field like term b_j which always favors one magnetic configuration in MTJ [29].

By including the STTs in the equation of motion of LLG, one obtains the generalized LLGS equation for a MTJ:

$$\frac{d\vec{M}}{dt} = -\gamma\vec{M} \times \vec{H} + \gamma\frac{\alpha}{M_s}\vec{M} \times \frac{d\vec{M}}{dt} + \gamma\frac{a_j}{M_s}\vec{M} \times \left(\vec{M} \times \vec{p}\right) + \gamma b_j \vec{M} \times \vec{p}\,. \tag{1.11}$$

From an energy point of view, only the damping term and the a_j term contribute to the total magnetic energy variation given by:

$$\frac{dE}{dt} = -\frac{\alpha}{\gamma M_s}\left(\frac{d\vec{M}}{dt}\right)^2 - \frac{a_j}{M_s}\frac{d\vec{M}}{dt}\left(\vec{M} \times \vec{p}\right) \ . \tag{1.12}$$

While the damping term is always negative (i.e. always brings the system toward its equilibrium), the energy contribution of STT will be either an energy source for the system or an additional dissipative (or damping) contribution. In the case of an energy source, a closed loop trajectory, i.e. a stable dynamical state, for the magnetic moment exists if the integral of $\frac{dE}{dt}$ over the period of the trajectory is zero. In this scenario, the STT is said to *compensate* the intrinsic damping. This condition is a prerequisite to steady-state oscillations of the magnetization under a current bias and occurs when

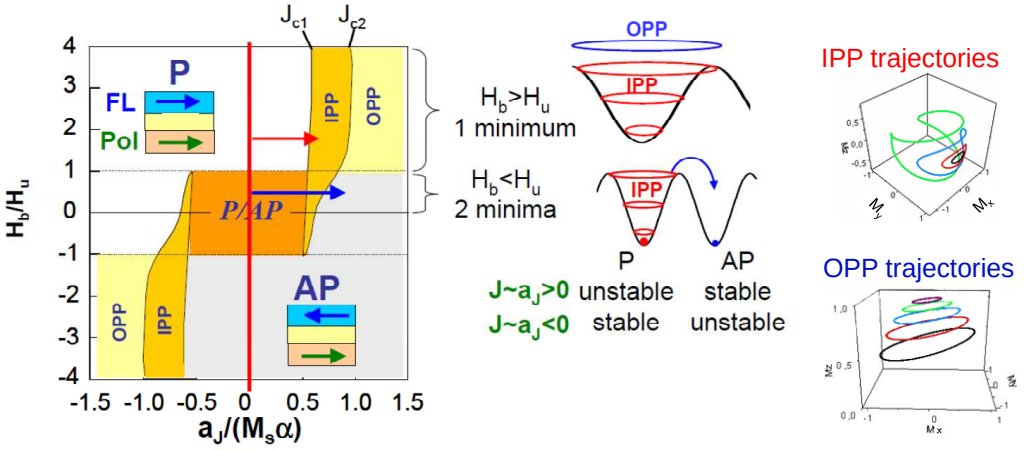

Fig. 1.10: State diagram of the magnetization state in In-plane magnetized structures. Only a_J is considered. For a constant applied field, two different evolutions of the magnetic state appear with increasing $|J|$. The system describes the IPP trajectory and then switching to the other static state for $H < H_b$. For $H > H_b$, the system passes from IPP to OPP. Right, IPP and OPP trajectories calculated from the integration of LLGS equation. Adapted from [26].

the current is strong enough. At this point the current corresponds to a critical value I_c, for which the auto-oscillation regime starts. To find the steady-state solutions, the detailed geometry must now be considered (applied field orientation, polarizer orientation, anisotropies and other interactions). The next section is dedicated to the most simple case that corresponds to the one studied in this thesis.

1.2.2 State Diagram of in-plane magnetized magneto-resistive devices

The simplest case is the one of an in-plane magnetized MTJ, where the free layer and polarizer layer are in-plane and collinear. If the b_j term is neglected, two magnetization dynamical modes occur under the influence of STT in its simplest form ($a_j \propto I$). When the free layer has a uniaxial anisotropy (given by an anisotropy field $\vec{H}_u$) in the same direction as the polarizer and the applied field, the state diagram is schematically similar to the one given in Fig. 1.10 at 0 K. At zero applied field ($H_b = 0$) and no current, there are two energy minima (P and AP state) and the initial state defines the evolution of the magnetization with applied current.

For example, for an initial P state, applying a positive current induces In-Plane Precession (IPP) trajectories above the critical current J_{c1} that compensates the damping term in Eq. 1.11. Then the switching occurs when $J > J_{c2}$ since the energy provided by the STT term will make the total energy higher than the energy barrier between P and AP states (see schematic with energy landscape of Fig. 1.10). When reducing the current back to zero, the system energy minimum exists and is stable in the AP state and will remain in the AP state.

When $H_b > H_u$, only the stable state is P (for realistic values of current). When increasing the current to positive values from zero, the system successively describes IPP trajectories (from J_{c1}) and Out-of Plane Precession (OPP) trajectories (from J_{c2}).

The transition between the static state to the IPP state will be of main interest to us. In terms of Eq. 1.11 it corresponds to a full compensation of the damping term around the magnetization equilibrium position. This physical picture based on damping and STT compensation is actually similar to any descriptions of a dynamical system. The transition between the stable state of the system toward a dynamical state is called a *bifurcation*. In the given case here this is a *supercritical Hopf bifurcation*, that has a strict mathematical definition, but that at last leads to steady state oscillation close to a limit cycle. The second bifurcation that happens between IPP and OPP is more complicated and some simulations predict chaos to appear at the IPP/OPP transition [30, 31].

1.2.3 State diagram with temperature

Since the resistance of a GMR or TMR structure depends on the relative angle between the free and the fixed layer (see for example Eq. 1.4), state diagrams can be deduced from the measurement of the resistance or the average resistance. For the static regime, it can be realized by monitoring the resistance (see Fig. 1.11-a,b), and for dynamic states, one can monitor the alternating dynamic resistance induced in the gigahertz (GHz) range (via a spectrum analyzer; see chapter 3). For that reason, direct comparison between experiments and expected state diagrams can be performed.

However, the model presented in Fig. 1.10 can be far from what is observed experimentally since it does not take into account the effect of temperature. For example, the experimental results from Schneider et al. [32] presented in Fig. 1.11-a,b clearly indicate that the window defined by switching boundaries decrease from the expected one when increasing the temperature. Another example is shown in Fig 1.11-c from direct integration of Eq. 1.11 when taking into account a fluctuating thermal noise field of the form [33]:

$$\langle H^i(t)H^j(t')\rangle = \frac{2\alpha k_b T}{\gamma_0 V \mu_0 M_s}\delta_{i,j}\delta(t-t') \ , \tag{1.13}$$

with i, j representing Cartesian coordinates and the brackets are the time average. This fluctuating field enters the effective field in the Eq. 1.11. Its main property is that it corresponds to a white Gaussian noise, only $\langle H^i(t)H^i(t)\rangle$ is non-zero.

This simulations show well the bi-stable state and IPP modes when including the temperature and a shift of critical switching field is also observed. While numerical state diagrams are very dependent on the model considered for the angular dependence of a_j term, it is interesting to point out two general features of state diagrams extracted from the numerical solution of LLGS (Eq. 1.11) with thermal noise. The first feature is how the noise affects the magnetization switching process in presence of STT. The second feature is how it affects the steady states precession of the magnetization. In the next subsection we indicate the role of noise on switching processes, while the effects on steady oscillations are only envisaged as an introduction for the chapter 2 dedicated to the general study of auto-oscillators in the absence and in the presence of noise.

1.2.3.1 Effects on the Switching Process

With the inclusion of temperature, the bistable region denoted "P/AP" is reduced due to thermal activation whereby $\vec{M}$ can overcome the energy barrier between the two minima

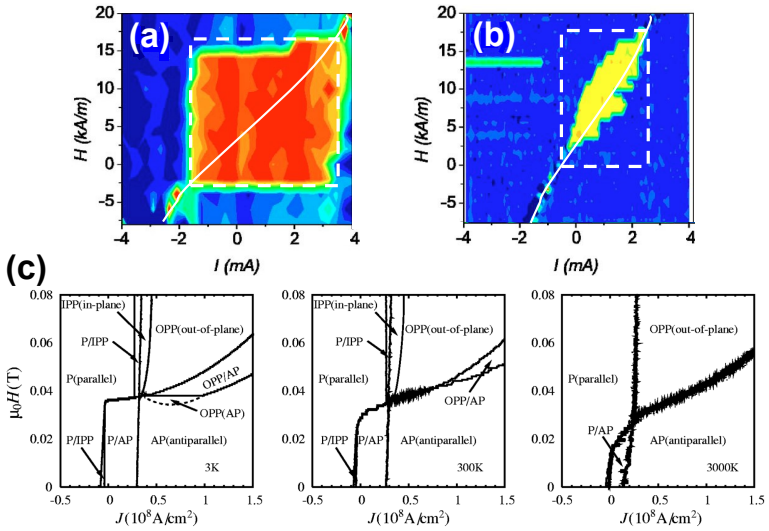

Fig. 1.11: Experimental phase diagram centered at the bistable "P/AP" region at (a) 5 K and (b) 300 K. From [32]. White dashed boxes represent the supposed 0 K bistable region. While parameters change with temperature (reducing the dashed white box by increasing temperature), it is clear that temperature also affects the observed P to AP or AP to P transition region. (c) State diagrams from numerical integration of LLGS with thermal fluctuations (from left to right: 3 K, 300 K, 3000 K). The hysteretic behavior found at 3 K for the IPP/P transition is only present if ones consider the Slonczewski formulation for a_j. Adapted from [34].

"P" and "AP". It leads to a non-trivial dependence of the critical lines (switching from AP to P or P to AP) with temperature. Defining a comprehensive predictive model for the magnetic particle under both current and temperature effects has attracted particular attention due to its impact on a large ensemble of memory cells such as in STT-MRAM technologies. From numerical simulations and experiments, the switching mechanism depends on the time scale of the current pulse width. As shown in Fig. 1.12, 3 main switching mechanisms exist in the macrospin approach in presence of thermal fluctuations.

Precessional switching occurs at very high current densities for which a direct (*ballistic*) switching of the magnetization occurs. The a_j term makes the magnetic energy variation in Eq. 1.12 so large that it is only possible to make a direct *ballistic* switching. In this case, at a constant current value, the switching time will arise from the initial angle of the magnetization with respect with the fixed magnetic moment. The effect of temperature on the switching time distribution will thus only depend on the initial magnetization angle distribution [35]. The mean switching time therefore only depends on the magnetization dynamics, even in the presence of temperature.

On the contrary, in the purely thermally activated regime, switching time only depends on the energy barrier KV, where V is the volume of the magnetic particle and K the anisotropy constant. In this case, switching can occur at $I < 0.5I_c$ for microsecond current pulse widths.

Finally, the *dynamical* regime corresponds to the case in which IPP trajectories first grow in amplitude until switching occurs. As shown in the schematic of Fig. 1.10, the IPP trajectory is at higher energy than the stable state. When the magnetic particle describes

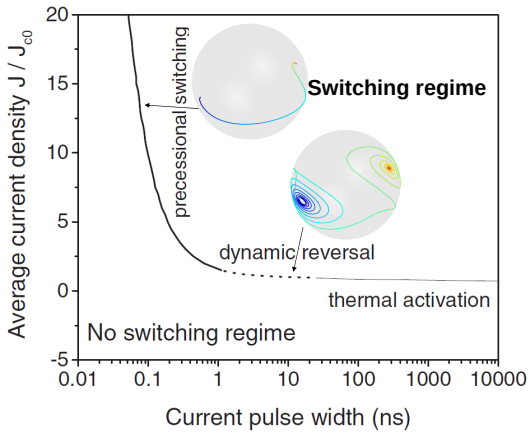

Fig. 1.12: Magnetization switching phase diagram adapted from [35]. There are three switching regimes, from left to right: precessional, dynamical and thermally activated switching, respectively.

an IPP, the energy barrier from this state to the switched state is reduced. Therefore, during the trajectory, the switching can be thermally activated in a way that the mean switching time will not depend only on the dynamic properties of the magnetization, but rather on a mix between thermally activated and dynamical processes (that in turn depends on the initial cone angle as for the *ballistic* regime). While the temperature dependence of the switching time in the macrospin approach is well understood, one of the main reasons why STT-MRAM is still not on the market is that for billions of MRAM cells, reliable and repetitive switching has to be established with the same current densities. However, some cells also undergo a switching process that depends on the micromagnetic configuration. For example, it has been shown that in perpendicular STT-MRAM, the switching occurs through domain wall (DW) nucleation [36, 37].

1.2.3.2 Effects on the Stable Dynamical States

Fig. 1.10-c shows that stable dynamical states of the magnetization exists whose critical lines (stable state to dynamical state or dynamical to stable state) are temperature independent (especially when $\vec{H} > \vec{H}_u$). Particularly, the bifurcation between a static state and IPP is temperature independent in LLGS, since temperature does not affect damping and STT terms (when thermal fluctuations are considered in the form of Eq. 1.13). However, material parameters (M_s, α) and a_j are temperature dependent and will induce a temperature dependence of critical lines j_{c1} experimentally (compare the white dashed boxes in Fig. 1.10-b,c).

In other words, while the average switching current is affected by both the experimental protocol (current pulse width, shape and sample temperature), the critical lines from static states to IPP modes are independent of it. This statement is strictly reserved to the Macrospin approach. Similarly to switching by nucleation in micromagnetism, spin wave modes can occur at the vicinity of I_c [38] and can modify the aforementioned bifurcation picture (this "picture" is used all along the thesis). In chapter 4, we will address the question of the critical current determination I_c in both macrospin simulations and experiments.

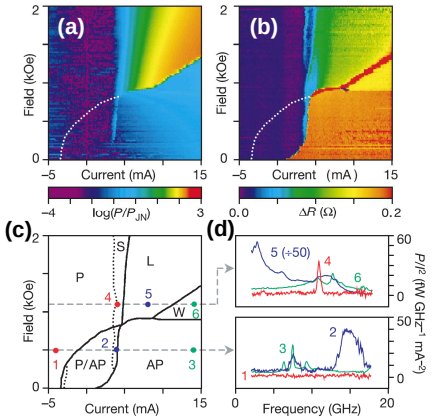

Fig. 1.13: (a) H-I diagram of the output power measured on a Co/Cu/Co nanopillar. (b) Differential resistance plotted in colors for the same (H-I) region. (c) Deduced state diagram. S and L refer respectively to small and high amplitude IPP modes. W refers to chaotic modes [40]. (d) Output Spectra for different operating points. From [39].

We now introduce the consequences of temperature on the steady state precession of the magnetization and especially on the IPP mode. In Fig. 1.13 we show the first experimentally measured dynamical state diagram by Kiselev et al. [39] with corresponding voltage output in the GHz range. The information extracted from both output power and differential resistance measurement indicate a good agreement with the numerical integration of LLGS. For the region "W", however, the Macrospin model fails to predict the mode since it is a non-uniform mode [40].

The feature that we will concentrate on is the linewidth broadening present in the emitted spectra of those structures under a current/voltage bias. This broadening is considered to be a consequence of the fluctuations of the trajectory due to the fluctuating field defined by Eq. 1.13. In Fig. 1.14 the macrospin trajectory is given with and without considering the fluctuating field. The calculated power spectral density (PSD) of the signal emitted from a MTJ is also given. It is clear that the noise broadens the linewidth of the microwave emission.

The fluctuating field is an additional contribution to the effective field in the LLGS equation 1.11. An analytical study of the impact of the noise on the system is difficult from this equation. Therefore, a mathematical formalism for oscillators will be used, which is a powerful tool to predict lineshape broadening of oscillation. In particular, it allows one to directly link the noise source to the oscillator output. Because the aim of this thesis is to describe the way the magnetization dynamics is affected by the noise (resulting in lineshape broadening), the description of LLGS as an oscillator is a prerequisite. A detailed description will be given in chapters 2 and 4, but we give a first outline of it here.

1.2.3.3 Spin Transfer Oscillator in presence of noise

Due to the magnetoresistive effect (see for example Eq. 1.4), we can consider that the STO output is an oscillating voltage $V(t)$ proportional to the angle formed by the polarizer and the free layer. We also only consider the first harmonic of this signal. Then the main angular frequency of $V(t)$ is $\omega_0 = 2\pi f_0$ and its mean amplitude V_0, so we can write:

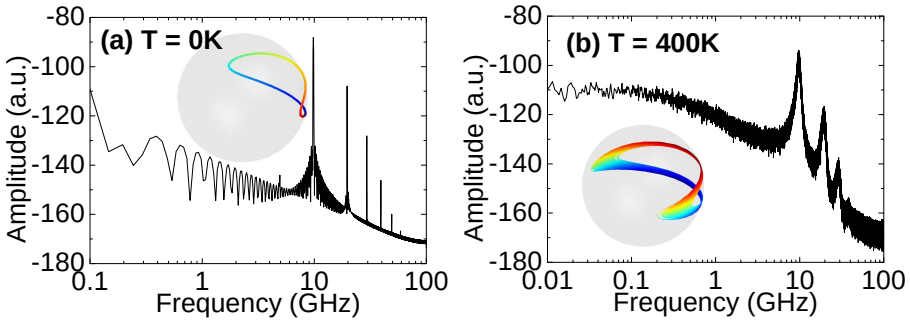

Fig. 1.14: PSD of the M_x component for a typical IPP mode for (a) $T = 0$K and (b) $T = 400$K. The broadening of the trajectory implies the broadening of the emission lineshape. Simulations by D. Gusakova.

$$V(t) = V_0 \cos(\omega_0 t) \ .$$

This output voltage corresponds to an ideal noiseless oscillator (LLGS without Brown fluctuating field, Eq. 1.13). Nonetheless, in a real system, noise is inevitable such that it affects the real oscillator. We distinguish noise that can affect the amplitude V_0 from the one that affects the phase term in the cosine. The inclusion of such noise terms leads on output voltage of the form:

$$V(t) = [V_0 + \epsilon(t)] \cos\left(\omega_0 t + \phi(t)\right) \ , \tag{1.14}$$

where $\epsilon(t)$ is the amplitude noise and $\phi(t)$ the phase noise. When $\epsilon(t) << V_0$ and $\phi(t) << 1$, signal analysis of those terms can be simplified as it will be shown for conventional electrical oscillators in chapter 3.

If we consider the power spectral density of $V(t)$, the oscillation power is spread around the main central frequency f_0, as a result of these noise contributions. Some examples are shown Fig. 1.15 for different noise contributions in phase or amplitude.

One of the main objectives of this thesis is to understand and analyze the amplitude and phase noise observed at the output signal of spin torque oscillators due to the thermal noise field Eq. 1.13. In order to achieve this, we will introduce in chapter 2 first the basic concepts of a noiseless oscillator and the role of damping and anti-damping terms to establish a link between such an oscillator model and LLGS in the form of KTS model. We then give the basic framework of autonomous (free regime) and non-autonomous (forced regime) dynamics of auto-oscillators, and of the autonomous dynamics of the auto-oscillator in presence of noise.

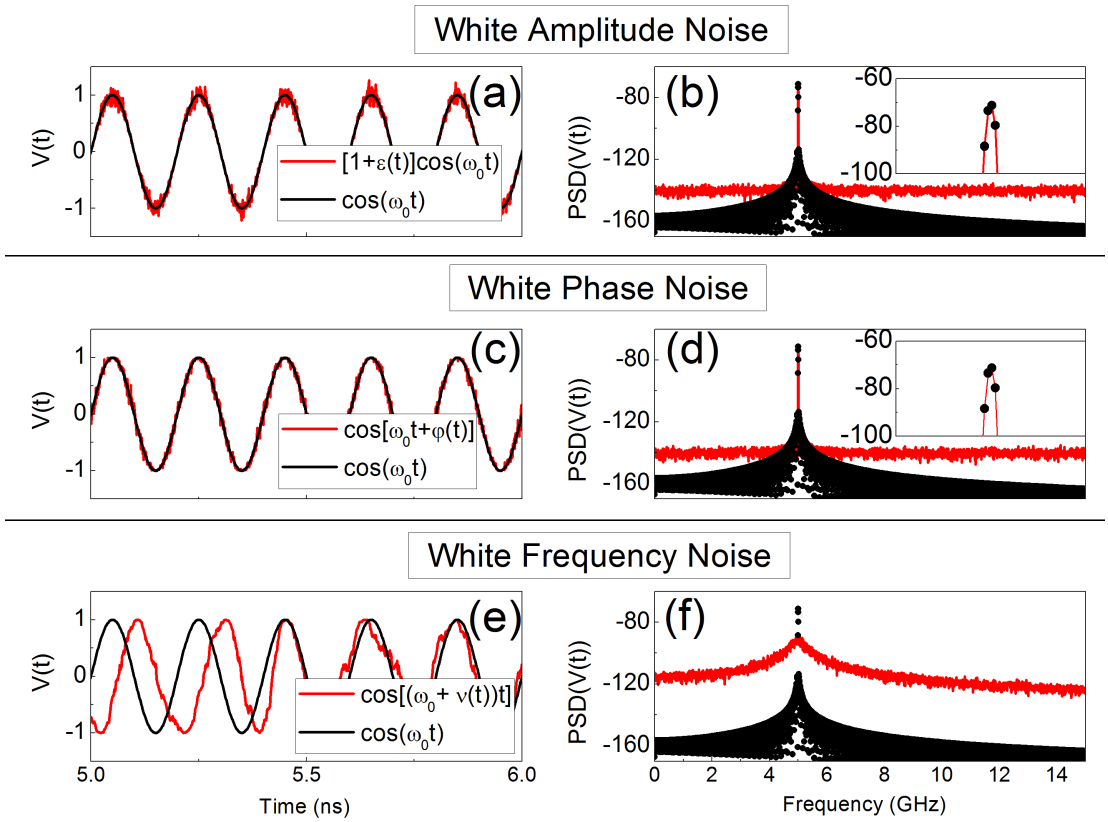

Fig. 1.15: Time varying output voltage and corresponding PSD. The simulated signal corresponds to Eq. 1.14 by including (a) and (b) white amplitude noise, (c) and (d) white phase noise and (e) and (f) white frequency noise. In the insets, the peaks near the oscillating frequency are compared to a signal without noise that is the black dot curve: instead of pure Dirac peak, it has a non-zero width since the PSD is obtained on a finite time trace. The integrated power of the PSD is the same for all signals with or without noise source. While the white amplitude and phase noise do not affect the width of the PSD at all (c) and (d), the white frequency noise - or random walk of phase - gives the well known Lorentzian spectrum (f).

Chapter 2

Context - Spin Torque Oscillator

This introductory chapter is dedicated to illustrate the mathematical and physical nature of oscillators that provide the framework for the Spin Torque Oscillator (STO). In the first section we give the basis of damped oscillators and how they differ from self-sustained oscillators. It will illustrate two of the main features of the magnetization dynamics: ferromagnetic resonance under current bias and the steady state oscillations of the magnetization induced by STT. Finally, we review results from literature that confirm specific aspects of the theoretical predictions that were obtained before or at the start of this thesis.

2.1 Oscillators: an introduction

Ideally, an oscillator is a system characterized by a periodic output in time. A simple example is the free pendulum at low angle. If we consider the angle θ defined as the angle between the weight vector $m\vec{g}$ and the vector formed by the string of the pendulum $\vec{OM}$ of length l (see Fig. 2.1), θ is a solution of:

$$\ddot{\theta} + \frac{g}{l}\sin(\theta) = 0 \ . \tag{2.1}$$

Eq. 2.1 is nonlinear by nature, but the small angle approximation allows one to write:

$$\ddot{\theta} + \frac{g}{l}\theta = 0 \ . \tag{2.2}$$

In this case the solution is simple and the period of the oscillation T is $2\pi\sqrt{\frac{l}{g}}$. In a more realistic system, there are energy losses as the oscillating system is always damped out towards the static equilibrium state. By considering the simplest form of damping, i.e. losses that are proportional to the angular velocity $\dot{\theta}$, Eq. 2.2 becomes:

$$\ddot{\theta} + \lambda\dot{\theta} + \frac{g}{l}\theta = 0 \ , \tag{2.3}$$

with $\lambda > 0$. The solution of Eq. 2.3 is such that $\theta(t) \xrightarrow{t\to\infty} 0$. Depending on the value of λ, the system can be either pseudo-periodic (damped oscillation) or either exponentially damped out to the equilibrium state. Actually such an oscillator θ is said to be a "damped harmonic oscillator" and is found in ubiquitous real systems in physics: pendulums, RLC

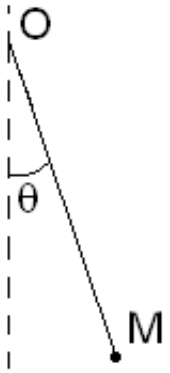

Fig. 2.1: Simple pendulum oscillator.

circuits, mass-spring systems, etc... From Eq. 2.3, it is obvious that a damped harmonic oscillator is not a "self-sustained" oscillator that has continuous oscillating outputs in time. In the following we give the main characteristics of a harmonic oscillator that is a "passive" - or driven - oscillator where steady-state oscillations are only possible when an oscillating driving signal is applied to the oscillator. In contrast to a "passive" oscillator we will introduce the notion of "self-sustained" oscillations (or "auto-oscillations") that do not need this additional driving force.

2.1.1 Damped oscillator, resonator and quality factor

To study Eq. 2.3 in the presence of an external driving signal, it is common to use a complex representation, because it has an easy relationship with the signal PSD:

$$\frac{d^2c}{dt^2} + 2\xi\omega_0\frac{dc}{dt} + \omega_0^2 c(t) = f(t) \ , \tag{2.4}$$

where $f(t)$ and $c(t)$ are complex functions, $\xi > 0$ is the damping ratio and $\omega_0^2 > 0$ the square of the oscillator angular frequency. When $f(t) = f_e \exp(iwt)$, the steady-state solutions are assumed to have the form:

$$c(t) = A(\omega)e^{\imath\omega t + \varphi(\omega)} \ ,$$

where $A(\omega)$ and $\varphi(\omega)$ are respectively the amplitude and the phase shift with respect to the external driving source such that:

$$A(\omega) = \frac{f_e}{\sqrt{(\omega_0^2 - \omega^2)^2 + (\lambda\omega)^2}} \ ; \tag{2.5}$$

$$\varphi(\omega) = \arctan\left(\frac{\lambda\omega}{\omega^2 - \omega_0^2}\right) \ , \tag{2.6}$$

with $\lambda = 2\xi\omega_0$, the damping rate of the harmonic oscillator.

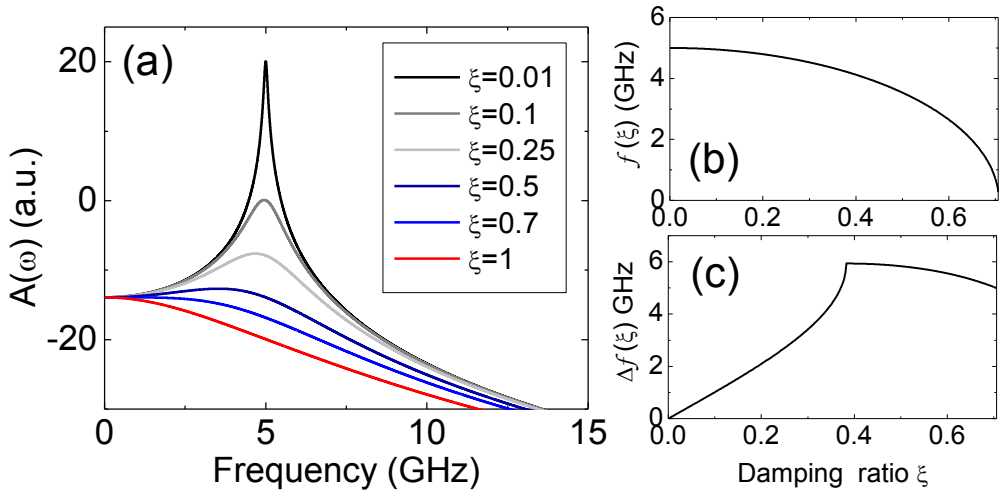

Fig. 2.2: (a) The oscillation amplitude $A(\omega)$ for different values of damping ratio ξ as calculated from Eq. 2.5. (b) The frequency at the maximum value of $A(\omega)$ (i.e. the resonant frequency) versus damping ratio ξ. (c) Full Width at Half Maximum Δf of $A(\omega)$ versus ξ. The mode frequency is $f_0 = \omega_0/2\pi = 5$GHz.

In Fig. 2.2 the amplitude part $A(\omega)$ is given for different damping parameters ξ. For under-damped systems ($\xi < 0.1$), we see that the main frequency of the damped harmonic oscillator is almost damping-independent, while it is shifted for higher values of ξ. The corresponding resonant angular frequency ω_r of the harmonic oscillator is then given by:

$$\omega_r = \omega_0\sqrt{1-2\xi^2}\,, \tag{2.7}$$

which is only valid when $\xi < 1/\sqrt{2}$. For larger values of ξ, the resonance frequency is "0", the system is said over-damped. Moreover in the case where $\xi \ll 1/\sqrt{2}$, the full width at half maximum (FWHM) scales linearly with the damping: $\Delta f = 2\xi\omega_0/2\pi$. Because of this linear dependence with $\lambda = 2\xi\omega_0$ below $\xi \approx 0.4$, the FWHM is a good indication of the quality factor Q of a damped oscillator or resonator with relatively small damping ratio ξ.

The quality factor Q relates to the energy dissipated during a cycle of oscillation by the system due to damping. Q is more precisely the ratio between the energy losses after one cycle and its initial energy stored. In the example of the pendulum discussed before, the initial energy stored is the sum of kinetic and potential energy. Hence a general expression for the Q factor is:

$$Q = 2\pi\frac{\text{Energy Stored}}{\text{Energy losses in a cycle}} = \frac{1}{2\xi} = \frac{\omega_0}{\lambda}\,. \tag{2.8}$$

For small damping factors, Q is given by $Q = f_0/\Delta f$. It is important to note that the Q factor is independent of the excitation itself, which can be noise sources or correlated inputs. This statement is only verified in linear damped oscillators, where the damping is independent from the excitation strength. The Q factor is the quantity to use when dealing with damped oscillators or resonators because it gives information about the system's damping. It is quite straightforward to understand that the quality factor Q

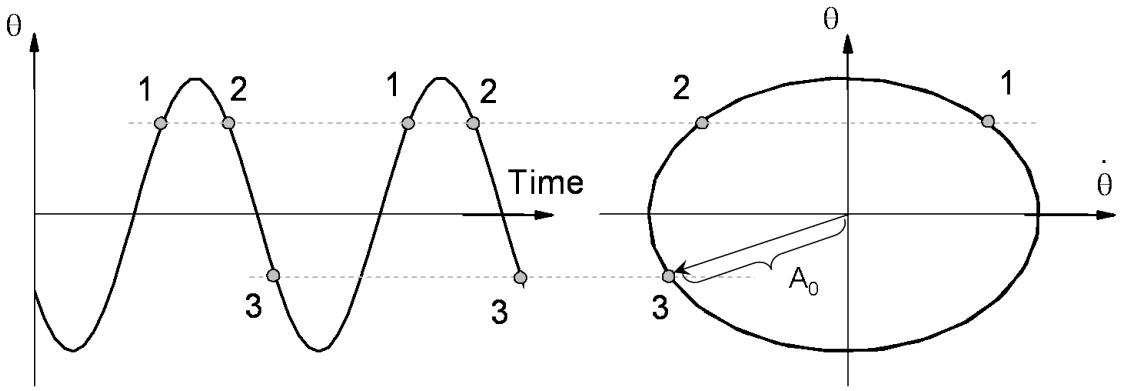

Fig. 2.3: Periodic oscillations are represented in a closed curve in the $(\dot{\theta}, \theta)$ plane. It allows a distinction between *growing* state 1 and *decreasing* state 2, while $\theta(1)$=$\theta(2)$. When the trajectory in the phase plane is a circle, the radius is noted A_0. Adapted from [41].

should not be used to describe ideal self-sustained oscillators because - by definition - their Q factor is infinite (there are no losses over a cycle of oscillations).

Besides, a general characterization of the resonator, the Q factor (as defined as $Q = f_0/\Delta f$) has no real significance because it is impossible to extract any information about the auto-oscillator characteristics, which is the main topic of this thesis. Indeed, when we compare Fig. 1.15 and Fig. 2.2 we see that the resonator quality and oscillator quality when defined as $Q = f_0/\Delta f$ is not valid to describe an oscillator output in the form of Eq. 1.14. According to Fig. 1.15 the oscillator quality depends, for instance, on whether the noise is located on the phase or on the amplitude of the total signal. That is why we will limit here the use of quality factor to the ferromagnetic resonance (FMR) which will be the topic of the section 2.2.1.

2.1.2 Notion of self-sustained oscillator

Self-sustained oscillators, in contrast to damped oscillators, will oscillate in time forever. Suppose $x(t)$ is the oscillating variable of the oscillator, which could be either the angle $\theta(t)$ of our pendulum, an output voltage, or the m_x component of the magnetic moment. To describe the state of the oscillator we need at least two parameters [41]. Indeed, as for the pendulum seen in Eq. 2.1, knowing $\theta(t)$ is not enough to predict $\theta(t + \delta t)$ unless $\dot{\theta}(t)$ is known. For the case of the pendulum, this is represented in Fig. 2.3 where the phase plane $(\dot{\theta}, \theta)$ describes the steady-state oscillator motion. In such a case, this plane is called *phase portrait* and the closed curve is called the *limit cycle*. A point on a phase portrait is called a phase point, and is represented in polar coordinates, such it has an amplitude A and an angle, or phase, $\phi(t)$.

If we represent now a damped oscillator in this phase portrait, without any forcing signal, we see that the system goes from the initial conditions $(A(t = 0), \phi(t = 0))$ towards a non-dynamical final state (static equilibrium $A = 0$). This case is represented in the Figs. 2.4-a,b; the damped oscillator goes back to the static equilibrium while "oscillating". If we consider now the case of a non-damped linear oscillator ($\lambda = 0$ see Eq. 2.2), the system evolves on a *closed trajectory* whose amplitude is given by the initial conditions $(A(t = 0), \phi(t = 0))$. This is represented Fig. 2.4-c. In contrast, Figs. 2.4-d,e show the

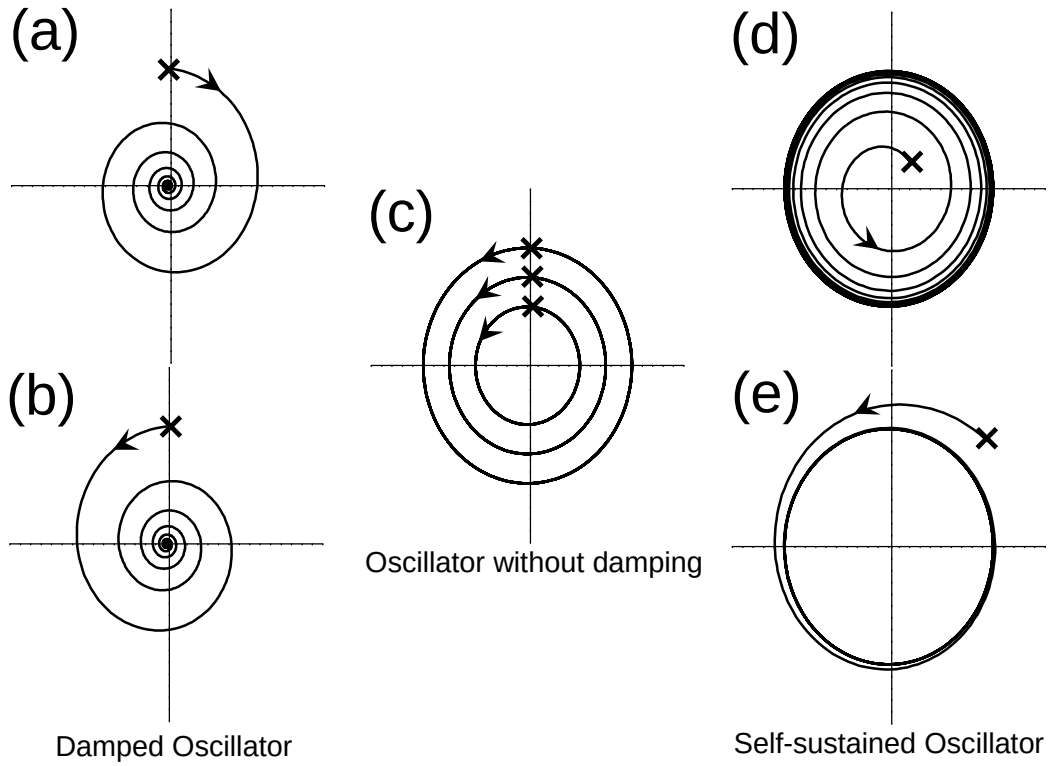

Fig. 2.4: (a) and (b) Phase portraits for damped oscillators. (c) Phase portrait of oscillators without damping as in Eq. 2.1, the actual (closed) trajectory taken depends purely on the initial conditions. On the other hand, limit cycles as shown in (d) and (e) for self-sustained oscillators are the same for different initial conditions. The relaxation rates are different in each cases. Initial states are marked with a cross.

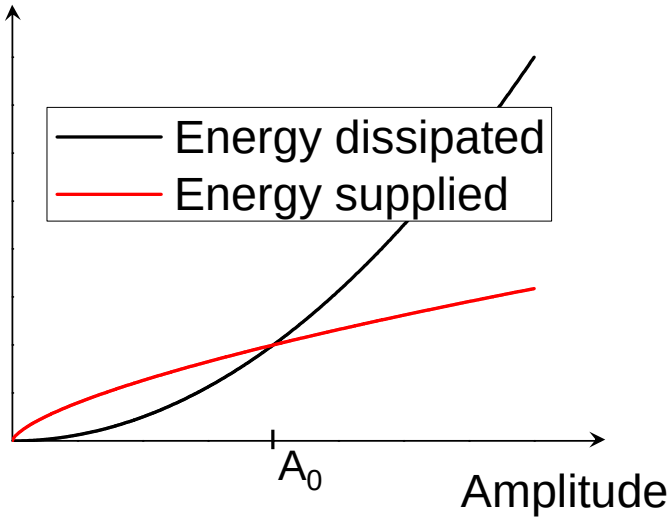

Fig. 2.5: A_0 is the equilibrium amplitude of the limit circle that corresponds to a ,balance between the dissipative (damping terms) and supplied energy (anti-damping term) along the limit cycle.

trajectories in the phase plane of a "simple" self-sustained oscillator where independent of the initial conditions, the system will end on a well defined *limit cycle* of given amplitude. The speed at which the oscillator reaches the limit cycle can be either slow (Fig. 2.4-d) or fast (Fig. 2.4-e). We will see later that the slower the return to equilibrium, the better (the higher) the performances (the quality factor) of the oscillator.

To highlight the main differences between those cases, we use a simple toy model based on physical considerations. Let us consider the case of Fig. 2.4-a,b. As discussed before, in this case, a dissipative damping enters in the dynamics of the system, that brings the system to an equilibrium trajectory (limit cycle). For instance in the case of Fig. 2.4-d "*something*" drives the system away from the static equilibrium (or initial position) towards the limit cycle, i.e. "*something*" restores the limit cycle and making the system's trajectory "grows". In the case of Fig. 2.4-e, dissipative damping restores the limit cycle by making the system's trajectory "falls" toward the limit cycle. The *something* is called - by opposition to dissipative damping - dissipative anti-damping. In the case of a self-sustained oscillator, we speak about the restorative damping terms, that are the dissipative terms that bring the system back to its limit cycle from either a higher or lower radius as depicted by Fig. 2.4-d,e. This notion is very important, because it defines self-sustained systems that are called autonomous oscillators (auto-oscillators).

2.1.2.1 Amplitude in self-sustained oscillator

An important consequence from the cases of Figs. 2.4-d,e is that the amplitude of the limit cycle is given by the equilibrium between the two dissipative terms as discussed in the following.

In the simplest form, we assume the trajectory of the limit cycle as a circle of radius A_0. A_0 is determined by the equilibrium between the two dissipative terms. The energy

lost (or gained) by damping (anti-damping) on a closed-loop trajectory of amplitude A is given in Fig. 2.5. When the system is on a trajectory such that $A < A_0$ ($A > A_0$), the energy supplied is higher (lower) than the energy losses through damping. A "stable" self-sustained oscillator is an oscillator where the state "naturally" converges to a limit cycle because of the competition of these damping/anti-damping terms. The phase portraits of Figs. 2.4-d,e, are two examples for reaching the limit cycle (slowly going to the limit cycle). This return to the limit cycle actually only depends on the form of the restorative terms around A_0. For example in Figs. 2.4-d,e, the relaxation times are different according to the initial condition $A(t=0) < A_0$ or $A(t=0) > A_0$.

However, for small perturbation from the limit cycle ($\delta A << A_0$), it is possible to consider the relaxation independent of the initial condition $A < A_0$ or $A > A_0$. In this case, a first order linearization of dissipative terms allows such considerations. Similarly to damped oscillator cases, one could then define a Q factor $Q^{oscillator}$ that determines how a deviation from the limit cycle trajectory is attenuated/damped. This Q factor is an extended concept from a damped oscillator. While the Q factor in a damped oscillator $Q^{resonator}$ only deals with the rate of energy losses, in self-sustained oscillator the notion $Q^{oscillator}$ is extended to both the rate of energy losses and gains.

As discussed in chapter 4, a key result of this work is that a quality factor for STOs can be defined, $Q^{STO} = \omega_g/\Gamma_p$, with ω_g the STO mode frequency and Γ_p the amplitude restoration rate. Those quantities will be defined later, while the Q factor discussion is only given here for the sake of generalizing oscillator concepts of different nature. For instance, in simple electrical oscillators that are mainly a resonator fed with a negative load [42], the energy losses and energy gains are made through the RLC tank circuit that can only receive or dissipate energy with its own $Q^{resonator}$ factor. This is why the $Q^{resonator}$ factor is often used for a self-sustained oscillator, especially in electrical circuit.

To summarize this section, we have presented the notion of a self-sustained oscillator which is determined by a well defined amplitude in the phase plane. It is the amplitude $A(t)$ that is responsible for the stable autonomous dynamical state of the system which as a constant value A_0 (or close to it) to define a limit cycle.

In contrast to the amplitude, we did not consider the phase $\phi(t)$, because the oscillating state happens whatever the phase is. In other words, the phase is "free" while the amplitude is "stable" in self-sustained oscillator [41]. We discuss in the next part about the phase in self-sustained oscillator.

2.1.2.2 Phase in self-sustained oscillator

In the previous section, we have shown that a self sustained oscillation occurs due to the compensation of the damping term (now called $\Gamma_+(A)$) and the anti-damping term (now called $\Gamma_-(A)$) that are found to be equal when the limit cycle is reached with $A = A_0$. If we consider the system on its limit cycle, the phase of the auto-oscillator is such that $\phi(t) = \omega_0(|A|)t$. Thus, if we consider A of the complex form $A = |A|e^{i\omega_0 t}$ we have:

$$\frac{dA}{dt} + i\omega_0(|A|)A + \Gamma_+(|A|)A - \Gamma_-(|A|)A = 0\ . \tag{2.9}$$

With a proper choice of $\Gamma_+(A)$ and $\Gamma_-(A)$, this equation describes all the physical properties given in the previous section. There is now a consideration to be done that

differs from electrical oscillator theory. If we consider Γ_+ and Γ_- are real, then the frequency dependence on the amplitude A is direct. This means $\omega_0(|A|)$ depends on $|A|$. Inversely, if we consider Γ_+ and Γ_- in complex forms, then ω_0 is independent of $|A|$; a phase shift (in the complex plane) between Γ_+ and Γ_- would then explain the frequency dependence versus A. The latter has been introduced to explain the Leeson effect [43, 44].

We will always consider Γ_+ and Γ_- real and we will assume a pure amplitude-frequency dependence upon the oscillating frequency. We will call such a system a "nonlinear" auto-oscillator but also refers to non-isochronous auto-oscillator in contrast to isochronous auto-oscillator (whose phase is independent from the amplitude $|A|$). An oscillator considered with Γ_+ and Γ_-, that are complex quantities, and the mode angular frequency ω_0 that is independent from A will be said a "quasi-linear" auto-oscillator (isochronous). All those terms are a misuse of language because as seen in part 2.1.2, any self-sustained oscillator is, by essence, nonlinear[1].

2.1.2.3 Noise in self-sustained oscillator

We are now interested in the effect the noise may have on the dynamics of the system we defined as a self-sustained oscillator (Eq. 2.9). The aim here is to obtain an output signal of the form of Eq. 1.14, that complies with our description of a self-sustained oscillator. Suppose we can linearize Eq. 2.9 near A_0 such that $|A| = |A(t)| = A_0 + \Delta A(t)$. Then it is possible to write the amplitude-phase equations such that:

$$\begin{aligned} \frac{d\Delta A}{dt} + 2\left[\frac{d\Gamma_+(|A|)}{dA} - \frac{d\Gamma_-(|A|)}{dA}\right] A_0 \Delta A = 0 \\ \\ \frac{d\phi}{dt} = -\omega_g - N\Delta A \end{aligned} \quad . \tag{2.10}$$

with $\omega_g/2\pi$ the frequency of the autonomous oscillator on the limit cycle, and N the linear approximation of $d\omega/dA$ around the point $A = A_0$. When $K(A) = \left[\frac{d\Gamma_+(|A|)}{dA} - \frac{d\Gamma_-(|A|)}{dA}\right] A_0 > 0$, a solution exists [42]. However, in Ref. [42], it should be noted that $N = 0$. Similarly to N, we can only take into account first order terms in $\Gamma_+(|A|)$ and $\Gamma_-(|A|)$, such that we define $\Gamma_A = K(A)$ =constant around $A = A_0$. As we introduced noise in equation 1.14 in both amplitude and phase terms, we assume now deterministic (or not) independent functions $f(t)$ and $g(t)$ that would respectively affect the amplitude and phase such that Eqs. 2.10 can be approximated by:

$$\begin{aligned} \frac{d\Delta A}{dt} + 2\Gamma_A A_0 \Delta A = f(t) \ , \\ \\ \frac{d\phi}{dt} + \omega_g + N\Delta A = g(t) \ , \end{aligned} \tag{2.11}$$

With the solution to Eqs. 2.11 we can now write the voltage signal $V(t)$ introduced in Eq. 1.14 such that:

[1] For example, without nonlinear terms, Eq. 2.9 cannot be obtained from Eq. 2.4.

$$V(t) = V_0 \left[1 + \Delta A(t)/A_0\right] \cos\left(\phi(t)\right). \tag{2.12}$$

Finally, we reach our objective that was to obtain a link between Eq 1.14 or 2.12 and the description of a self-sustained oscillator that was not too restrictive in terms of the exact physical nature of the oscillator.

2.1.2.4 Conclusion on self-sustained oscillators

To summarize this introduction on oscillators, we gave definitions as to what constitute an oscillator, a damped oscillator, and a self-sustained oscillator. In damped oscillators, the amplitude always decays exponentially towards zero, but can be stabilized by a periodic driving force (see Eq. 2.5). This amplitude depends on the excitation frequency, and is largest at the resonance of the system. In self-sustained oscillators, their nonlinear nature insures the stability of the oscillator along a "limit cycle". The limit cycle in self-sustained oscillators is the trade-off between inherent losses of the system and a constant energy supply. We have seen that the rate at which the system returns to the equilibrium tells us about the quality of the self-sustained oscillator. In the case of perturbations of this dynamical equilibrium, such as noise, linearized equations 2.11 allow studying the phase and amplitude dynamics of the oscillator. We would like to emphasize that in most cases no analytical treatment of nonlinear differential equations governing the dynamical system is possible; therefore the definition of the limit cycle and the linearization of the dissipation near it are prerequisites to the analytical study of an autonomous auto-oscillators.

We have seen in chapter 1 that the magnetization under a spin polarized current bias is equivalent to an autonomous self-sustained oscillator since STOs exhibit an infinite oscillating voltage at their output. We present in the next section 2.2 a model to obtain Eqs. 2.11 from the LLGS equation. Since these steps are non-trivial, we summarize in the following this formalism.

2.2 Spin Transfer Oscillators

The basic idea of this section is to show how it is possible to find a general equation of the form of Eq. 2.9 for the magnetization dynamics from physical considerations. We then compare this model to the state-of-the-art experimental literature. We start in the next section by the linearized LLGS around the static equilibrium to obtain the equation of motion for a damped oscillator Eq. 2.4. This will be followed by a nonlinear model of the magnetization dynamics that is linearized around a limit cycle to give Eq. 2.9. This model will be of use to study perturbations of the nonlinear magnetization dynamics by the noise. This will allow to describe the features of a noisy STO output signal.

2.2.1 Magnetism and damped oscillator: FMR

Starting from Eq. 1.7, we linearize the LLGS equation for a magnetization whose static equilibrium is along the Z-axis, similar to Eq. 2.1 to obtain [45]:

$$\begin{pmatrix} \dot{m_x} \\ \dot{m_y} \end{pmatrix} = -\frac{\gamma_0}{1+\alpha^2} \begin{bmatrix} \alpha\tilde{H} & H \\ -\tilde{H} & \alpha H \end{bmatrix} \begin{pmatrix} m_x \\ m_y \end{pmatrix}. \tag{2.13}$$

$\tilde{H}$ is the field felt by the magnetic moment when $m_y = 0$ and H when $m_x = 0$. By combining the system (2.13), it follows:

$$\begin{cases} \ddot{m}_x + \frac{\gamma_0}{1+\alpha^2}\alpha(H+\tilde{H})\dot{m}_x + \left(\frac{\gamma_0}{1+\alpha^2}\right)^2 H\tilde{H}m_x = 0 \\ \\ m_y = -\frac{(1+\alpha^2)}{\gamma_0 H}\dot{m}_x - \alpha\frac{\tilde{H}}{H}m_x \end{cases}. \tag{2.14}$$

With $\omega_0^2 = {\gamma_0^2}/{(1+\alpha^2)^2} H\tilde{H}$ and $\lambda = {\gamma_0\alpha}/{1+\alpha^2}(H+\tilde{H})$, we find the same equation as Eq. 2.4 for m_x. We can note that $\omega_0/2\pi$ is the Larmor frequency and that the quality factor, Q, is not in a simple relation with the Gilbert damping α. As we will discuss later, λ is the linear damping rate Γ_0, and its expression actually takes on different forms as we change field orientations, include anisotropy and so on.

This introduction to damped oscillators and the way we transpose its formalism to the LLG equation in presence of STT (Eq. 1.11) is useful to understand why we speak of Spin-Transfer Torque Oscillator (STO). As discussed earlier, the STT will have two effects on the dynamics of the magnetization. The first one, through the a_j term (see Eq. 1.10), will affect the effective damping rate λ^{STT}. The second effect, due to b_j term (see Eq. 1.8), will affect the oscillator eigenvalue ω_0^{STT} as a field would do. Finally, the modification of Eq. 2.4 should be such that the solutions ${\omega_0}^{STT}$ and λ^{STT} are:

$$\begin{aligned} \omega_0^{STT} &= \gamma_0\sqrt{(H-b_j)(\tilde{H}-b_j)} \\ \\ \lambda^{STT} &= \gamma_0\frac{\alpha(H+\tilde{H}-2b_j)-2a_j}{1+\alpha^2} \end{aligned}. \tag{2.15}$$

These results are similar to the direct eigeinvalue of the matrix equation of Eq. 2.13 including the STT, in the case of the in-plane collinear case (See Refs. [46, 47]). The advantage of Eq. 2.15 is that it allows a direct comparison with the damped oscillator theory that is less obvious in the form of Eq. 2.13 in the damped region. At the critical current, the damping λ^{STT} becomes 0, and the system should be periodic with time with its initial amplitude. The initial amplitude refers to the angle θ formed by the initial magnetic moment position and the effective field H or $\tilde{H}$. To linearize LLGS (Eq. 2.13), θ is considered small. Due to damping λ^{STT}, the angle remains small and the linearization is justified. When λ^{STT} is negligible the linearization is no more valid since the system is allowed to shift away from the static equilibrium position. Therefore, when STT fully compensates damping, large angle magnetization would be possible, and the linearized Eq. 2.13 is no longer appropriate.

This illustrates that the use of damped oscillator equations, or the linearized LLGS equation around the equilibrium position of the magnetization moment, to describe the self sustained magnetization dynamics is not appropriate. In the next section, we present a formalism for self-sustained oscillations and subsequently treat their stabilities. We finally show how this formalism is applied to large angle magnetization dynamics, i.e. when the STT compensates fully the ferromagnetic damping.

2.2.2 KTS Model

A formalism for STO in terms of nonlinear dynamical equation in the presence of noise was first described within the KTS model, that refers to scientists J.-V. Kim (IEF Orsay), V. Tyberkevych and A.N. Slavin (Oakland University) [48]. It is compounded of two distinct parts. A first part of the KTS model is using a spin-wave model, or formalism, to isolate the important physical variables that matter for the dynamics of the system. The second part of the KTS model is a phenomenological description that takes into account the thermal fluctuations, or perturbations, acting on the system. The latter is written using the newly formed variables from the spin-wave model.

According to V. Tyberkevych and A. N. Slavin's own words, this theory is based on the "classical quasi-Hamiltonian formalism for spin-waves" [49]. Substantially, it is said that in STO nano-structures among the manifold of different spin-waves, a single spin-wave mode is driven into auto-oscillation thanks to the compensation of the Gilbert damping term by the STT. J.-V. Kim introduced thermal noise [50] to the dynamics of this spin wave, that impacts both - and separately - its amplitude and phase. Finally, the full derivation leads to an explanation of the power distribution of STOs versus applied current [51], prediction of FWHM versus field orientation and applied current [52] and the temperature dependence of STO noise linewidth [53]. All results and details of the KTS model have been summarized in a tutorial [54]. In the following we present the essential features of this model while keeping in mind that a rigorous demonstration can be found in literature [49].

2.2.2.1 From the LLGS equation to an autonomous auto-oscillator equation

We have seen in part 1.2.1 that the LLGS can be expressed in the form:

$$\frac{\partial \vec{M}}{\partial t} = \gamma \left[\vec{H}_{eff} \times \vec{M} \right] + \vec{T}_{\epsilon} \, , \tag{2.16}$$

with $\vec{T}_{\epsilon}$ representing the damping and STT torques and where the effective field $\vec{H}_{eff}$ is the derivative of the magnetic free energy of the system W:

$$\vec{H}_{eff} = -\frac{\delta W}{\delta \vec{M}} \, . \tag{2.17}$$

Firstly, damping and STT torques are considered as perturbations, that is to consider W_0 as the "zero order" free energy[2] of the limit cycle (a closed loop trajectory of the magnetization). This energy only depends on applied, dipolar, anisotropy and exchange fields. Under these conditions, one can consider Eq. 2.16 in the form:

[2] b_j term also enters W_0, see discussion part 1.2.1

$$\frac{\partial \vec{M}}{\partial t} = \gamma \left[\vec{M} \times \frac{\delta W_0}{\delta \vec{M}} \right] + \vec{T_\epsilon} \ . \tag{2.18}$$

Because the norm of $\vec{M}$ is conserved, Eq. 2.18 has two dimensions. Contrary to the part where we discussed FMR and small precession angles of the magnetization to lead to Eq. 2.14, we do not consider the small angle approximation in the following. However, it is still possible to write Eq. 2.18 with a complex variable $a(t) = a(\vec{M}(t))$. A convenient choice of the variable is given by the Holstein-Primakov transformation. Depending on the system's symmetry, this transformation has a different form. This transformation is canonical, which means that it does not change the Hamiltonian of a system, i.e. its energy, and thus solutions in the canonical form can be transformed back to the real coordinates that are solutions of Eq. 2.18. After transformation, Eq. 2.18 becomes a perturbed Hamiltonian equation with Hamiltonian $\mathcal{H} = \gamma W_0 / 2M_s$:

$$\frac{\partial a}{\partial t} = -i \frac{\delta \mathcal{H}}{\delta a^*} + \vec{F_a} \ , \tag{2.19}$$

where $\vec{F_a}$ is the "perturbation force" with the form:

$$\vec{F_a} = \frac{\partial a}{\partial \vec{M}} \cdot \vec{T_\epsilon} \ . \tag{2.20}$$

It is now possible to expand the Hamiltonian $\mathcal{H}(a, a^*)$ and the perturbation force $\vec{F_a}(a, a^*)$. This is done by considering not so large $|a|$. However, within this single canonical transformation, the Hamiltonian is still a complicated function of (a, a^*). Two additional canonical transformations are required to lead to an equation in "c-variables" such that:

$$\frac{\partial c}{\partial t} = -i \frac{\delta \mathcal{H}_c}{\delta c^*} + \vec{F}_d + \vec{F}_J \ , \tag{2.21}$$

where the Hamiltonian $\mathcal{H}_c$ (in the Macrospin approximation that neglects spatial variation of local magnetization) is written:

$$\mathcal{H}_c = \omega_0 |c|^2 + \frac{N}{2} |c|^4 \ , \tag{2.22}$$

and the dissipative force $\vec{F}_d$ and the current induced force $\vec{F}_J$ have the form:

$$\begin{aligned} \vec{F}_d &= -\Gamma_0 (1 + Q|c|^2) c \\ &, \\ \vec{F}_J &= -\Gamma_J (1 + Q_{ST}|c|^2) c \end{aligned} \tag{2.23}$$

with ω_0, N, Γ_0 the Gilbert damping rate (λ in Eq. 2.14), $\Gamma_J = \sigma I$, $Q_{ST} = -1$ and Q that are functions of the canonical transformations and material parameters (and the mode profile). Finally, Eq. 2.21 can be written in the form:

$$\frac{dc}{dt} = -i\omega(|c|^2)c - \Gamma_+(|c|^2)c + \Gamma_-(|c|^2)c \ . \tag{2.24}$$

Similar to Eq. 2.9, Eq. 2.24 is a nonlinear differential equation that describes the dynamics of the magnetic moment in presence of STT.

We have thus seen that it is possible to find a dynamical equation for the magnetization that has the mathematical form of a general self-sustained oscillator. This is possible through the calculation of the system's Hamiltonian and several canonical transformations[3]. Because this model is generic, some specifics might have disappeared. For instance higher order terms in $|c|^2$ in Eq. 2.23 have been neglected to only take into account the direct effect of a bias DC current or also field that explain some features of parametric excitations. Moreover this model is said to be classical, because it does not consider quantized spin waves. A similar approach of the derivation of the quantized spin wave dynamic through a Hamiltonian can been found elsewhere [55]; it explains as well spin wave coupling [56] and it has been derived in the presence of a b_j term [57] and thermal noise [58].

In order to find solutions of Eq. 2.24 in the form of a limit cycle, we can separate real and imaginary part of Eq. 2.24 to obtain an equation for the amplitude (or rather the power $p = |c|^2$) and the phase:

$$\begin{aligned} \frac{dp}{dt} + 2\left[\Gamma_+(p) - \Gamma_-(p)\right] p = 0 \\ , \\ \frac{d\phi}{dt} + \omega(p) = 0 \end{aligned} \tag{2.25}$$

with $p = |c|^2$, $\phi = \arg(c)$ and $\omega(p) = \omega_0 + Np$ as defined in the Hamiltonian $\mathcal{H}_c$.

Next, we consider small mode perturbations around the auto-oscillating state (limit cycle) with mean power p_0 such that $p(t) = p_0 + \delta p(t)$. Linearization of Eq. 2.25 yields:

$$\begin{aligned} \frac{d\delta p}{dt} + 2\Gamma_p \delta p = 0 \\ , \\ \frac{d\phi}{dt} + \omega_g + N\delta p = 0 \end{aligned} \tag{2.26}$$

where $\omega_g = \omega(p_0)$ is the generation frequency, $\Gamma_p(p_0)$ is the amplitude restoration rate given by $(\Gamma_0 Q - \Gamma_J)p_0$, and defined similarly as in Eqs. 2.11. As for Eqs. 2.11, $\Gamma_p > 0$ insures that stable solutions exist. Moreover, Γ_J depends on the total current I.

As described in Fig. 2.5, in order to establish a stable limit cycle of amplitude $p = p_0$, damping terms should cancel exactly at $p = p_0$, such that $\vec{F}_d = \vec{F}_J$. From this equality one can define the current above which the steady state solution occurs. In Eq. 2.25, $p \approx 0$ is stable as long as $\Gamma_-(0) \leq \Gamma_+(0)$. Then at and above the critical current I_{th},

[3]Successive transformations can be reduced to only one depending on the geometry of the system. Transformation steps have been originally proposed in Ref. [49] in order to explain the different steps to reach Eq. 2.24 from Eq. 2.16. During the process, many terms are neglected both in the Hamiltonian and in the corresponding perturbation forces from heuristic arguments. We eventually give in chapter 6 a similar approach closer to the magnetization dynamics of our structures (IPP mode) in order to explain fractional synchronization. In Ref. [49] fractional synchronization is neglected for the purpose to simplify the equation in c-variables (read p.1922 of Ref. [49]).

$\Gamma_-(p_0) = \Gamma_+(p_0)$ is verified for any $I > I_{th}$. Therefore, with $\zeta = I/I_{th}$ and $\vec{F}_d = \vec{F}_J$ one obtains:

$$p_0 = \frac{\zeta - 1}{\zeta + Q}. \tag{2.27}$$

Finally, we can write $2\Gamma_p = (\zeta - 1)\Gamma_0$, which is a simple function of the supercriticality parameter ζ. Following the discussion made in part 2.1.2, Γ_p is related to the quality factor $Q^{STO} \propto 1/\Gamma_p$ of the auto-oscillator. In particular, Γ_0, that is the linear damping rate or FMR linewidth, scales linearly with the Gilbert damping α such that $\Gamma_0 \sim 2\alpha\omega_0$, a direct consequence of which is that the "quality factor" of the STO will depend directly on its FMR linewidth[4]. This quality factor Q^{STO} has no direct links with the spectral purity of the STO. In this case Q^{STO} relates to the timescale required to recover from an external perturbation, or equivalently, the timescale required for the oscillator to go to another state (by tuning the applied DC current through the structure for instance).

For example, Γ_p plays an important role in the characteristic timescale required to pass from an autonomous state to a synchronized state by an external signal as studied by mean of macrospin simulations in Ref. [59]. Furthermore, the model predicts a frequency dependence upon the applied DC current in STOs that is the non-isochronous property of STOs. It fully describes in a simple way what is usually seen in experiments and simulations of STOs of various configurations: a shift in frequency versus the applied current, the possibility to synchronize to an external source and the possibility to mutually phase lock different STOs.

The main advantage of the KTS model is that it has transformed a quite complicated equation (LLGS Eq. 1.11) into a simpler and conceptually more transparent one (Eq. 2.26) that can been adapted to describe the autonomous properties (i.e. the frequency dependence) of the magnetization dynamics for any magnetization configuration and STO structure (for example see the Ref. [60]). In the next section we give examples of experimental results for the non-autonomous regime of STOs.

2.2.2.2 KTS model in literature

Besides describing the influence of noise and the substantial linewidth broadening that will be discussed in section 2.2.3, the spin-wave model from the KTS theory also provides the framework for coupling, synchronizing, modulating STOs, i.e. for a non-autonomous formalism. We first summarize results from literature that do not take into account the noise factor in Eq. 2.24.

Mutual phase locking of STOs

As a first example we mention the mutual phase locking of STOs. It is straightforward to couple two or more STOs using the formalism of Eq. 2.24 by introducing a coupling factor $\beta_{i,j}$ between two oscillators i, j such that:

[4] Γ_0 is the "Full" Gilbert linear damping rate, while the "half" Gilbert linear damping rate Γ_G is such that $2\Gamma_G = \Gamma_0$.

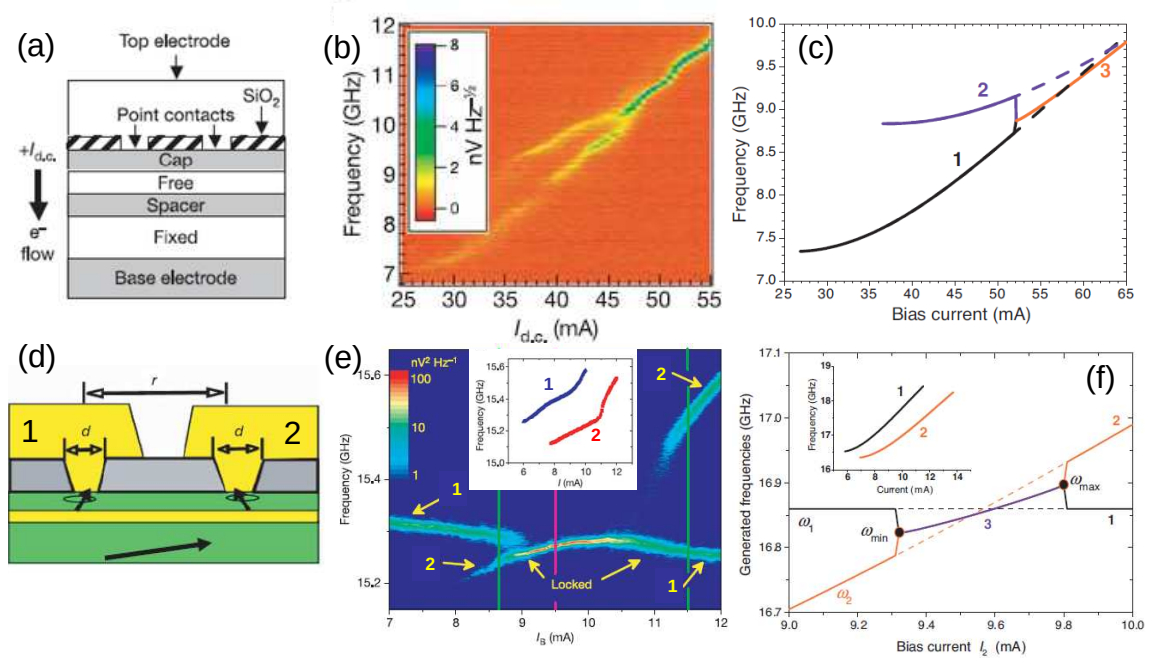

Fig. 2.6: Top: experiment and theory for the experiment of Mancoff et al. (a) STO structure, from [62], (b) Spectra observed when increasing the bias DC current to the structure from [62]. (c) KTS model applied to the structure from [61]. While there are some quantitative differences, the theory qualitatively agrees well. Bottom: experimental and theoretical results for the experiment of Kaka et al. (d) STO structure, the bias current of both STOs is controlled independently, from [63]. (e) Spectra observed when increasing the bias current of STO 2 while STO 1 has a constant DC bias. Insert: independent measurement of the frequency versus bias current for both STOs adapted from [63]. (f) Spin-wave model applied to the structure from [61]; a qualitative agreement is found.

$$\frac{dc_i}{dt} + i\omega_i(|c_i|^2)c_i + \Gamma_+(|c_i|^2)c_i - \Gamma_-(|c_i|^2)c_i = \sum_j \beta_{i,j}c_j. \tag{2.28}$$

The solution to Eq. 2.28 is shown in Fig. 2.6-c,f for two oscillators and explains well [61] the mutual phase locking of different STO structures through spin waves found experimentally by Mancoff et al. [62] and Kaka et al. [63].

Injection locking experiments

Besides mutual phase locking, the spin-wave formalism of the KTS theory explains as well the injection locking experiments to an external signal. An example of injection locking study by Zhou et al. [59] has explained the transient in the synchronized state in macrospin simulations. Another achievement of the spin-wave model is to explain the locking range, i.e. the frequency band δf_e over which an STO can be synchronized, with respect to its nonlinear frequency shift parameter N that appears in the phase equation of 2.26. While injection locking in STOs has been observed in the early stages of STO development [64], Georges et al. [65] experimentally confirmed that the coupling

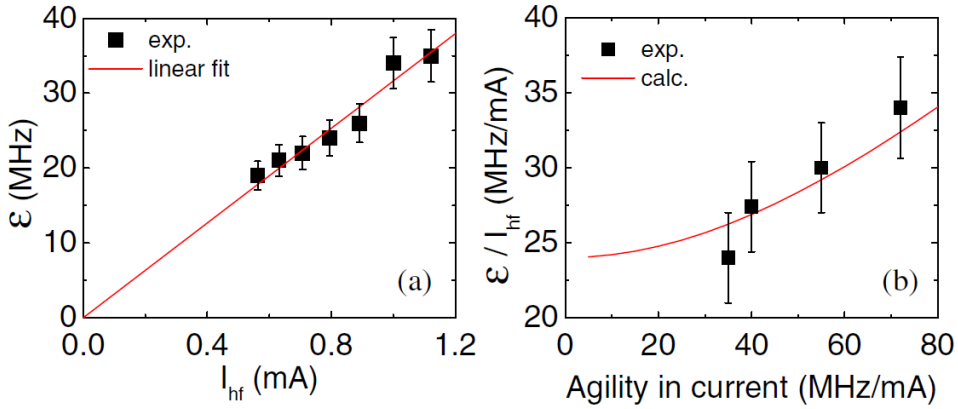

Fig. 2.7: (a) Coupling strength ϵ versus RF current amplitude. (b) Normalized coupling strength versus frequency tunning. Frequency tunning is proportional to the nonlinear frequency shift N. Black squares are experimental data and the red curve is an analytical fit from the KTS model. From [65].

strength ϵ, similar to the locking band δf_e, is a function of the frequency-shift N (see Fig. 2.7). Injection locking can be explained within the spin-wave model of the KTS theory considering a driving signal at frequency ω_e with initial phase ψ_e such that :

$$\frac{dc}{dt} + i\omega(|c|^2)c + \Gamma_+(|c|^2)c - \Gamma_-(|c|^2)c = -\frac{\sigma\Delta I \tan(\gamma_p)}{2\sqrt{2}} e^{-i\omega_e t - \psi_e s}, \tag{2.29}$$

where γ_p is the angle between the equilibrium orientations of the magnetization vector of the "free" and "pinned" magnetic layers of the STO [66]. By expanding in amplitude-phase equation, it leads to:

$$\begin{aligned} \frac{d\delta p}{dt} + 2\Gamma_p \delta p &= 2\frac{|-\sigma\Delta I \tan(\gamma_p)|}{2\sqrt{2}} \sqrt{p_0}\cos(\omega_e t + \phi - \psi_e) \\ \frac{d\phi}{dt} + \omega_g &= -\frac{|-\sigma\Delta I \tan(\gamma_p)|}{4p_0\sqrt{2}} \sin(\omega_e t + \phi - \psi_e) - N\delta p \end{aligned} \quad . \tag{2.30}$$

By introducing an effective phase $\tilde{\phi}$ such that:

$$\tilde{\phi}(t) = \phi(t) - \nu\frac{\delta p}{2p_0}, \tag{2.31}$$

with $\nu = p_0 N/\Gamma_p$, the dimensionless nonlinear amplitude phase coupling parameter. With Eq. 2.31, the phase equation in Eq. 2.30 becomes:

$$\frac{d\tilde{\phi}}{dt} + \omega_g \approx -\frac{|-\sigma\Delta I \tan(\gamma_p)|}{4p_0\sqrt{2}} \sqrt{1+\nu^2}\sin(\omega_e t + \tilde{\phi} - \psi_e + \arctan(\nu)), \tag{2.32}$$

where the ϵ of Fig. 2.7 is exactly the sine prefactor in Eq. 2.32.

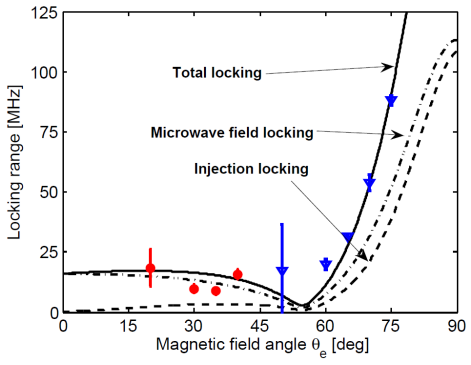

Fig. 2.8: The measured locking range versus out of plane field angle θ_e. The locking range corresponds to the sum of the direct RF spin torque contribution as well as the RF Oersted field generated by the microwave current. The three lines are calculated from the KTS model. The non-trivial dependence of the locking range versus the out of plane field angle is explained by the variation of the nonlinear frequency shift N with θ_e. From [67].

Another work to be mentioned is the injection locking experiment by Bonetti [67] where the locking range has been measured as a function of out of plane field angle in nanocontact based STOs. As we can see in Fig. 2.8 the locking band is explained through the KTS model when both RF oersted field and RF spin torque are considered in Eq. 2.24.

In addition, in Eq. 2.32 a phase shift equal to $\arctan(\nu)$ appears in the phase term of the sine that renders the self-synchronization of STO arrays more difficult. Circuit engineering allows in this case to compensate such a drawback [68]. We have addressed the issue of injection locking assuming that the driving force directly affects the dynamics of $c(t)$ in Eq. 2.24. One may argue that an RF current would only affect the dissipative anti-damping term Γ_- in the Eq. 2.24 resulting in a pure real contribution of the RF current to the Eq. 2.24 as it is the case during frequency modulation experiments discussed latter (see Eq. 2.33 and compare with Eq. 2.30). In chapter 6, this issue is discussed, where a direct derivation of the synchronization using LLGS is given. It leads, for some cases, to a pure "amplitude origin" of the locking phenomenon through the nonlinear amplitude phase coupling N.

Frequency modulation

Another example of experimental results that can be well explained by the KTS model involve experiments on frequency modulation (FM) [69, 70, 71, 72]. When modulating the DC current at a relatively low angular frequency ω_m with the amplitude depth ϵ (such that $I(t) = I_{DC}[1+\epsilon\cos(\omega_m t)]$), this modulation current directly modulates Γ_- at this frequency. Thus Eq. 2.25 is transformed into:

$$\begin{aligned} \frac{d\delta p}{dt} + 2\Gamma_p \delta p - 2\epsilon\Gamma_-(p_0)p_0\cos(\omega_m t) = 0 \ , \\ \frac{d\phi}{dt} + \omega_g + N\delta p = 0 \ . \end{aligned} \tag{2.33}$$

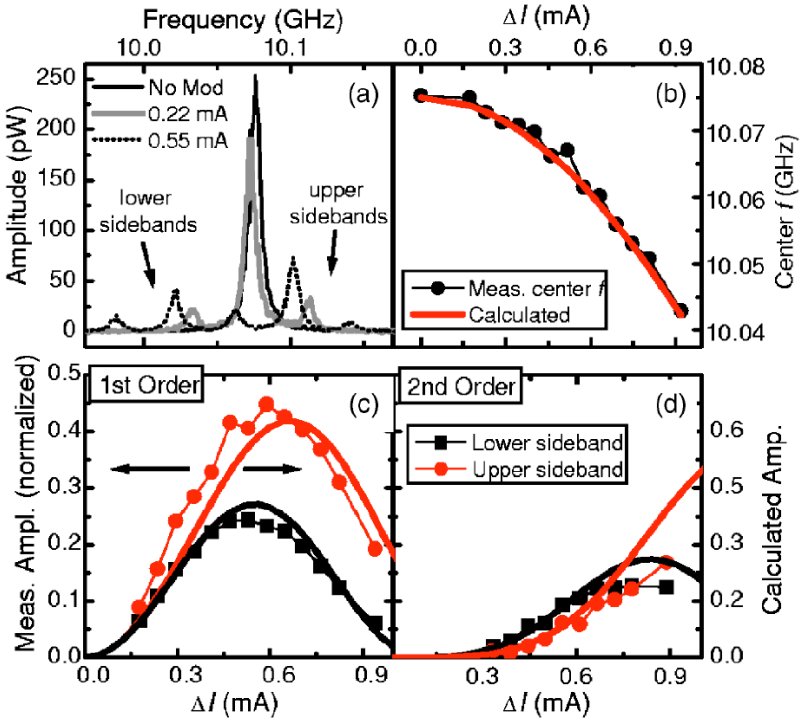

Fig. 2.9: (a) PSD of the STO output (for a nanocontact) with and without modulation current. (b) Shift of the center frequency versus modulation amplitude $\Delta I = \epsilon I_{DC}$. Measured normalized sideband amplitude (squares) and calculated one (full lines) from a nonlinear frequency modulation model using first order sidebands (c) and second-order side-bands (d). A linear modulation model is unable to explain the frequency-shift versus ΔI, and the asymmetry between the upper and lower sideband amplitude which should be equal in a linear modulation model. From [69].

The system 2.33 has the solutions :

$$\begin{aligned} d\delta p(t) &= \epsilon \frac{2\Gamma_-(p_0)p_0}{\sqrt{\omega_m^2 + 4\Gamma_p^2}} \cos(\omega_m t + \psi) \ , \\ \phi(t) &= -\omega_g t - \epsilon \frac{N 2\Gamma_-(p_0)p_0}{\omega_m \sqrt{\omega_m^2 + 4\Gamma_p^2}} \sin(\omega_m t + \psi) + \phi_0 \ , \end{aligned} \tag{2.34}$$

with $\psi = -\arctan(\omega_m/2\Gamma_p)$. The final output signal of an STO modulated through its DC current has thus both a sinusoidal varying amplitude and phase. The resulting spectra has a non-trivial form. First explanations and analysis have been given by Pufall et al. [69] where the obtained spectra of the STO under modulation current have been characterized by a typical Bessel-like spectra as shown in Fig. 2.9. A combined nonlinear FM amplitude modulation (AM) model [73] explained the exact value of the sideband amplitude in an FM experiment [70] for the case of a non-isochronous STO characterized by a nonlinear f vs. I dependence. It has been found that a nontrivial nonlinear frequency shift, i.e. a frequency that is not linear with applied current, would also change the mean mode frequency and the amplitude of sidebands. Indeed, Eqs. 2.34 do not consider a possible second order power dependence of the power on the modulating current. This shows one of the simple linear approximation of the KTS model. We will show in chapter 5 a different derivation from Eq. 2.33. Experiments done in this thesis in section 5.1 aim to give insights on this second-order power dependence under modulating current that is obtained solely from the KTS model without further considerations. Moreover, from Eq. 2.34, we see that varying the modulation angular frequency ω_m would change the modulation capabilities of the STO on both phase and amplitude/power. This has not been measured experimentally yet and will be another result of section 5.1.

We have shown in this part that the KTS model is able to explain all interactions that occur in STOs with an external reference signal. FM, injection locking, and mutual phase locking are easily explained thanks to the oscillator formalism brought within of the KTS model. Another major achievement of the model involves providing a full description of the STO dynamics in the presence of thermal noise, as discussed in the following

2.2.3 The thermal noise model in the KTS theory

In the previous parts, we discussed the deterministic nature of Eq. 2.24 to illustrate the oscillation of an STO on a limit cycle. When a stochastic force $f_n(t)$ acts on the system, such as a thermal fluctuating field in the LLGS equation, Eq. 2.24 becomes, with $|c|^2 = p$,

$$\frac{dc}{dt} + i\omega(p)c + \Gamma_+(p)c - \Gamma_-(p)c = f_n(t). \tag{2.35}$$

Here, the purpose is to study the stochastics of the complex variable $c(t)$. In mathematics, stochastics relate to the study of the time evolution of a system defined as a random variable, which in our case is $c(t)$.

2.2.3.1 Diffusion constant from The Fokker-Planck formalism

We have studied in detail the deterministic component of the system, i.e. the limit cycle, and how the system returns to it. Here, the goal is to give the statistical solution of Eq. 2.35. This requires some assumptions that have to be made. The first one is that noise will only contribute "reasonably" to the dynamics of the system, i.e., the noise does not perturb the system too much so that we can still linearize Eq. 2.35. Second is a consideration on the noise term $f_n(t)$ due to the interaction with the thermal bath. Because $f_n(t)$ is phenomenological, its expression should verify a proper thermodynamical behavior of the STO in the state of thermal equilibrium (i.e. the Boltzmann distribution of the system state when $\Gamma_-(p) = 0$) [54]. We will see that the correct choice for f_n is a white Gaussian noise of the form:

$$\langle f_n(t) f_n(t') \rangle = 0, \qquad \langle f_n(t) f_n^*(t') \rangle = 2D_n \delta(t - t'), \tag{2.36}$$

where $D_n(p)$ is the diffusion constant that characterizes the noise amplitude when the oscillator has the power p. We now focus on the determination of $D_n(p)$. The probability distribution function $\mathcal{P}_{eq}(p, \phi)$ of the system should lead to the Boltzmann distribution at thermal equilibrium ($\Gamma_-(p) = 0$) such that [51]:

$$\mathcal{P}_{eq}(p, \phi) \propto \exp\left(-\frac{\mathcal{E}(p)}{k_b T}\right), \tag{2.37}$$

where k_b is the Boltzmann constant, T the temperature and $\mathcal{E}(p)$ is the energy of the oscillation such that:

$$\mathcal{E}(p) = \lambda \int_0^p \omega(p')\, \mathrm{d}p' \approx \lambda \mathcal{H}_c, \tag{2.38}$$

λ depends on the normalization of the system energy (i.e. from real coordinates to c-variables) that occurs during the transformation from Eq. 2.18 to Eq. 2.19. λ also depends on the effective volume V_{eff} of the magnetic material involved in the oscillation. Finally λ is written as:

$$\lambda = V_{\text{eff}} M_s / \gamma. \tag{2.39}$$

While 2.35 is not deterministic, the Fokker-Plank equation is a deterministic equation for the probability function $\mathcal{P}(p, \phi)$, which, in the case of STO:

$$\frac{\partial \mathcal{P}}{\partial t} - \frac{\partial}{\partial p}[2p(\Gamma_+ - \Gamma_-)\mathcal{P}] - \omega \frac{\partial \mathcal{P}}{\partial \phi} = \frac{\partial}{\partial p}\left(2pD_n \frac{\partial \mathcal{P}}{\partial p}\right) + \frac{\partial}{\partial \phi}\left(\frac{D_n}{2p}\frac{\partial \mathcal{P}}{\partial \phi}\right). \tag{2.40}$$

The left hand side comes from the deterministic part of Eq. 2.35 and the right-hand-side (RHS) part is related to the thermal noise acting on the distribution. Eq. 2.40 represents a general formalism to analyze dynamical systems in the presence of noise. If we neglect the RHS (i.e. the noise), any initial distribution (or any initial condition in power and phase of the STO) will end on the limit cycle. The drift term in power, i.e. $2p(\Gamma_+ - \Gamma_-)$, gives the relative speed with which the distribution $\mathcal{P}(p, \phi)$ reaches $p = p_0$, at which the term $2p(\Gamma_+ - \Gamma_-)$ will be zero (limit cycle condition). At the same time, after the

transient period, the drift term in phase ω describes on the "natural" drift with time that occurs with the phase of the distribution, i.e., the frequency $\omega(p_0)$. If we now analyze the RHS of Eq. 2.40 we see that it corresponds to a diffusion operator, and its coefficient is precisely what we would like to determine. To do so, we consider only the steady-state solution of the distribution $\mathcal{P}_0(p,\phi)$, $\frac{\partial \mathcal{P}}{\partial t} = 0$. Because phases are equally possible in the steady-state regime, we consider $\mathcal{P}_0(p,\phi) = \mathcal{P}_0(p)$. We finally arrive at the equation:

$$\frac{\partial}{\partial p}\left[2p(\Gamma_+ - \Gamma_-)\mathcal{P}_0 + 2pD_n\frac{\partial \mathcal{P}_0}{\partial p}\right] = 0, \tag{2.41}$$

whose formal solution is:

$$\mathcal{P}_0 = \mathcal{N}_0 \exp\left[-\int_0^p \left(\frac{\Gamma_+(p') - \Gamma_-(p')}{D_n(p')}\right) \mathrm{d}p'\right], \tag{2.42}$$

with $\mathcal{N}_0$ that depends on the normalization condition of the distribution. We finally compare this solution 2.42, which is valid for any applied current - with the Boltzmann distribution Eq. 2.37 at equilibrium ($\Gamma_-(p) = 0$) to find the condition that should fit $D_n(p)$:

$$D_n(p) = \Gamma_+(p)\eta(p) = \Gamma_+(p)\frac{k_b T}{\lambda\omega(p)}, \tag{2.43}$$

where $\eta(p)$ is the noise power of the oscillation. This result is one of the most important in the KTS model and will be used in chapter 4 of the thesis. To illustrate the importance of it, we summarize in the following results from literature that were reported before and throughout the first year of my thesis.

2.2.3.2 Amplitude noise in autonomous STOs

Since the KTS model provides the power distribution of the system going from thermal equilibrium ($I = 0$) to a dynamical state($I > I_{th}$), it allows one to calculate the mean oscillation power $\bar{p}$ and the power fluctuation (variance) Δp^2 from $\mathcal{P}_0$:

$$\bar{p} = \int_0^\infty p\mathcal{P}_0(p)\,\mathrm{d}p\ , \quad \Delta p^2 = \overline{p^2} - (\bar{p})^2, \tag{2.44}$$

where $\overline{p^2} = \int_0^\infty p^2\mathcal{P}_0(p)\,\mathrm{d}p$. All these formulations lead finally to what is shown in Fig. 2.10, where the distribution function for different $\zeta = I/I_{th}$ and reasonable values of STO parameters are shown. We can see that thermal noise makes a non zero mean power when $\zeta < 1$, that is for the thermal FMR-mode in the sub-threshold regime. Finally it gives an intuitive definition of the critical current from experiments because the inverse of the power is proportional to $(I_{th} - I)$ in the sub-threshold regime (see inset in Fig. 2.10). It should be noted that within a similar approach, Kudo et al. found a similar result [74].

This theoretical description was initially done to determine the power dependence with current observed experimentally as a first step of the demonstration of noise properties of STOs and finally the observed linewidth in STO RF emission. Later, based on measurement of Quinsat et al. [76], Nagasawa et al. [77] directly compared the width of the power distribution experimentally to the one predicted by the KTS model (see Fig. 2.11) and found a good agreement with theory (more details in chapter 4). The

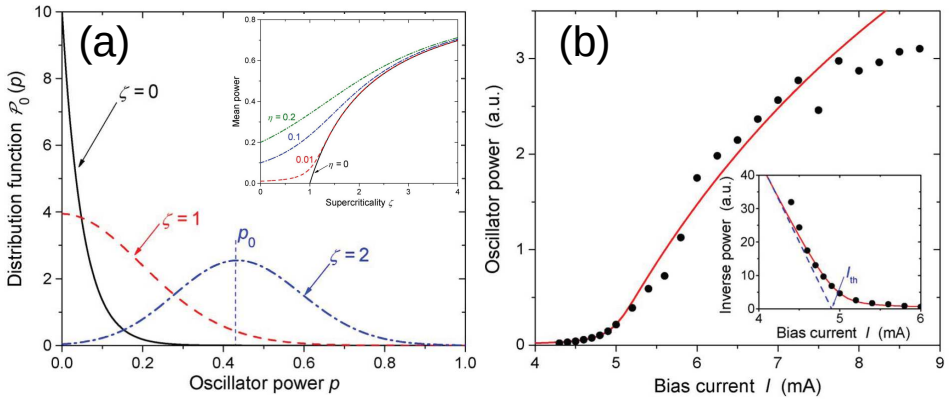

Fig. 2.10: (a) $\mathcal{P}_0(p)$ for different supercriticalities ζ with $\eta = 0.05$. Inset: dependence of $\bar{p}$ for different values of η (or temperatures) versus the supercriticaility ζ. From [54]. (b) Comparison between model and experiments of Mistral et al. [75]. Inset shows the same data but the inverse power $1/\bar{p}$ is plotted versus bias current from which it is possible to extract the critical current I_{th}. From [51].

experiment of Nagasawa et al. is a straightforward demonstration of the KTS model since it shows that the noise origin is indeed due to thermal fluctuations of the magnetization in MgO-based STO (at least at room temperature).

2.2.3.3 Amplitude noise relaxation and its link to the phase noise

With the definition of the diffusion constant Eq. 2.43, Eq. 2.35 can be transformed, using $\tilde{f}_n(t) = f_n(t)e^{-i\phi(t)}$, into:

$$\begin{aligned} \frac{d\delta p}{dt} + 2\Gamma_p \delta p &= 2\sqrt{p_0} Re[\tilde{f}_n(t)] \\ \frac{d\phi}{dt} + \omega_g + N\delta p &= \frac{1}{\sqrt{p_0}} Im[\tilde{f}_n(t)] \end{aligned} \quad . \tag{2.45}$$

Eq. 2.45 is of main importance for this thesis, because it allows a simple expression for both amplitude (power) and phase fluctuations. We first discuss the amplitude/power equation. The autocorrelation function of power fluctuation is expressed by:

$$\langle \delta p(t)\delta p(t-\tau)\rangle = \mathcal{K}_{\delta p}(\tau) = \frac{\Gamma_+(p_0)}{\Gamma_p}\eta(p_0)p_0 e^{-2\Gamma_p \tau}. \tag{2.46}$$

Bianchini et al. [78] computed the autocorrelation function of power fluctuations and extracted Γ_p from single shot time domain measurements of the output voltage of an MTJ based STO. As shown in Fig. 2.12, Γ_p lies in the range of tens of MHz.

In the phase equation of Eq. 2.45, the phase has a direct contribution from power fluctuations. It is convenient to express the solution of the phase equation by the time varying phase variance $\Delta\phi^2(t)$:

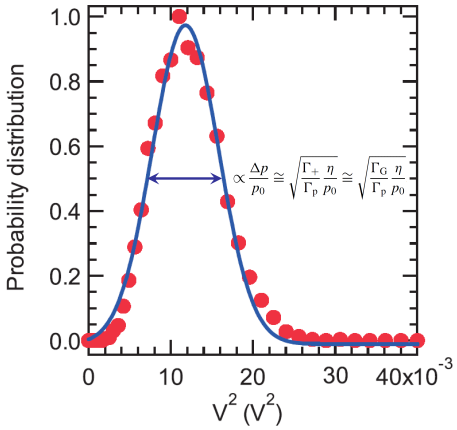

Fig. 2.11: Using a single shot measurement technique, it is possible to extract the envelope of the output signal $V(t)$ of the STO. The distribution of the square of the envelope is then fitted and a good agreement with theoretical description is obtained. From [77].

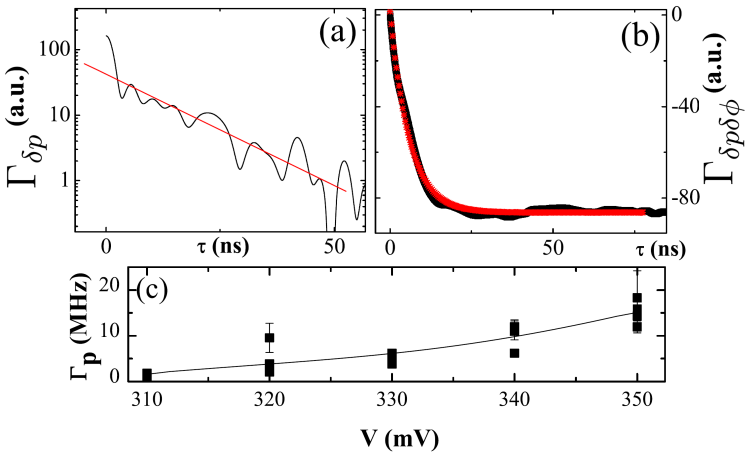

Fig. 2.12: (a) The power fluctuation autocorrelation function $\Gamma_{\delta p} = \mathcal{K}_{\delta p}$ for a MTJ-STO. (b) The power-phase cross correlation function $\Gamma_{\delta p \delta \phi} = \mathcal{K}_{\delta p \delta \phi}$ from the same set of data. The red curve is an exponentially decay fit with a time constant equal to $1/2\Gamma_p$. From [78].

$$\Delta\phi^2(t) = 2\pi\Delta f_0 t + 2\pi\Delta f_0 \nu^2 \left[t - \frac{1 - e^{-2\Gamma_p t}}{2\Gamma_p} \right], \tag{2.47}$$

where Δf_0 is the linear linewidth of the STO. The term $\Delta\phi^2(t) \sim 2\pi\Delta f_0 t$ is typical of a classical random walk of phase for a linear isochronous oscillator while the additional term comes from the nonlinear amplitude phase coupling present in non-isochronous STOs. This is called the nonlinear contribution to the phase variance. For short time scales ($2\Gamma_p t \ll 1$), the exponent can be expanded such that this nonlinear contribution to the phase is zero. Hence the cross correlation $\mathcal{K}_{\delta p \delta\phi}$ between phase fluctuations $\delta\phi$ and power fluctuations δp gives zero at small τ but has a non-zero correlation when $\tau \gg 1/\Gamma_p$, showing that phase fluctuations originate from power fluctuations at long timescales. This is shown by the measurement of Bianchini et al. in Fig. 2.12-b, where a nonzero cross correlation product between phase and amplitude fluctuations is found for $\tau \ll 1/\Gamma_p$.

Many other confirmations of the KTS model through experiments were found in recent years when comparing the STO characteristics from experiments with model predictions, especially the FWHM. However, they are all based (except our latest example) on the approximation that the phase variance $\Delta\phi^2(t)$ is linear in time. Because access to the direct time traces through single shot experiments can be difficult, the only quantity measurable is the PSD of the output signal $V(t)$ or equivalently the autocorrelation function $\mathcal{K}_V$ that is written in the form:

$$\mathcal{K}_V(\tau) \approx R_0(p_0^2 + \mathcal{K}_{\delta p}(\tau)) \exp\left(-i\omega_g \tau - \frac{\Delta\phi^2(\tau)}{2} \right), \tag{2.48}$$

where $\mathcal{K}_{\delta p}(\tau) \ll p_0^2$ and thus can be neglected in general and R_0 is a normalization constant. Because the PSD of a signal with a Lorentzian form derives from an autocorrelation function that has an exponential decay linear in time, Eq. 2.48 is often approximated by:

$$\mathcal{K}_V(\tau) \approx R_0(p_0^2) \exp\left(-i\omega_g \tau - \Delta f_0 (1 + \nu^2)\tau \right). \tag{2.49}$$

This approximation leads to an approximate solution for the observed FWHM in STO derived from the KTS model,

$$\Delta f \approx 2\Delta f_0 (1 + \nu^2)\ . \tag{2.50}$$

While Eq. 2.50 is a very convenient way to emphasize the major result in Eq. 2.47, it is a limiting approximation which removes all specific interest of the KTS model. This model aims to explain the subtle interplay between phase, amplitude and relaxation phenomena in STOs. While it might be convenient to fit all observed FWHM with formula 2.50, it gives actually no real information on the performances of the STO in the autonomous or non-autonomous regimes and may lead to inconsistent results. For example, in the work of Bianchini et al., this equation is not at all satisfied since $\Delta f \approx \Delta f_0$, because the nonlinear contribution in this specific measurement does not affect the linewidth. Nevertheless, amplitude fluctuations indeed enters the phase variance as we have already discussed. Besides works from Bianchini et al. [78] and Nagasawa et al. [77], STOs are rarely studied in the time domain with single shot instruments so that the time-dependence of the phase variance is not determined directly from experiments.

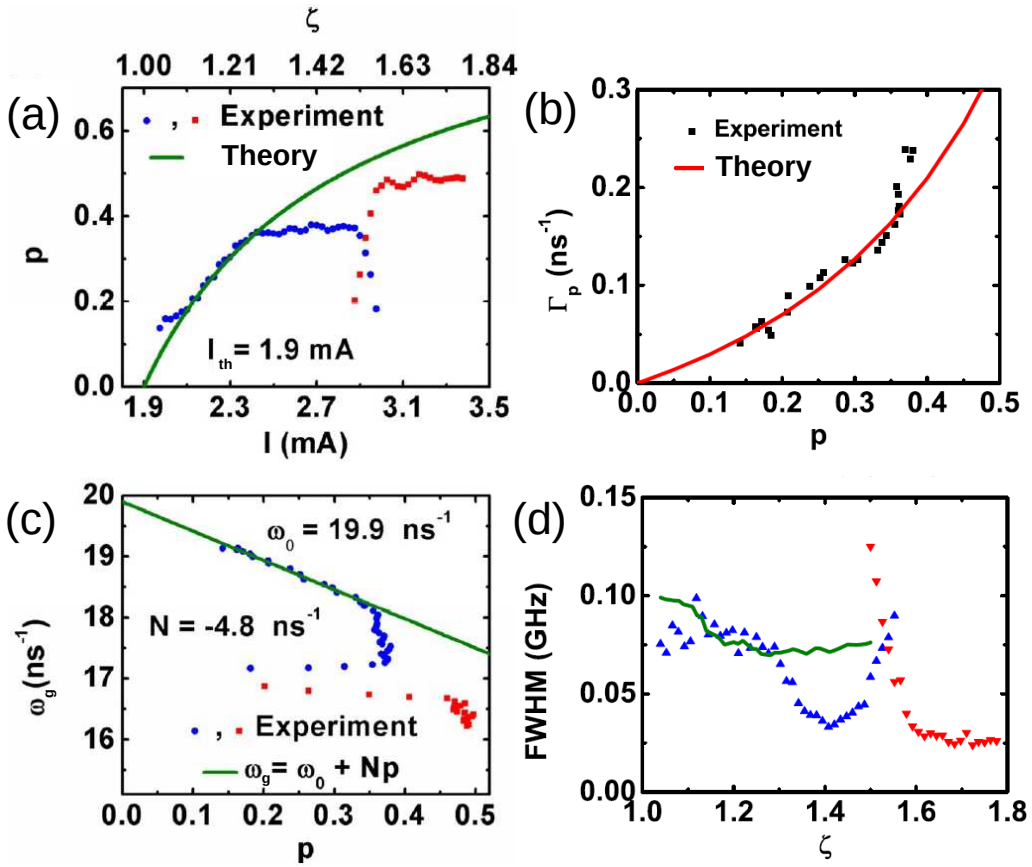

Fig. 2.13: (a) Calculated power from the total output power of the STO. (b) Estimation of Γ_p versus estimated power p. Note that for $p = 0.3$ (or $\zeta \approx 1.3$) $\Gamma_p/\pi = 41$MHz. (c) Comparison of the observed ω_g to the theoretical one obtained from a fit. Note that $|\nu| \approx 5 \sim 10$. (d) Comparison of the FWHM extracted by fitting the Fourier Transform of the measured PSD with the analytical formula Eq. 2.48 and neglecting amplitude noise contributions to the PSD of the signal. Experimental blue and red points are two different modes. Adapted from [79].

Furthermore, the parameters ν and Γ_p are in most experimental cases fitted since no analytical formulation of those exist (especially in nanopillars). It is therefore important to characterize them in real experiments.

Before closing this introduction, we would like to give an example of successful comparison of the KTS theory with experimental work in the frequency domain. One work to be mentioned is the one of Boone et al. [79] with the explicit title "*Experimental test of an analytical theory of spin-torque-oscillator dynamics*". In their work they extract all important parameters, Γ_p, N and p_0, from frequency measurements of the first harmonic. As shown in Fig. 2.13, the authors use nonlinear parameter fits to explain the experimentally observed FWHM. As shown explicitly in Fig. 2.13-a,c; when the KTS model fails to predict the correct dependence versus applied current, all the parameters (power, frequency, FWHM) diverge. The authors invoke the STT angular dependence to explain the discrepancy between experiments and model for $1.3 < \zeta < 1.5$ and mode hoping from $\zeta > 1.5$.

The second work worth mentioning, which is based on frequency domain experiments,

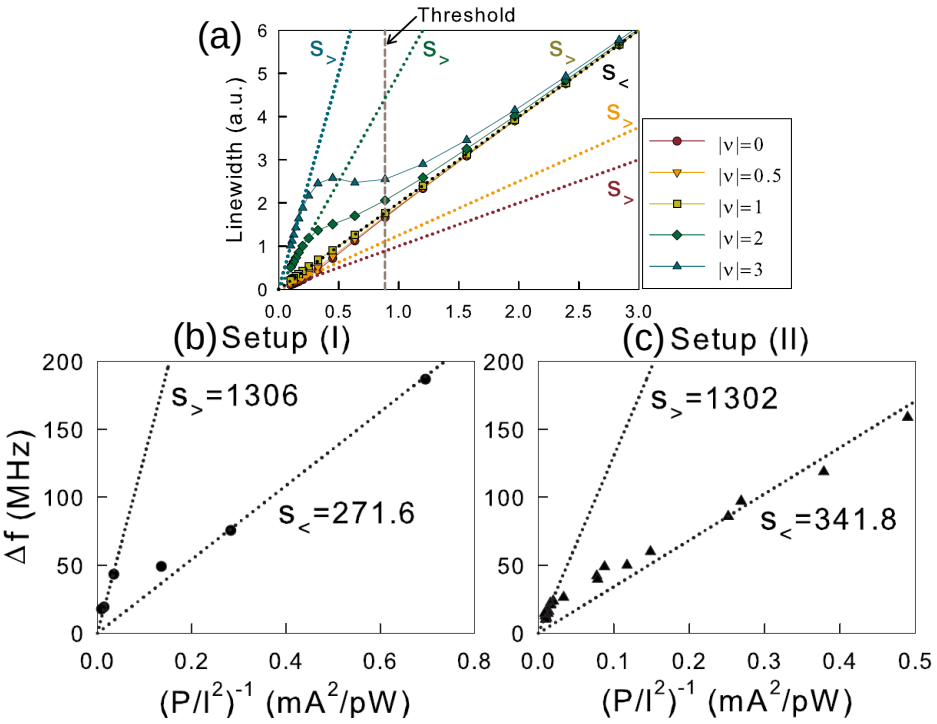

Fig. 2.14: (a) Plots of FWHM versus E_{osci} for different ν. $S^<$ and $S^>$ denote respectively the slope of the limit behavior of the FWHM below and above the threshold. Results are directly obtained from Eq. 2.40. (b) and (c) are experimental plots for two different devices (or setup). $\nu \sim 2.9$ for Setup I and $\nu \sim 2.6$ for Setup II. From [80].

is the one of Kudo et al. [80] underline the fact that because the KTS model is a generic model for non-isochronous auto-oscillators, similar to the theory of a single mode laser, the FWHM should have two asymptotic behaviors, one below the threshold current ($\Delta f^{<}$) and another behavior slightly above ($\Delta f^{>}$). Similarly to the KTS model, they introduced the oscillation energy E_{osci} that is proportional to the emitted power of the STO. Two limiting behaviors of the linewidth of the STO can be deduced from it:

$$\begin{aligned} \Delta f^{<} &= \frac{\Gamma_G}{\pi}(k_b T/E_{osci}) \quad \zeta < 1 \\ &, \\ \Delta f^{>} &= \frac{2\Gamma_G}{2\pi}(k_b T/E_{osci})(1+\nu^2) \quad \zeta > 1 \end{aligned} \tag{2.51}$$

where $\Gamma_G = \Gamma_+(0)$ is the damping rate at thermal equilibrium. We note that $\Delta f^{>}$ corresponds to Eq. 2.50 (with $\Delta f_0 = \frac{\Gamma_G}{2\pi}(k_b T/E_{osci})$). As shown in Fig. 2.14, theoretical predictions fit to experimental data on MTJ-STOs. For this, they considered the oscillation energy E_{osci} proportional to the measured signal power divided by I^2. From the ratio of the slope $S^{<}$ and $S^{>}$ obtained by considering two different trends of the FWHM versus the inverse power, they extracted the nonlinear parameter ν. However, this method is unable to provide the value of Γ_p. Nevertheless, we will use it as an alternative method to obtain the value of ν in our experiments chapter 4.

2.3 Summary

To conclude, we have given an overview of oscillators, damped oscillators, isochronous auto-oscillators, non-isochronous auto-oscillators and the application of their formalism to spin torque driven magnetization dynamics. The KTS model provides a means to transform the LLGS equation into a general oscillator equation, from which the basic behavior in the autonomous regime and in the non-autonomous regime can be derived. The transformation from the (exact) LLGS to the KTS model (with some approximations) isolates the important physical variable of a specific mode profile, represented by the nonlinear parameters N and Γ_p. Only for simplified (high symmetry) cases and for "extended film" modes these parameters can be calculated analytically.

Hence, one needs experimental tools to extract these parameters and that the KTS model is valid for most situations of the autonomous and the non-autonomous regimes of the STOs. In particular, the phenomenological noise model in the KTS theory provides a means to study the linewidth broadening, i.e. the phase noise, that is also relevant for applications. This is the main aim of Part II (chapters 3 and 4), which is the main result of this thesis where the time domain noise spectroscopy (TDNS) technique will be developed to analyze amplitude and phase noise properties in the autonomous regime. This method will be then applied in Part III (chapters 5 and 6) to the non-autonomous dynamics of STOs, respectively the modulation and the synchronization.

Part II

Experimental techniques and autonomous regime under noise

This part presents the first half of the achievements of this thesis that is the study of the STOs in their autonomous regime. Part III will be dedicated to non-autonomous studies of STOs as perspectives for more extensive studies where I used the techniques developed in chapters 3 and 4.

Because the experimental results on the autonomous regime of STOs are not possible without the development of the appropriate experimental techniques, chapter 3 describes the general concepts for understanding and measuring the noise properties of an auto-oscillator of any physical nature.

In the past, the noise properties of STOs have not been studied in a way that addresses directly the parameters relevant for the development of RF applications. As discussed in part I, the measurement of the linewidth is not directly related to the real performances of STOs in terms of the Q factor, for example. In addition, the linewidth gives almost no information on the nature and on the origin of the noise acting on the magnetization in STOs. The time domain noise spectroscopy technique described in chapter 3 permits phase and amplitude noise, specifically for STO performance, to be analyzed. Furthermore, this technique provides a means to study many fundamental aspects of the magnetization dynamics in the presence of noise in STOs.

In chapter 4 these techniques are applied to MTJ devices, whose results will be compared systematically to the KTS model and to macrospin simulations. Although some experiments exist that verify the KTS model, as discussed in the introduction Part I (section 2.2.3 on state-of-the-art literature, i.e. until 2012), a more detailed verification from a systematic analysis has been missing. In particular, the nonlinear parameters Γ_p and ν, which depend on the excitation mode profile, are difficult to derive theoretically. Therefore they need to be extracted experimentally to provide an input to theory. We have also shown in part I that the noise model in the KTS theory is "phenomenological". One underlying motivation of chapter 4 is therefore to see to what extent this phenomenological model is appropriate. The motivations for this systematic experiment/theory comparison is thus twofold where the combined goal of extracting the nonlinear parameters from the noise studies will be demonstrated on the example of the IPP excitation mode in MgO based STOs.

The derived method also provides a tool to characterize phase noise that is the relevant technological parameter. We present first measurements of phase noise values in a large range of frequency (100 kHz to 1 GHz) for MTJ devices. Although this is demonstrated for specific IPP modes of planar MTJs, the technique and its conclusions can be applied to all types of excitation modes in nanopillar and nanocontact structures. This method is then adapted to the analysis of the non-autonomous dynamics as it will be shown in Part III.

Chapter 3

Experimental techniques

The measurement of RF electrical signals in the GHz range requires special techniques. This chapter is dedicated to a detailed presentation of the STO measurements in the GHz range. From a theoretical point of view, it helps to introduce basic notions of noise the in oscillator. From an experimental point of view, it is the key aspect of my thesis and the work I have achieved for the characterization of STOs presented in the following chapters. It is subdivided into two different sections.

The first section refers to the intrinsic low output power generated by the nanoscale nature of the STO enhanced by the impedance mismatch found between MTJ-based STOs with conventional RF objects. We show how to extract the correct generated power of an MTJ-based STO.

The power measurement is related to the magnetization dynamics through the magnetoresistance of the STO. For example, first measurements of STOs based on the GMR effect by Kiselev et al. [39] have shown an output power of around 10 pW (-80 dBm), taking the reduction of power due to the measurement chain into account. From this output power, the authors were able to determine the equivalent cone angle precession of the in-plane precession (IPP) mode in the macrospin approach (see section 1.2.2), confirming the physical origin of the oscillating voltage observed in their magnetoresistive devices. The use of the real output power (or mode power) of the STO will be also of importance for the comparison with the KTS model. Being aware of the power transmission issues and the impedance mismatches that occur in a RF measurements will be valuable when dealing with advanced RF techniques discussed in the following chapters (e.g., modulation and synchronization experiments).

The second section reviews methods to determine frequency instabilities of frequency synthesizers, i.e., phase and amplitude noise. We first review the concept of signal noise in conventional electrical oscillators with the aim of defining STO signal noise properties for typical RF applications. In particular, we give the mathematical concepts of the noise and the means to measure it experimentally. Since the nanoscale nature of STO makes them very sensitive to noise, we show how conventional signal analyzer tools fail to determine their noise performance. As a consequence I finally describe the method I developed for this noise characterizations of STOs that is also suitable for any conventional oscillators.

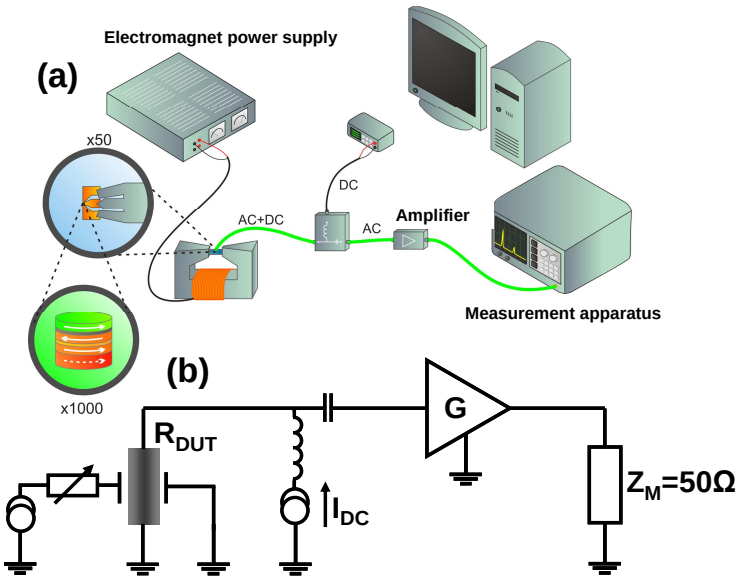

Fig. 3.1: (a) Experimental measurement chain of the STO. An electromagnet controls the local field on the DUT/STO. A dc current is applied to the STO. A bias-tee allows the ac component of the current to be extracted, which is then amplified and measured with a dedicated instrument. Adapted from [81]. (b) Equivalent circuit of the total chain. The measurement is done on a 50Ω load after the gain amplification of the chain G. R_{DUT} is more complex than only a resistance (see section on de-embedding).

3.1 Specifics of RF measurements

To examine the detailed steps in the measurement of STOs, we will use an experimental setup schematically given in Fig. 3.1-a. The corresponding equivalent circuit is shown in Fig. 3.1-b. Following Fig. 3.1, the Device Under Test (DUT) is measured at one end of the measurement chain (characterized by $Z_M = 50\Omega$). The signal received by the measurement apparatus is thus strongly affected by the power transmission along the measurement chain, and must be corrected in some way.

For this purpose, let us first give some basic issues of the power transmission in RF circuits. From this will follow the direct application to the power transmission between each component of the chain and between the DUT/STO and the chain. Finally we give basic information on the measurement apparatus in the frequency domain and traps to avoid.

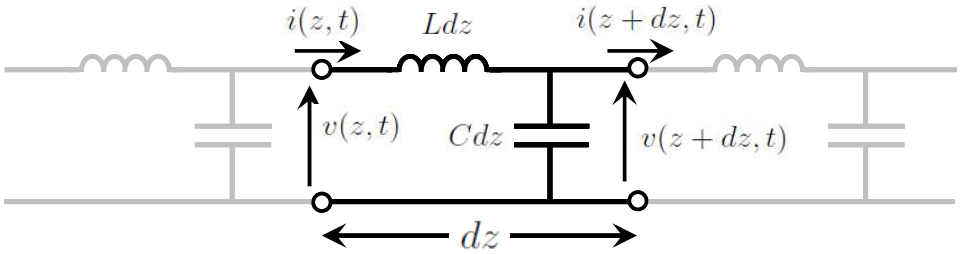

Fig. 3.2: Voltage $v(z,t)$ and current $i(z,t)$ definitions in the lumped-element equivalent circuit of a transmission line of portion dz.

3.1.1 Transmission line theory

The quasi-static approximation that allows the use of Kirchhoff's law is not suitable for gigahertz signals at the component level. For instance, if we consider a 10 GHz signal, the wavelength is about 3 cm that is a similar length to most of the components found in Fig. 3.1. Therefore, the electromagnetic wave formalism, provided by Maxwell's equations, is used to describe the propagation of microwaves along the measurement chain. Here the microwave signal is considered as a power quantity (a wave) that propagates into a certain direction. Most of the RF components are waveguides that guide the microwave from their input port to their output port. The description of the propagation of the power through the different components makes use of continuity equations given by Maxwell's equations. The following part briefly summarizes the wave theory of basic RF concepts.

To take into account the spatial variation along a wave guide, the telegraph model is used (see Fig. 3.2). The wave continuity allows one to consider the infinite medium along which the wave propagates on infinitesimal parts of size dz where Kirchhoff's law is valid. If the (propagative) line is lossless, only a linear capacitance C and linear inductance L is needed to define the propagation of the wave described (v,i).

The system presented in Fig. 3.2 satisfies the wave equations for cosine-based phasors[1] $V(z)$ and $I(z)$ (derived from $v(z,t) = V(z)e^{i\omega t}$ and $i(z,t) = I(z)e^{i\omega t}$):

$$\begin{cases} \frac{d^2V(z)}{dz^2} - \gamma^2 V(z) = 0 \\ \\ \frac{d^2I(z)}{dz^2} - \gamma^2 I(z) = 0 \end{cases}, \tag{3.1}$$

where $\gamma = \alpha + i\beta$ with $\beta = \omega\sqrt{LC}$ and $\alpha = 0$ (in the case of lossless line). The solutions are given by:

$$\begin{cases} V(z) = V_0^+ e^{-\gamma z} + V_0^- e^{\gamma z} \\ \\ I(z) = I_0^+ e^{-\gamma z} + I_0^- e^{\gamma z} \end{cases}, \tag{3.2}$$

[1]Phasors are mathematical quantities where the oscillating term ωt are removed in order to simplify equations. It is also considered as a physical quantities when dealing with noise in the next section.

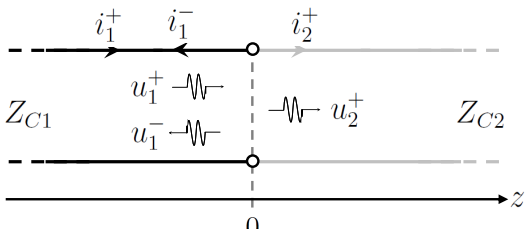

Fig. 3.3: Two semi-infinite media linked at $z = 0$ with two different characteristic impedances Z_{C1} and Z_{C2}.

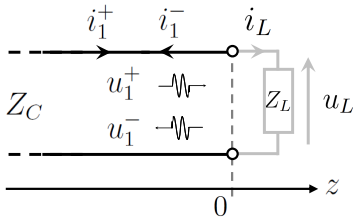

Fig. 3.4: Transmission line terminated by a load of impedance Z_L.

V_0^+ and I_0^+ propagate in the $-z$ direction, while V_0^- and I_0^- propagate in the $+z$ direction. An important notion is the characteristic impedance Z_c of the line: V_0^+/I_0^+ that describes the inductive/capacitive ratio of a line. For historical reasons, the common value used for conventional components[2] in the RF range is $Z_c = 50\Omega$.

3.1.2 Impedance matching

The interest of the characteristic impedance is to describe the reflection and transmission coefficients at the interface of two different media. In the case of Fig. 3.3, an incoming wave (u_1^+, i_1^+) will split into a transmitted wave (u_2^+, i_2^+) and a reflected wave (u_1^-, i_1^-). We define the reflection Γ and transmission T coefficients such that:

$$\Gamma = \frac{u_1^-}{u_1^+} \quad T = \frac{u_2^+}{u_1^+} \,. \tag{3.3}$$

The continuity conditions $i_1^+ = i_1^- + i_2^+$ impose $\Gamma + {}^{Z_{C1}}/_{Z_{C2}} T = 1$ such that:

$$\Gamma = \frac{Z_{C1} - Z_{C2}}{Z_{C1} + Z_{C2}} \quad T = \frac{2Z_{C2}}{Z_{C1} + Z_{C2}} \,. \tag{3.4}$$

The impedance mismatch between the two media leads to a reflected wave (and thus power) that decreases the transmitted power. This is the case in a load terminated line. As shown in Fig. 3.4, if we consider a transmission line terminated by a load of impedance Z_L, with $Z_{C2} = Z_L$, the reflection coefficient takes the form:

$$\Gamma = \frac{Z_C - Z_L}{Z_C + Z_L} \,. \tag{3.5}$$

[2]By convention or consensus the characteristic impedance of most of RF components is 50Ω.

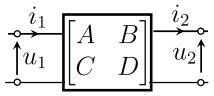

$$\begin{pmatrix} u_1 \\ i_1 \end{pmatrix} = \begin{bmatrix} A & B \\ C & D \end{bmatrix} \begin{pmatrix} u_2 \\ i_2 \end{pmatrix}$$

Fig. 3.5: Transmission Matrix (ABCD) with corresponding inputs and outputs.

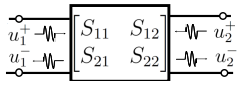

$$\begin{pmatrix} u_1^- \\ u_2^- \end{pmatrix} = \begin{bmatrix} S_{11} & S_{12} \\ S_{21} & S_{22} \end{bmatrix} \begin{pmatrix} u_1^+ \\ u_2^+ \end{pmatrix}$$

Fig. 3.6: Scattering Matrix with corresponding inputs and outputs.

Thus impedance and characteristic impedances for a discrete element are equivalent ($Z_{C2} = Z_L$). This part highlights the importance of matched components for the measurement of RF signals. Indeed, any impedance mismatch leads to reflected waves that turn into stationary waves, which should be avoided. This aspect needs to be taken into account when one wants to know the real emitted power by the DUT, i.e. to extract the exact oscillation power emitted by the STO.

3.1.3 Microwave Network analysis

In order to extract the exact voltage/current at the output of the STO, each component (probes, amplifiers, cables, ...) is described by a transfer function that links the output (u_2, i_2) of a component to its input (u_1, i_1). For this the **Transmission Matrix** ($ABCD$ or T matrix) is used that easily links inputs and outputs (see Fig. 3.5).

From the form of the T matrix, it is possible to compute a chain of several components by using matrix products [82]. Since T is not directly accessible experimentally (because most of instruments measure voltages) only the **Scattering Matrix** (S-matrix) can be measured.

As shown in Fig. 3.6, the scattering matrix formalism has a very direct use for the physical interpretation of its elements. For instance, S_{21}, i.e. the ratio of output voltage to the input voltage, is actually the (voltage) gain of the component: if its two ports are matched, S_{21} of a component gives its power gain.

Since S matrices cannot be multiplied, the experimental protocol is to separately measure the S-matrix of each RF component, then to convert them into T matrices that they can be combined. Finally the total S-matrix is computed back to obtain the total measurement chain gain. As shown in Fig. 3.7, the total gain measured with a vector network analyzer (VNA) of the full chain measured at once (S_{21} from the Direct measurement) corresponds well to the computed gain from separate measurements of each component using T (or $ABCD$) matrices.

Since a MTJ-based STO has a load impedance of about 300 Ω – 1 kΩ, the signal generated in the STO is not fully transmitted to the measurement chain because of the load mismatch problem discussed above. Moreover, the STO is "*embedded*" in coplanar waveguide electrodes. Our next exercise is to explain how, from the measurement of reflected power with a VNA, the exact power generated by the STO can be extracted. Together with this de-embedding this protocol allows both versatility and accuracy of different STO measurements.

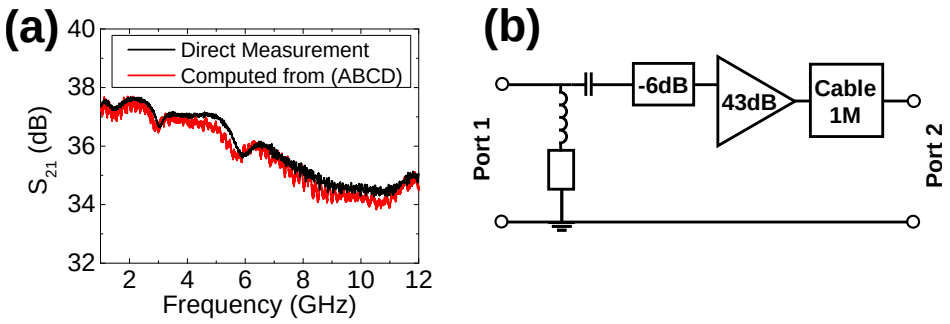

Fig. 3.7: Example of the use of the (ABCD) transmission matrix for a typical chain gain of the STO measurement setup, with gain $G \approx 37$. The product of transmission matrices (ABCD) in red corresponds to the measurement of the full gain of the chain, in black. (b) Schematic of the typical chain gain, from left to right : bias-tee, 6 dB attenuator, 43 dB amplifier and 1 meter of RF cable.

3.1.4 Gain correction and de-embedding

Two different geometries of coplanar waveguide exist. The first one is called "transmission device" that are similar to coplanar wave guide transmission lines whose central line is split into tow parts to contact the MTJ. Those devices act as quadrupole components with input and output ports. This is of interest when one wants to input RF signals to the STO (e.g. modulation and synchronization experiments discussed in part III). The second coplanar waveguide geometry is called "reflection device". This one is presented in Fig. 3.8-a with a zoom at the position of the MTJ device.

To take into account the specifics of the electrode geometry of the STO reflection device, a model has been described [45, 47] in order to have access to the real output power of the STO. This model is represented in Fig. 3.8-b. The capacitance effect mainly originates from the overlap of the electrodes at the position of the MTJ device (see the capacitance formula in Fig. 3.8-a, with $\epsilon_r = 10$ for alumina that is used to electrically isolate the two electrodes, spaced apart by the distance $e = 35$nm). When measured with a VNA, the reflected power S_{11} (see Eq. 3.5) at the input of the STO corresponds to the one reflected from the equivalent impedance in Fig. 3.8:

$$Z_{eq} = \left(r_l + \frac{R_{MTJ}}{1 + (R_{MTJ} C\omega)^2} \right) + j \left(L\omega - \frac{R_{MTJ}^2 C\omega}{1 + (R_{MTJ} C\omega)^2} \right). \tag{3.6}$$

A fitting procedure of $Z_{eq} = 50\frac{S_{11}+1}{S_{11}-1}$allows the electrode parameters r_l, L and C to be found. As shown in Fig. 3.8-a,b, the obtained capacitance value indeed corresponds to the overlap of electrodes in this case. Since the capacitance value is "low", its effect is negligible on the power transmission from the MTJ to the 50Ω chain (see Fig. 3.8-d and the effect of a higher value of the capacitance on the power transmission). In the case presented here, the high resistance value of the MTJ reduces considerably the transmitted power to the chain that is 10 times lower than the measured one (see Fig. 3.8-d).

In order to avoid the high impedance mismatch between the MTJ-based STO and the 50Ω chain, a high-Z input amplifier has been realized by the Leti in 2008 for the specific purpose to be used in MTJ-based STOs [83]. This high-Z amplifier allows to match a high input source to a 50Ω measurement chain. In this way, all the power generated

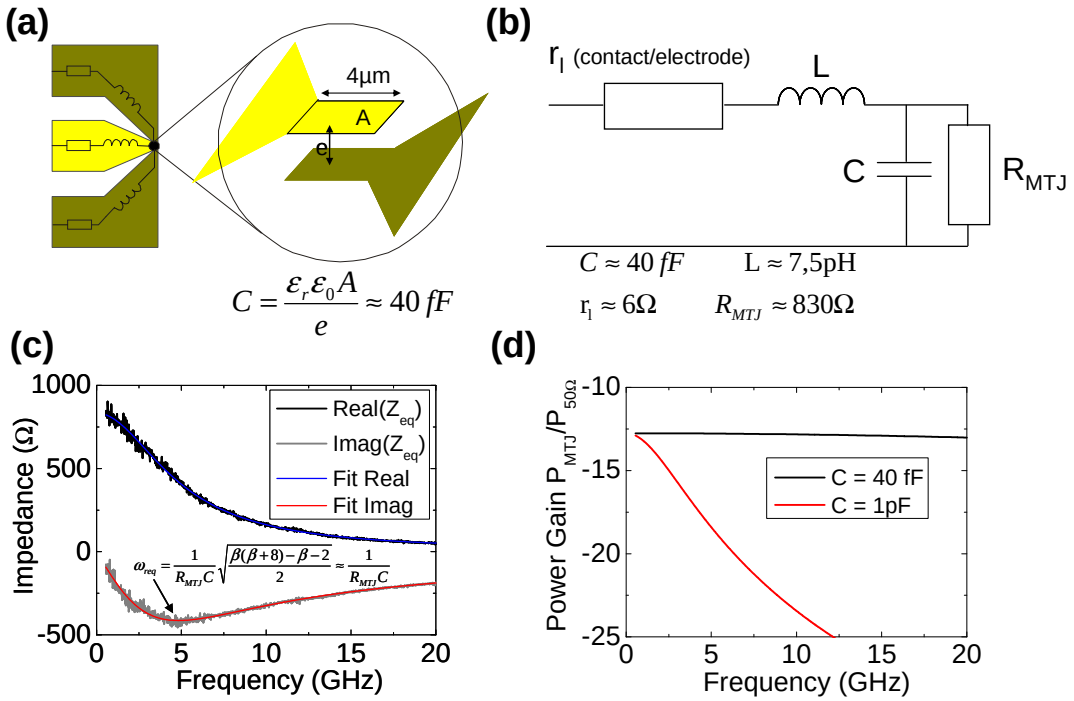

Fig. 3.8: (a) Schematic view of the STO geometry encapsulated in its electrodes. The electrode overlap of the coplanar waveguide electrode implies a capacitance effect between top and bottom electrodes. (b) Block diagram of the equivalent electrical circuit and the fitted value for each component. (c) Real and imaginary part of the impedance of the junction encapsulated in its electrodes measured by means of VNA. The fitted curves correspond to the model Eq. 3.6. $\beta = R_{MTJ}^2 C/L$. (d) Effect on the transmitted power generated at the MTJ to a 50Ω load for $C = 40$ fF (the design used in this thesis) and $C = 1$ pF (wrong design). When the capacitance is low, the transmitted power from the MTJ to the measurement chain is mainly affected by the common load mismatch implied by the voltage divider formed by the high-Z value of the MTJ compared to 50Ω. When C is such that $\omega_{res}/2\pi < 1$ GHz, an additional effect is seen in the GHz range where the transmitted power is affected by the capacitance and non-negligible. It requires then to take into account not only the voltage divider, but also the capacitance effect in order to retrieve the real power emitted by the MTJ.

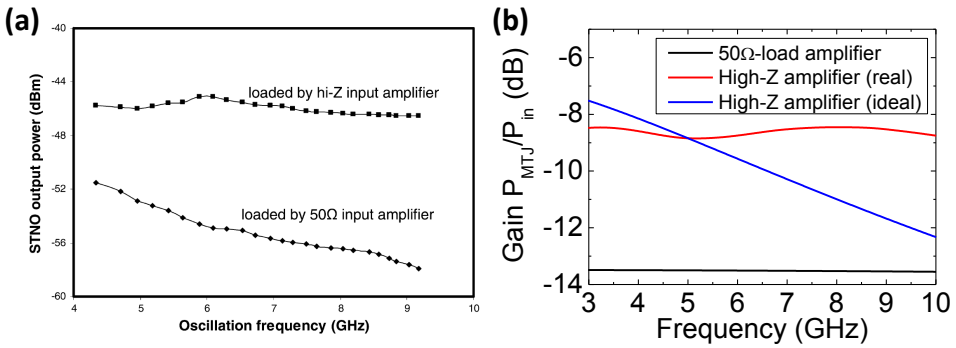

Fig. 3.9: (a) Measured output powers of an STO (after gain correction) when the pillar is connected through a high-Z input amplifier and a 50Ω input amplifier. The power measured differs by about 6 dB. From [83]. In the case where the STO is connected to the 50Ω input amplifier, the decrease of output power is due to the fact that the gain of the chain was considered constant while it decreases with frequency (see Fig. 3.7). (b) Simulated power gain for different input impedances of the amplifier. In the case of an ideal high-Z input amplifier, the gain would decrease with frequency, but the simulation with the real input impedance makes the transmitted gain almost constant in the frequency range considered. The difference between the real high-Z amplifier and the 50Ω input amplifier is about 5 dB. Simulation parameters: $C = 40$ fF, $R_{MTJ} = 1$ kΩ, $L = 7.45$ pH and $r_l = 6$ Ω.

in the STO can be transfered to the measurement chain. As shown in Fig. 3.9-a, the high input amplifier can enhance the measured power on a 50Ω chain. The simulation results shown in Fig. 3.9-b indicate the interest of such an amplifier for the measurement of STO. Since the sample requires to be bonded to this high-Z amplifier, we do not use it in experiments. Nevertheless, this experimental achievement highlights the interest of the de-embedding model and its accuracy. In particular, this model will be of use when injecting high frequency signals to the STO, but also to estimate the real oscillation power generated by the STO.

We now focus on the last components of the RF chain that is the Spectrum Analyzer (SA). This instrument allows to "locate" a given signal in the frequency space. The way this "frequency localization" occurs is described in the next section. We also discuss the limitations of this technique to highlight the need for the signal analysis of STOs.

3.1.5 Measurement of the voltage PSD

As discussed in part 1.1.2, the tunnel conductance of an MTJ depends on the relative angle between free and pinned layers. When steady-state oscillations occur, we assume it generates an oscillating voltage:

$$V(t) = V_{\mathrm{RF}} \cos(2\pi f_{\mathrm{RF}} t). \tag{3.7}$$

The problem is now to measure and to locate the component V_{RF} in frequency space. One solution is to directly acquire this voltage in time domain and to perform a Fast Fourier Transform (FFT) using digital signal processing (DSP) techniques. However, due to electronic limitations, this technique was limited until the end of the 1990s to signals whose frequencies are below 40 MHz [84]. This is explained by the low speed of electronic

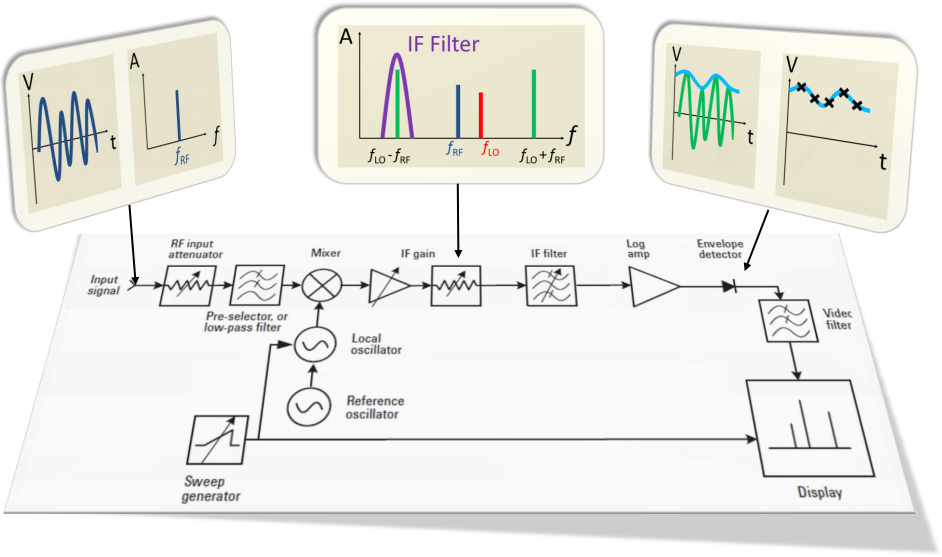

Fig. 3.10: Block diagram of a typical (super-)heterodyne method used in a conventional spectrum analyzer in the GHz range. The signal is in a first stage multiplied with the local oscillator signal. The resulting signal is filtered out thanks to the IF filter. The envelope of this low frequency signal is extracted with a diode detector and then digitalized. The current technology trend is to digitize directly the IF signal for post-treatment. Adapted from [84].

circuits and the weak dynamic range of digitizers. Very recent instruments allow such analysis to be performed for GHz signals. Their advantage is that they allow the separate study of amplitude and phase of a signal as well as single-shot measurements, as it will be shown in section 3.2.3.2.

To have both the precise measurement of V_{RF} and f_{RF} of a single tone signal such as the one of Eq. 3.7, the Heterodyne method used by spectrum analyzers (SA) in Fig. 3.10 remains the most accurate in the GHz range[3]. This method consists of multiplying the RF signal to be measured by a reference signal given by the local oscillator (LO), of known amplitude V_{LO} and known frequency f_{LO}. The frequency of the LO is ramped such that it varies with time. The mixer insures the multiplication of the RF and LO signals. The cosine product provides the frequency sum $(f_{\mathrm{RF}} + f_{\mathrm{LO}})$ and difference $(f_{\mathrm{RF}} - f_{\mathrm{LO}})$. This signal is then directed to the intermediate frequency (IF) bandpass filter of center frequency f_{IF} and the width RBW (resolution band width). Finally, the signal envelope is measured with an envelope detector to provide a point in the spectrum. By sweeping the frequency of the LO, a full spectrum of the input signal can be obtained that have necessarily a finite width.

This spectrum will depend on the conditions of the measurement. Indeed if we imagine distinguishing two signals that have a frequency difference of 100 kHz, the RBW should be below 100 kHz. Moreover, the LO ramp setting must be such that it allows one to distinguish the two signals separated by 100 kHz. The measurement precision of the value V_{RF} will depend on the detection mode, i.e. the way the envelope is acquired.

[3]Actually, the method presented in Fig. 3.10 is the super-heterodyne method, since the IF is fixed. But we still refer to this method as heterodyne method in the following.

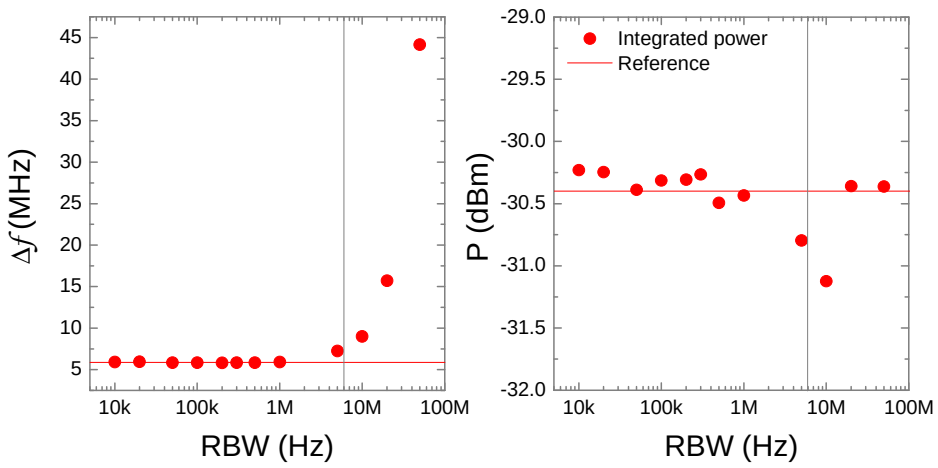

Fig. 3.11: Signal characteristics of a Lorentzian signal of $\Delta f = 6$ MHz and $P = -30.5$ dBm generated by a signal generator with different RBW used for the measurement with a SA. (left) Measured FWHM Δf versus the RBW. (right) Measured power versus RBW. This signal parameters are close to those of an STO after amplification. From [81].

In consequence, the measurement conditions (RBW, sweep procedures, detector type, averaging, ...) must be defined with respect to the signal that is to be acquired. For instance, from Fig. 3.11-a it appears that the RBW should be fixed two to three times lower than the STO's FWHM in order to provide its correct value. Indeed in the example of Fig. 3.11, the correct evaluation of the FWHM of a Lorentzian signal of $\Delta f = 6$ MHz and power $P = -30.5$ dBm (parameters are set in the signal generator menu) is obtained when the $RBW < \Delta f$. Nevertheless, the correct determination of the real signal power is only made possible with a very high RBW[4]. Typically, the detector type and the averaging methods will also influence the shape of the measured peak (see Ref. [81]). For example the measurement settings in Fig. 3.11-b make the power measurement "almost" reliable even if the RBW is below the total "frequency spreading" of the signal to measure. The simplest way to achieve such an "almost" correct power measurement with $RBW < \Delta f$ is to set the RBW at least four times smaller than Δf. In addition the sweeping procedure should be such that a point in frequency is measured every RBW (no overlapping points). When a frequency domain measurement is reported for STOs, we use such kind of conditions in the SA settings. Indeed, the effect of measurement conditions on the obtained spectra are well known but need to be adjusted to the specific signal to be measured and the information one wants to obtain (see for example cases discussed in [81, 84, 85]).

Finally, even with the most careful measurements of STOs, the different noise contributions make a reliable and precise measurement of STO's "main" characteristics FWHM Δf difficult [85].

In conclusion, we have shown how it is possible to correct the gain of the chain in order to extract quantitatively the voltage/power emitted from an STO. Since this

[4]To estimate the power of a signal spread onto a frequency span Δf_{span}, there is no other choice than to make the power measurement with a frequency aperture higher than Δf_{span}.

voltage is proportional to the angle formed by the pinned and free layer, it gives information on the dynamics that takes place in the structure. In this way, the measurement can be qualitatively and quantitatively compared to simulations of the excitations. The most important message to retain here is that, in addition to the importance of the estimation of the power for RF application of STOs, the measured power will depend on the frequency because of the specifics of RF measurements techniques. When a measurement is done on STOs, it is important to give all the required information (SA setup, gain calibration procedures) in order to compare with theories but also in order to compare the efficiency of the different devices measured, excitation schemes and so on. While measurements with the SA provide Δf, they do not provide a deeper insight into its origin, in particular, as to amplitude and phase fluctuations that, as outlined in chapter 2, determine Δf.

The next section describes a time domain noise spectroscopy technique (TDNS) that allows one to analyze amplitude and phase of the signal, by using signal analysis techniques. The development and the validation of this technique throughout my thesis is one of the main achievements of this work. The result obtained on STOs with this technique will be given in chapter 4.

3.2 The time-frequency measurement

The techniques of the previous section were developed and adapted to STO characterization before the start of my thesis [47, 81]. The very recent time domain characterization techniques [76, 77, 78, 85, 86] of STOs developed throughout my thesis have considerably enlarged the information that can be gained from experiments on the nonlinear dynamics in STOs. We give here the necessary knowledge adapted from time-domain metrology that can be applied to STOs.

Since STOs are very similar to voltage control oscillators (VCO), we review the historical development of their characterization (that we have referred to "signal analysis"). The most common way to characterize auto-oscillators of different nature is the phase and amplitude noise plot that will be discussed intensively. The understanding of these plots requires some mathematical definitions, especially related to noise properties.

We finally introduce the phase noise measurement techniques with frequency domain instruments that are essentially based on heterodyne methods/schemes. We show their limitations for the characterization of STOs and therefore describe our own developed technique. The detailed description of this technique presented in this work aims to provide the necessary information to reproduce the same measurements. Also, it is given the main limitations of the techniques and its possible solutions.

3.2.1 Introduction to signal analysis

In the previous part we discussed the power measurements of an RF signal that is supposed to have a single frequency tone. Since STOs are nanoscale devices, they are very sensitive to noise. In chapter 2 section 2.2.3, it has been described how the noise affects the linewidth Δf of STOs via phase fluctuations ϕ and amplitude fluctuations δa. Substantially, we explain here the link between ϕ and δa and the lineshape broadening

(i.e. Δf) of the PSD of voltage, and why their characterization is of importance for both applicative and fundamental research. We now consider the general form of a single frequency tone ν_0 signal of amplitude A_0 affected by phase $\phi(t)$ and amplitude $\delta a(t)$ noise [87, 88]:

$$V(t) = A_0(1 + \delta a(t)) \cos(2\pi\nu_0 t + \phi(t)). \tag{3.8}$$

Historical definition of the phase noise

First of all, let us define the *historical* notion of the single-side band (SSB) $\mathcal{L}(f)$ (pronounced *script ell* of f) defined as the ratio of the power found in 1 Hz bandwidth at a frequency f to the carrier frequency ν_0 and the total signal power:

$$\begin{aligned} \text{OLD: } \mathcal{L}^{\text{old}}(f) &= \frac{\text{power in one sideband per unit of Hz}}{\text{total signal power}} \\ &\sim \frac{S_\phi}{2} \text{ when } \phi << 1 \text{ and } \delta a \text{ neglected} \\ \text{NEW:} \mathcal{L}^{\text{new}}(f) &= \frac{\text{power in one sideband due to phase noise per unit of Hz}}{\text{total signal power}} = \frac{S_\phi}{2} \end{aligned} \quad , \tag{3.9}$$

where S_ϕ and $S_{\delta a}$ are respectively the PSD of phase noise and amplitude noise for a signal expressed as in Eq. 3.8. $\mathcal{L}(f)$ is expressed in decibels (dB) and since it is relative to the carrier power and measured on 1 Hz, its unit is dBc/Hz. The definition based on power ratio, $\mathcal{L}^{\text{old}}(f)$, is illustrated in Fig. 3.12. This definition of $\mathcal{L}(f)$ corresponds to an *old* definition of oscillator noise but is still used nowadays in frequency metrology [87]. The second definition ($\mathcal{L}(f) = S_\phi/2$) is now considered as the *new* definition of $\mathcal{L}(f)$ and is equivalent to the *old* one for relative low phase noise values as well as negligible amplitude noise [89]. That is why $\mathcal{L}(f) = S_\phi/2$ is considered since 1997 as the *exact* definition of SSB noise of an oscillator output voltage [87]. As we said, the old definition is equivalent to the new definition when amplitude noise is negligible and phase noise is small. Therefore, the old definition used when referring to the spectral purity of the STO when measuring the FWHM is not correct (since 1997). This old definition is based on the former means to measure the quality of a frequency synthesizer (oscillator) that were based on heterodyne methods (see for example Fig. 3.10). Indeed if we consider a heterodyne setup, where the carrier suppression is realized by signal mixing in quadrature, the mixer output is given by:

$$\begin{aligned} V_{\text{MIXER}}(t) &= A_0 \sin(2\pi\nu_0 t + \phi(t)) \cdot \cos(2\pi\nu_0 t) \\ &= A_0/2 \sin(\phi(t)) + A_0/2 \sin(4\pi\nu_0 t + \phi(t)) \end{aligned} \quad . \tag{3.10}$$

Filtering the signal at $2\nu_0$ insures that only $\sin(\phi)$ is measured. When $\phi(t) \ll 1$, $\sin(\phi) \sim \phi$. Computing of the PSD of this filtered $V_{\text{MIXER}}(t)$ signal is thus equivalent to computing the PSD of phase fluctuations $\phi(t)$.

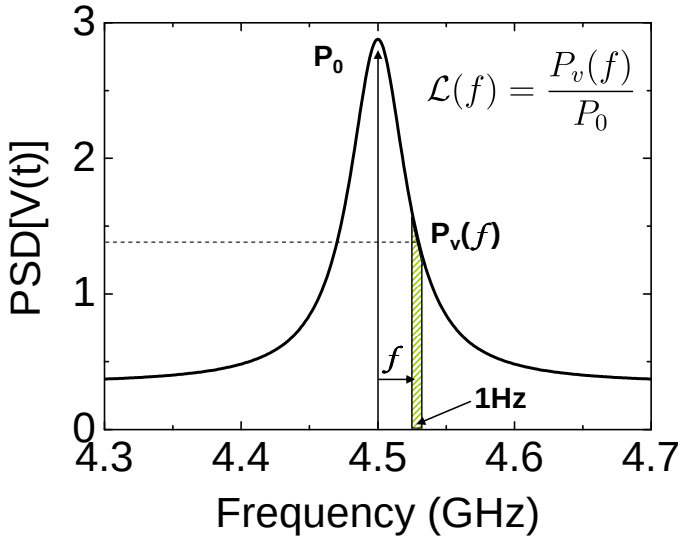

Fig. 3.12: $\mathcal{L}(f)$ is measured as the ratio of the power $P_v(f)$ measured on a 1Hz bandwidth at an offset frequency f from the carrier frequency and the total signal power P_0 is defined as the area under the curve of the PSD of $V(t)$. Here the case is presented where the PSD is a Lorentzian function centered at $\nu_0 = 4.5$GHz.

When $S_\phi(f)$ is represented or plotted, the quantity is called the double-side band (DSB) noise[5] that is twice $\mathcal{L}(f)$ and expressed in dBc/Hz or dB.rad^2.Hz^{-1}. The role of amplitude noise (AN) $\delta a(t)$ on the spectral purity of a signal is often negligible. The reason is that in Eq. 3.8, the dominant signal is $G_{phase}(t) = A_0 \cos(2\pi\nu_0 t + \phi(t))$ while the signal $G_{amp}(t) = A_0 \delta a(t) \cos(2\pi\nu_0 t + \phi(t))$ is an order below since $\delta a(t) \ll 1$. Therefore, only phase noise (PN) $\phi(t)$ is considered when dealing with the spectral purity of a signal emitted from a "stable" oscillator. Fig. 3.13-a schematically illustrates the quasi-linear oscillator theory [42, 90, 91]. This simplified model considers that the PSD of the total voltage S_V is $S_V \propto (G_{phase}(\omega) + G_{amp}(\omega))$, and that $G_{amp}(\omega) \approx S_{\delta a}$. Fig. 3.13-b shows the experimental verification for a VCO that amplitude noise is much below the phase noise in RF oscillators in general [89]. The evolution of the definition of $\mathcal{L}(f)$ is closely related to the historical development of telecommunication technology. To highlight the importance of the spectral purity in telecommunications, and therefore of phase noise, we detail the issue of phase noise in real applications.

Spectral purity, $\mathcal{L}(f)$ and phase noise in telecommunications

Since practical devices emit and receive (transceivers) voltage in communication protocols, it is important that each signal does not influence its neighborhood. Therefore, a telecommunication protocol always has restrictions on spectral purity on signals used. To insure that two neighboring signals do not affect each other, the $\mathcal{L}(f)$ is recommended to be below a certain value for different frequency offsets from the carrier frequency. In table 3.1 the required SSB is given for different widely spread telecommunication standards. In the case of GSM, the channel width is 200 kHz (in

[5]The PSD of $\phi(t)$, $S_\phi(f)$ is the single-sided power spectral density [87]. There is no ambiguity in the definitions.

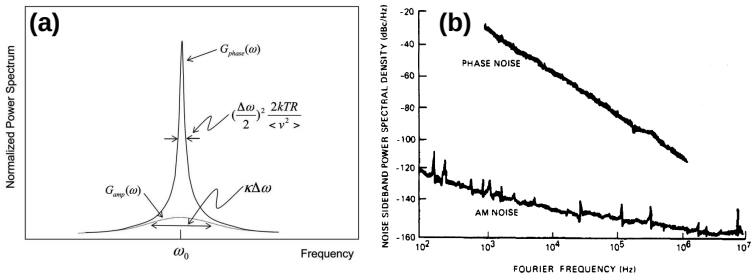

Fig. 3.13: (a) Schematic representation of the linear oscillator theory, where $G_{phase} = S_\phi$ and $G_{amp} = S_{\delta a}$. From [91]. (b) Measurement of phase noise S_ϕ and amplitude noise $S_{\delta a}$ on a Gunn Diode oscillator ($\sim$ 40 GHz). From [89].

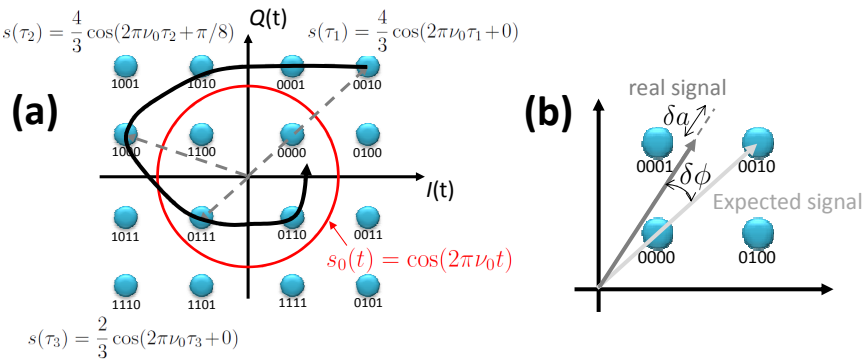

Fig. 3.14: (a) Constellation Diagram of a 16QAM signal. Example of amplitude and phase modulations of $s_0(t)$ that insure correct formation of bits. The black curve is the signal trajectory in the I/Q plane. (b) Effect of noise on the bit coding. Phase and amplitude noise may induce bit error.

Europe) and the requirement is given to indeed not "overlap" on neighbors. In the case of the global positing system (GPS) and wireless local area network (WLAN or WIFI), there is respectively no channel width (only 1 GPS signal) and overlapping channels! The reason is that these standards need protocols such that a noisy carrier frequency should not induce any errors in data transmission, especially in digital telecommunications.

The best example to understand the importance of having a low $\mathcal{L}(f)$ in data communications, and easy to understand from the definition of phase portrait in chapter 2, is the quadrature amplitude modulation (QAM) or I/Q modulation. In this case information can transit through amplitude modulations (AM) and phase modulations (PM) of the carrier signal whose frequency is ν_0. The signal has the form:

$$s(t) = I(t)\cos(2\pi\nu_0 t) + Q(t)\sin(2\pi\nu_0 t)\ , \tag{3.11}$$

where $I(t)$ and $Q(t)$ are modulating signals. If we mix this signal to a mixer in and 90°-off phase with the LO, we can easily reproduce the parametric graph $Q(t)$ versus $I(t)$. Fig. 3.14 shows the example of 16-QAM that uses both AM and PM of the carrier signal. All I/Q combinations are marked with their "digital signification". We also plot a signal over one carrier period that has both AM and PM. To "read" the I versus Q signal, it is necessary to have a clock that indicates when the reading should be done.

Standard	Frequency to carrier	Max $\mathcal{L}(f)$ allowed
GSM/DCS	200 kHz	-74 dBc/Hz
	400 kHz	-106 dBc/Hz
	600 kHz	-121 dBc/Hz
	1.6 MHz	-131 dBc/Hz
	3 MHz	-141 dBc/Hz
	20 MHz	145 dBc/Hz
GPS	10 kHz	-70 dBc/Hz
	70 kHz	-70 dBc/Hz
	1 MHz	-105 dBc/Hz
BlueTooth	1 kHz	-78 dBc/Hz
	20 kHz	-78 dBc/Hz
	500 kHz	-95 dBc/Hz
	1.5 MHz	-119 dBc/Hz
	2.5 MHz	-130 dBc/Hz
802.11 WLAN	1 kHz	-80 dBc/Hz
	15 kHz	-80 dBc/Hz
	1.5 MHz	-120 dBc/Hz
	10 MHz	-129 dBc/Hz
	30 MHz	-140 dBc/Hz

Table 3.1: Required $\mathcal{L}(f)$ value for different telecommunication standards at different f.

In the example of Fig. 3.14, two readings are *exactly* separated by $|\tau_i - \tau_{i+A}| = 1/4\nu_0$. It is straightforward to communicate digital information with such an encoded signal. However, because noise can affect both amplitude and phase of the carrier signal, it may appear that the modulated signal does not appear where it should. It may have some bit errors. This is why carrier signals as in GPS or WLAN must have very low $\mathcal{L}(f)$ in general since, from its definition in Eq. 3.9, $\mathcal{L}(f)$ is an indication on the frequency stability of the oscillator.

Correct formulation of the phase noise

Since we have reviewed the reason why phase noise is important in oscillators, we focus on the mathematical definition of phase noise. Following the representation in Fig. 3.14, we represent the noisy carrier signal in the I/Q plane, similar to phase portrait, and we focus on its temporal evolution. Since the total phase of the signal $\Phi = 2\pi\nu_0 t + \phi(t)$ runs at a constant velocity $2\pi\nu_0$, we can remove this phase accumulation to form a vectorial representation of s_0 that is the *phasor*. At a time t, the phasor coordinate is $(A_0(1 + \delta a(t)); \phi(t))$ in the phase plane, only the PN and AN appear.

The complete form of PN $\phi(t)$ is [88]:

$$\phi(t) = g(t) + \Delta\Phi \sin(2\pi f_m t) + \delta\phi(t), \tag{3.12}$$

where $g(t)$ is a deterministic function that takes into account the aging of the oscillator frequency (that is often known), $\Delta\Phi$ is the amplitude of the periodic phase modulation

with a frequency f_m, and $\delta\phi(t)$ a random fluctuation of the phase.

The first term $g(t)$ is compensated by calibration. The phase modulation term originates from the oscillator electrical environment, for example a DC coupled power supply will induce such modulation tones (in electrical oscillators). While the two first terms originate from direct deterministic perturbations of ω_g or $\Gamma_\pm$ terms, as defined in Eq. 2.24 in chapter 2, $\delta\phi$ is closely related to the internal structure of the oscillator. In the case of STOs, we have identified its origin from the stochastic processes $f_n(t)$ introduced in Eq. 2.24. Because it is the one of interest for us, we consider from now $\delta\phi = \phi$. At this point, the definition of stochastic processes is needed, especially to understand the notion of PSD when dealing with the PSD of ϕ.

Note on Stochastic processes

A stochastic process $y(t)$ has a strict mathematical definition that can never be checked in real systems because time is irreversible: we cannot measure the same quantity twice starting from the same initial time t_0. Indeed a stochastic process is a collection of random variables X, i.e. a time-indexed family of random variables [92]. It means that:

$$y(t) = X \ \forall t \ . \tag{3.13}$$

While it seems to be an over constructed entity, studying the stochastic process $y(t)$ is not equivalent to studying the distribution function of X versus the time t. For example, if we study N times the same process $y^{i\leq N}(t)$ on $t \in [0, +\infty[$, we have $\forall\ t\ y^i(t) \neq y^j(t)$ for $i \neq j$. $y(t)$ is indeed a realization of the random variable X at the time t. Fig. 3.15 schematically shows a stochastic process $y(t)$ and the probability distribution function (PDF) of the random variable X for two different times τ_1 and τ_2. We note that the PDF of X at time τ_1 is different from the one at time τ_2. Such a process is called non-stationary, since the PDF of X is not constant over the experiment. In contrast to what is shown in Fig. 3.15, the stochastic process $y(t)$ must be considered *stationary* in oscillator models, in order to insure that the measurement of the PSD of ϕ is possible. The stationary property of a stochastic process insures that $\forall t \in [0, +\infty[$, and the PDF of X remains unchanged. In addition to our STO measurements, we assume the ergodicity of the process. In other words we assume the stochastic process to be ergodic in oscillator models. This means that by taking sufficiently long time series $y(t)$, the distribution of $y(t)$ converges to the probability distribution of the random variable X.

Yet $\phi(t)$ is considered to originate from an ergodic stationary processes that is $f_n(t)$. It allows then to study a single realization of the oscillator phase to determine its noise properties and, from the phase noise studies, to extract the key parameters of the KTS model as we will see in chapter 4. In chapter 2, $f_n(t)$ has been considered as a white Gaussian process, which means that X is a Gaussian variable whose PDF does not change with the time. It has been used to determine the PDF of the amplitude that, by heuristic arguments, gave the variance of the Gaussian variable X from $f_n(t)$.

Since computing the PSD of a stochastic process requires it to be both ergodic and stationary, it is of main importance that the noise quantities we are about to extract (δa and ϕ) are modeled such in KTS theory. We can highlight the fact that from these only considerations, the model is phenomenological. Indeed, we would like to highlight that,

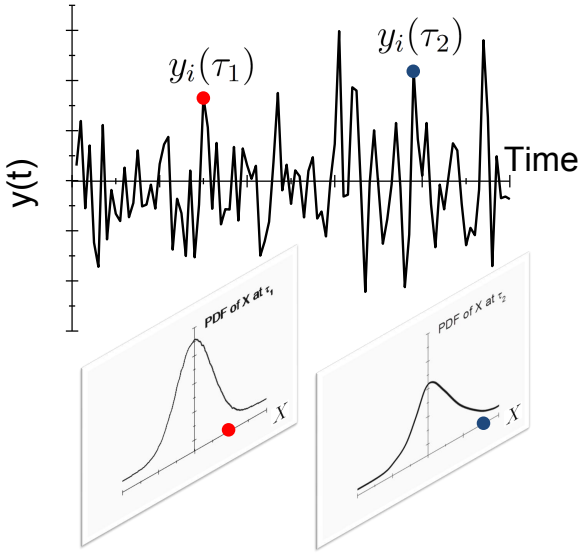

Fig. 3.15: Stochastic process $y_i(t)$ measured during the ith experiments between $t = 0$ and $t = \infty$. Two PDFs of X are represented for different time τ_1 and τ_2. We note that the two PDFs can be different at different times and that $y_i(\tau_1)$ and $y_i(\tau_2)$ are actually respectively one unique realization of X at time τ_1 and τ_2. Of course, only one "measurement" $y(t)$ can be realized experimentally. To define more precisely one experiment with noise, it requires thus to make some hypotheses such as stationarity and ergodicity.

in the real systems, it is rather difficult to check whether the noise quantities are both stationary and ergodic. In any fields, modeling oscillator involves to consider ergodic stationary processes in order to define, measure and compute fluctuating quantities that are never measured as such [88, 93, 94]. It turns out that the fact to point out such inconvenient proves, of the non-correct description of the noise quantities, is called "Model pathology" and, in our case, would be an ultimate barrier before bring into play chaotic dynamics of the magnetization. The "model pathologies" of the KTS theory will be discussed in the next chapters. However, the "model pathologies" will have some direct impacts on the measured noise variances as it will be discussed in the experimental part of this chapter.

S_ϕ *and its derivatives*

Before coming to extracting phase noise from STO measurements, we review the main features of phase noise found in conventional oscillator measurements. We previously mentioned the PSD of phase fluctuation ϕ. The correct mathematical definition of the PSD of any time function $z(t)$ is:

$$S_z(f) = \left\langle \lim_{T\to\infty} \left[\frac{1}{T} \left| \int_{-\frac{T}{2}}^{\frac{T}{2}} z(t) e^{-i2\pi ft}\, dt \right|^2 \right] \right\rangle , \tag{3.14}$$

where $< \cdot >$ is the time average, i.e. the infinite repetition of the realization over an infinite time. When dealing with PSD of noise quantities, we understand that the notion of stationarity and ergodicity are primordial to define the PSD on finite length segments.

Then, in practice, the PSD is calculated as the square of the modulus of the Fast Fourier Transform (FFT) of the quantity $z(t)$. We will especially focus on the PSD of phase fluctuations $\phi(t)$ and amplitude fluctuations $\delta a(t)$. It is also important to introduce other fluctuation functions that are used by RF engineers to characterize noise properties of electrical oscillators. While all those definitions are derived from the phase noise $\phi(t)$, those derivatives are useful at different levels, since they express different aspects of the phase (frequency) fluctuations behavior of an (electrical) oscillator. These three definitions are:

- It is convenient to introduce the instantaneous time deviation $x(t)$ defined as:

$$x(t) = \frac{\phi(t)}{2\pi\nu_0} \,. \tag{3.15}$$

  ν_0 is considered as a reference frequency. For example, if we consider the time given by our clock, when we said that we have 25 seconds advance compare to the real time, we use this definition. We estimate the time deviation from another time reference. In our case, we evaluate $x(t)$ with the zero-crossing method (ZCM) defined later.

- In terms of data representation, we also use the frequency noise $\Delta\nu(t)$. We define the frequency noise as the time derivative of the phase noise:

$$\Delta\nu(t) = \frac{1}{2\pi}\frac{d\phi(t)}{dt} \,. \tag{3.16}$$

- The relative frequency fluctuation $y(t) = \Delta\nu(t)/\nu_0$ is also used to compare the quality of an oscillator of different carrier frequency. In this way the value of $S_y(f)$ at a certain offset frequency f can be compared for electrical oscillators of different frequency.

The PSDs of those quantities are related to each other:

$$S_\phi = \left(\frac{1}{f}\right)^2 S_\nu = (2\pi\nu_0)^2 S_x = \frac{\nu_0^2}{f^2} S_y, \tag{3.17}$$

where we write $S_{\Delta\nu} = S_\nu$ for simplicity. Thus, when dealing with noise processes affecting the system, phase noise, frequency noise, jitter noise (introduced later) are equivalent since they are all linked by a simple relationship. Fig. 3.16 shows typical phase noise plots in power law that can be found in electrical oscillators and their corresponding name is given in table 3.2 when we either deal with phase or frequency noise.

Table 3.2 and Fig. 3.16 illustrates the origin and the type of the noise measured. Indeed, despite the need for characterizing the oscillator's noise for applications as discussed above, noise measurements give information on the origin of the perturbation the oscillator is subjected to.

The order of the noise type presented in the Fig. 3.16 is often observed in this way in real VCOs. Indeed, the different noise types are supposed independent (and

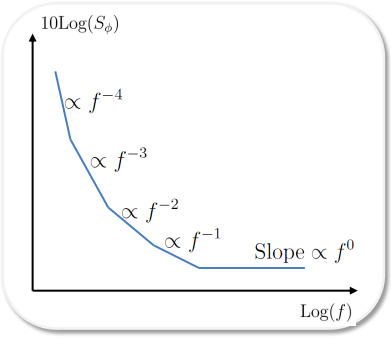

Fig. 3.16: Model of phase noise in power laws. On a log-log plot, S_ϕ has different slopes depending on typical noise contributions (see table 3.2).

$S_\phi(f) \propto f^{-a}$	Type of phase noise	Type of frequency noise	Typical origin in VCOs	Origin in the case of STOs
a = 0	White Phase noise	-	External White Noise	External white noise [86, 76]
a = 1	Flicker Phase noise	-	Electronic noise	(not yet observed)
a = 2	Random walk Phase noise	White frequency noise	Thermal noise	Thermal noise (Mag. field)
a = 3	-	Flicker frequency noise	Resonator	(indeterminate) [85, 76]
a = 4	-	Random walk frequency noise	environment	Non-linear effect [48, 54]

Table 3.2: Different noises modeled by power laws and their usual origin in all-electrical VCOs [88]. An attempt to summarize the noise types origin for STOs is presented.

therefore exists at all frequencies[6]). In this case, at very high frequencies, only a white phase noise of phase can be seen. When decreasing the offset frequency, it appears that lower (negative) power law are now observable over higher power law noises. This representation of the phase noise plots helps to determine (and characterize) the different noise origins and strengths in electrical VCOs.

As we have seen in chapter 2, the phase and amplitude noise of STOs are related to the noise source in a nonlinear manner (see Eq. 2.24). Therefore, the direct comparison between experimentally determined PSDs and KTS theory allows one to: (i) check the validity of the KTS model, (ii) extract the key parameters for practical STO modeling, (iii) analyze the underlying origins of the lineshape broadening Δf in STO by varying different predicted parameters (e.g. the dependence of Δf upon Γ_p and ν) and (iv) understand the limitations of the KTS model.

These motivations show, that apart from technological interests, phase noise plots are a powerful tool for addressing fundamental issues of STOs.

In the next sections, we focus on the experimental characterization of phase noise based on heterodyne method usually applied to conventional VCOs to show its limitations when applied to STOs. We then introduce signal analysis procedures to extract phase and amplitude fluctuations directly from a real signal $V(t)$ of the form of Eq. 3.8. This time domain method is then compared to conventional signal analyzer instruments, which justifies the correctness of the time domain measurements provided by the developed method.

3.2.2 Phase noise from frequency domain measurement

This section describes frequency domain based methods for phase and amplitude noise characterization. The first objective of this part is to describe the *reference* measurement method that is compared with the method developed in the time domain. The second objective of this part is to explain why STO phase noise cannot be measured by this simple frequency based method.

3.2.2.1 Phase noise measurement with a commercial signal analyzer

Phase noise measurements using a signal analyzer is a modified version to the (super-)heterodyne method presented in Fig. 3.10, where the LO is now exactly the one of the RF signal and in in-phase quadrature with the signal to characterize and is equivalent to the measurement of $\mathcal{L}(f)$ from its *old* definition. Usually an adaptive filter is placed before the down-converted signal that selects only a certain frequency span. A choice of simple FFTs (with time filters) is realized to perform the best accurate measurement. As already discussed this method implies that the signal has: (i) a negligible amplitude noise and (ii) a low phase noise such that $\sin(\phi(t)) \approx \phi(t) \ll 1$.

The assumption (i) insures that the noise signal at the output of the mixer is only due to phase noise and not due to amplitude noise. The assumption (ii) makes the PSD of the mixer signal equivalent to the one of ϕ (the *old* definition, the one measured by

[6]This is only a model for the different noises! For example, the *ultraviolet catastrophe* in the case of Johnson Nyquist implies that electrical white noise is bounded at high frequency.

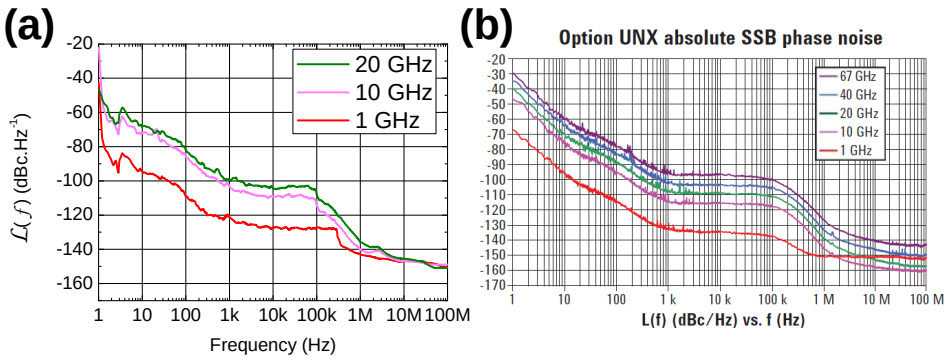

Fig. 3.17: (a) Heterodyne method applied to determine the SSB phase noise of an Agilent PSG E8257B microwave source with an R&S FSUP26®signal analyzer. (b) Data sheet of the Agilent source found in [95]. While mismatch of values can be due to a long term drift of the source compared to its data sheet specifications, it is interesting to note that the PN at the 1 kHz of the 10 GHz signal is exactly $20\log(N) = 10$ times higher than the 1 GHz PN at 1 kHz value, where N is the ratio of the frequencies $N = 10$ GHz/1 GHz. This is typically the case when the signal is obtained by frequency multiplication of a lower frequency signal. (This is also correct for the 20 GHz signal).

this technique, converges to the new definition of $\mathcal{L}(f)$). If $\phi(t)$ is too large, the phase quadrature is no longer satisfied and the method fails. In other words, the LO should be changed accordingly with the phase noise. It becomes important when trying to measure low frequency phase noise (or the long time stability of a RF synthesizer). In our case (we're not yet interested in long term stability of STOs), (ii) is a blocking point since STOs are very noisy oscillators. Nevertheless, the method applies well to "stable" oscillations (see the case describes in Fig. 3.17) and will be the reference method to which we will compare the technique developed in section 3.2.3.2.

Point (i) is also a blocking point since, in the presence of AN (and no significant PN), the method fails to predict the correct phase noise value. This is illustrated in Fig. 3.18, where an artificial white Gaussian amplitude noise is added to a "stable" signal synthesizer (Agilent®PSG E8257B microwave source) signal. The signal analyzer (in our case a Rhodes&Scwartz FSUP26®that uses an heterodyne detection scheme) returns the old definition of $\mathcal{L}(f)$, that is not equivalent to the real S_ϕ. This is due to the presence of AN in absence of significant PN; the output value of the mixer (see Eq. 3.10) is still interpreted as PN. Since this method fails to correctly describe the nature of the noise (PN or AN), it will be of limited use for the study of STO's noise[7].

As a consequence, we have to find an alternative method of characterization of PN and AN in STO that is reliable with the STO noise properties. Before describing this method, we present a reliable measurement of the amplitude in the case of very low phase noise. The description of this technique aims to provide a simple AN technique that serves as a reference when comparing with our own AN analysis method.

[7]However, close to the carrier, i.e. for low frequency offset, only phase noise is problematic; indeed when $f \ll \Delta f$, $S_\phi \gg S_{\delta a}$ in auto-oscillator (remember that in auto-oscillator the amplitude is stable, the phase is free, see chapter 2).

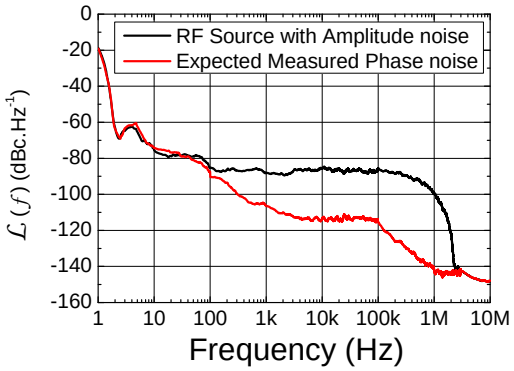

Fig. 3.18: Measurement of the SSB of the RF source with an additional Amplitude Noise in black compared to the SSB of the RF source phase noise without AN in red. This example illustrates perfectly that what is measured with a heterodyne-like method is the noise power found at a certain frequency offset from the carrier frequency and not the real phase noise. Phase noise is measured only when AN is negligible (and Eq. 3.10 is verified), that is not the case here in black.

3.2.2.2 Amplitude Noise measurement

The simplest AN characterization method consists of analyzing the output signal of an amplitude signal detector, typically a diode detector (see Fig. 3.19-a). The output of an amplitude detector is analyzed either by a FFT analyzer (FFT analyzers have better sensitivity than (super-)heterodyne SA for frequencies lower than 10MHz), or as in our case by acquiring the direct output voltage with an oscilloscope and computing the FFT of it. Since the diode detector output varies with the signal frequency, it is possible that additional noise occurs in the measurement because of the phase (frequency) noise of the measured signal and not because of its amplitude noise. Indeed diode detectors often have a frequency-dependent conversion factor. This simple method however works with stable frequency sources. The previous example of Fig. 3.18 AN can be measured with this technique as illustrated in Fig. 3.19-b for different strength of amplitude noise (modulation of 10% and 50% from the initial amplitude). In this case we can see that the noise present close to the signal (the *old* definition of $\mathcal{L}(f)$) is equal to the amplitude noise, in absence of significant phase noise. The reference signal has, however, an AN below the resolution of this simple experimental setup (below -140 dBc/Hz).

As we have seen, there exist basic phase and amplitude noise characterization techniques using the frequency domain. Those techniques are called such since the signal analyzers do not analyze the direct oscillating voltage, but a "converted one" assuming different hypothesis on the signal to measure. Therefore, contradictory results may appear if the signal under analysis does not satisfy some prerequisites, for example, signals with very low AN and relatively low PN. Moreover, the only determination of PN with simple heterodyne method does not provide enough information on the nature of the noise (AN or PN). As a consequence, we adopted the PN and AN measurement techniques based on time domain signals for the study of the STO noise characteristics. In the next section we give the most straightforward time domain technique that consists in directly extracting time varying phase and amplitude.

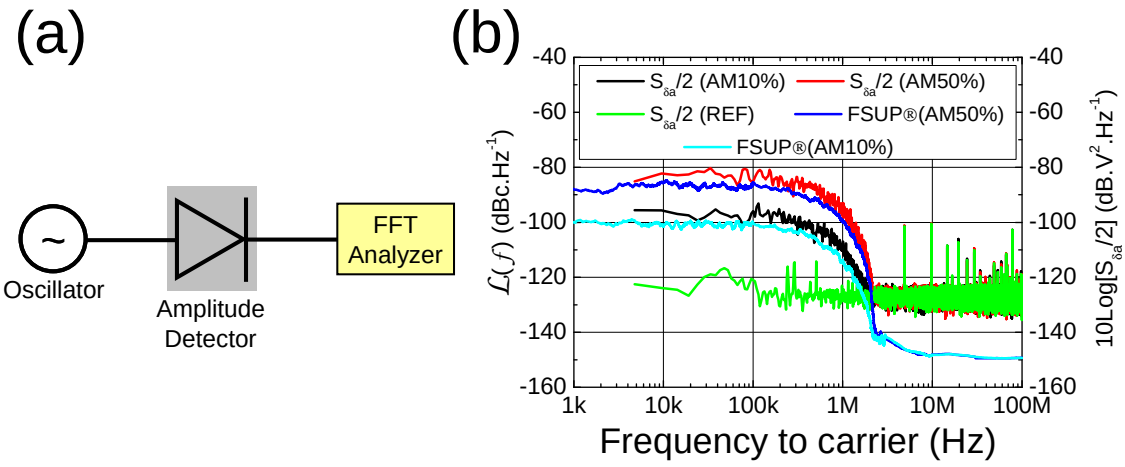

Fig. 3.19: (a) Schematic of the AN detection method. In our case, the amplitude detector is a simple diode detector (from KRYTAR, Model 201B), instead of an FFT analyzer, a 50Ω oscilloscope is used to get the detector output. A simple FFT is applied to the output signal. (b) Comparison between SSB measurements with an FSUP®and the direct measurement of $S_{\delta a}$ with the diode detector. Different white Gaussian AN amplitudes (in percent of A_0) are compared to the reference signal of the detector (no additional AN). We note the strong thermal noise background of the diode technique that is not optimized at all and is only presented here for the sake of illustration.

3.2.3 Phase and Amplitude noise Measurement from a Time signal

We have subdivided this section into two parts. The first is dedicated to tools used to analyze in depth the signal characteristics in the time-frequency domain. The second part is dedicated to the experimental protocol that I developed and used for the subsequent analyses.

3.2.3.1 Signal analysis of a noisy oscillator output signal

It is possible to extract the amplitude and phase noise spectra from the acquisition of the real signal $V(t)$ in different ways. Here we introduce two different methods.

The Zero-Crossing Method

The first one, which is very intuitive, is the zero-crossing method (ZCM) originally proposed by Keller et al. for the characterization of STO phase noise [86]. The idea is as follows. On a time trace of length T, the mean oscillator frequency ν_0 is estimated. Then, the instantaneous time deviation $x(\tau)$ is calculated each time the signal crosses zero. Since $x(\tau)$ is not defined on the same time basis as the real signal, some care is taken to compute the FFT of $x(\tau)$ [86]. Calculating the PSD of $x(\tau)$ leads to $S_\phi(f)$ (see Eq. 3.17). It is a very straightforward way to have access to phase noise from a time series.

Fig. 3.20 shows the ZCM applied to a simulated signal in the presence of random

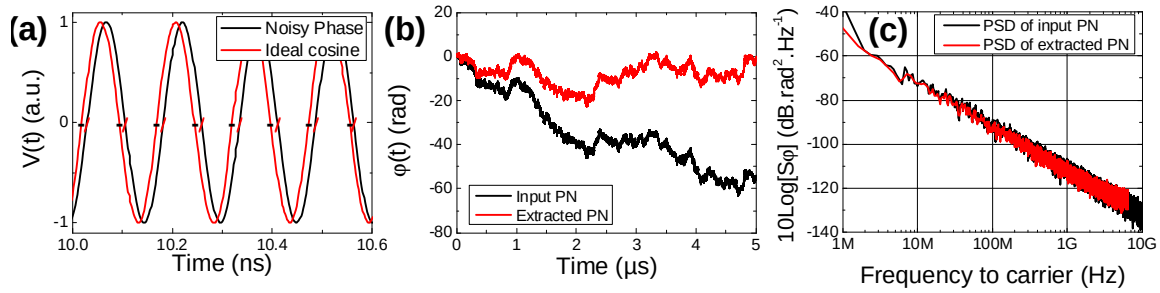

Fig. 3.20: (a) Evaluation of the ZCM. The instantaneous time deviation is compared to an ideal cosine signal with frequency ν_0. (b) Comparison between the input PN $\phi(t)$ and the one extracted from ZCM. It is interesting to note that the input noise, a random walk in phase, strongly deviates from zero over the 5 µs while the one extracted from the ZCM "sticks" around zero. This is because a random walk might give an apparent "linear drift" of the phase in the realization timespan (in this case about -60 rad after 5 µs). In the analysis, this is then converted to a frequency shift in ν_0 (in this case about -2 MHz, less than 0.1% of ν_0). It is very related to the definition itself of the mean frequency when there is a noisy phase term in the cosine. (c) Comparison of the PSD of the input PN (in black) and the one measured with ZCM (in red). We indeed have a random walk of phase with the characteristic f^{-2} slope. We note that since there is the compensation of the linear drift of the PN, the high frequency noise in the PSD of the extracted data via ZCM looks "white", i.e. with an f^0 slope.

walk of the phase[8], with no amplitude noise (see the figure caption and the discussion below about the exact determination of the frequency ν_0). In Fig. 3.20-a we present the estimation of the crossing points (slash symbols "/") compared to the expected ones ("-" symbols) from an ideal cosine signal. The extraction from the ZCM of the phase (realization) $\phi(t)$ versus time corresponds to the noise input given in Fig. 3.20-b. We can see that the mean deviation of the phase noise extracted by ZCM over the full experiment is zero, whereas the input phase noise has a non-zero mean deviation. Here we face a "model pathology", where because of the realization itself, we cannot determine the actual realization of the noise (compare black and red curves in Fig. 3.20). Indeed, a pure random walk has a zero mean deviation after a given time, which can only be checked by averaging an infinite number of realizations. Since in Fig. 3.20 we show only one sample over all possible realizations, we have the appearance of a "linear drift" of the phase over the timespan of the realization. This linear drift is eliminated when computing back the phase noise, in the case where the frequency ν_0 is unknown. The direct consequence of this is that, while the extracted phase noise by the ZCM is correct from quite low to quite high frequency, a certain saturation (a f^0 slope) in the high frequency phase noise component extracted by ZCM appears, as well as poor estimates of the first low frequency points. The problem here is that we cannot be "certain" of the frequency of the measured signal, only with an accuracy of the experimental timespan, that is not sufficient in the presence of phase noise. This problem is not specific to the ZCM but a general problem in time/frequency metrology: the determination of the "exact time" is always "uncertain".

[8]To build the total phase of the signal, starting from $\Phi(0) = 0$, we choose the next total phase value of the cosine as: $\Phi(t + \Delta t) = 2\pi\nu_0\Delta t + \Phi(t) + X$, where X is a Gaussian random variable whose PDF variance is constant over the time.

To evaluate the amplitude noise, a similar method to ZCM consists in evaluating the amplitude of the signal at each extrema of the signal (eventually interpolated). However, in this case, only the AN distribution can be studied and not it's time evolution, since the amplitude maxima appear at random time (due to oscillator phase noise) compared to the time of the measurement system. Because of these difficulties, $S_{\delta a}$ is not calculated by this method.

Extraction method of phase and amplitude via the analytical signal

The general problem is to determine both the instantaneous phase and amplitude of a noisy signal. The best way to do so is to use the notion of the analytic signal $z(t)$ which is a complex number, i.e., to consider that the measured voltage $V(t)$ is actually only the real part of the analytical signal (AS). We consider that the AS "evolves" in the phase plane. There exists a mathematical transformation, the Hilbert Transform H, that projects the real part of an AS onto its imaginary counter part. Defining $H_V(t)$ as the Hilbert transform of $V(t)$, $H_V(t)$ is the convolution product between $V(t)$ and $1/\pi t$:

$$H_V(t) = \frac{1}{\pi} PV \int_{-\infty}^{+\infty} \frac{V(t')}{t - t'} \, dt' \, , \tag{3.18}$$

where PV is the *Cauchy principal value* such that $H_V(t)$ is defined (it means that the integral exists). It is now possible to give the analytical formulation of the signal $V(t)$:

$$z(t) = V(t) + iH_V(t) = A(t)e^{i\Phi(t)} \, , \tag{3.19}$$

with $A(t)$ and $\Phi(t)$ respectively the instantaneous amplitude and total phase of the signal. In the case of a signal of the form of Eq. 3.8, the Hilbert Transform Eq. 3.19 is one of the correct mathematical approach to obtain the corresponding AS [96].

In addition to the HT, there is actually another more straightforward way to obtain the analytical signal Eq. 3.19. Indeed, Eq. 3.8 can be written as:

$$V(t) = A_0(1 + \delta a(t)) \cos(\Phi(t)) = \frac{A(t)}{2} \left(e^{i\Phi(t)} + e^{-i\Phi(t)} \right) \, . \tag{3.20}$$

By simply ignoring the "negative" frequency part in the spectrum of $V(t)$, $z(t)/2$ is formed. Thus, in practice, a first FFT is performed on $V(t)$. The negative frequency values are set to zero and the inverse FFT is performed on these "filtered" data. The result is $2z(t)$. Actually, this way of forming the AS, is the admitted definition of the AS in RF engineering, since this field only deals with "pseudo"-periodic signals that are expandable in Fourier series (sum of cosines).

The argument of the complex AS provides the total phase $\Phi(t)$ and its modulus the amplitude $A(t)$. From it, the phase noise $\phi(t)$ can be deduced:

$$\Phi(t) - 2\pi\nu_0 t = \phi(t) \, . \tag{3.21}$$

We have already pointed out the problem of extracting the center frequency ν_0 from a noisy cosine signal. Here, we give the method to extract ν_0. It is well known that the exact angular frequency $2\pi\nu_0$ from a finite time length T is only known with a precision of $2\pi/T$.

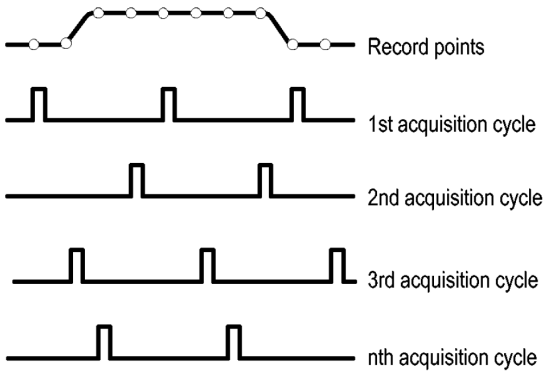

Fig. 3.21: Principle of the stroboscopic or the Equivalent-Time measurement. The same signal is sampled several times with a low SR. After all acquisitions are realized, the total signal is constructed. From [97].

Moreover, as seen in the ZCM, it is possible that the phase noise $\phi(t)$ itself has a linear drift with time. On a real signal acquired with the sampling rate f_{sample}, the best is to consider the average $\langle \phi(t)\phi(t+1/f_{sample})\rangle = 0$. It is to assume that at very high frequency, the *observed* phase noise is white. Therefore, this hypothesis makes the high frequency phase noise white (see the high frequency tails in Fig. 3.20-c). As we will see later, this approximation is generally verified for experiments (presence of white high frequency phase noise), but not in macrospin simulations. Assuming $\langle \phi(t)\phi(t+1/f_{sample})\rangle = 0$, it follows:

$$\left\langle \frac{\Phi(t+1/f_{sample}) - \Phi(t)}{1/f_{sample}} \right\rangle \approx 2\pi\nu_0 \ . \tag{3.22}$$

Similarly the relative amplitude noise is defined:

$$\delta a(t) = \frac{A(t)}{A_0} \tag{3.23}$$

with $A_0 = \langle A(t)\rangle$, which means that $\delta a(t)$ has a zero mean distribution.

As seen here, the method based on the AS is the *perfect* tool to extract the instantaneous phase *and* amplitude from a signal. In the next part we give test cases to prove the method on real signals. We also give an overview of the limitations of this method.

3.2.3.2 Experimental extraction of Phase and Amplitude

This section describes in detail the experimental protocol. We first describe briefly the oscilloscope settings. We then apply the developed time domain technique to real signals. Finally we give the limitations of the technique on real signals.

For time domain measurements, there exist two main classes of instruments. To foresee the interest of single shot experiments compared to stroboscopic experiments, we first introduce the stroboscopic instruments.

Stroboscopic oscilloscopes are of use to study purely repetitive signals. Their internal triggers allows sampling the signal to very high sampling rates (SR) but at different time

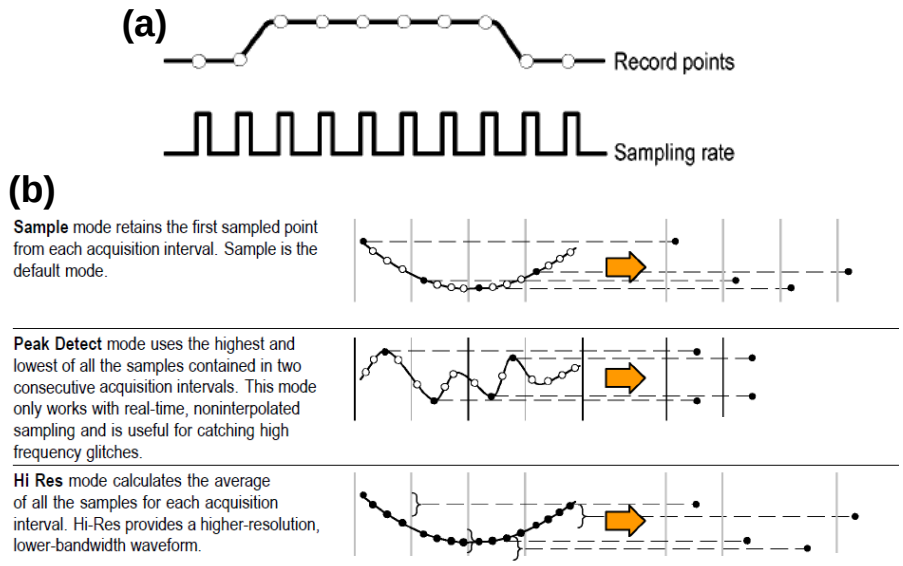

Fig. 3.22: (a) Principle of a single-shot acquisition. (b) The different measurement modes during the acquisition time. From [97].

intervals. For example, a stroboscopic oscilloscope will have a real sampling rate of few hundred of MHz but can display a point every 1 ps, i.e. an equivalent-time SR of 100 GHz! They actually slightly change the position of their triggering between each measurements to reconstruct a signal with such a high sampling rate (see Fig. 3.21). However, it relies on the assumption that the signal measured is reproducible. These instruments are used in differential time-domain spectroscopy where a GHz or THz input is sent to the DUT and the resulting output is measured by the stroboscopic instrument. The method is valid since the same input is sent to the DUT from the first to the last measurement. As a consequence, they are of limited use in the study of noise or rare events.

The second kind of time domain measurement is done via single-shot oscilloscopes (SSO). The interesting aspect of those instruments is the very high SR available (about tens of GHz). Contrary to stroboscopic instruments, SSOs only acquire the signal once at a very high sampling rate. There are different acquisition modes (see Fig. 3.22), we prefer the *Sample* or *HiRes* modes.

Apart from the sampling rate (50 GHz in our case), the electrical bandwidth (EB) on SSOs is of significance. The EB is the frequency span over which the apparatus acquires data (the aperture of the detectors). This parameter is of importance since a signal that is not in the EB cannot be measured. On the other hand if the EB is too wide, the detectors integrate too much electrical noise. Roughly, a detector at a temperature T that is composed of a resistance R will integrate the noise power $4k_b\mathrm{TR}\times\mathrm{EB}$. The higher the EB, the lower will be the signal to noise ratio at the output of the detector.

To overcome this problem (the EB should be about the sampling rate), gigahertz range SSOs use several detectors with different triggering in time with lower SR and thus with lower EB. The SR of the SSO (50 GS/s in our case) is actually four times the SR of 12.5 GS/s on a 16 GHz EB. Indeed, the input signal is first separated into four channels that acquire with a SR of 12.5 GS/s. To reconstruct the signal with a SR of 50 GS/s,

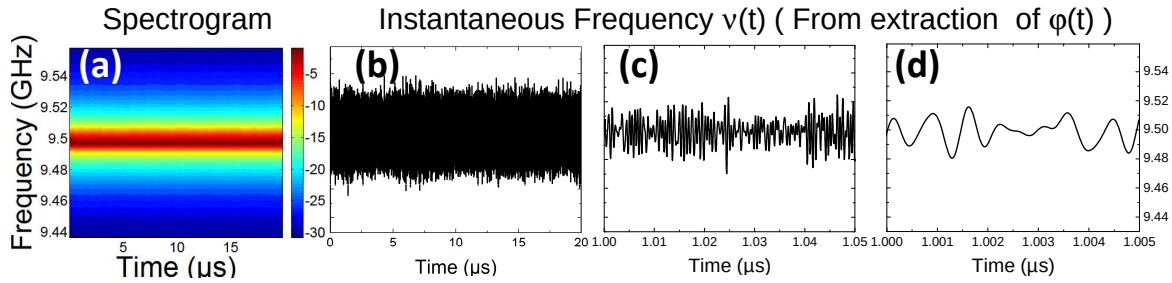

Fig. 3.23: (a) Spectrogram of a measured RF signal with FM of 100 kHz of deviation (window size: 8192 points (163.84 ns) and window overlap: 25%). (b)-(d) Instantaneous frequency $\nu(t)$ computed from the extraction of $\phi(t)$ using the Hilbert Transform (HT) with different timescales. In (d), the sinusoidal-like instantaneous frequency appears because of the bandpass filter (4 GHz) applied to the signal before HT post-processing. The oscillation frequency is about 2 GHz.

the four channels have a known delay of a quarter of 80 ps (that is 12.5 GS/s). This sampling technique allows a good signal to noise ratio and a high SR, compensating a relatively low EB. There are other advantages of such a "four-channel-in-one" technique, for example the digitizers can work at lower frequencies. Nonetheless, the delay between acquisition channels need to be controlled perfectly.

In the following we give examples of the efficiency of the method from an experimental point of view. In all cases, we consider signals with relatively low phase noise (generated by an Agilent®PSG E8257B analog source) in order to compare with the frequency domain method presented in section 3.2.2.

Demonstration of the time-technique on real noisy oscillators

The first case corresponds to a signal at $\nu_0 = 9.499$ GHz with a white Gaussian frequency noise (FN) generated via the internal noise source of the RF signal generator, with a "frequency deviation" set to 100 kHz. It means that the frequency is allowed to vary by 100 kHz from its initial frequency ν_0 in a white Gaussian manner. This type of phase noise is similar to the expected one for STOs (a random walk of phase gives a Lorentzian shape signal PSD), but of smaller amplitude. Indeed, its relatively weak strength makes the signal still measurable on our commercial signal analyzer (e.g. the FWHM is smaller than few kHz).

In Fig. 3.23 we give a spectrogram of the signal and the instantaneous frequency $\nu(t)$ obtained by the AS. The spectrogram is obtained by making a sliding FFT to the signal and using a density plot to represent the time evolution of the power spectrum. It is very sensitive to the window size (that gives the frequency precision) and the overlap of windows (that gives the time precision). The first comment is that spectrograms (whatever the windows used) cannot reproduce or "track" frequency fluctuations, nor give accurate description of its fluctuation. Indeed, the spectrograms rely on sliding FFT to evaluate the power at a certain frequency. Therefore, the higher the window size over which the FFT is performed, the better is the frequency accuracy. To have a 100 kHz accuracy would require at least a 10 microsecond segment length. However, the frequency

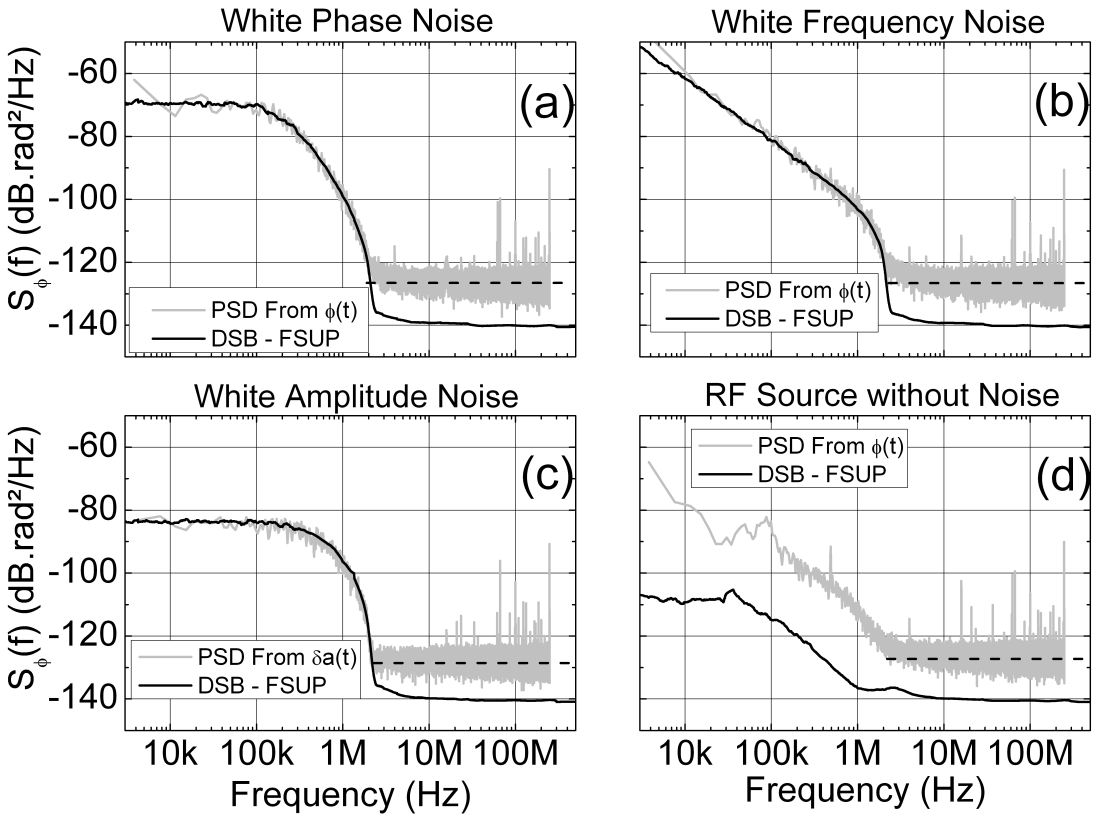

Fig. 3.24: Comparison of the FSUP results (in black) to the time domain results (in gray) (a) for a signal with white Gaussian phase noise, (b) for a signal with white Gaussian frequency noise, (c) for a signal with white Gaussian Amplitude noise. (d) Comparison of the phase noise extracted from time domain (in gray) for a signal with AN only and the phase noise obtained from the FSUP without any noise source (in black). One would expect to obtain the black curve with the time domain techniques. However, because of SSO's inner clock phase noise, the gray curve is obtained. (a)-(d): the dashed black curve is the intrinsic noise floor of the time domain technique. In all cases $\nu_0 = 9.49$ GHz.

varies in a white Gaussian way (i.e. at all timescale with the same amount), making it impossible to "see" such a small FN using spectrograms. We rather use the determination of the instantaneous frequency $\nu(t)$ using the Hilbert Transform (Eq. 3.19). In this case, frequency fluctuations are clearly visible. As shown in the Fig. 3.23-d, fast frequency fluctuations are filtered because of the digital bandpass filter applied to the signal; the frequency seems to "oscillate". In practice, this digital filter insures to get rid off low frequency noise as well as neighboring signals. The band of the filter is large enough to make sure that fast events are not missed in the signal.

The DSB phase noise resulting from the FN is presented in Fig. 3.24-b. The measurement from the time domain (in gray) is compared with the one of the FSUP®from frequency domain (in black). A similar result is found by both methods; it proves the usefulness of the time domain techniques.

Finally, we demonstrate that the method based on the time-domain also works for white Gaussian noise of phase (see Fig. 3.24-a) and of amplitude (Fig. 3.24-c). We note that for amplitude plots, only the $S_{\delta a}$ obtained from time domain is compared with the measurement from the FSUP®(see discussion in the above section 3.2.2). We can comment on the specific signature on the S_ϕ and $S_{\delta a}$ plots induced by these noise contributions. The typical behavior expected from a white noise frequency, or white phase or amplitude noise (see Table 3.2), is obtained in the 1 kHz to 2 MHz range. The cut-off of the noise at 2 MHz is actually due to the internal noise source of the RF generator that has a limited bandwidth for generating this three kinds of noise. In other words, the frequency or amplitude of the RF generator cannot be changed in a "white Gaussian" way below (resp. above) the µs (resp. MHz) timescale (resp. frequency-scale). We see the interest of phase noise plots (over spectrograms, for example) as a characterization tool: phase noise plots provide information on the timescales and on the nature of the noise affecting the real oscillator. We discuss now the major limitations of this technique and the main features to take care of.

Limitations due to physical/mathematical principles

We now subdivide the time trace of 1 ms used in Fig. 3.24-b into 50 time traces of shorter timespan of 20 µs. Three different S_ϕ obtained from these shorter time traces can be seen in Fig. 3.25. The first conclusion is that the noise level (for example the value $S_\phi(f = 1\text{MHz})$) varies a lot among this three plots, so that S_ϕ from short time domain traces do not correspond to the one given by the FSUP®. We can see that even the correct timescale for the noise is not properly defined. The length of the short time traces (20 µs) are close to the noise time scale that ranges from the ms to the µs (the f^{-2} slope in the curve of S_ϕ spans from 1 kHz to 2 MHz, see Fig. 3.24-b). As a result the noise power (the area under the curve) is not well determined on this 20 µs measurement long and neither is ν_0, the oscillation frequency. Indeed, this noise power, i.e. the phase noise variance $< \phi^2 >$, cannot be really well defined because we don't have a clear realization of the random walk of phase. Somehow, the ergodic properties $\phi(t)$ that are used when computing the FFT of our signal are not respected in these (short) experiments: the noise realization does not represent its properties in the time span of the measurement.

To overcome this timescale mismatch, a 1 ms long time trace is acquired (that was

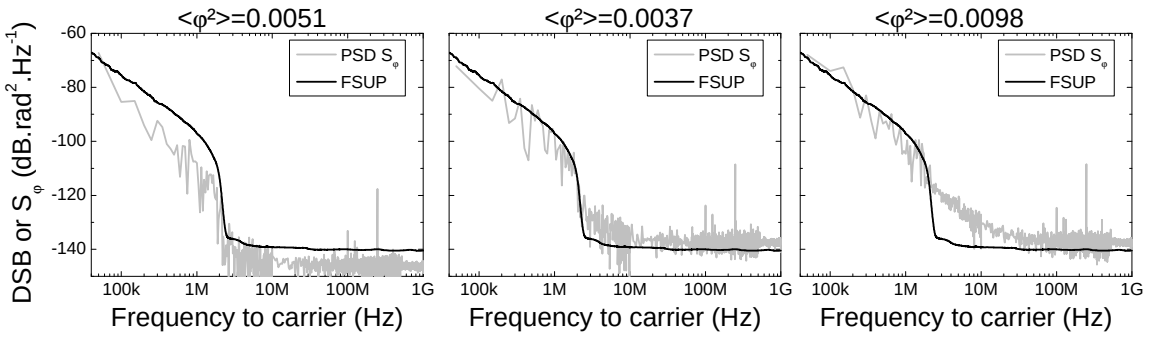

Fig. 3.25: Comparison of DSP measured from FSUP and the PSD of $\phi(t)$. $\nu_0 = 9.5$ GHz and white Gaussian FN of variance 100 kHz is applied. It is clear that the noise has a cut-off frequency at 2 MHz. The direct effect on the phase noise extraction is that the estimation of the random walk of phase that happens from the µs timescale is wrongly estimated on a 20 µs time trace long. For example, the phase variance $< \phi^2 >$ obtained on each 20 µs varies with a factor 4. This explains the discrepancy with the FSUP measurement in both noise amplitude and nature.

used for Figs. 3.24). Since the time trace is now composed of 50 million points, a specific routine needs to be used. Indeed, the required FFT cannot be performed on 50 million points with normal computer programs (such as MATLAB®). Time traces are cut into fifty files of 1 million points and the time varying phase is computed for all 50 segments (as shown in Fig. 3.25). Since the phase is continuous on a single-shot experiment, the 50 phase parts can be reconstructed into one. The total phase is under-sampled in order to perform the FFT on a phase trace that is composed of 1 million points and lasts 1 ms (the SR decreases). The result of such a procedure is shown in Fig. 3.24 for the different noise sources. It is to be noted that the average phase variance after 20 µs of the 1 ms long signal is $< \phi^2 >= 0.0052$[9].

A similar problem is found in the case of a white Gaussian AN that is added to the RF signal. The problem discussed above is linked to the stationary and ergodic properties of the measured signal. Indeed, the 20 µs long time traces do not allow one to consider the ergodicity of the measured signal. A straightforward method is to study the distribution of the AN measured with the SSO[10]. According to Fig. 3.26-a, the Gaussian distribution of the AN is clearly not found when studying the distribution of the "measured" amplitude noise on short time traces (20µs) with respect to the timescale of the amplitude noise. However, we recover the Gaussian distribution when we increase the sample length to 1 ms (see Fig. 3.26-c). Since, again, the noise timescale is of the order of µs, only a long time trace of 1 ms allows one to recover the Gaussian distribution of the AN. In this case, the measured stochastic properties (i.e. the slopes of $S_{\delta a}$) can be correctly described with these longer time traces (compare Fig. 3.26-b and Fig. 3.26-b with Fig. 3.19-b).

The limitation we have just discussed is not really related to the technique itself, but

[9]The phase variance for a random walk of phase is defined by $< \phi^2 >= Dt$, where D is the drift constant and t the time. Therefore the phase variance in a random walk of phase is linearly dependent over the time. When comparing the phase variance from two different measurements, it is important to compare on the same time span.

[10]Again the phase variance in the case of random walk of phase is time dependent. In the case of white amplitude noise, the variance of amplitude noise is constant.

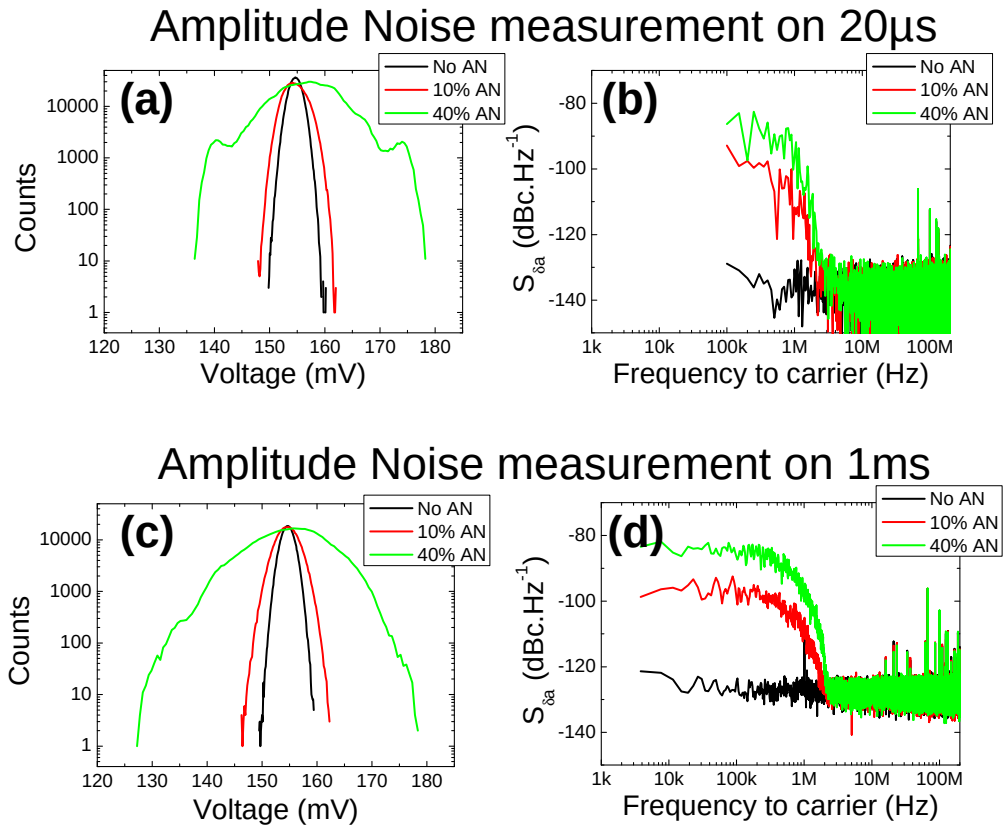

Fig. 3.26: (a) Distribution of the amplitude (voltage) measured on a 20 µs long time trace. (b) PSD of amplitude noise δa for the different source configurations obtained from 20 µs long time traces. (c) Distribution of the amplitude (voltage) measured on a 1 ms long time trace. (b) PSD of amplitude noise δa for the different source configurations obtained from 1 ms long time traces. Since AN is a white Gaussian noise only from 2 MHz (or every 0.5 µs), the distribution of $\delta a(t)$ is not representative of the PDF of the AN on short time traces. This proves that 20 µs is not enough to provide a qualitative description of the noise in this case.

rather to a mismatch between the timescale of our measurement and the timescale of the noise we want to measure. Therefore, we can call such an issue an *extrinsic* limitation of our technique (not instrument dependent). We now describe *intrinsic* limitations of the techniques, i.e. instrumentation related limitations.

Limitations due to instrument capabilities

Fig. 3.24-d shows the main limitation of the method. The gray lines in Fig. 3.24-d correspond to the phase noise extracted from the signal generated by the RF generator where AN was added. Yet, this exact gray curve can be reproduced using the RF generator without any AN, and more extensively, with any other RF generators with ultra-low phase noise performances (not shown here).

In fact, we are facing the limit of the phase noise measurable by the SSO. Indeed, let us imagine that the signal sent to the SSO is pure, namely for all t, $\phi(t) = 0$. Of course such a source does not exist. If such a signal is sent to the SSO, the obtained phase noise should be zero. As discussed on the operating principle of the SSO, all single shot acquisitions of a time trace are separated by 20 ps, provided by the sampling rate of the SSO. However, the inner clock time of the SSO can drift such that along the measurement time, the acquisition time has "drifted away". It means that to take a time trace lasting 1 ms, the perfect source will appear perfect, *if and only if* the SSO exactly samples the time trace every 20 ps. It is obviously impossible to have such an ideal inner clock, and more generally, it is the main problem in time-metrology; the measurement of ultra-stable oscillators is very sensitive to the instruments and the methods used.

The gray curve in Fig. 3.24-d is actually the template from which all phase noise measured above will be considered as correct. The specifications of the time stability of the SSO inner clock can be found in Ref. [98]. However these specifications refer to jitter time rather than referring to phase fluctuations of the inner time reference of the SSO. The jitter is especially used in modern digital processing units to describe the quality of signal edges, it gives roughly the dispersion of the instantaneous time deviation $x(t)$ after a certain time τ. The link with phase noise is thus straightforward:

$$J^2_{RMS}(\tau) = \frac{2}{(2\pi\nu_0)^2} \int_{\frac{1}{\tau}}^{\infty} \mathcal{L}(f) df \ , \tag{3.24}$$

where of course practical measurement imposes a finite value of the integral. In Table 3.3 the jitter specifications of the SSO is given as well as the jitter calculated from Eq. 3.24 from the DSB of Fig. 3.24-d. We can see that indeed the jitter obtained from 3.24-d is below the maximum allowed jitter value for the SSO we are using (DPO TEKTRONIX®72000D).

The last aspect of the limitation of the PN measurements coming from the instrument is the thermal noise floor observed at very high frequency with the time domain technique. We will see later that in the case of STOs, this noise floor does not have the same origin as the one discussed here. We have seen that the samplers integrate a noise power proportional to their temperature and the EB. As shown in Fig. 3.26-a,c, there is a non-negligible broad distribution of the amplitude of the "pure" RF generator (black curves labeled as "No AN"). This contribution gives an amplitude noise power of about

jitter at τ	jitter from $\mathcal{L}(f)$	jitter from SSO's Specs
1 µs	62 fs	$<$ 250 fs
10 µs	115 fs	$<$ 250 fs
100 µs	228 fs	$<$ 350 fs
1 ms	380 fs	$<$ 650 fs

Table 3.3: Comparison of the jitter noise given from the SSO's phase noise measurement Fig. 3.24-d to the one specified by the SSO's manufacturer.

130 dBc/Hz at 1 MHz, while from the data sheet it is expected at least a figure below 140 dBc/Hz at 1 MHz for the RF generator. It is worth noting that this noise is a white noise, i.e. the same value of the PSD for all frequencies. Actually, a white Gaussian amplitude noise is automatically converted to phase noise (and *vice versa*). As seen in Fig. 3.27, any short term noise contribution can be interpreted as a phase and amplitude fluctuation in the phase plane. However, since this fluctuation is white, the resulting AN and PN are also white. It results that a noise floor appears in the phase noise plot for very high frequency and has the same order of magnitude as the amplitude noise. In other words, the PN and AN floor observed experimentally originate from SSO converter noise and are of similar magnitude. As shown by the black curves in Fig. 3.26-b,d, this white noise is present at all frequencies. In the case of STOs, the amplitude noise floor found (and the resulting phase noise floor) have a different origin [86, 76] from the sampler noise. This will be discussed in the part dedicated to STO measurement.

We have demonstrated the possibility to experimentally study the phase and amplitude noise of an auto-oscillator by means of time domain techniques. The following chapters (4 to 6) are dedicated to the study of MTJ STOs using this technique. We therefore present here the general properties of MgO based in plane-magnetized MTJ STOs. Their frequency spectra were already well characterized in our group and show qualitatively similar characteristics as devices described in literature.

3.3 Presentation of the tunnel junction devices

The magnetic tunnel junction devices studied in this thesis have been fabricated by Hitachi GST (San José) and consist of an in-plane magnetized pinned and free layer, where the magnetizations are collinear in zero applied field. They are nano-pillars patterned using electron-beam lithography and ion milling, with the stack composition: (seedlayers)/IrMn (6.1)/PL/MgO (0.9)/FL/Ru/Ta. The pinned layer (PL) is a CoFe(1.8)/Ru/CoFeB(2) Synthetic AntiFerromagnetic (SAF) trilayer, while the free layer (FL) is a CoFe(0.5)/CoFeB(3.4) bilayer.

On a wafer, each MTJ has a different TMR value as well as a different resistance area (RA) product (that is a size independent measure of the MTJ resistance) because of the various distributions of MTJ parameters (size of the MTJ, local thin film in-homogeneities,...). The mean TMR ratio is 80% and the mean RA is about $1\Omega.\mu m^2$.

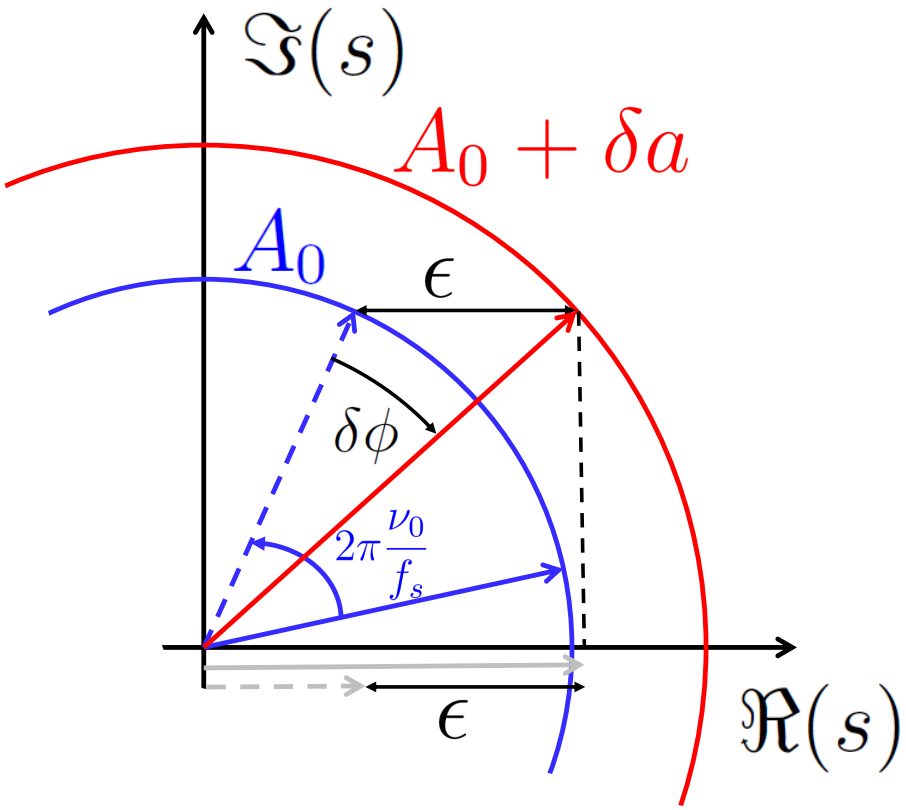

Fig. 3.27: The effect of an additional noise source ϵ on the signal processing. Note that ϵ can be independent from the oscillating voltage $V(t)$. For simplicity, we consider here that it shifts the AS in the phase plane as if it only acted on the real part of the signal (the measured signal without ϵ is the dashed gray vector). While the AS advances with $2\pi\nu_0/f_s$, this noise ϵ is interpreted as a sum of an amplitude noise term δa and a phase noise term $\delta\phi$.

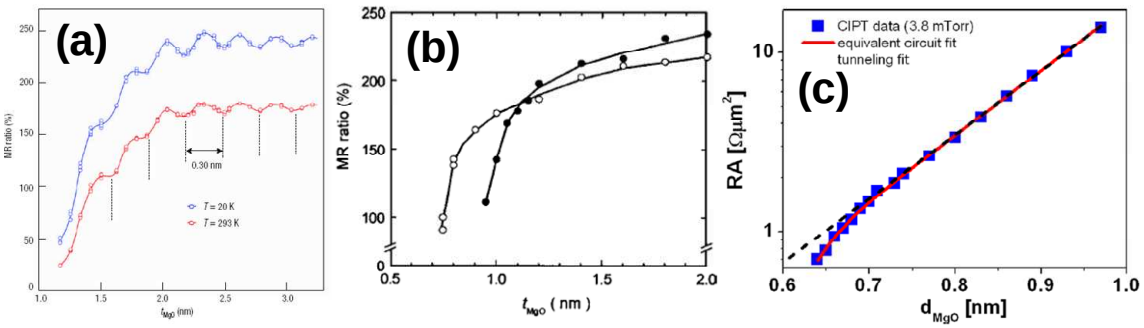

Fig. 3.28: (a) Dependence of the TMR ratio on the MgO barrier thickness for epitaxial Fe/MgO/Fe MTJs grown by Molecular Beam Epitaxy. From [99]. (b) Dependence of the TMR ratio versus MgO thickness with different growth conditions. From [100]. (c) RA versus MgO thickness for ultra-low MgO thickness. The dashed line is the exponential behavior expected from a pure tunneling regime. The red curve is a fit in the presence of metallic nano-bridges inside the MgO barrier. From [101].

The TMR ratio is given by the spin-polarization at the electrode interfaces (see Eq. 1.2 for example) while the RA is mainly due to the MgO barrier thickness (see for example Eq. 1.4).

Because ultra-low RA MTJs are of interest for practical devices (STT-MRAM, STO, read head in hard disk drives), they have been intensively studied. Figs. 3.28-a,b shows examples of the experimental correlation between TMR ratio and RA observed for ultra-low RA junctions (i.e. for low MgO thicknesses), which can be found in literature [99, 100]. The drop of the TMR ratio versus the thickness of the MgO film at very low thickness is due to pinholes in the MgO barrier. "Pinholes" are a generic term for local defects of local inhomogeneities in the MgO barrier. As shown in Fig. 3.28-c, the presence of pinholes or nano-bridges [101] is accompanied with an additional reduction of the RA product (compared with the expected exponential decrease of the RA with the MgO thickness). It is a real engineering challenge to produce ultra-low RA MTJs with high TMR ratios. An important point is to grow the stack at very low deposition rate such that it is possible to control the barrier thickness distribution and to obtain correct homogeneous barrier stoichiometry.

Since the STT effect requires high current densities and the MgO barrier can only sustain a finite amount of voltage, the lower the RA, the higher the current that can flow through the MTJ before reaching the breakdown voltage of the MgO [102]. Therefore, to study the dynamic excitations of the magnetic layers in MTJs, we will use these ultra-low RA MTJs, or, equivalently, ultra-thin MgO Barriers (below 10 angstroms). In addition to the difficulty of growing ultra-thin MgO oxide layers, the process to pattern and to encapsulate the MTJs in their contact electrodes induces apparent RA and TMR distributions, since parallel or serial resistances affect both the TMR ratio and the RA product.

As shown in the example of Fig. 3.29 taken from Ref. [103], the junctions with ultra-low RA product can exhibit either a pure tunnel transport behavior, a pure ohmic transport, or a mix of both. As discussed in Ref. [103], the barrier quality can be related to the *average* TMR and *average* RA product. Indeed, the "quality" can be somehow related to the transport - tunnel or ohmic - exhibited by the junction. Akerman et al. [104] experimentally verified that the only correct criterion to determine the tunneling regime was the one of the temperature dependence (i.e. there is tunneling transport if the resistance increases when decreasing the temperature). Therefore, the MTJ with a high *average* TMR and a relatively high *average* RA product (RA $\approx 1.4\ \Omega.\mu m^2$) exhibits "pure" tunneling transport (see Fig. 3.29-b). Lower *average* RA product junctions exhibit successively a mixed regime for RA $\approx 0.8\ \Omega.\mu m^2$ (see Fig. 3.29-c) and a "pure" ohmic regime for RA $\approx 0.2\ \Omega.\mu m^2$ (see Fig. 3.29-d). To summarize, in ultra-low MgO thicknesses, "conductive" nano-channels (due to pinholes) may appear that they affect the "pure" tunnel transport behavior of a MTJ when dealing with ultra-low RA MTJs. Therefore, in our devices provided by Hitachi it is possible to find such behavior as shown in our previous studies, on the same wafer one can find devices with high TMR (HTMR) and devices with low TMR (LTMR) characterized by the presence of pinholes. In this thesis, in order to compare to theory, we have selected HTMR devices that are pinhole free and exhibit high TMR and high RA values.

Several studies relate the barrier quality in a MTJ to its breakdown process

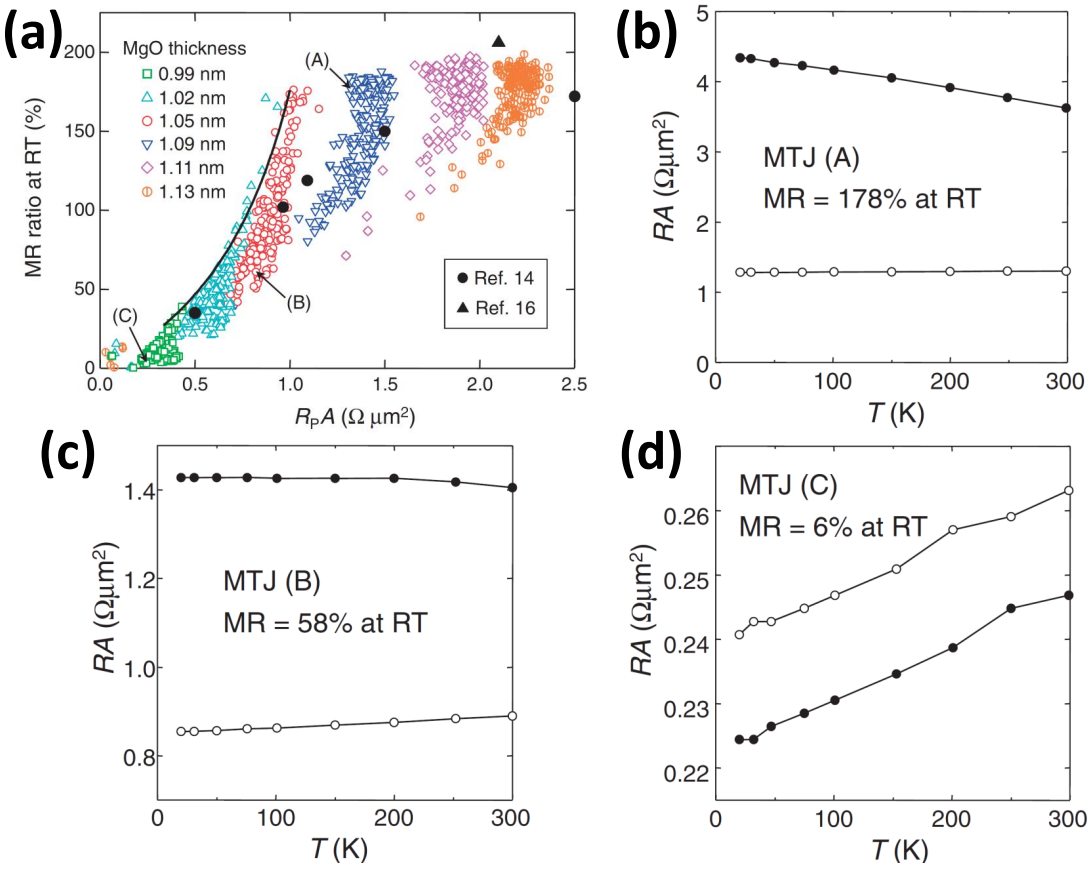

Fig. 3.29: (a) TMR ratio versus RA product for MTJs with different MgO thicknesses. The solid line corresponds to a possible MTJ of RA = 1Ω.μm^2 and 170 % TMR ratio with a shunt resistance from 0.5 to ∞ Ω. (b)-(d) Temperature dependence for the MTJs with TMR ratio and RA product given in Fig. (a). The dependence varies from pure Tunneling (b) to pure ohmic (d). In (c), the transport is a mix between ohmic and tunnel transport. From [103].

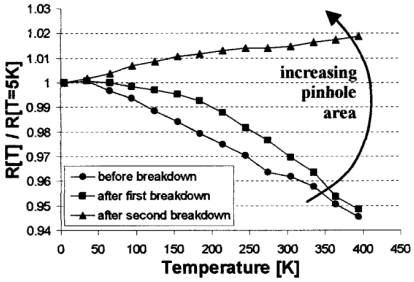

Fig. 3.30: Temperature dependence of an MTJ resistance during its conditioning (decreasing overall resistance by current/voltage stresses). From [107].

[105, 106, 107, 108, 109, 110]. There are two main breakdown processes [111, 112]. One is called intrinsic and is due to an abrupt breakdown of the barrier. In terms of energies involved, it is related to the energy bond found between the elements in the barrier and at the interfaces with the metallic electrodes. The second process, called *extrinsic*, is due to the formation of pinholes that gradually increase in size [107, 113]; it is related to electromigration and element diffusion. For example, Oliver et al. [107] showed that by applying several voltage stresses to the MTJ, the temperature dependence of the MTJs resistance can gradually change from the tunnel to the ohmic regime (see Fig. 3.30).

In our case, i.e. devices from Hitachi with a mean RA of $1\Omega.\mu m^2$, the dynamical behavior of the magnetization is dependent on the breakdown process that will happen in the MTJ after current/voltage stresses. Indeed, previous STT excitation studies made on in-plane magnetized MTJ-based STOs have shown that the excitation mode does depend on the barrier quality [81, 114, 115]. The extrinsic breakdown, which occurs in high-value of TMR (HTMR), is coupled to "standard" excitation schemes. Here standard excitation modes/schemes refer to the similitudes of the measurements within the macrospin simulations of an in-plane magnetized thin film patterned into a circular shape (see phase diagrams of Fig. 1.10 and Fig. 1.11 in section 1.2.2). This is in contrast to low-valued TMR (LTMR) MTJs (characterized by extrinsic breakdown) where "non-standard" excitation modes appear. The two behaviors have been described in detail in [81, 114]. We would like to emphasize that these two "dynamic" populations, related to barrier qualities and to the value of the RA product, is not a process-dependent feature. As shown in Fig. 3.31, the LTMR (and HTMR, not shown here) behavior is also clearly reproduced with an ion beam sputtering system. The study by Matsumoto et al. [116], on MTJ stacks grown by MBE, shows HTMR dynamic-like behavior (i.e. the standard behavior) in high TMR ratio junctions (and pure tunnel transport behavior). Finally, other groups also reported a change of the dynamic magnetization excitations when degrading the MTJ tunnel barrier (see Refs. [19, 117, 118]). It is worth noting that similar dynamical HTMR/LTMR correspondences to the barrier quality has been reported in the works of Nazarov et al. [119, 120].

While the dynamic mode excited in LTMR is still unclear, it is obvious that it is related to the presence of the degraded barrier quality inducing a non-homogeneous spin-polarized current profile. Al-Mahdawi et al. [121] reproduced LTMR dynamic behavior on in-plane magnetized MTJs with a nano-oxide layer [122, 123]. The barrier of those MTJs is made

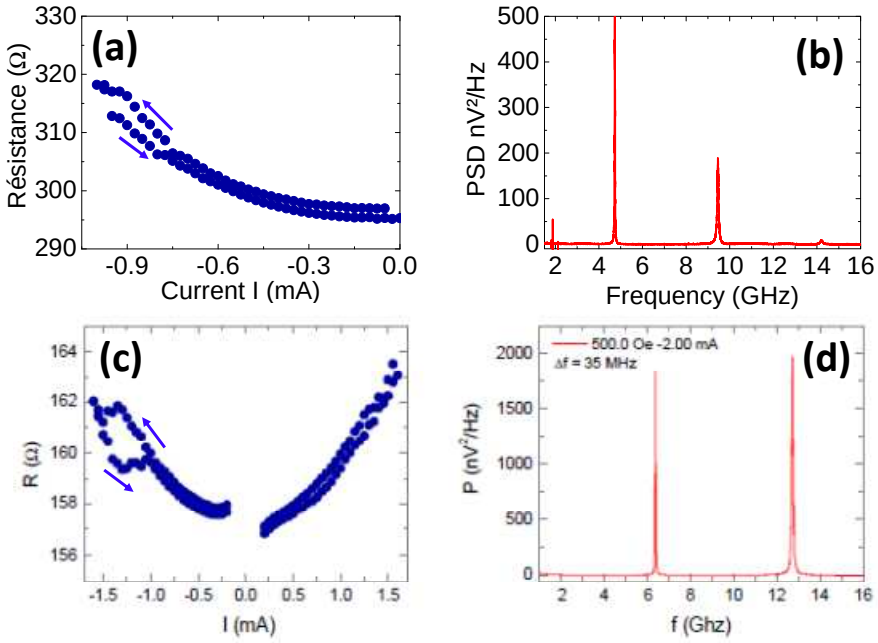

Fig. 3.31: (a) Resistance versus applied current for a LTMR-MTJ grown by an IBS tool. (b) Typical spectra of an LTMR-MTJ grown by an IBS tool. (c) Resistance versus applied current for a LTMR-MTJ grown by a magnetron sputtering tool. (b) Typical spectra of an LTMR-MTJ grown by a magnetron sputtering tool. (c) and (d) from [81]. The difference in frequency found in the two measurements is explained by the applied field (200 Oe) in (b) compared to 500 Oe in (d).

Name	Type and Ø	TMR	RA($\Omega.\mu m^2$)	J_c (A/cm^2)	Section
Sample A	HTMR Ø85nm	77%	1.5	1.76×10^7	4.1
Sample B	HTMR Ø75nm	77%	1.5	1.53×10^7	4.1
Sample C	HTMR Ø75nm	74%	1.5	1.76×10^7	4.2 & 4.4
Sample D	HTMR Ø85nm	75%	1.3	1.76×10^7	4.2
DevA	HTMR Ø85nm	81%	1.4	1.12×10^7	4.5
DevB	HTMR Ø75nm	90%	1.6	1.47×10^7	4.5
DevC	HTMR Ø62nm	86%	2.2	0.99×10^7	4.5
No name	LTMR Ø85nm	49%	0.88	0.91×10^7	4.6
No name	HTMR Ø62nm	83%	1.86	1.12×10^7	5.3
No name	HTMR Ø85nm	79%	1.55	0.97×10^7	6.2.1.1
No name	LTMR Ø115nm	64%	1.24	0.77×10^7	6.2.1.2

Table 3.4: Summary of all samples presented in this manuscript. TMR and RA have been calculated under a bias current of 50 µA. The critical current density J_c has been measured by the time domain method given in Chapter 4, except for the HTMR device in section 6.2.1.1 where we used the linear decrease of the linewidth with I in the sub-threshold regime.

of several nano-confined ohmic paths in the barrier, grown on purpose. However, even micro-magnetic simulations with non-homogeneous current density across the junction still fail to predict the excitation modes found in LTMR devices [124, 125]. Possibly more advanced simulations might be required with coupled transport/micromagnetic simulations, where it has been shown that non-homogeneous STT can take place in NOL structures [126].

Because these two populations of MTJs result in two different dynamics in our samples, we divided the study of our samples in two. Because only the HTMR-MTJs exhibit an excitation scheme that can be linked to macrospin LLGS simulation and therefore straightforwardly to the KTS model, HTMR samples will be the focus of our study.

The magnetization dynamics that appear in LTMR samples have already been observed in time domain in Ref. [115] where the excited mode exhibit a telegraph-type switching between static and dynamical state as also observed in time domain in spin-valve structures by Krivorotov et al. [127]. From another work of Krivorotov et al. [128], the lifetime of the dynamic mode is several milliseconds at 20K while the lifetime at room temperature can be expected around the nanosecond timescale as it is the case in the measurements of Houssameddine et al. [115]. In Chapter 4, we present typical phase and amplitude noise plots from LTMR devices [76]. Table 3.4 gathers all typical information from all devices measured in this manuscript.

3.4 Conclusion

In this chapter we have presented the main aspects of the measurement techniques used to study STOs. In a first section we described the two main aspects (signal amplitude and STO's frequency fluctuations) to take care of when measuring STOs in the frequency

domain with a spectrum analyzer. Then we introduced the notion of phase and amplitude noise in oscillators and their impact on applications but also their possible origins. Thirdly, we have introduced and validated the measurement of phase and amplitude noise from a technique based on time domain. In the following, this technique will be referred to as the time domain noise spectroscopy (TDNS). This developed technique that I developed constitutes a key result of this thesis. This technique allows one now to study the phase and amplitude noise characteristics of STOs. Throughout the thesis we focus on HTMR MTJ devices provided by Hitachi. These devices exhibit a "macrospin"-like IPP mode and are the ones that will find in best agreement with the KTS model. The next chapter is dedicated to their detailed study in the above and below threshold regime by means of the TDNS technique.

Chapter 4

Amplitude and phase noise of STO

We have identified in chapter 2 the importance of the phenomenological KTS model for addressing the central question of the effects of the noise on the dynamics of the magnetization under spin polarized currents. The KTS model involves a perturbation approach to the problem, which means the fluctuations are treated as perturbations of the main solution given by the "semi-classical nonlinear Hamiltonian". The aim of this chapter is to describe to what extent the phenomenological approach of the noise in the KTS model can serve experimentalists to characterize the STO dynamics from electrical measurements. The same approach is applied to macrospin simulations, in the presence of a fluctuating thermal noise field, which are setup-noise free and a textbook example for the extraction of key parameters. Results from simulations can also be compared to the results obtained from real measurements. The key parameters are the amplitude restoration rate Γ_p, the dimensionless nonlinear amplitude phase coupling ν and the "linear linewidth" Δf_0 (i.e. the noise strength affecting the system see chapter 2).

We have introduced at the end of the chapter 3 HTMR MTJ devices. They will be the focus of this study since they exhibit a behavior that can be directly compared to the KTS model and simulated macrospin excitations of the in-plane magnetized MR devices (we neglect the effect of b_j in our MTJs). For this, we will detail the KTS model in the sub-threshold ($I < I_c$) and above threshold regime ($I > I_c$) in light of our experimental (and simulation) results. This involves the analysis of the phase and amplitude noise in the frame of the KTS model using the techniques we developed in chapter 3.

The study of the harmonic signals of an IPP trajectory is investigated in both experiment and simulation. Since the generation of multiple harmonics at the STO output is one of the signatures of the nonlinear nature of the magnetization dynamics, we show how the nonlinear parameters of the KTS theory can be extracted from the analysis of these harmonics.

Finally we investigate LTMR MTJ devices, where the presence of flicker noise in the phase and amplitude noise PSD can be attributed to the poor barrier quality of these devices.

4.1 $I < I_c$: Damped Harmonic Oscillator

This part aims to compare the phenomenological KTS model to the experimental results in HTMR-MTJs in the subcritical regime. The measurements on HTMR samples are

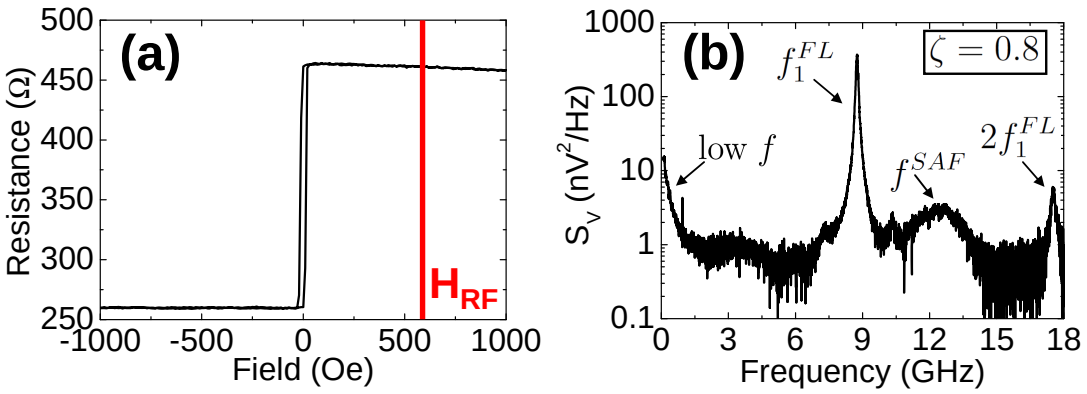

Fig. 4.1: (a) Resistance versus field hysteresis loop for Sample A. (b) Typical excitation spectrum in the sub-threshold regime ($\zeta = 0.8$) where first and second harmonics of the FL are visible. We note the presence of FMR-SAF mode as well as the presence of low frequency noise.

intensively compared to macrospin simulations (b_j term excluded) that allow one to change the temperature (strength of the noise) without changing material parameters (that experimentally vary with the temperature). In other words, it means that we can really see the effect of the noise strength on the dynamic properties of the system. The power distribution and its relaxation is studied in the sub-threshold regime, since from general oscillator theory, the linewidth of the resonant spectra originates mainly from amplitude relaxation.

This section is organized as follows: we first introduce the KTS model in the subcritical regime in detail, we then compare this model with the experimental and macrospin simulations results and we finally discuss the temperature effect in the below threshold regime by considering the harmonic oscillator model of the magnetization near its equilibrium position.

4.1.1 Model description

We focus on the resolution of Eq. 2.24 in presence of noise:

$$\frac{dc}{dt} + i\omega(|c|^2)c + \Gamma_+(|c|^2)c - \Gamma_-(|c|^2)c = f_n(t). \tag{4.1}$$

We consider the solution of Eq. 4.1 near zero oscillation power $p \approx 0$:

$$c(t) = \int_{\infty}^{t} f_n(t') \exp\{-[i\omega_i(0) + \Gamma_+(0) - \Gamma_-(0)](t - t')\}dt' \, . \tag{4.2}$$

Since $f_n(t)$ is a stochastic process, it is impossible to express a solution to Eq. 4.2 without the measure of $f_n(t)$. However, it is possible to express the statistical properties of the solution 4.2 by the autocorrelation function of $c(t)$, $\mathcal{K}_c(\tau)$ that is:

$$\mathcal{K}_c(\tau) = \bar{p} \exp(-i\omega_0\tau - [\Gamma_+(0) - \Gamma_-(0)]\tau), \tag{4.3}$$

where $\bar{p} = \frac{D_n(0)}{2[\Gamma_+(0)-\Gamma_-(0)]}$ is the mean oscillation power and $\omega_0 = \omega(0)$ is the zero power mode frequency (see chapter 2 and [54]). The term $\Gamma_s(\zeta) = \Gamma_+(0) - \Gamma_-(0)$ in Eq. 4.1 is the

sub-threshold damping of the system. This term gives the decay of the autocorrelation function in Eq. 4.3, it gives the speed with which the system goes back to equilibrium. We have shown in section 2.2.1 how the linearized LLGS equation around the magnetization equilibrium can be written in terms of a damped harmonic oscillator. The characteristic time with which the system returns to its equilibrium is inversely proportional to λ^{STT}. In our case, we use Γ_s that is the damping rate of the *energy* given by:

$$\Gamma_s(\zeta) = \Gamma_+(0)(1-\zeta) = 2\Gamma_G(1-\zeta) \ , \tag{4.4}$$

where Γ_G is the linear damping rate, in the absence of a spin polarized current. It gives exactly half the FMR FWHM (that is $2\Gamma_G/\pi$ when $I = 0$) of the susceptibility spectra of the magnetization. Indeed, the Fourier Transform (FT) of Eq. 4.3 is a Lorentzian function:

$$S(\omega) = \bar{p}\frac{2\Gamma_s}{(\omega-\omega_0)^2+\Gamma_s^2} \ . \tag{4.5}$$

The solution 4.5 (or equivalently Eq. 4.3) implies that the exponential decay solely originates from the mode amplitude relaxation toward the equilibrium position of the magnetization. In this case, the Lorentzian function Eq. 4.5 originates from the amplitude/power relaxation only. We recall that if a voltage is of the form of:

$$V(t) = A(t)\cos(\omega_0 t + \phi(t)) \ ,$$

the autocorrelation function of $V(t)$ is an exponential decay only if $\phi(t)$ is a random walk process (and $A(t) =$ constant) or the autocorrelation function of $A(t)$ is an exponential decay and $\phi(t) =$ constant.

In other words, the sub-threshold linewidth is *necessarily* given by the amplitude exponential relaxation. It is very important to understand that the amplitude fluctuation δa decays as fast as the power fluctuation δp ($\delta p \approx 2\delta a$). Therefore, the decay of amplitude fluctuations δa will be 2 times faster than the decay of the autocorrelation function of the mode $c(t)$. The way it should be understood is that the energy of the system goes twice as fast as the oscillating system and so do the losses.

From the equation of motion for c, Eq. 2.24, one can derive the equation for power p:

$$\frac{dp}{dt} + \Gamma_+(p)p - \Gamma_-(p)p = 2\sqrt{p}f_n(t)f_n^*(t), \tag{4.6}$$

where the noise term is now a non-stationary Gaussian process (see discussion below). For the sake of simplicity, it is assumed that $2\sqrt{p}f_n(t)f_n^*(t) = 2\sqrt{\bar{p}}f_n(t)f_n^*(t)$. Therefore, Γ_s (the mode relaxation rate) and $2\Gamma_s$ (the energy relaxation rate) describe the same phenomenon.

4.1.2 Experiments of subcritical regime and comparison to the KTS model

We now compare this model to experiments. We present the result from Sample A that is a circular MTJ of 85 nm of diameter. The measured TMR ratio is 76.9% and the RA= 1.5Ω.µm^2. Fig. 4.1-b shows a typical excitation spectrum ranging from 100 MHz to

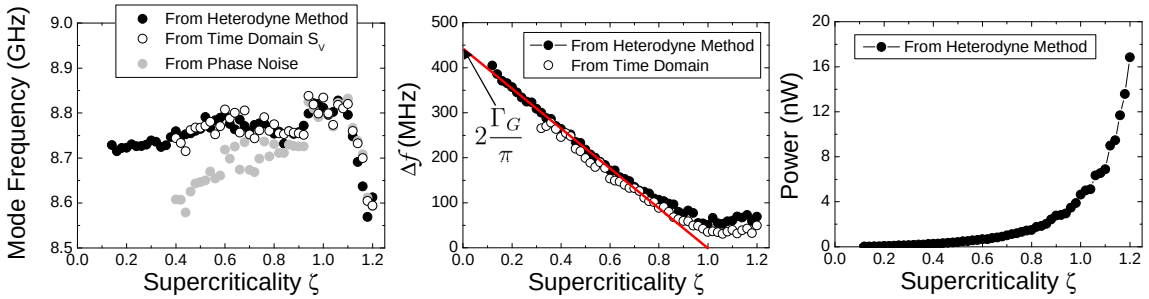

Fig. 4.2: (a) Current dependence of the mode frequency for Sample A. Three measurement methods are presented, the first one is the heterodyne method (black dots). In the second method, we first compute the PSD of the voltage acquired by the SSO and then fit S_V with a Lorentzian function (white circles). In the third case, we estimate the signal frequency from phase noise analysis (gray dots). In this latter case, for $\zeta < 1$, the frequency obtained does not fit the one measured by other method since when the amplitude of the oscillation becomes zero, the phase is also considered to "advance" with a zero frequency. In average, the frequency is therefore smaller than the real one.(b) Measured FWHM versus the supercriticality ζ. Again we compare the Lorentzian fits applied to the signal either measured by heterodyne method (black dots) and time domain method (white circles). The red line represents the linear decrease of linewidth with ζ. ζ is evaluated by this method and confirmed by the amplitude distribution plots (see Fig. 4.13).(c) Power dependence versus ζ. $\zeta = 1$ corresponds to an applied current density of $J_c \approx 1.76 \times 10^{11}$ A/m^2.

18 GHz for a supercriticality $\zeta = I_{th}/I = 0.8$. Besides the first and second harmonic FL excitation peaks, a SAF excitation peak and low frequency noise is visible.

Using the spectrum analyzer (e.g. heterodyne method), we have measured the mode frequency (black dots in Fig. 4.2-a), the FWHM Δf (black dots in Fig. 4.2-b) and the mode power (black dots in Fig. 4.2-c), calculated from the area under the curve of the Lorentzian fit of the peak. The linear extrapolation of sub-threshold linewidth indeed confirms the linear decrease of the FWHM with ζ, as expected from Eq. 4.5 (e.g. Eq. 4.4).

In order to further verify the model, we performed time domain (TD) measurements with a SSO. Both the frequency and the linewidth extracted from TD agree with values measured by the heterodyne method as shown by the white circles in Figs. 4.2-a,b. For $\zeta < 1$, a substantial increase of the "*mode*" frequency[1] in the sub-threshold regime followed by the decrease of the frequency mode for $\zeta > 1$ is observed. It is to note that this behavior is very reproducible among different samples (see for example Fig. 4.3) with different slopes, and will be discussed later.

To confirm the resonant origin of the linewidth, i.e., that the linewidth is given by power fluctuations around the equilibrium, we consider now the time domain signal obtained for $\zeta < 1$ for the sample A. A typical TD signal, where the instantaneous amplitude $A(t)$ has been extracted via a Hilbert Transform, is presented in Fig. 4.4 for different ζ. The left panels give in black typical signals filtered with a 4 GHz bandpass filter centered on the mode frequency with their corresponding instantaneous amplitude. We can see that upon increasing the current, the signal coherence and amplitude increase.

[1]According to damped harmonic oscillator theory presented in chapter 2, below the threshold value $\zeta = 1$, the maximum peak power corresponds to a *resonant* frequency that differs from the *mode* frequency of the system.

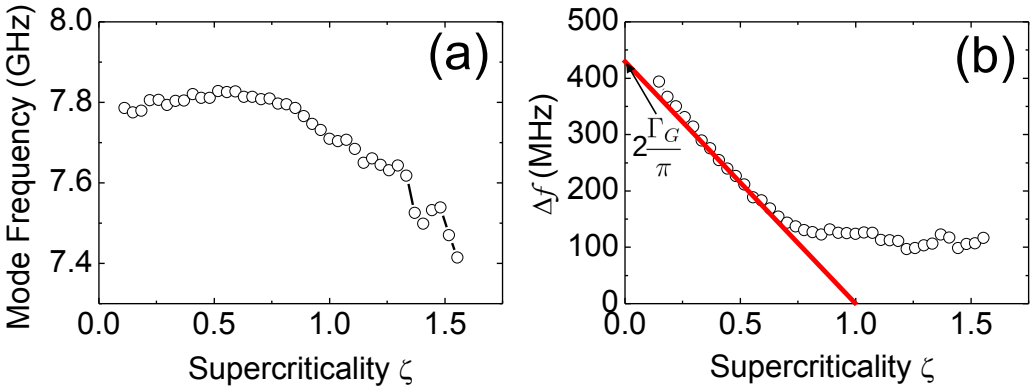

Fig. 4.3: (a) Current dependence of the mode frequency for Sample B. (b) Linewidth versus ζ. The red line represents the linear decrease of linewidth with $\zeta < 1$ according to Eq. 4.3. $\zeta = 1$ corresponds to an applied current density of $J_c \approx 1.53 \times 10^{11}$ A/m^2.

The middle panels give the voltage distributions of the signals; these voltage distributions are Gaussian, as expected for fluctuations of the magnetic moment around its equilibrium position. In the right panels we give the autocorrelation function of the amplitude fluctuations (in black) with an exponential decay fit (in red).

The autocorrelation functions of $\delta a(t)$ in Fig. 4.4 show a clear exponential decay of the oscillation power. Experimentally, for small $\zeta < 0.5$, the signal is hidden by the experimental noise such that the determination of $2\Gamma_s$ is not easy (see right panels of Fig. 4.4-a). With increasing signal power (by adding more current), the relaxation phenomena in the amplitude can be clearly distinguished from the setup noise, even in linear scale (see right panels of Figs. 4.4-b,c).

Finally, we compare the relaxation rate $2\Gamma_s/\pi$ of the amplitude to the linewidth Δf value[2] extracted from S_V in Fig. 4.5-a. The comparison clearly shows that $\Delta f = \Gamma_s/\pi$ and thus indicates the origin of the sub-threshold linewidth in the case of STOs that is solely due to the amplitude relaxation. It is also observed that the above-threshold linewidth near $\zeta = 1$ is given by this amplitude relaxation rate. Before conducting further investigations, we would like to compare the experimental results to macrospin simulations that are the resolution of the full LLGS equation (without b_j term). We verify that Γ_s/π is equal to Δf_1 in Fig. 4.5-b for $T = 400$ K. In this case, evaluation of Γ_s is possible even at very low supercriticality ζ since no noise from the measurement setup is present (i.e. virtually infinite sensibility).

In the experimental sub-threshold case (similar picture can be drawn from macrospin simulations), we see from the left panels in Figs. 4.4-a,b that the oscillation "starts" and is then "damped out". The distribution of the magnetization is Gaussian up to $\zeta = 0.9$ and centered around zero amplitude. The distribution functions of voltage are given for different ζ in Fig. 4.6. To highlight the discrepancy from the pure Gaussian distribution for $\zeta > 0.8$, we have represented those distributions on a logarithmic scale in Fig. 4.6-b. Above $\zeta = 0.9$, the system tends to be stabilized in the auto-oscillating regime; now the voltage population is centered around two finite/nonzero values of the voltage (positive and negative voltage) rather than only one (zero mean amplitude).

[2]We consider the mode linewidth Γ_s/π as representative of the damping rate Γ_s in units of Hz.

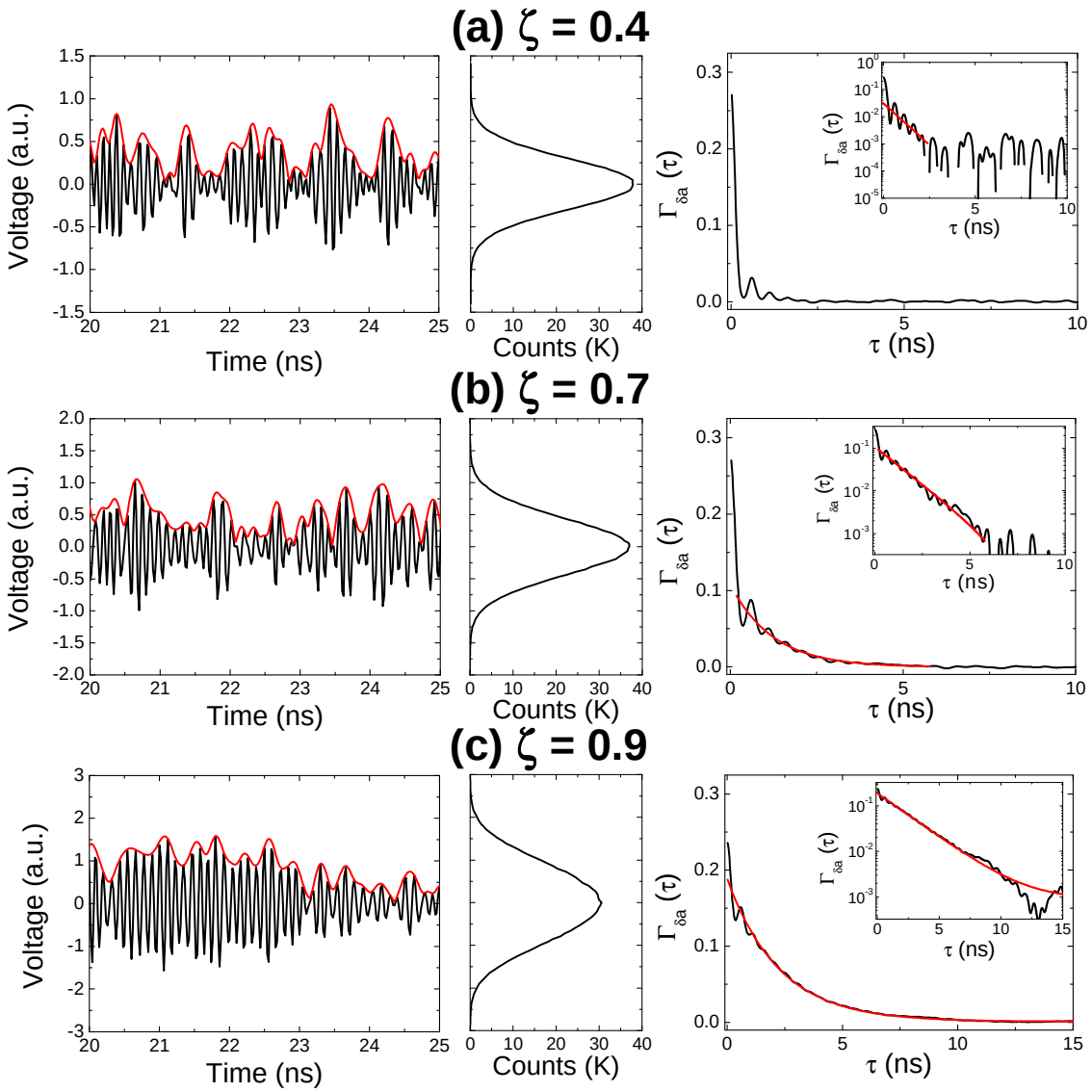

Fig. 4.4: Signal and amplitude analysis of TD measurements on Sample A for different supercriticality parameters (a) $\zeta = 0.4$, (b) $\zeta = 0.7$ and (c) $\zeta = 0.9$. Left column is TD signal measured with SSO (in black) and the extracted instantaneous amplitude (in red). Middle column: distribution of the voltage signal. Right column: autocorrelation function of the amplitude fluctuations. In red is a fit of the data with an exponential decay to obtain Γ_s. Inset: autocorrelation function on a log scale. A 4 GHz digital bandpass centered around the mode frequency is applied to the TD. The distribution function of voltage when $\zeta = 0.9$ is still roughly Gaussian.

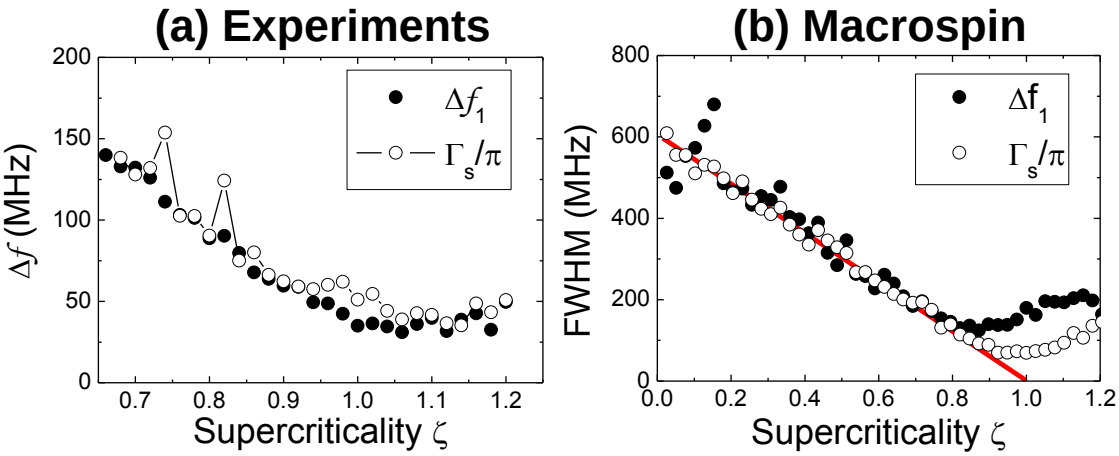

Fig. 4.5: (a) Comparison of Γ_s/π and Δf_1 versus the supercriticality ζ for sample A. The fact that the two measurements are still correlated above ζ close to 1 can be understood by the fact that the amplitude noise has a non-negligible contribution to the PSD S_V. (b) Linewidth dependence and Γ_s/π versus ζ for a Macrospin simulation performed at 400 K. The red line gives the linear decrease of the FWHM and Γ_s/π with supercriticality as expected from the KTS model.

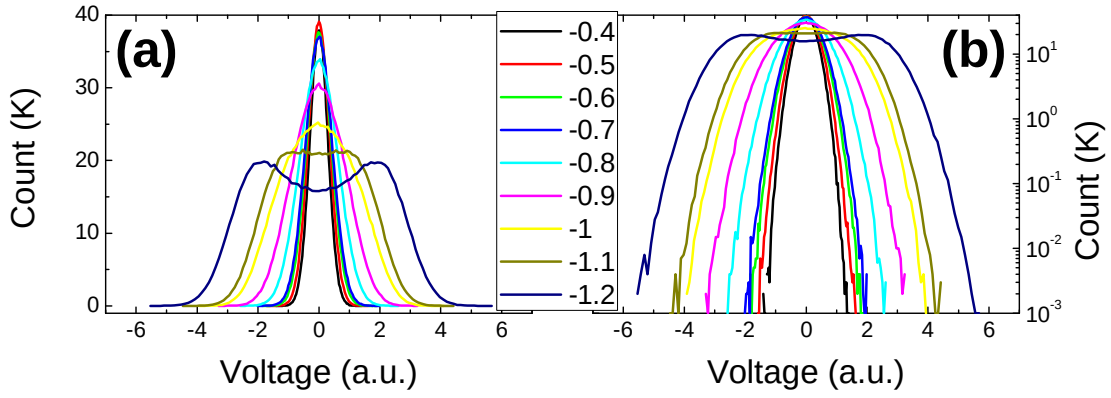

Fig. 4.6: Distribution function of the voltage for different ζ in linear (a) and logarithmic scale (b). A non trivial distribution is observed for $\zeta \geq 0.9$.

Physically, the regime below $\zeta = 0.9$ corresponds to a push-pull regime of the magnetization towards its equilibrium position induced by the thermal noise. This damped oscillating regime is governed by the fluctuation/dissipation phenomena around the equilibrium, as shown by the voltage distribution function in Figs. 4.4 and 4.6. Adding a spin-polarized current reduces the overall damping that finally increases the relaxation time, but also the width of the voltage distribution that remains Gaussian. When the magnetization describes relatively small deviations from the equilibrium, the linearization of LLGS found in section 2.2.1 (the linearized Eq. 2.13 or Eq. 2.14) is still correct; and indeed the amplitude relaxation rate Γ_s decreases linearly.

For larger currents $\zeta \approx 0.9$, the "relatively" low resulting damping rate (λ^{STT}) allows "relatively" large deviations from equilibrium. It results in a distribution that cannot be described anymore by a Boltzmann distribution with a reduced damping term and centered around $p \approx 0$. In this case, the linearization of LLGS is no longer valid, which explains the non-trivial relationship of the sub-threshold linewidth (or restoration rate Γ_s) with applied current. In terms of the KTS model, the sub-threshold linewidth Δf_{sub} is no longer equivalent to $\Gamma_+(0) - \Gamma_-(0)$ but should be equal to $\Gamma_+(\bar{p}) - \Gamma_-(\bar{p})$, where $\bar{p}$ is such that $\Gamma_+(0) - \Gamma_-(0) << \Gamma_+(\bar{p}) - \Gamma_-(\bar{p})$.

The next section aims to give more details on the transition between the linear and the nonlinear regime. The discussion is oriented towards two main features of the harmonic oscillator: a power response proportional to the noise strength, a noise free *resonant frequency* and *quality factor* and finally a damping-dependent *resonant frequency*.

4.1.3 The damped harmonic oscillator: towards the nonlinear regime driven by temperature

One direct consequence of the interpretation of the measurements and KTS model for $\zeta < 1$ implies that the sub-threshold linewidth, i.e. the amplitude relaxation rate, is independent of the noise strength acting on the magnetization. However, the mean magnetization deviation, or $\bar{p} = \Gamma_+(0)\frac{\gamma k_B T}{V M_s \omega(0)}$ (with V the volume of the magnetic material involved in the dynamics), is dependent of the noise strength (namely the temperature T). As a consequence, the total power should increase with increasing temperature since it allows larger deviations of the magnetization from its equilibrium. In addition, the measurement of the sub-threshold linewidth is supposed not to change with temperature, as a consequence of a linear damped harmonic oscillator model. Indeed, on experiments, Fig. 4.7-b confirms such a prediction for the power dependence. In the mean time, the sub-threshold linewidth exhibits a non-trivial dependence with temperature for different ζ. For example, around $\zeta \approx 0.6$, the sub-threshold linewidth remains unchanged with temperature (see Fig. 4.7-c), while Γ_G ($= \Delta f(\zeta = 0)$) seems to increase by a factor of 3.

While some material parameters may change with temperature, allowing for variations in the value of Γ_G; in some cases, Γ_G appears two to four times larger at 20 K than the value at 300 K. In terms of material parameter variations, Γ_G is the product of the Gilbert damping α times the magnetization M_s added to the anisotropy fields (for in-plane easy axis configurations). For the example in Fig. 4.7, M_s did not to vary much in the temperature range studied; the variation is not more than 20%. Concerning the damping parameter α and anisotropy fields, the answer cannot be so straightforward. Patton and

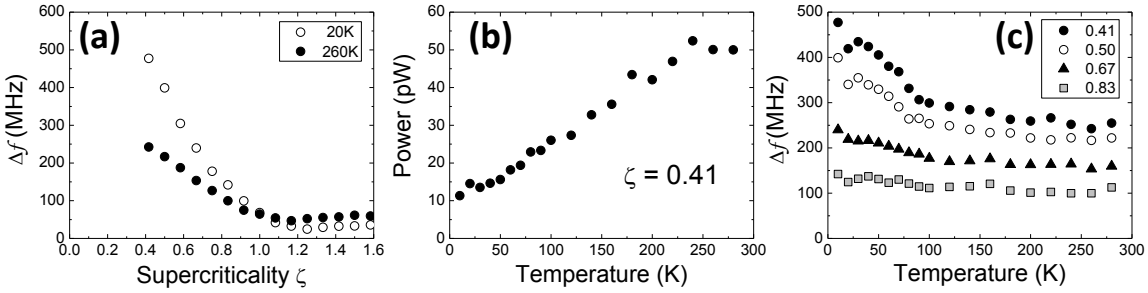

Fig. 4.7: (a) FWHM versus ζ at $T = 20$ K (white circle) and $T = 260$ K (black dots). (b) Integrated power versus T at $\zeta = 0.41$. The offset value might be due to experimental setup, the standing wave or electrical noise. (c) FWHM versus ζ for different ζ. The increase of the subcritical linewidth below $T = 100$ K may have different origin. For DevC. Experiments by J.-F. Sierra.

Wilts [129] reported an increase of FMR linewidth around $T \approx 80$ K because of the oxidation condition of the Py layer at its interface. This effect has also been evidenced in Ref. [130]. Also, Sierra et al. [131] showed that in MTJ stacks (e.g. in a trilayer Py/AlO/Py thin films), an enhancement of the FMR linewidth can be obtained, from 50% to more than 100% because of the presence of soft-Hard layer coupling (e.g. frustration near interfaces). In CoFeB thin films, a recent study by Yu et al. [132] evidenced an increase of the damping by a factor of 3 when the temperature was decreased from 300 K to 5 K. Therefore, the direct experimental response is uncertain of the real origin of this increase of FMR damping rate at low temperatures, since the origin of damping is itself subject to debate.

From macrospin simulations, it is possible to intentionally use temperature independent materials parameters (α, M_s, ...) . In this way we can compare the influence of noise (strength) on the magnetization dynamics only that is impossible in real experiments.

Fig. 4.8-a shows that in the case of macrospin simulations, the sub-threshold linewidth is independent of temperature (ranging from T= 50 K to T= 600 K), confirming the relaxation origin of the sub-threshold linewidth up to $\zeta \approx 0.6 \sim 0.8$. Indeed, in contrast to what is observed in experiments, there is no dependence of Γ_G with the temperature. In the macrospin simulations, $2\Gamma_G/\pi \approx 650$ MHz.

On the other hand, the effect of noise combined with the damping rate on the *resonant frequency* is less clear from simulations. In Fig. 4.8-b we show the frequency versus ζ for different T. There is an upward peak frequency shift with increasing ζ for $T = 50$ K. In this case, we can suppose that the thermal noise strength, is not sufficient to lead to any nonlinear effects up to $\zeta \approx 0.9$.

Indeed, entering the nonlinear regime (from $\zeta \approx 0.9$) would induce a power dependent frequency (i.e. $\omega(p)$), and a power dependent damping terms ($\Gamma_+(p)$ and $\Gamma_-(p)$) as explained earlier. In this case, we can suppose that the *resonant frequency* has an upward shift of 50 MHz toward the *mode frequency* of the harmonic oscillator. We note that this value is in agreement with a damping rate initially a tenth of the *mode frequency* as depicted in Fig. 2.2 of section 2.1.1.

In the simulations of Fig. 4.8-b, it is less clear whether this upward shift appears

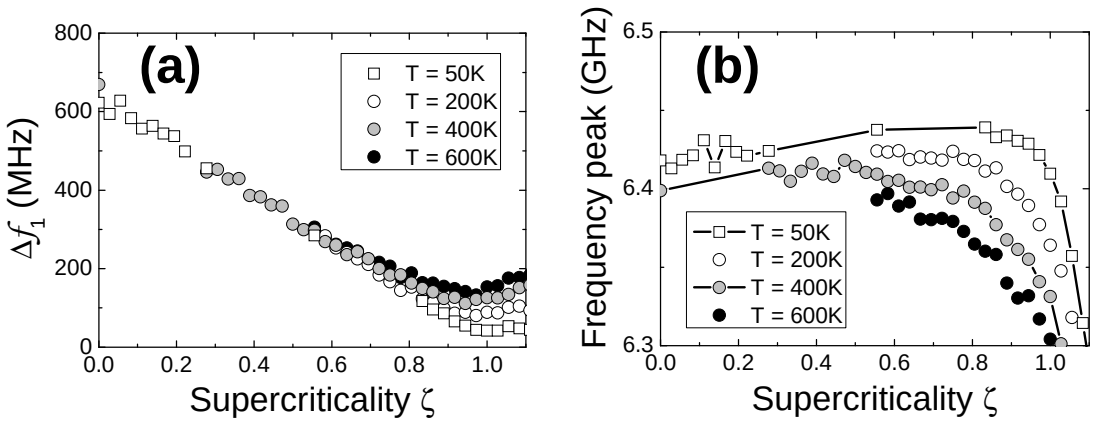

Fig. 4.8: (a) Linewidth versus ζ for different temperatures. (b) Observed frequency peak in macrospin simulations versus ζ for different temperatures. The *resonant frequency* shifts upward with increasing ζ. Also, because of the temperature, the frequency peak near the threshold is also affected by the nonlinear regime (downward shift near $\zeta = 1$). Simulations by D. Gusakova.

for higher temperature since the nonlinear regime, i.e. the downward shift in frequency (typical for IPP modes) appears at lower ζ value such that the upward shift of the *resonant frequency* is not clearly visible (for example, see grey dots from $\zeta \approx 0.6$). Indeed, in this case, thermal fluctuations may allow the system to reach relatively high power values.

This appearance of the downward shift of the *resonant* frequency in the sub-threshold regime for $0.6 < \zeta < 1$ and for higher temperatures is well correlated with the substantial increase of FWHM compared to the linear decreasing trend (see Fig. 4.8-a).

The slight increase of frequency versus the applied current in experiment (Fig. 4.2-a) may have a similar origin: the upward frequency shift of the *resonant frequency* is correlated with the decrease of the damping term. Of course, such an increase could also be due to the b_j term introduced in section 1.2.1.2 (see also Eq. 2.15) that is present in our MTJ devices (but has been neglected in simulations). Moreover, the increase of frequency with respect to applied current in the sub-threshold regime is found with different slopes as seen by the example of another Sample B in Fig. 4.3. It is to note that the applied field angle is also different from the different sample measurements. The *relative* field angle difference[3] between sample A and B is about 10°.

There exists one study in the literature on the sub-threshold frequency and linewidth in MTJ-based STO from Georges et al. [134]. In the sub-threshold regime, the authors observed an increase of linewidth together with an increase of a frequency shift with current (see Fig. 4.9). This result seems to be in agreement with the aforementioned picture of damped harmonic oscillator whose subthreshold effective damping decreases with increasing ζ. When the damping rate (1.2 GHz) is about a fifth of the *mode frequency* (5.5 GHz that appears around the threshold current value), the *resonant frequency* is

[3]Samples have a circular shape, but still some shape anisotropy or uniaxial anisotropy is present (see Fig. 4.1-a). Moreover, pattern processes and annealing conditions may create an "easy axis" distribution among samples. Simple angular dependence MR measurements do not provide enough resolution for the determination of the exact easy axis direction, since it can be different from the "polarizer direction". Polarizer direction can be easily determine by frequency measurement as shown in Ref. [133].

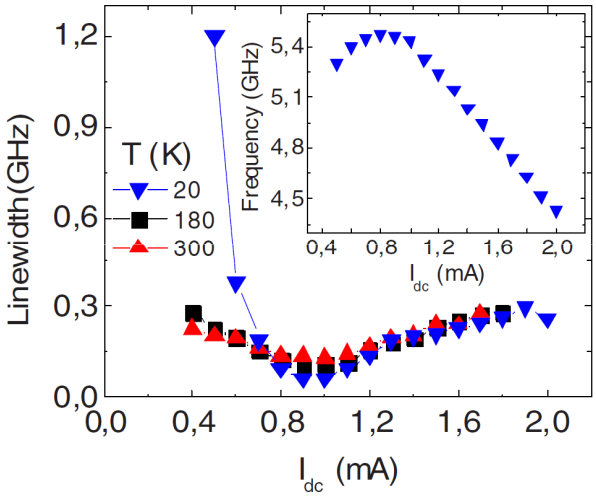

Fig. 4.9: Linewidth dependence versus applied DC current measured at different temperatures. Inset: Frequency versus applied current for $T = 20$ K. The critical current $I_c \approx 1$mA. From [134].

shifted downward compared to the *mode* frequency (by more than 200MHz), as observed in the inset of Fig. 4.9. This interpretation is also consistent with the fact that when reducing the damping rate to a more conventional value by applying more bias current, the *resonant frequency* becomes closer to the probable (necessary higher) *mode frequency*. Indeed, the equality between *resonant frequency* and *mode frequency* is indeed almost true in the case of damped harmonic oscillators with relatively low damping rate. Of course, we cannot claim to be able to re-interpret all the experimental data in the Ref. [134], since all experimental conditions are not given in detail.

To further confirm this hypothesis, we have also conducted macrospin simulations with a larger damping parameter α in order to enhance the downward shift in the *resonant frequency* when $\zeta \approx 0$, in Fig. 4.10, with $\alpha = 0.1$[4]. In this case, the effect on resonant frequency and sub-threshold damping is straightforward. When increasing the current (ζ), the resonant frequency shifts upwards as expected with a decrease of the damping rate of a harmonic oscillator. We conclude that the LLGS equation, and therefore the magnetization dynamics, in the low current regime ($\zeta < 1$) is equivalent to an harmonic oscillator with damping rate λ^{STT} and *mode* frequency ω_0^{STT}. We have shown that our data are in agreement with this model interpretation.

Finally, we would like to stress that we cannot explain the substantially large increase of the linear damping rate Γ_G that is observed experimentally when lowering the temperature. It is possible, for example, that spin frustration (spin glasses or strong anisotropies) occur in the ferromagnetic electrodes at the vicinity of the MgO interface. In this case, it is to note that the fluctuation-dissipation theorem might not be valid anymore.

In conclusion, we have experimentally verified that a STO in the below-threshold regime behaves as a regular damped harmonic oscillator up to $\zeta \approx 0.8$ with power-independent

[4]This value can be found in some ferromagnetic metallic alloys, such as FePt.

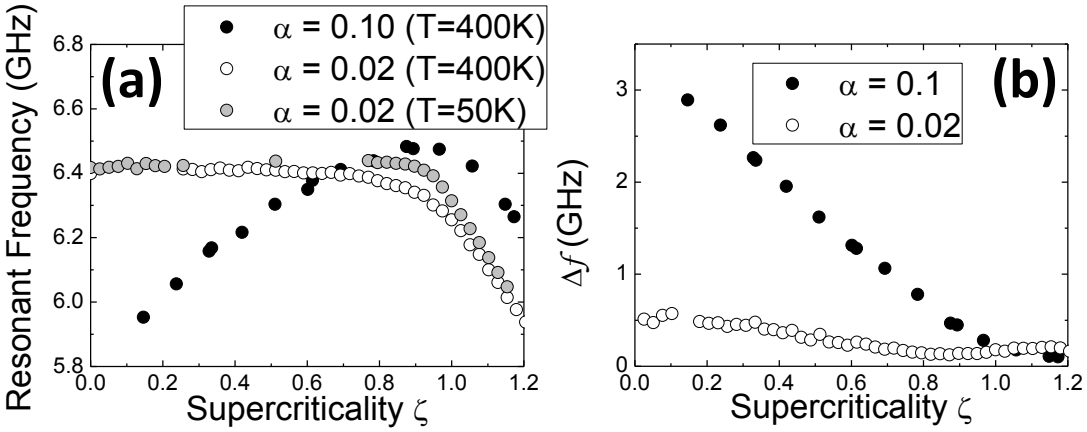

Fig. 4.10: (a) Sub-threshold resonant frequency versus ζ as observed in macrospin simulations for different values of the damping constant α or the temperature. (b) Sub-threshold linewidth for different α values. While α directly influences Γ_G, it does not change the linear decrease of linewidth with ζ, for $\zeta < 1$. Simulation by F. Garcia.

dissipative terms (actually, $p \approx 0$ when $\zeta < 0.8$). Slightly above this value, the nonlinear dependence of the dissipative terms starts to influence the magnetization dynamics in the presence of noise. Indeed, the system has to be considered to be out of equilibrium, and the exchange with the thermal bath, i.e. the dissipation, becomes nonlinear. It is however unclear whether this effect is due to a nonlinear effect in the positive damping Γ_+ or whether it is solely due to the nonlinearities in Γ_- (e.g. $Q = 0$?). Nevertheless, it is clear that the below-threshold regime linewidth observed in STO (up to $\zeta \approx 0.8$) is given by the dissipation terms involved in the magnetization dynamics, the damping term and the STT term. Between $0.8 < \zeta < 1$, the internal physical picture is less clear, but the linewidth observed in S_V is still related to the amplitude relaxation phenomenon (same order of magnitude). We also noted a resonant frequency variation due to the temperature in this regime, even for low damping constants ($\alpha \approx 0.02$). Even if the KTS model assumes $\alpha \ll 1$ such that no distinction is made between *resonant* and *mode* frequency, we confirmed that the sub-threshold linewidth is given by the damping terms as expressed in the KTS theory.

4.2 $I > I_c$: Non-isochronous Auto-Oscillator

We now focus on the above-threshold regime, $\zeta > 1$. As explained in section 2.2, linearization of Eq. 4.1 around the limit cycle $p_0 =< |c|^2 >$ leads to an equation that describes the evolution of power fluctuations δp and the total phase Φ:

$$\begin{aligned} \frac{d\delta p}{dt} + 2\Gamma_p \delta p &= \xi_1(t) \\ \frac{d\Phi}{dt} + \omega_0 + N\delta p_0 + N\delta p &= \xi_2(t) \end{aligned} \quad . \tag{4.7}$$

$\xi_1 = 2\sqrt{p_0}\Re(f_n)$; $\xi_2 = 1/\sqrt{p_0}\Im(f_n)$, ω_0 is the eigenfrequency, and $\omega_g = \omega_0 + Np_0$ the mode frequency. In the above-threshold regime, $p_0 > 0$, the frequency shifts. This shift in frequency is proportional to N, which is negative for the in-plane precession mode, as expected from the KTS model [54]. In many other auto-oscillators, e.g. lasers, N is small (more explicitly $\nu \ll 1$). Such oscillators are called *isochronous*, in the sense that their auto-oscillation frequency is independent of the amplitude. STOs, however, belong to the class of *non-isochronous* auto-oscillators where the generated frequencies $\omega_g(p)$ depends strongly on the auto-oscillation amplitude.

In the following, we sub-divide this section into four subsections.

- The first one is a discussion on the power distribution found in experiments and its comparison with the model in the autonomous regime for STOs.

- The second subsection describes the amplitude noise relaxation phenomenon that allows to extract the nonlinear amplitude restoration rate Γ_p (when $\zeta > 1$).

- The third subsection explains why the *non-isochronous* property (or nonlinearity of the auto-oscillation frequency) provides a mechanism to convert the amplitude noise into phase noise so that it creates an additional effective source of a non-white (correlated) phase noise that substantially broadens the generation linewidth. The direct consequence of the study of the phase noise is the extraction of ν.

- We end the section by a discussion on the effect of the nonlinear parameter on the value of the measured FWHM. In particular, we concentrate on the discussion on the physical meaning of the linear linewidth Δf_0.

Unless noted otherwise, the experimental results presented were obtained with Sample C (Fig. 4.11), which has been measured well above $\zeta = 1$. Macrospin results are also analyzed up to $\zeta = 2$. From the frequency dependence shown in Fig. 4.11-a,d, the mode exhibits a clear redshift with ζ for $\zeta \geq 0.8$ in both experiments and simulations. Redshift means "frequency decrease", blueshift means "frequency increase", similarly to the light color that tends to red (low frequency) or blue (high frequency) in the Doppler effect. This redshift is the signature of the nonlinear amplitude phase coupling N introduced in the KTS model.

During the discussion, the macrospin results will be analyzed in a similar manner as the experimental results (the macrospin simulation parameters are given in Fig. 4.11-f). The main advantage of the macrospin simulations over the experimental results is that all components (m_x, m_y, m_z) of the magnetization can be analyzed. Moreover the macrospin simulations are free of setup noise (as we have seen in the below threshold regime section 4.1) and there are no measurement artifacts. Therefore, we can make a comparative study of the experimental and macrospin results in order to see exactly which points of the KTS model can be addressed experimentally. Indeed, we have to keep in mind that the KTS model requires a canonical transformation of the magnetization dynamics while in most experiments only the first harmonics signal projected on the polarizer direction is analyzed (i.e. experimentalists measure only the magnetoresistance of the device).

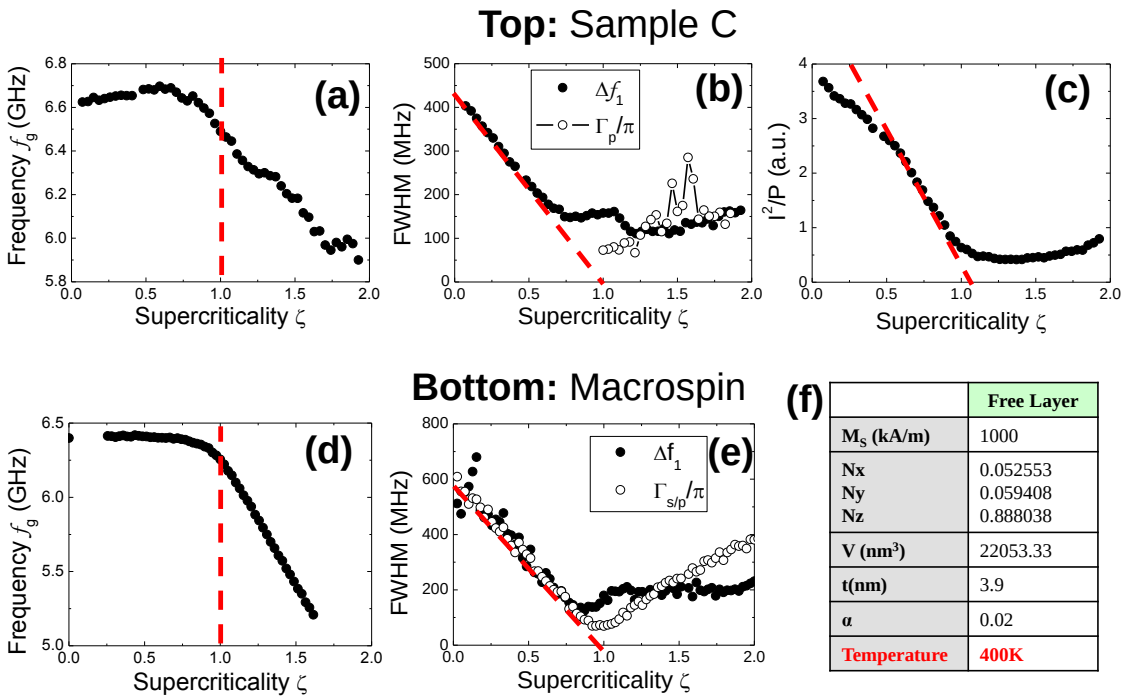

	Free Layer
M_S (kA/m)	1000
Nx Ny Nz	0.052553 0.059408 0.888038
V (nm^3)	22053.33
t(nm)	3.9
α	0.02
Temperature	400K

Fig. 4.11: Top panel: Sample C. (a) Peak frequency versus ζ for sample C (TMR= 74% and RA= 1.5Ω.µm^2, the sample has a circular shape with a diameter of 75 nm). (b) Γ_p and Δf_1 versus ζ. (c) Inverse mode power versus ζ. The critical current has been obtained by a linear interpolation of the sub-threshold linewidth. It corresponds to the interpolation of the inverse of the mode power versus ζ. Bottom panel: macrospin simulations by D. Gusakova (integration time: of 5 µs). (d) Peak frequency versus ζ. (e) Γ_p and Δf_1 versus ζ. (f) Simulation parameters. The anisotropy constant is set to 0, there is only shape anisotropy (elliptical shape : 90×80 nm^2, applied field of $H_{app} = 31830$ A/m.

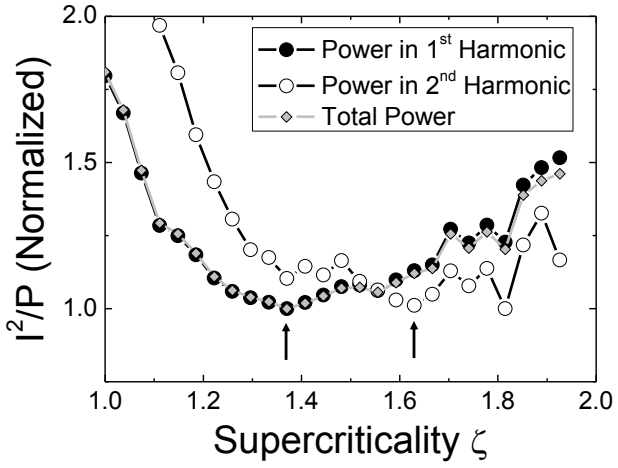

Fig. 4.12: Comparison of the normalized inverse power $1/P$ integrated either on the first harmonic only (black dots), or on the second harmonic only (white circles) or on the total signal (gray diamonds) calculated as the area under curve of S_V obtained from frequency domain experiment. Black arrows indicate the maximum of the power found for each harmonic.

4.2.1 Power Distribution in the Above-Threshold Regime

A central point of the KTS model is the power distribution probability in the presence of noise. Here we compare the distribution functions of amplitude and power available from both experiments and macrospin simulations. The first interest of the power distribution functions is the determination of the critical current I_c from which the auto-oscillating (autonomous) regime starts.

In section 2.2, it has been predicted that the linear extrapolation of the linewidth and the linear extrapolation of the sub-threshold inverse power provide the value of the critical current. From Figs. 4.11-b,c, this prediction is confirmed experimentally ($I_c = 0.675$ mA or $J_c = 1.53 \times 10^7$ A.cm^2). For very low signal power (for $\zeta < 0.5$), the measurement noise is close to the STO's output power such that the inverse mode power appears lower than the expected one (see Fig. 4.11-c). Nevertheless, between $0.5 < \zeta < 0.9$, a clear linear trend appears. Slightly above the threshold, the mode power (measured at the first harmonic) seems to decrease with increasing ζ from $\zeta = 1.35$. A possible explanation is that the mode power is not necessarily given by the first harmonic peak. Indeed Fig. 4.12 shows that if we consider the second harmonic, the inverse power of the second harmonic rises around $\zeta = 1.65$. It follows that the integrated power of the first and second harmonic peak seem to be representative of the mode power only until $\zeta \approx 1.3 \sim 1.6$. Before giving a possible explanation of this observation, we comment on the power distribution obtained from TD measurement.

We already discussed about the power distribution function of the oscillation with supercriticality for $\zeta > 1$ in section 2.2. Fig. 4.13 shows both signal amplitude (from $V(t)$) and signal power (from $V^2(t)$) distributions for the three different devices (Samples A, B and C). The power distribution function at the threshold value ($\zeta = 1$) corresponds to the one predicted by KTS model (see Fig. 2.10 in section 2.2.3) in all cases.

Nevertheless, for higher values of ζ, above $\zeta > 1.5$, the mean power seems to saturate and the distribution is no longer Gaussian. Moreover, the saturation in power also appears

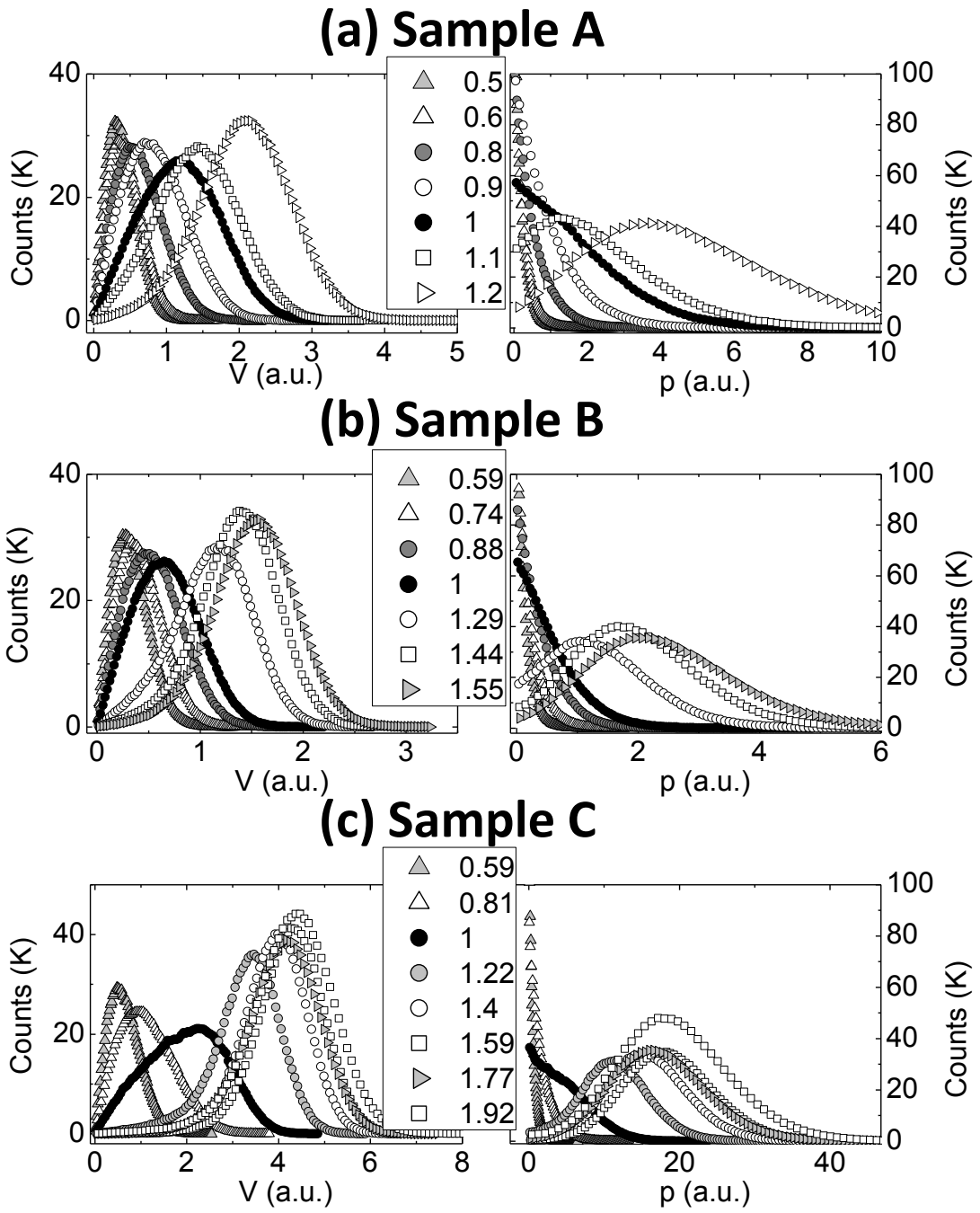

Fig. 4.13: Amplitude distribution (left) and power distribution (right) for the different samples discussed in the text and for different ζ. The black dots correspond to $\zeta = 1$. For value larger than $\zeta \approx 1.5$, the power and amplitude distribution look unchanged with increasing ζ.

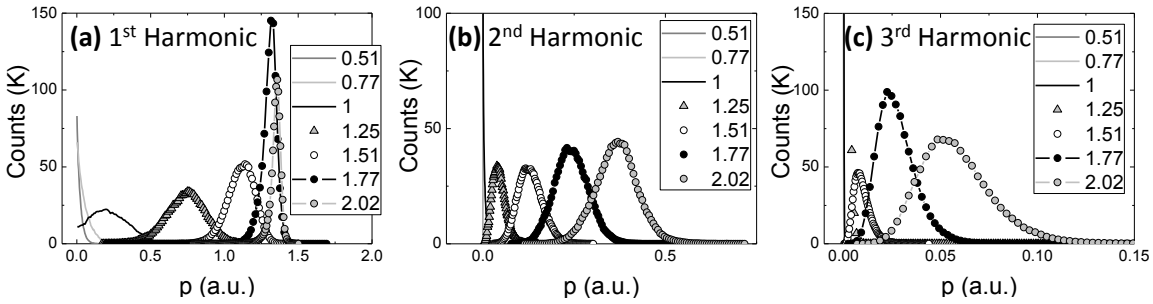

Fig. 4.14: Power distribution as calculated from macrospin simulation after filtering around the first harmonic (a), the second harmonic (b), and third harmonic (c).

for Sample C, as already observed in the frequency domain experiments[5].

From macrospin simulations, the study of the magnetization dynamics can determine whether this effect is also seen or not. If we now consider the "power" distribution in each harmonic of a macrospin simulation for different ζ, we see in Fig. 4.14 that we can indeed reproduce non-Gaussian power distributions and mode power saturation. From this, we can conclude that the total power is given by the sum of all harmonic powers in the case of LLGS.

The main conclusion here is that above a certain applied current $\zeta > 1.5$, it seems that the power and the power fluctuations extracted from the first harmonic of the signal is not the correct parameter to be compared with the KTS theory. Since a non-Gaussian power distribution has been also reported by Nagasawa et al. [77] for $\zeta > 1.5$, we can investigate the possible reasons for that discrepancy between KTS theory and experiments or simulations.

We identify and sort the three probable hypotheses (according to their relevancy):

- Nagasawa et al. [77] explained the discrepancy in the power variance between the KTS model and their experiments by a possible chaotic behavior of the mode above the value $\zeta > 1.5$. Since this has been also observed in our macrospin simulation, we can dismiss this argument. Yet, we can consider that the angular dependence of the STT term (not taken into account in the KTS model, but in our macrospin simulations) may be at the origin of the model/macrospin or experiment discrepancy. A way to verify this hypothesis would be to not take into account the angular dependence in the a_j term of the macrospin simulations.

- Another cause of this discrepancy between theory and experiment might be that despite the Gaussian distribution of the "force" given by the (stationary and ergodic) Gaussian process $f_n(t)$, it may turn out that the resulting mode power distribution is no more Gaussian (i.e. $p(t)$ does not have the same stochastic properties as $f_n(t)$), due to a chaotic behavior.

  The second possibility is that $f_n(t)$ is no longer stationary. This could be possible considering that power fluctuations might be such that a variation of $D_n(p_0 + \delta p(t))$

[5]The right panels of Fig. 4.13 give the distribution of the voltage square V^2. To be correct, one should compare the voltage square divided by the square of the current (V^2/I^2). Nevertheless, on can distinguish the saturation of the distribution of the V^2 for $\zeta > 1.5$ in the left panel of Fig. 4.13-c.

makes $f_n(t)$ neither stationary nor ergodic anymore. In this case, the PDF of X depends on $p(t)$ (non-stationary) and therefore the distribution of $f_n(t)$ also depends on its own realization (non-ergodic). Typically, shot noise is a non-stationary white noise process [92], since the amount of current noise depends on the amount of total current that is thus time dependent. This statistical inconsistency ignored in the KTS model (in order to simplify the solution of the equations) may appear here in light of these measurements and/or simulations. V. Tiberkevich has proposed [135] to use the conditional probability applied to the power fluctuation in order to elucidate such effects in experiments and macrospin simulations.

Also, we note the existence of Flicker noise or $1/f$ noise in the PSD of power fluctuation in STOs [85, 76]. Historically, this noise has been measured in many different fields (biology, physics, chemistry, social science) and has still uncertain origins. This noise typically induces more "model pathologies" than it could solve our problem in detail. Nevertheless, $1/f$-like noise may induce such a non-Gaussian distribution of power fluctuation (but does not explain the observed power saturation seen).

- Finally, we give the most probable cause of this discrepancy, which involves attributing incorrectly the experimental variables to those of the theory. During the canonical transformation of the LLGS equation to the c-variable equation used in the KTS model, what is done is a transformation of the "elliptic IPP trajectory" to a "circular c-variable trajectory". Elliptic trajectories lead to: (i) the projection of the magnetization dynamics that has several harmonics and (ii) a velocity of the magnetization that is not constant along the trajectory (generation of harmonics). A circular trajectory has no harmonics since the velocity is constant along the trajectory. Therefore, considering the measurement of the first harmonic-peak as a description of the system power is not correct.

While we cannot dismiss inconsistencies in the KTS model itself, or eliminate the fact that we have no chaotic trajectories in the experiments, we investigate in more detail the third hypothesis: a model-experiment misinterpretation. By applying the correct transformation of the magnetization vector into a c-variable trajectory from macrospin trajectories, one can retrieve the real mode power even at high values of ζ. Fig. 4.15 indeed shows how filtering the first harmonic of the real macrospin trajectory still induces elliptical representation of the trajectory and not a circular trajectory. If the transformation from the magnetization vector to c-variables is done correctly, the power distribution fits the expected behavior, i.e. an increase of total mode power and a Gaussian distribution of the power distribution.

Therefore, from pure macrospin considerations, the non-Gaussian distributions found in our measurement, and possibly that of Nagasawa et al. [77], can be attributed to the incomplete comparison that can be made between the *real* magnetization dynamics and the *effective* measured signal. This conclusion will be of importance when we will study the variance of the power distribution as a tool to extract the linear linewidth Δf_0 in the following sections. Yet, we have demonstrated the usefulness of the power distribution functions to determine the critical current value I_C. This is realized by identifying the typical shape of the power distribution for $\zeta = 1$. Also, we have found a good agreement

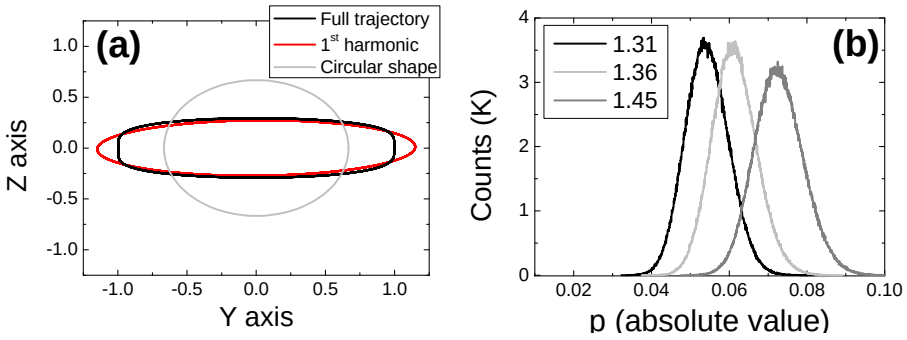

Fig. 4.15: (a) Representation of the magnetization trajectory in the YZ plane (in black), when considering only the first harmonic (in red) and a circular trajectory (in gray) as expected from the KTS model. (b) Power distribution for different ζ. The power is obtained by transforming real macrospin trajectories into power p. Courtesy of F. Garcia.

in the prediction of the sub-threshold inverse power dependence upon current as a means to determine the critical current I_C in our devices.

4.2.2 Amplitude Noise Relaxation

In this section we focus on the time varying power fluctuation distributions. As explained in section 2.2.3, power fluctuations (or amplitude fluctuations) are correlated in time, i.e. the power fluctuation at $t+\tau$, $\delta p(t+\tau)$ is correlated with the power realization at t, $\delta p(t)$, such that the time average of the product $\delta p(t)\cdot\delta p(t+\tau)$ is non zero ($<\delta p(t)\cdot\delta p(t+\tau)>\neq 0$ at short timescale τ).

The autocorrelation function $\mathcal{K}_{\delta p}$ of the power fluctuation δp, solution of Eq. 4.7, can be written as:

$$\mathcal{K}_{\delta p}(\tau) = \frac{4\pi\Delta f_0 p_0^2}{\Gamma_p}\exp(-2\Gamma_p\tau). \tag{4.8}$$

Since $2(A_0)^2\delta a \approx \delta p$ it follows[6] that:

$$\mathcal{K}_{\delta a}(\tau) = \frac{\Delta f_0}{f_p}\exp(-2\Gamma_p\tau), \tag{4.9}$$

where $f_p = \Gamma_p/\pi$ is the frequency at half width at half maximum (HFWM) of the power fluctuations[7]. It is also more convenient to express the solution 4.9 through its FT, to form the PSD of amplitude fluctuations:

$$S_{\delta a}(f) = \frac{\Delta f_0}{2\pi}\frac{1}{f^2+f_p^2}\,. \tag{4.10}$$

Interestingly, in the amplitude fluctuations, it is possible to extract the "linear" HWHM Δf_0 of the STO, the amount of noise available by the STO that affects both the amplitude

[6] $A_0^2(1+\delta a)^2 = p_0+\delta p$, it comes: $\delta p/p_0 = 2\delta a + (\delta a)^2$. $(\delta a)^2 << \delta a$.

[7] Be careful that here, f_p defines a half width and not a full width as usual. Plotting f_p together with the FWHM Δf_1 of the oscillation, could show that Δf_1 and f_p are of the same order or not, as discussed in section 4.1.

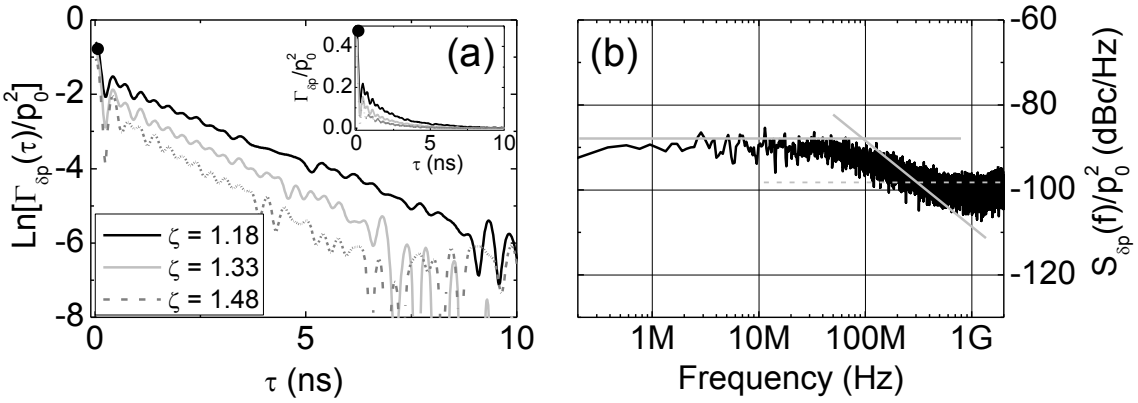

Fig. 4.16: (a) Normalized autocorrelation function $\mathcal{K}_{\delta p}$ for different ζ on a logarithmic scale. Inset: linear scale. (b) Corresponding $S_{\delta p}$ for $\zeta = 1.33$. The black dot in (a) represent the white Gaussian electrical noise due to setup noise. In the Fig. (b), this noise contribution corresponds to the dashed gray line.

and the phase. This subsection aims to prove that we experimentally observe that 4.10 applies to our STOs. The discussion is as follows:

- We identify the amplitude fluctuation relaxation phenomenon in both experiment and macrospin simulations, and show how to extract the Γ_p value.
- We discuss the electrical thermal noise floor found experimentally and its effect on the quantities defined in Eq. 4.9 and 4.10.
- We retrieve the "linear" HWHM Δf_0 of the STO from the amplitude fluctuation autocorrelation function.

4.2.2.1 Extraction of Γ_p

We now compare the measured time varying amplitude noise $\delta a(t)$ (or $\delta p(t)$) with the predicted one and the one obtained from macrospin simulations. Fig. 4.16 shows both normalized $\mathcal{K}_{\delta p}$ and normalized $S_{\delta p}$ for sample B.

It is important to note that the characteristic frequency $f_p = \Gamma_p/\pi$ is independent of the absolute value of power fluctuations ("Δf_0") or of the contribution of noise setup (that is discussed later). This frequency actually determines the frequency up to which the system responds independently from the frequency of the perturbation; above this frequency an excitation will be attenuated. Another "physical argument" is to say that for $f < f_p$ (or for times $t > 1/f_p$), a perturbation has been fully damped out (return to equilibrium position) while for $f > f_p$, the fluctuations are adding up (random walk of power fluctuations). Let us consider these two limiting behaviors of the system amplitude in presence of noise. For low frequency perturbations[8], e.g. $f \ll f_p$, we can write:

[8]Remember that the white Gaussian noise can be considered as a perturbation with an equivalent strength for all frequencies.

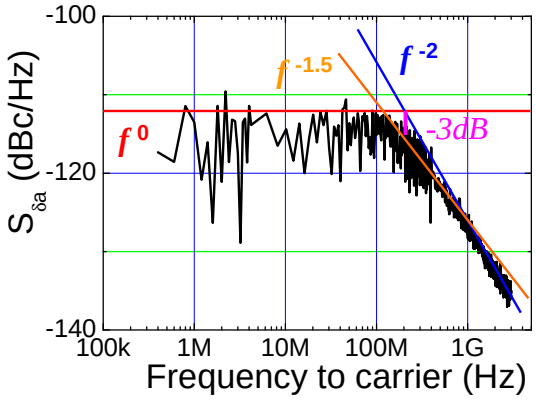

Fig. 4.17: $S_{\delta a}(f)$ for a macrospin simulation with trend curves of different slope. f_p corresponds to the point where $S_{\delta a}(f_p = 250\text{ MHz})$ is equal to $S_{\delta a}(0) - 3$ dB. A curve with an equation $f^{1.5}$ is neither predicted nor a good "limit" trend for $S_{\delta a}$.

$$S_{\delta a}(f) = \frac{\Delta f_0}{2\pi f_p^2} \ . \tag{4.11}$$

This is to consider that the response of the system is of the same nature as the excitation force: white Gaussian[9] below the frequency f_p.

For $f \gg f_p$, it becomes:

$$S_{\delta a}(f) = \frac{\Delta f_0}{2\pi f^2} \ , \tag{4.12}$$

which is the form a of random walk of amplitude fluctuations (see Table 3.2). The power fluctuations are accumulating in the presence of a white Gaussian noise. These two trends are seen in the amplitude noise plots of Figs. 4.19, for both macrospin (Fig. 4.19-a) and experiments (Fig. 4.19-b). In our case, $1/f_p$ gives the timescale at which the energy is exchanged with the thermal bath in the STO. Indeed, if we imagine an instantaneous deviation of the system from p_0 by an amount δp_0, we have to wait the time $1/f_p$ to recover, to dissipate (thanks to Γ_+ or Γ_-) toward the system power, p_0.

We would like to stress here that the two Eqs. 4.11 and 4.12 are asymptotic behaviors of Eq. 4.10. As shown in Fig. 4.17, one has to be careful when dealing with the interpretation of the slopes on a double log plot. For example at $f = f_p$, the real value of the amplitude noise is $S_{\delta a}(f_p) = S_{\delta a}(0) - 3\text{dB}$ on the logarithmic scale. Around the roll-off (i.e. around $f \approx f_p$), no specific slope can be fitted. Moreover, any other slopes would have no real physical meaning, i.e. when $S_{\delta a}$ would be plotted only up to f_p, a wrong conclusion might be drawn from the slope.

Comparing to the macrospin model and then similarly to the FMR linear damping rate Γ_G, which relaxes a small perturbation towards magnetization equilibrium position, Γ_p/π is related to the relaxation of small perturbations of power towards the mean power of the oscillator p_0 (in FMR, $p_0 \approx 0$). That is why Γ_p/π is expected to be of the order of Γ_G/π. From KTS model we have indeed:

[9]We do not discuss anymore about the non-stationary nature of this solution, i.e. that $S_{\delta a}$ is not supposed to exist.

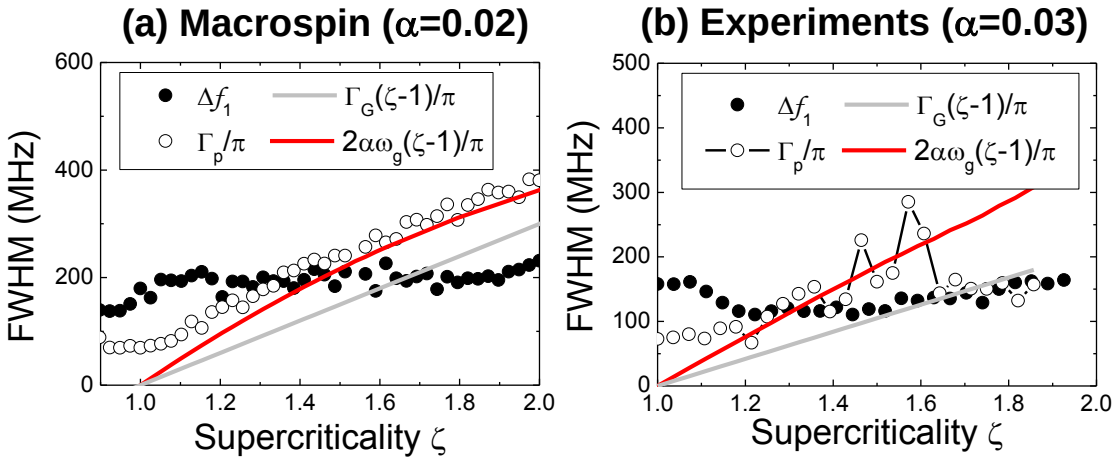

Fig. 4.18: FWHM Δf_1 and $2\Gamma_p/\pi$ versus ζ from macrospin simulations (a) and experimental results (b). The best fit of Γ_p/π (in red) is obtained with the Eq. 4.13 for the macrospin. The experimental comparison with theoretical equations is difficult due to the non-trivial dependence f_p versus ζ observed experimentally.

$$\Gamma_p = \Gamma_G(\zeta - 1) \ .$$

From Fig. 4.3, the experimental full width $2\Gamma_G/\pi$ is expected to be around 420 MHz, which gives Γ_p/π to be 70 MHz, while the TDNS gives $f_p = 85$ MHz for $\zeta = 1.33$. This can be considered as an additional proof of the phenomenological KTS model. Physically, it confirms that the intrinsic linear damping Γ_G is a key parameter for the nonlinear regime in the STO.

However, when we compare $\Gamma_G(\zeta - 1)/\pi$ to the value of Γ_p/π obtained from the macrospin simulations, the values do not coincide as well (see gray curve in Fig. 4.18-a). Instead, the equation:

$$\Gamma_p = 2\alpha\omega_g(\zeta - 1) \ , \tag{4.13}$$

seems to be satisfied (see red curve in Fig. 4.18-a), with ω_g the mode frequency when $p = p_0(\zeta)$. To obtain that equation, we simply assumed the damping term to be $\Gamma_+(p) = 2\alpha\omega_g(1+Qp)$. It is however unclear whether a similar equation describes the experimental results better (the main reason is that α is unknown for the devices). This result is not predicted exactly in this form from the KTS model. Nonetheless, if we consider the "physical" oscillator picture, we see that the harmonic oscillator formed by the STO in the sub-threshold regime has a linear damping rate $\Gamma_G \approx \alpha\omega_0$ (in the isotropic case in section 2.2.1). This is possible since the damping (ratio) α fits the losses of one "turn/cycle" of the magnetization by definition. Similarly, we can consider that even in the "nonlinear" regime, the exchange with the thermal bath is still given by α times the magnetization frequency, which is ω_g and not ω_0.

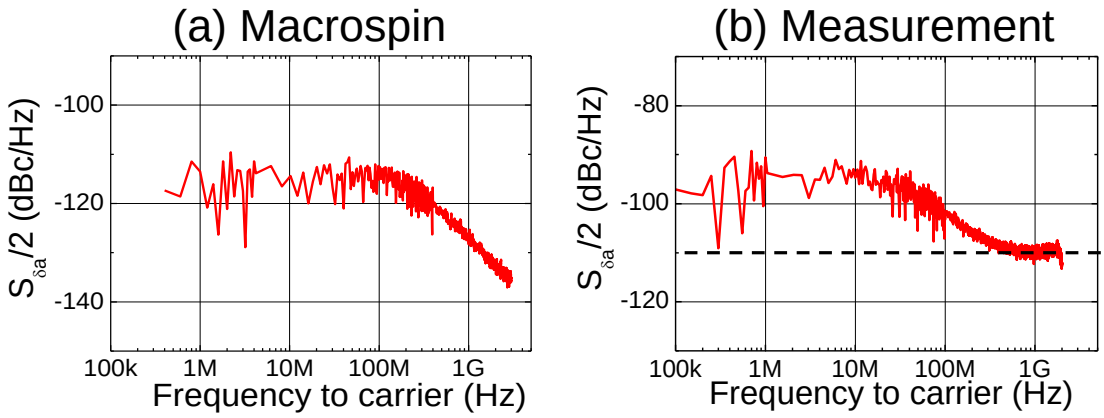

Fig. 4.19: (a) Amplitude noise extracted from a macrospin simulations. (b) Amplitude noise extracted from a real measurement. In the macrospin simulation, there is no thermal noise floor background (the dashed line in experimental results).

4.2.2.2 Influence of thermal Johnson-Nyquist noise in Amplitude noise measurements

Before extracting the prefactor of the amplitude noise correlation function $\mathcal{K}_{\delta a}$, it is worth pointing out that an additional white noise is observed experimentally in comparison to macrospin simulations. This noise provides an additional contribution at $\tau = 0$ for $\mathcal{K}_{\delta p}$ (see black points in Fig. 4.16-a) or a thermal noise floor in $S_{\delta p}$ (see dashed line in Fig. 4.16-b).

To identify this noise, we now consider our measurement setup that is composed of: (i) the resistance of the MTJ, R_{MTJ} and (ii), the amplifier with a gain G and a noise factor F with a bandwidth B. It implies that the total electrical noise power generated by the structure, and measured by the SSO, is given by [82]:

$$S_{\mathrm{noise}} = \frac{R_{\mathrm{MTJ}}^2}{(R_{\mathrm{MTJ}} + R_{50\Omega})^2} \times 4k_B G T_0 F R_{50\Omega} \approx 2.2710^{-14}\mathrm{V}^2/\mathrm{Hz}\ , \tag{4.14}$$

where F (= 2.5 dB) and G(= 43 dB) are expressed in linear units, $T_0 = 300$ K and $R_{\mathrm{MTJ}} = 560\ \Omega$. It follows, with a signal peak value of 20 mV measured on the SSO [86], that $S_{\delta p}/p_0 \approx -105$ dBc/Hz. From this, we consider that the noise floor of our measurement is given by the electrical Johnson-Nyquist noise generated by the resistance of our MTJ. This is consistent with macrospin simulations in Fig. 4.19, where no such electrical noise floor is found for $S_{\delta a}$ (compare high frequency noise in Fig. 4.19-a with Fig. 4.19-b).

4.2.2.3 Extraction of Δf_0 from amplitude noise

Following this comment, we extract the amplitude noise variance $\Delta f_0/f_p$ by the fit of the autocorrelation function Eq. 4.9 and not by fitting the width of the amplitude distribution. Indeed, while the width of the amplitude distribution is given by the *measure* of $\mathcal{K}_{\delta a}(\tau = 0)$ (black dot in Fig. 4.16-a), the *most accurate* value of the amplitude noise variance is given by the fit of the full autocorrelation function of amplitude fluctuation, i.e. by a

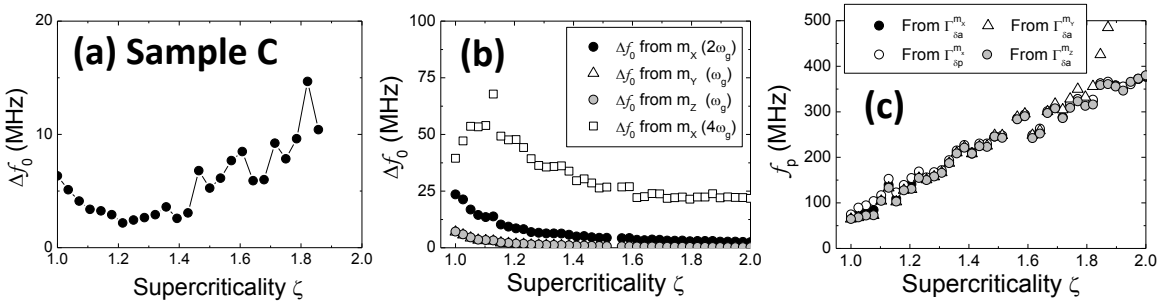

Fig. 4.20: (a) Extraction of Δf_0 versus ζ from amplitude noise of Sample C. (b) Extraction of Δf_0 versus ζ from amplitude noise on different harmonics (number in parenthesis) from macrospin simulations. (b) Extraction of Γ_p/π from amplitude noise from different magnetization components of the macrospin simulations. The extraction of Γ_p is independent from the harmonic or coordinate considered. Γ_p extracted from power or amplitude fluctuations give the same results.

linear extrapolation to $\tau = 0$ in Fig. 4.16-a (about a half of the value marked by the black dot in Fig. 4.16-a).

Fig. 4.20-a shows the extraction of Δf_0 for sample C considering the amplitude noise only (Eq. 4.9). We see that Δf_0 increases with ζ from $\Delta f_0 \approx 5$ MHz at $\zeta = 1.2$ ($\Delta f_1 \approx 100$ MHz) to $\Delta f_0 = 15$ MHz at $\zeta = 1.8$ ($\Delta f_1 \approx 150$ MHz). We can attribute the large value of Δf_0 at the vicinity $1 < \zeta < 1.2$ and the subsequent decrease to the proximity of the Hopf bifurcation (around $\zeta \approx 1$, amplitude fluctuations can be very large, ranging from $p = 0$ to $p = p_0(\zeta)$). In the literature, Nagasawa et al. [77] performed an amplitude noise study with TDNS. From the variance of the power distribution one can estimate that in their experiment $2\Delta f_0$ is about 6 MHz, for a total peak linewidth of 46 MHz[10]. In the experiment of Bianchini et al. [78], $2\Delta f_0 \approx 50$ MHz, for a mode linewidth of 50 MHz[11]. Therefore, the value $\Delta f_0 \approx 5 \sim 20$ MHz we have obtained is in the range of magnitudes expected from other works in literature that aimed to extract Δf_0.

Fig. 4.20-b shows the extraction of Δf_0 from the autocorrelation function Eq. 4.9 of each component of the magnetization from macrospin simulations. We also compare the value of Δf_0 extracted from the fourth harmonic, i.e. the second harmonic in the m_X time trace. We see that, depending on the magnetization component considered, the value of the extracted Δf_0 varies much at a given ζ. The question is now to figure out whether this extraction makes sense or not. The answer is probably no, since the harmonics do not represent necessarily the full stochastic properties of the magnetization (see discussion in the above section 4.2.1). To really confirm the trends between measurements and simulations it would require to perform the transformation of the magnetization trajectories as explained above. This would lead to a correct extraction of Δf_0 and that would probably help to better understand what to expect from Δf_0 versus ζ. Nevertheless, this would only be possible in macrospin simulations, as discussed in the above section 4.2.1 since in experiments, only the projection of the magnetization on the

[10]Nagasawa et al. only focused on power fluctuation variance in Ref. [77], with $\Gamma_p = 0.2$ ns^{-1} [76], we obtain this value of Δf_0.

[11]In the introduction, we have already discussed that this result was consistent with Γ_p/π smaller than the linewidth value.

polarizer direction is measured. We propose in section 4.2.4.3 and 4.4 other techniques that give other measurements of Δf_0.

Still, the relaxation constant f_p is independent of the strength of the fluctuation (i.e. the value of Δf_0). It implies that Γ_p can be extracted from the study of any harmonics of the signal and will be the same. Fig. 4.20-c shows this property on the three different coordinates m_x (that "oscillates" at $2\omega_g$ and $4\omega_g$), m_y and m_z (that "oscillate" at ω_g). Fig. 4.20-c also shows that the power fluctuations δp and amplitude fluctuations δa give the same f_p value.

In conclusion, the study of amplitude fluctuations allowed us to extract the key parameters Γ_p and Δf_0. Δf_0 gives information on the noise strength acting on the system and can be extracted from amplitude fluctuations of the oscillating signal output of the STOs. Nevertheless, the obtained value is subject to discussion and the extraction method. Γ_p gives the rate of energy exchange with the thermal bath (and spin polarized current flow) in the nonlinear regime. The demonstration of the existence of the relaxation phenomenon, required to stabilize an auto-oscillation regime, and is in qualitative and in quantitative agreement with the KTS model. This parameter Γ_p is of main importance for potential applications of STOs in real RF devices. Its role is essential for applications of STOs and f_p will be the main focus of the part III of this thesis (chapters 5 and 6).

The next section is dedicated to information that can be obtained from the phase noise study.

4.2.3 Phase Noise of the Free Running STO

In the previous section we have analyzed in detail all information that can be obtained from the study of amplitude/power fluctuations from TDNS. We now focus on information that can be obtained from the study of the phase noise. Contrary to the below-threshold regime, the spectral purity of the STO is driven by the phase noise in the above threshold regime.

When the amplitude noise is not supposed to influence directly the spectral purity [54, 42], the autocorrelation function $\mathcal{K}_c(\tau)$ of the c-variable is given by:

$$\mathcal{K}_c(\tau) \approx p_0 e^{i<\phi(\tau)-\phi(0)>} \exp[-\Delta\phi(\tau)^2/2]. \tag{4.15}$$

The quantity $< \phi(\tau) - \phi(0) > / \tau$ is the mean angular frequency of the auto-oscillation, ω_g. Here $\Delta\phi^2(\tau)$ is the time varying phase variance that is derived from the phase variance equation. The phase variance Eq. 2.47 can be derived from the Eq. 2.35:

$$\Delta\phi^2(\tau) = 2\pi\Delta f_0\tau + 2\pi\Delta f_0\nu^2\left[\tau - \frac{1-e^{-2\Gamma_p\tau}}{2\Gamma_p}\right], \tag{4.16}$$

with $\nu = Np_0/\Gamma_p$, the dimensionless nonlinear amplitude phase coupling. The first term of the RHS is called the linear contribution of the phase noise. The second term is the nonlinear contribution of the phase noise and is originating from the nonlinear amplitude-phase coupling, i.e. it originates from amplitude noise. When this nonlinear contribution is neglected, $\Delta\phi^2(\tau) = 2\pi\Delta f_0\tau$, Δf_0 is thus the "linear" linewidth of the STO. From the phase equation in Eq. 4.7, one can define the PSD S_ϕ of phase fluctuation ϕ:

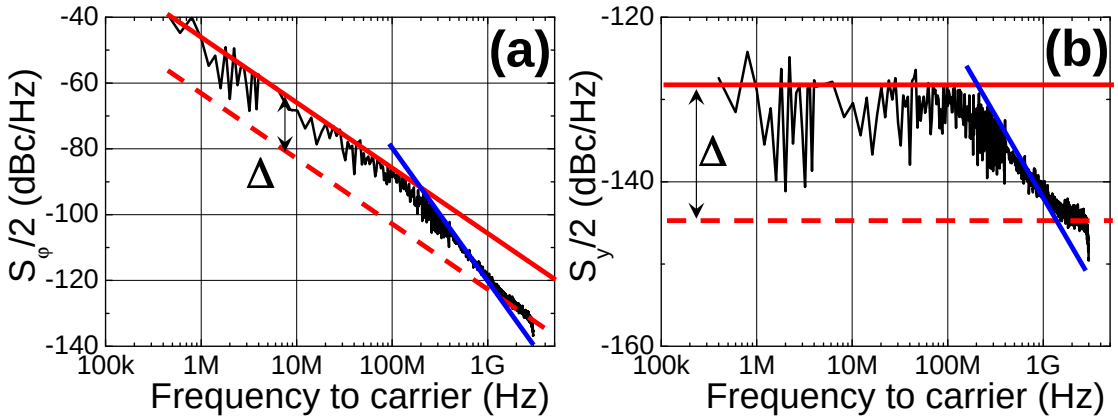

Fig. 4.21: (a) Phase noise plot obtained from macrospin simulations for $\zeta = 1.43$. The nonlinear contribution and linear contribution are represented by the red solid and dashed lines respectively. The red lines have a slope of -20 dB/decade, while the blue line has a slope of -40 dB/decade. (b) S_y plot. Since $S_y \propto f^2 S_\phi$, the $1/f^2$ slopes of S_ϕ become flat in log-log plots. Transitions are well identifiable.

$$S_\phi(f) = \frac{\Delta f_0}{\pi f^2} + \frac{\Delta f_0}{\pi f^2} \frac{\nu^2 f_p^2}{f_p^2 + f^2} \,, \tag{4.17}$$

We can identify two different noise contributions in S_ϕ. Correspondingly, the left term of the RHS of Eq. 4.17 is the linear contribution to the phase noise, while the right term of the RHS is the nonlinear contribution to the phase noise. While the linear contribution is the direct effect of noise on the phase term, the nonlinear contribution is the noise on the phase term originating from the amplitude fluctuations. Since the frequency depends on the amplitude of the auto-oscillation (i.e. STOs are non-isochronous oscillators), it naturally induces this "nonlinear" contribution.

Fig. 4.21-a shows a typical phase noise plot for a macrospin time trace (from m_x at $\zeta = 1.43$). From it, three trends of the phase noise can be found. Again, we can discuss the high, intermediate and low frequency limits of Eq. 4.17:

$$\begin{cases} S_\phi \approx \frac{\Delta f_0}{\pi f^2}(1+\nu^2) & \text{For } f < f_p \\ S_\phi \propto \frac{1}{\pi f^4} & \text{For } f_p < f < f_p\sqrt{\nu^2-1} \\ S_\phi \approx \frac{\Delta f_0}{\pi f^2} & \text{For } f > f_p\sqrt{\nu^2-1} \end{cases} , \tag{4.18}$$

which are equivalent to three different slopes in a log-log plot of S_ϕ (as shown in Fig. 4.21-a).

It is also possible to perform the PSD of the relative frequency fluctuation $y(t)$ (see Eq. 3.17 in section 3.2.2), where the slope changes can be better identified (see Fig. 4.21-b). When increasing the frequency, a first slope change appears around $f_p = 220$ MHz. This change can be easily understood as the roll-off of the amplitude fluctuations already discussed.

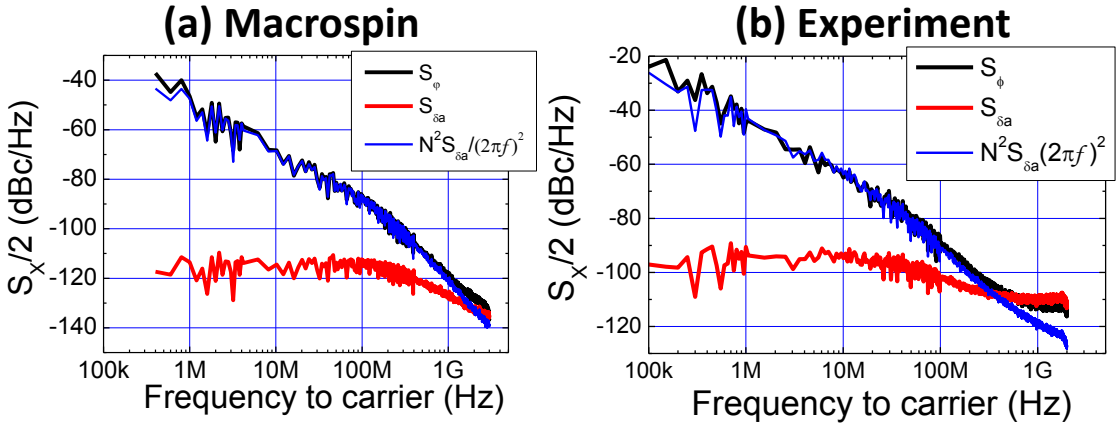

Fig. 4.22: Phase (in black) and amplitude (in red) noise PSD for a macrospin simulation (a) and experiment (b). The blue curve is computed from the amplitude noise (arbitrary chosen N). This blue curve corresponds to the nonlinear contribution of the phase noise. We see that this noise contribution falls "below" the "linear" contribution of the phase noise (around 1 GHz) in macrospin simulations. Experimental results from sample D, details can be found in [76].

Indeed, from $f = 0$ Hz to $f = f_p\sqrt{\nu^2 - 1}$, the phase noise is given by the "nonlinear contribution". The nonlinear contribution is the amplitude noise that is integrated in the phase noise. As seen in Fig. 4.22-a for macrospin simulation, the phase noise coming from the amplitude noise is the main contribution to phase noise. It is also seen experimentally in Fig. 4.22-b. In consequence, we say that the linewidth (the spectral purity) is dominated by the nonlinear contributions/effects in the above-threshold regime. Indeed, we have seen from Fig. 4.18 that $f_p > \Delta f$, the frequency $f = \Delta f/2$ lies in the regime where the nonlinear contribution of the phase noise is still dominant[12]. The "linear" contribution (dashed lines in Fig. 4.21-a,b) is almost 20dB below the "nonlinear" contribution (full lines in Fig. 4.21-a,b). The "linear" contribution refers to the direct contribution of the thermal noise on the phase noise. In contrast to the "nonlinear" or indirect contribution, that is the phase contribution of amplitude noise. It is clear with this picture that the low frequency phase noise, or the phase variance at long timescales, is fully correlated to the amplitude noise. The high frequency phase noise ($f >> f^p$), is independent of the amplitude noise. Γ_p distinguishes the two contributions.

If we now compare the limiting behavior, it appears that the nonlinear parameter ν can be obtained directly from the phase noise plots. Indeed, the difference Δ in the log-log plot of the phase noise, as drawn in Fig. 4.21, is the ratio of the two limiting trends with a f^{-2} slope in S_ϕ or f^0 in S_y. It is straightforward to see from Eqs. 4.18 that $\Delta = 1 + \nu^2$. In Fig. 4.23, the nonlinear parameter ν extracted in this way is given as a function of ζ for both macrospin and measurements[13]. We see that its typical value is about $|\nu| \sim 5.5$ in macrospin and $|\nu| \sim 2$ in experiments, and that in both cases, $|\nu|$ tends to decrease with increasing ζ.

[12]Except in the case of Bianchini et al. [78] (we often refer to this measurement since it is the only one to compare with in literature).

[13]The sign of ν can be determined by the frequency shift (redshift or blueshift) observed with current. In the case of IPP mode, $\nu < 0$.

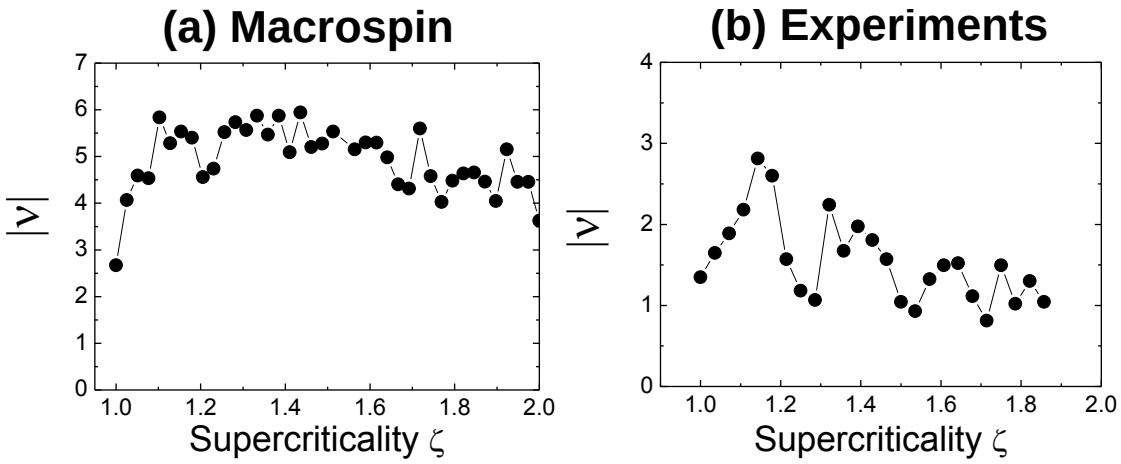

Fig. 4.23: Dimensionless nonlinear phase-amplitude coupling parameter ν extracted by phase noise plots from (a) macrospin simulations and (b) experimental results on Sample C.

We should note that the thermal noise floor affects the determination of the linear contribution of the phase noise experimentally and therefore Δ. Since it is impossible to get rid of this noise (it originates from electrical Johnson-Nyquist noise), the extraction of $|\nu|$ is limited to the fact that at high f S_ϕ is hidden by the setup noise.

For MTJs[14], another available method to extract ν in the free running regime has been given in Ref. [80] and reminded in the introduction section 2.2.3. It consists in identifying the sub- and above- threshold regimes and distinguishing the two different associated power dependencies of the linewidth. It supposes actually that ν, Δf_0 and the damping rate are constant along ζ. The method is shown in Fig. 4.24, where from the ratio of the slopes $S^>$ and $S^<$, we obtain $|\nu| = \sqrt{2S^>/S^< - 1} \approx 2.32$. This value is similar to the one extracted from TDNS. This determination of $|\nu|$ from two independent techniques (one uses time domain signal at a given ζ, the other uses frequency domain data from the overall trend) confirms the validity of both approaches.

In conclusion, the KTS model together with the phenomenological description of the noise (see chapter 2) is able to predict the noise properties of spin torque auto-oscillators. In the next section, we engage a discussion on the consequence on the FWHM measured in STOs by means of spectrum analyzer from the phase variance equation.

4.2.4 FWHM in the case of non-isochronous auto-oscillator

4.2.4.1 Analytical expression of the FWHM

We have given the expression of the phase variance in the case of a non-isochronous auto-oscillator (see Eq. 4.16), and we focus now on its link with the FWHM. Since the phase variance is not linear in time, the shape of the PSD of the resulting signal is not Lorentzian. Indeed, to be Lorentzian, the autocorrelation function of the signal (see Eq. 4.15) must be a pure first order exponential decay with time. Second order exponential decay (e.g. e^{-t^2}) provides a Gaussian function of the PSD of the signal.

[14]The technique developed by Boone et al. [79] for GMR spin-valves is very dependent on the structures studied and it requires many assumptions in order to extract p and Γ_p.

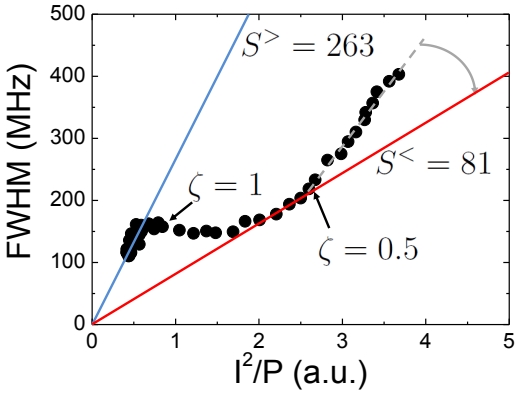

Fig. 4.24: Linewidth versus inverse oscillation power for sample C. From the inverse power dependence of the linewidth, we have seen in section 4.2.1 that below $\zeta = 0.5$, the inverse power was underestimated. The increase of I^2/P for $\zeta > 1.6$ noted in section 4.2.1 does not affect the determination of $S^>$.

Using the full $\Delta\phi^2(\tau)$ expression, no analytical solution of the FWHM exists. However, one can consider the "limiting" cases of the FHWM (see for example the model from Kudo et al. [80] used previously), depending on the timescales in Eqs. 4.18 (with $|\nu| > \sqrt{2}$):

$$\begin{cases} \Delta f \approx 2\Delta f_0(1+\nu^2) & \text{For } \frac{1}{\Delta f} > \frac{1}{f_p} \\ \Delta f \approx |\nu|\sqrt{2\Delta f_0 \Gamma_p} & \text{For } \frac{1}{f_p} > \frac{1}{\Delta f} > \frac{1}{f_p\sqrt{\nu^2-1}} \\ \Delta f \approx 2\Delta f_0 & \text{For } \frac{1}{\Delta f} < \frac{1}{f_p\sqrt{\nu^2-1}} \end{cases} . \tag{4.19}$$

From Fig. 4.18, we see that the approximation $\Delta f \approx 2\Delta f_0(1+\nu^2)$ is only correct for $\zeta > 1.6$. Moreover, it corresponds to a limiting behavior and not to an exact solution; $\Delta f \approx 2\Delta f_0(1+\nu^2)$ is satisfied only if the inequalities in Eq. 4.19 are large (i.e. $\frac{1}{\Delta f} > \frac{1}{f_p}$).

In the following, we give a "phenomenological" means to extract the FWHM from the time varying variance as suggested by V. Tiberkevich [136]. We can consider that, when the time varying variance is equal to 2π, the correlation time τ corresponds to the inverse value of the FWHM. While this statement is exact for the case of Lorentzian shape, i.e. $\Delta\phi^2(t) \propto t$, it only gives a relative error less than 6% in the case of a Gaussian shape, i.e. $\Delta\phi^2(t) \propto t^2$.

A qualitative argument for this phenomenological consideration is the following. The FWHM physically represents our uncertainty to locate the mean frequency of the oscillation such that there are equal "chances" that the oscillation frequency is $f = f_g + \Delta f/2$ or $f = f_g - \Delta f/2$. In other words, the total phase diffuses "on average" between a signal at frequency $f = f_g + \Delta f/2$ and the one at frequency $f = f_g - \Delta f/2$. After the time $1/\Delta f$, a signal whose frequency is $f_g \pm \Delta f/2$ will be phase shifted by π compared to the signal of frequency f_g. If now, we consider our signal, the phase noise is "on average" about 2π or $\mp\pi$ after having spent the time $1/\Delta f$. Since the phase variance represents the "average" amount of phase deviation with time, we can write:

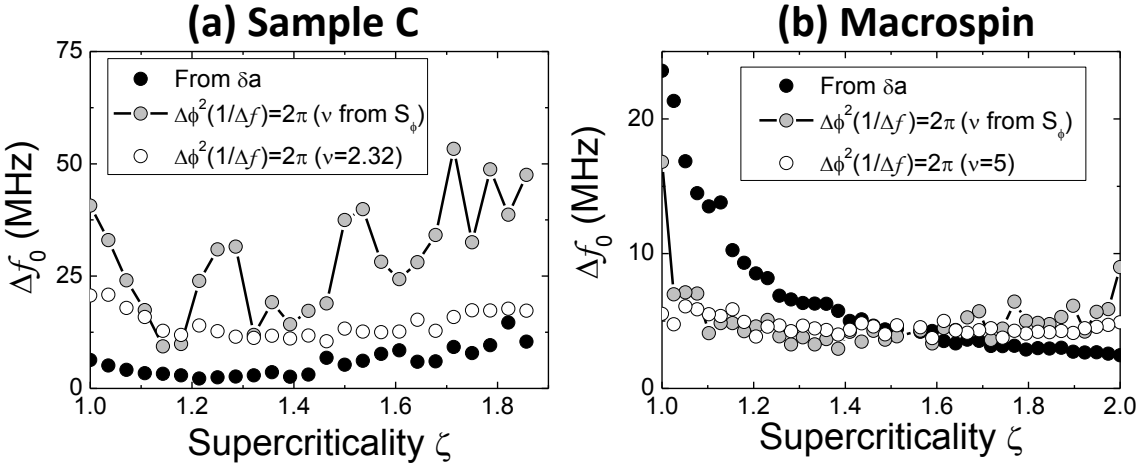

Fig. 4.25: (a) Comparison of the values of Δf_0 versus ζ obtained by different techniques on Sample C. From the amplitude noise variance (black dots), resolving Eq. 4.20 with ν extracted from the phase noise plots (gray dots) and $\nu = 2.32$ extracted from the Kudo's technique found in Ref. [80] (open dots). (b) Similar comparison on macrospin simulations. $\nu = 5$ corresponds to the mean value obtained from the analysis of phase noise plots.

$$\Delta^2\phi(1/\Delta f) = 2\pi \ . \tag{4.20}$$

This equation defines the FWHM of a given signal expressed by its autocorrelation function of the form of Eq. 4.15. Eq. 4.20 is general, and independent of the value taken by Δf_0, ν and Γ_p. When taking an infinite number of realizations of the phase of our STO and $\phi_{0\leq i\leq\infty}(\tau)$, the width of the distribution of the phases $\phi_{0\leq i\leq\infty}(1/\Delta f)$ is 2π; Eq. 4.20 is the exact meaning of phase variance $\Delta\phi^2(\tau)$ for $\tau = 1/\Delta f$.

It makes this expression much more useful than Eq. 4.19 and provides an analytical expression to extract the FWHM.

4.2.4.2 Signal FWHM Δf and linear HWHM Δf_0

In sections 4.2.2 and 4.2.3, we have shown how to extract Γ_p and ν from phase and amplitude noise. With Eq. 4.20 it is also possible to extract Δf_0, since Δf is known.

Fig. 4.25 shows the extraction of Δf_0 from Eq. 4.20 in both experimental results (Fig. 4.25-a) and macrospin simulations (Fig. 4.25-b) using different assumptions for the value of the dimensionless nonlinear parameter ν. Indeed, we have experimentally measured that ν depends on the supercriticality ζ via S_ϕ, and we also extracted the value of $\nu = 2.32$ from Δf versus $1/p_0$ dependence. Therefore, experimentally, we reproduce these two cases for the extraction of Δf_0 from Eq. 4.20. We have also observed a similar decrease of $|\nu|$ with ζ in macrospin simulations, to compare with a ν independent of ζ, we also extract Δf_0 in macrospin simulations assuming that $\nu = -5$ over the whole range of supercriticality.

The first comment is that the HWHM Δf_0 is indeed on the order of MHz as expected from theory [48] and our previous measurement from amplitude noise in section 4.2.2.3 (black dots in Fig. 4.25). The second comment is about the trend of Δf_0 versus ζ: *is it*

an increasing or a constant value versus ζ? From Fig. 4.25, we see that it depends on the assumption made on ν. Indeed, if the decrease of $|\nu|$ with ζ from Fig. 4.23 is confirmed and real, then the increase of Δf_0 with ζ exists. If we consider a constant value for ν, Δf_0 seems constant over ζ. This trend is well reproduced in both experimental results and macrospin simulations. While in macrospin simulation, the increase of Δf_0 with ζ is not clear.

4.2.4.3 Discussion on Δf_0 parameter

The variation of Δf_0 with ζ (or p) is of main importance. In the KTS model, the diffusion "constant" is nonlinear (see Eq. 2.43):

$$D_n(p) = \Gamma_+(p)\eta(p) = 2\Delta f_0(p)p \ , \tag{4.21}$$

such that, in presence of STT and in the nonlinear regime ($p > 0$), the noise strength acting on the system in its nonlinear regime ($p > 0$) is not the same as the noise strength acting on the system at equilibrium ($p = 0$). Brown's model [33] involves applying the fluctuation-dissipation theorem to a magnetic particle at equilibrium (static state), while the KTS model extends this concept to the out-of-equilibrium state.

We recall here the origin of $D_n(p)$ in the case of the KTS model. In the presence of thermal noise k_bT, the oscillator "state", such as any system, is spread, with a diffusion constant D given by the Einstein-Smoluchowski relation:

$$D = \mu k_b T, \tag{4.22}$$

with $\mu = v_d/F$ being the mobility of the particle in the context of Brownian motion, i.e. its sensitivity to the noise, where v_d is the drift velocity and F the force strength that drives the particle motion. While it is not clear how to identify qualitatively those quantities in our system (we have an angular motion and not a linear motion), the diffusion constant found in the KTS model is written:

$$D(p_0) = \frac{\Gamma_+(p_0)}{\lambda\omega(p_0)} k_b T. \tag{4.23}$$

Interestingly, if we identify all terms from the Einstein-Smoluchowski equation, we can probably anticipate that $v_d \sim \Gamma_p(p_0)$ instead of $\Gamma_+(p_0)$ since the drift velocity around the system energy p_0 has been identified as the restoration rate Γ_p. This "phenomenological argument" is not in contradiction with the original proof of the KTS model, since one can show that when identifying Eq. 4.23 with the Boltzmann distribution of power, the restoration rate (at the equilibrium) is $\Gamma_+(0) = 2\Gamma_G$.

By now, it is hard to draw any conclusions since the contradictory results on the variation of Δf_0 over ζ cannot lead to a straightforward conclusion regarding the strength of the noise from our measurements or simulations. Only a decrease of Δf_0 versus ζ would possibly lead to $D_n(p) \approx$ constant for $p > 0$. The fact that the diffusion constant D_n is not a constant when increasing the bias current makes already a "physical" representation of its meaning difficult.

Finally, we would like to comment on the numerous successful examples of the Fokker-Planck equation applied to predict the switching of the magnetization under the

combined influence of spin transfer torque and thermal fields. All those theories assume a constant diffusion "constant" D in agreement with Brown's model [33] (and therefore those examples are well verified by macrospin simulations including a Brown thermal fluctuation field Eq. 1.13 in section 1.2.3). To open the discussion on this "phenomenological" model of the noise, we quote the introduction of the paper by Brown from 1963 [33]:

> "This problem [the magnetization behavior under the influence of a thermal bath] can be approached through simplifications that have proved successful in the theory of the Brownian motion and other stochastic processes. The most important simplification is the assumption that the random thermal forces have a correlation time much shorter than the response times of the system (e.g,. of the Brownian particle). This simplification makes possible the replacement of an integral equation (the Smoluchowski or Chapman-Kolmogoroff equation) by a partial differential equation (the Fokker-Planck equation). In effect, it reduces the random forces to a "purely random" process, with a "white" spectrum. According to the quantum-mechanical Nyquist formula, the spectrum of thermal agitation forces may be regarded as white up to a frequency of order of $kT/h(\approx 10^{13}$ $\sec^{-1}$ at room temperature); this corresponds to correlation times of the order 10^{-13} sec."

It opens some questions about the model of the fluctuations themselves when applied to the power oscillation fluctuations. We have previously highlighted the different formulation from the Smoluchowki approach and the Fokker-Planck one in the KTS model presented in chapter 2, without any further proofs. When the temperature decreases, is the "thermal" noise still "white"? Also, considering that $\Delta p_0/p_0$ can be large (see Fig. 4.13), is the approximation of the non-stationary process $\sqrt{p(t)}f_n(t) \approx \sqrt{p_0}f_n(t)$ physically correct?

Those questions are beyond the scope of this thesis. However, we will keep in mind the interrogation of the "whiteness" of the noise when presenting the results on experimental measurements of the temperature dependence of STO noise properties and their comparison with the macrospin model (that assumes the "whiteness" of the thermal noise for all temperatures).

4.3 Conclusion on the systematic comparison of KTS theory to experiments

We have seen how, from TDNS, that it is possible to extract the key parameters that govern the dynamics of the magnetization in the nonlinear regime under spin-polarized currents. We described the KTS model in the light of our experimental and macrospin simulation results. We have explained the two limiting behavior of the STO. In the below-threshold regime, the STO is a simple harmonic oscillator whose spectral purity is driven by the amplitude relaxation only. When it enters the nonlinear regime ($\zeta \approx 0.9$), the damping and anti-damping terms become nonlinear.

Slightly above the threshold ($\zeta \approx 1.1$), a nonzero power p_0 is stabilized due to the compensation of the damping and the anti-damping term. We have verified that any

fluctuations around p_0 are stabilized by the amplitude restoration rate Γ_p. The major effect of this parameter has been identified as the timescale required to exchange energy with the thermal bath or spin-polarized current flow. This property will be the subject of the chapter 5.

The fluctuations around this mean power of oscillation induces a nonlinear contribution to the phase noise. In simulations and in experiments, we found that this nonlinear contribution enhances the phase noise above the linear contribution: the system nonlinearities provide a substantial linewidth broadening. This phenomenon is solely due to the non-isochronous nature of the STO; their auto-oscillation frequency is strongly dependent on the power of oscillation. It leads to the definition of the dimensionless nonlinear amplitude phase coupling parameter $|\nu|$ which has been extracted here.

Finally, the KTS model includes a Fokker-Planck formalism for the auto-oscillating state. From this formalism the diffusion constant $D \propto \Delta f_0$ is extracted. Since the TDNS technique allows to provide a tool to study the variation of the nonlinear parameters Γ_p, ν and Δf_0 versus ζ, we found some unexpected results such as a nontrivial (unexplained) dependence of ν and Δf_0 versus ζ in both macrospin and experiments. We discuss in more detail this question in the next section, where a novel independent extraction technique of these parameters is developed. We will not answer definitively the question of the model validity, but we will rather give a "nonlinear" solution of the STO in presence of noise. Indeed, our main problem in the TDNS technique is that the diffusion of the noise into the harmonics of the signal remains unclear since no canonical transformation is possible experimentally. In fact, the presence of harmonics is the signature of the nonlinear behaviors of the STO. The next section aims to give insight on the full analytical solution of the magnetization dynamics under a spin polarized current.

We would like to end this summary by listing the points we have highlighted during the systematic study of experimental measurements and macrospin simulations from TDNS and KTS theory:

- The results from the TDNS technique show a good agreement between experiments and KTS model in the below- and the above-threshold regime.

- Experimental data available from the magnetoresistance of the device do not allow a systematic comparison to the KTS model concerning amplitude variance, because of the canonical transformation involved in the KTS model.

- Simultaneous studies of amplitude and phase fluctuations allow the subtle interplay/coupling in the magnetization dynamics to be described in detail.

- From the TDNS technique, one is able to extract Γ_p, and to have a reliable measure of ν.

- Δf_0 can be extracted both by the analysis of the variance of amplitude fluctuations and by the analysis of the phase noise. Both approaches lead to inconsistent results.

- Finally, the TDNS analysis leads to a probable power dependence of the non linear parameter $\nu(p)$ and $\Delta f_0(p)$.

4.4 Study of Δf of higher harmonics

We have highlighted the problem of the canonical transformation required by the KTS model. This model assumes that the signal in c-variable is mono-chromatic, i.e. has only one harmonic component. We therefore put forward this argument as a possible cause of the divergence between our experimental results and the KTS model. We can consider this section as a renormalization of our (multi-harmonic real) signal to the canonical transformed c-variables of the KTS model. Here we use this discrepancy as a tool to extract the nonlinear parameters ν, Γ_p and Δf_0.

The LLGS equation is a system of nonlinear differential equations. In particular, the norm of the magnetization is constant:

$$M_x^2 + M_y^2 + M_z^2 = M_s^2 \ . \tag{4.24}$$

We consider the case where the magnetic field is applied along the direction of M_x (IPP case). Because of the norm conservation, Eq. 4.24, we can do a Taylor expansion:

$$M_x/M_s = 1 - \frac{1}{2M_s^2}(M_y^2 + M_z^2) - \sum_{n=2}^{\infty} \frac{(-1)^n(2n)!}{(1-2n)(n!)(4^n)M_s^n}(M_y^2 + M_z^2)^n \ , \tag{4.25}$$

since $(M_y^2 + M_z^2) < M_s^2$. If now we consider an oscillating solution, i.e. $M_y(t) = M_y^0 \cos(\omega t + \phi_y^0)$ and $M_z(t) = M_z^0 \cos(\omega t + \phi_z^0)$, one obtains:

$$\begin{aligned} M_x(t)/M_s \approx 1 &+ A\cos(\phi_y^0 - \phi_z^0) + B\cos(2\omega t + \phi_y^0 + \phi_z^0) \\ &+ \sum_{n=2}^{\infty} C_n \cos[n(2\omega t + \phi_y^0 + \phi_z^0)] + D_n \cos[n(\phi_y^0 - \phi_z^0)] \ , \end{aligned} \tag{4.26}$$

where A, B, C_n and D_n are constants given by M_z^0 and M_y^0. Interestingly, it generates a signal at "zero" frequency and twice the mode frequency.

The aim of this section is to take advantage of this nonlinear property (Eq. 4.25) of the LLGS equation to extract noise properties in signal harmonics. It is to note that the different canonical transformations introduced in section 2.2 aimed to get rid of this higher order polynomial terms of the magnetization coordinates in Eq. 4.25. Here we demonstrate that there is a difference between *isochronous* and *non-isochronous* auto-oscillators in the linewidth values of higher generation harmonic due to the nonlinearity of the generation frequency in the latter case. Then, it is demonstrated how this difference provides an alternative method to the TDNS technique to determine the intrinsic nonlinear parameters of the auto-oscillator, such as the nonlinear coefficient of linewidth broadening ν and the damping rate of the amplitude fluctuations Γ_p, that determine the non-autonomous auto-oscillator dynamics. Also, it provides a measurement of the linear linewidth Δf_0 that is independent of Γ_p and ν.

4.4.1 Model description

The general theory of linewidth for an *isochronous* auto-oscillator was developed in [42, 137]. It was shown in [137] that the phase variance $\Delta\phi^2$ of an auto-oscillator increases

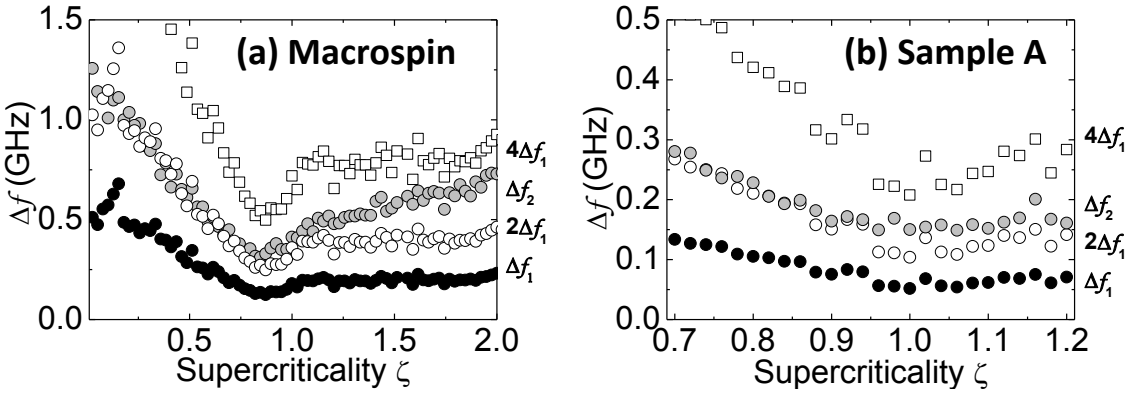

Fig. 4.26: FWHM Δf_1 and Δf_2 extracted from PSDs (a) for macrospin simulations and (b) for experiments on MTJs (sample A). In the simulations the even (odd) harmonics were obtained from the PSD of the in-plane magnetization parallel (perpendicular) to the static equilibrium orientation. In (a) and (b) the Δf_2 values (gray circles) are compared with $2\Delta f_1$ (open circles) and $4\Delta f_1$ (open squares).

linearly with time τ ($\Delta\phi^2 \sim \tau$, corresponding to a "random walk" of phase), and that the generation line has a Lorentzian shape. Considering that the phase variance of the nth harmonic is given by:

$$\Delta\phi_n^2 = n^2\Delta\phi, \tag{4.27}$$

and, since the phase undergoes a "random walk" in the *isochronous* case ($\Delta\phi^2 \sim \tau$), it results that the spectrum of the nth *isochronous* auto-oscillator harmonic has a Lorentzian shape with the linewidth [137]:

$$\Delta f_n^{iso} = n^2\Delta f_1^{iso}\,, \tag{4.28}$$

which is n^2 times larger than the fundamental linewidth Δf_1^{iso}.

We would like to note that the linewidth of the nth harmonic in a *passive (damped) isochronous resonator*, or harmonic oscillator, is determined by a different relation:

$$\Delta f_n^{res} = n\Delta f_1^{res}\,, \tag{4.29}$$

and is only n-times larger than the passive resonator linewidth Δf_1^{res} determined by the resonator damping (as shown earlier for $\zeta < 1$).

In the case of a *non-isochronous* auto-oscillator [54] the shape of the generation line becomes non-Lorentzian [38], and the phase variance of the main frequency is a nonlinear function of τ (see Eq. 4.16). As such, the expression 4.28 will not hold in the non-isochronous case and the main goal here is to find a correct description for linewidth of the nth harmonic in a STO.

First of all, to illustrate the importance of this problem we demonstrate that the linewidth of higher harmonics in STOs, indeed, deviates substantially from the classical relation 4.28 established in Ref. [137]. In Fig. 4.26 we present the linewidth of a main auto-oscillation mode Δf_1 (black filled circles) and the linewidth of its second harmonic Δf_2 (gray filled circles) measured experimentally on sample A as a function of the

supercriticality parameter ζ. In the same figure, we show for comparison values of $2\Delta f_1$ (open circles) and $4\Delta f_1$ (open squares). The experimental linewidths were obtained from the Lorentzian fits of the power spectral density (PSD) of the magnetoresistive voltage signal acquired in the frequency domain.

The behavior of the linewidth Δf_2 of the second harmonic in our "macrospin" simulations (see Fig. 4.26-a) is qualitatively similar to the behavior of Δf_2 in the experiment (see Fig. 4.26-b) in both the subcritical and supercritical regime. In particular the second harmonic Δf_2 of the second harmonic in the subcritical regime ($\zeta < 1$) (or *harmonic oscillator*) regime practically coincides with $2\Delta f_1$.

For $\zeta < 1$, the FWHM of the first harmonic corresponds to half the FWHM of the amplitude/power signals, which is the energy dissipation rate of the system. The energy dissipation rate is independent of the harmonic considered (see Fig. 4.20-c) as demonstrated elsewhere [136]. Therefore considering the signal $c_n(t)$ of the nth harmonic ($c_n(t) = c_1^n(t)$ with $c_1(t)$ the solution of the Eq. 4.1), one obtains:

$$\mathcal{K}_n(\tau) =< c_n(t)c_n^*(t+\tau) >= n!c_0^n \exp[in\omega_0\tau - n\Gamma_s\tau] \,, \tag{4.30}$$

where the mode amplitude c_0 is proportional to the noise power.

Two important properties follow from this equation. The first is that in the subcritical regime $\zeta < 1$ the lineshape of the main mode and all its harmonics are Lorentzian[15] and that the corresponding linewidth of the nth harmonic is related to the linewidth of the main mode by Eq. 4.29. This theoretical result is confirmed by both simulations and experiment shown in Fig. 4.26 for the second harmonic. Here, it is clear that Eq. 4.29 holds up to the point $\zeta = 0.95$, where nonlinear terms in Eq. 4.1 become important (see also discussion in section 4.1.3). The second important property is that the fundamental linewidth is given by the amplitude relaxation rate with $\Delta f_1 = \Gamma_s/\pi \propto (1-\zeta)$. This result is confirmed by the almost linear decrease of the linewidth with ζ seen in Fig. 4.26 and has already been discussed in section 4.1.

For the auto-oscillation regime ($\zeta > 1$), it is clear from Fig. 4.26 that the linewidth of the second harmonic does not follow the predictions of the isochronous theory [137], and that the experimental and numerical ratios of the second harmonic to the fundamental mode are smaller than expected from Eq. 4.28, but larger than expected from Eq. 4.28, i.e. they lie in the interval $2\Delta f_1 < \Delta f_2 < 4\Delta f_1$. To understand the qualitative reason of this discrepancy we present below an analytical derivation of the higher harmonics linewidth in a general non-isochronous auto-oscillator that applies to STOs.

In the supercritical regime, when the oscillation power substantially exceeds the noise level (this condition is typically satisfied for $\zeta > 1.05$), the amplitude fluctuations do not contribute *directly* to the correlation function $K_n(\tau)$, and it is determined solely by the phase decoherence, $K_n(\tau) \propto exp(-n^2\Delta\phi^2)$. For a non-isochronous oscillator, however, the amplitude fluctuations change the phase dynamics through the nonlinear amplitude-frequency coupling (N or ν), and the phase variance $\Delta\phi^2$ is determined by Eq. 4.16.

The phase variance Eq. 4.16 is plotted in Fig. 4.27-a for typical STNO parameters. As discussed previously, one can distinguish three regimes. For long time scales $\tau \gg 1/2\Gamma_p$

[15] In Chapter 2, we have seen that in the low damping ratio approximation, the harmonic oscillator exhibits a Lorentzian shape in presence of noise

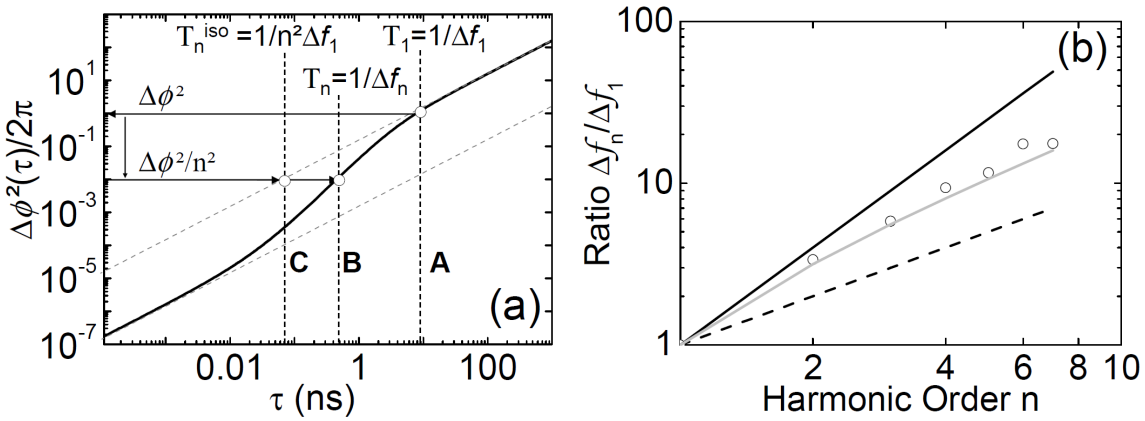

Fig. 4.27: (a) Calculated phase variance $\Delta\phi^2(\tau)$ from Eq. 4.16 using $\Delta f_0 = 10$MHz, $1/\Gamma_p = 3.18$ns and $\nu = 10$. Point A corresponds to $1/\Delta f_1$, Point B corresponds to the expected coherence time $(1/\Delta f_n)$ for the harmonic $n = 10$ for the non-isochronous oscillator and point C corresponds to the isochronous oscillator; (b) Ratio $\Delta f_n/\Delta f_1$ versus harmonic order n from simulations. Black dashed and solid lines are for $\Delta f_n = n\Delta f_1$ and $\Delta f_n = n^2\Delta f_1$, respectively. The gray line shows the values calculated from Eqs. 4.16, 4.31 with the nonlinear parameters Γ_p and ν extracted from the first harmonic signal. Dots are the results of a "macrospin" numerical simulation performed for $\zeta = 1.8$.

and for short time scales $\tau \ll 1/(2\Gamma_p\nu^2)$ the phase variance is linear in τ, while in between the phase variance is quadratic in τ [53].

To find the generation linewidth Δf_n from the phase variance $\Delta\phi^2$ one should, in principle, find the generation spectrum as a Fourier transform of the correlation function $K_n(\tau)$, which cannot be done analytically. It is clear, however, that at the correlation time $T_n = 1/\Delta f_n$ the value of the nth harmonic phase variance $n^2\Delta\phi^2(T_n)$ should be of the order of unity (as discussed in section 4.2.4):

$$\Delta\phi^2(T_n) = 2\pi/n^2 \ . \tag{4.31}$$

Eq. 4.31 gives an *exact* value of the linewidth Δf_n for a pure random-walk process $\Delta\phi^2 \sim \tau$, and its error does not exceed 6% in the quadratic region $\Delta\phi^2 \sim \tau^2$.

Combining Eqs. 4.16 and 4.31, one can easily understand why for a non-isochronous oscillator the linewidths Δf_n deviate from the well-known relation 4.28. The fundamental linewidth Δf_1 corresponds to the coherence time $T_1 = 1/\Delta f_1$ for which the phase variance is $\Delta\phi^2(T_1 = 1/\Delta f_1) = 2\pi$ (line A in Fig. 4.27-a). The linewidth Δf_n of the nth harmonic is then found as the inverse of the coherence time $T_n = 1/\Delta f_n$ for which the phase variance is $2\pi/n^2$ (line B in Fig. 4.27-a). It can be seen immediately that the corresponding coherence time in the case of a non-isochronous oscillator (line B) is larger than for an isochronous one (line C), whose phase variance is linear in time for all time scales (pure random walk phase). Correspondingly, the linewidths of higher harmonics are smaller than predicted by Eq. 4.28 with $\Delta f_n < n^2\Delta f_1$. Moreover, since the logarithmic slope of $\Delta\phi^2(\tau)$ changes between 1 ($\Delta\phi^2 \sim \tau$) and 2 ($\Delta\phi^2 \sim \tau^2$), for a general non-isochronous oscillator the linewidth Δf_n always lies in the interval $n\Delta f_1 < \Delta f_n < n^2\Delta f_1$ as has been found in experiment and in simulations, Fig. 4.26. Thus by fitting the experimental (or

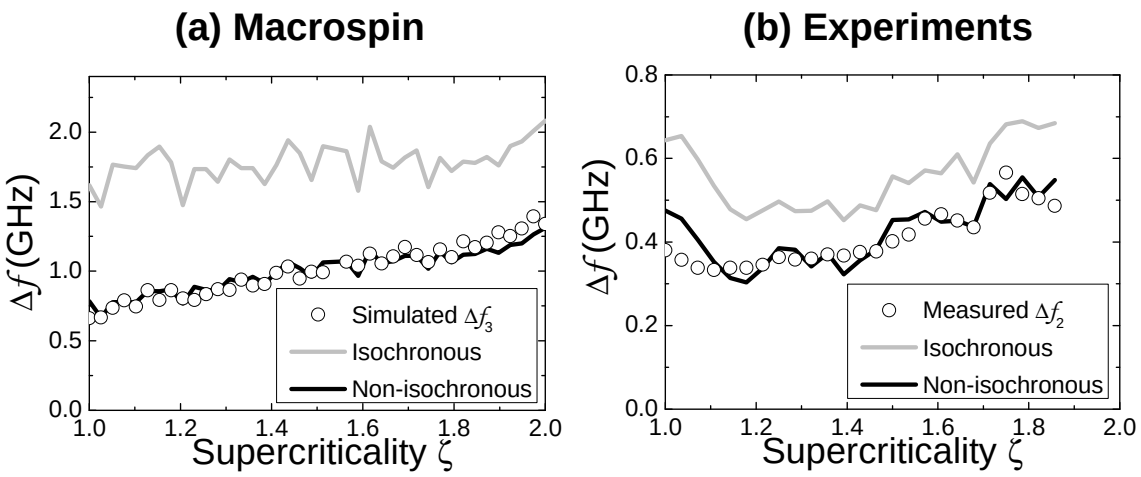

Fig. 4.28: Comparison of the nth harmonic linewidth extracted from the PSD numerically calculated for $n = 3$ (a) and experimentally measured for $n = 2$ (b) (open dots) with the results obtained from our analytical model 4.16 and 4.31 (black line) and the results of the model [137] (gray line). Measurements were done on Sample C.

numerically calculated) dependence $\Delta f_n(n)$ using Eq. 4.31 it is possible to determine the nonlinear auto-oscillator parameters ν and Γ_p (see section 4.4.2 below).

In order to further verify the presented theoretical description, we compare the linewidth of the higher harmonics obtained from a Lorentzian fit of the numerically calculated PSD (open dots in Fig. 4.28) to the results obtained from the analytical model Eqs. 4.16 and 4.31 (black lines in Fig. 4.28). For the analytical model the nonlinear parameters ν and Γ_p of the auto-oscillator were extracted in each case independently from the phase and amplitude noise of the first harmonic (fundamental frequency) following section 4.2, and the intrinsic linewidth Δf_0 was calculated from Eq. 4.16 for Δf_1. Using the set of values $\Gamma_p, \nu, \Delta f_0$, obtained solely from the analysis of the signal at the fundamental frequency, we then calculated Δf_n from Eqs. 4.16 and 4.31 to obtain the black lines in Fig. 4.28. One can see that the model Eqs. 4.16 and 4.31 give a good description of Δf_n in the auto-oscillation regime $\zeta > 1$, as shown in Fig. 4.28-a for the third harmonic obtained from macrospin simulations and in Fig. 4.28-b for the second harmonic measured experimentally. In Fig. 4.27-b, this is shown more explicitly for the macrospin simulation for orders $n = 2$ to 7. In contrast to the analytical model, the derivation using Eq. 4.28 for an isochronous oscillator (gray lines in Fig. 4.28) does not provide a good description. In particular, the analytical model in agreement with the macrospin simulations predicts the increase of Δf_3 with supercriticality ζ (see Fig. 4.28-a) due to the variation of Γ_p and ν with ζ (with $\Gamma_p = 0.2 \sim 1.2ns^{-1}$ and $\nu \sim 5$). In contrast, the isochronous oscillator model [137] predicts an almost constant Δf_3 since Δf_1 in this particular case does not vary significantly with supercriticality (compare gray line and open dots in Fig. 4.28-a).

4.4.2 Extraction of nonlinear parameters through harmonic linewidth analysis

An important consequence of the analytical description is that it is possible to extract, via the analytical model Eqs. 4.16 and 4.31, the three parameters Γ_p, ν and Δf_0 that define many properties of the dynamics of the system by measuring experimentally the linewidths of three harmonics in a non-isochronous auto-oscillator. This method of extraction of the nonlinear auto-oscillator parameters is very general and can be used for auto-oscillators of different physical nature over a wide range of auto-oscillation amplitudes (or supercriticalities ζ). It is of particular importance when the time domain data from the auto-oscillator (i.e. used in Ref. [76, 78, 85]) are not available.

In our experimental case, we only have access to the two first harmonics. One of the nonlinear parameter needs to be assumed to solve the three (minus one) equations. Experimentally, the system:

$$\begin{cases} \frac{2\pi}{1} = 2(2\pi)\Delta f_0 \left[(1+\nu^2)\frac{1}{\Delta f_1} - \nu^2 \frac{1-e^{-2\Gamma_p \frac{1}{\Delta f_1}}}{2\Gamma_p} \right] \\ \frac{2\pi}{2^2} = 2(2\pi)\Delta f_0 \left[(1+\nu^2)\frac{1}{\Delta f_2} - \nu^2 \frac{1-e^{-2\Gamma_p \frac{1}{\Delta f_2}}}{2\Gamma_p} \right] \\ \nu \text{ is known or } \Gamma_p \text{ is known or } \Delta f_0 \text{ is known} \end{cases} , \tag{4.32}$$

is thus solved. Since this system 4.32 is nonlinear, it might be possible that this system does not converge for a given set of parameters. Moreover, there are many variations of Γ_p and ν versus ζ that may be attributed to some extraction errors. Therefore, a fitting routine with interpolated input parameters (ν and Γ_p) is also presented (for experiments only).

The results of the fit from Eqs. 4.32 on Sample C are presented in Fig. 4.29. To obtain the value Γ_p presented in Fig. 4.29-c, we use the value of ν obtained from the TDNS technique (see Fig. 4.23-b), which varies with ζ. We can see that this procedure of extraction of Γ_p (black dots) quantitatively and qualitatively agree with the value of Γ_p obtained from the TDNS technique in section 4.2.2. Since the extraction of ν from TDNS leads to "oscillations" with ζ, we also used an interpolated value of ν (shown by the red curve in Fig. 4.29-b) to extract Γ_p from the harmonic linewidth analysis shown by the red curve. In this case, the value obtained from the interpolated value of ν is even better. Finally, in Fig 4.29-a, the value of Γ_p obtained from the assumption of a constant $\nu = -2.32$ over the whole range of the supercriticality is shown in gray dots. In this last case, we can see that Γ_p continues to increase with ζ for $\zeta > 1.6$, while other fits of Γ_p (obtained with a decreasing ν) confirm the saturation of the value of Γ_p for $\zeta > 1.6$ observed from the TDNS technique extraction. It is clear that this method is suitable to extract, at least quantitatively, the value of Γ_p solely from frequency domain measurements of the two first harmonics (ν can then be obtained from the dependence of Δf_1 versus I^2/P as shown in section 4.2.3). Regarding the variation of Γ_p versus ζ, together with the analysis of the harmonic linewidths, it seems to indicate a relative decrease of $|\nu|$ with ζ.

When we solve Eqs. 4.32 with an assumed value of Γ_p, we reproduce qualitatively (i.e. a decrease of $|\nu|$ versus ζ) and quantitatively (e.g. $|\nu| \approx 2$) the value of $|\nu|$ obtained from the analysis of the phase noise (see Fig. 4.29-b).

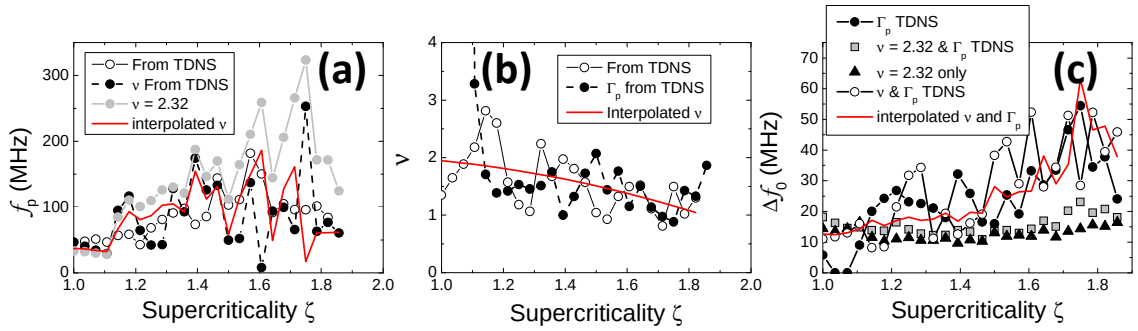

Fig. 4.29: (a) Comparison of Γ_p obtained with Eq. 4.32 and the one from TDNS method. The gray dots correspond to the case where $|\nu| = 2.32$ is assumed constant. The black dots use the value of $|\nu|$ obtained by TDNS. The red line is obtained with the interpolated value of $|\nu|$ obtained by TDNS as shown in (b). (b) Comparison of $|\nu|$ obtained by TDNS (white circles) and using Eq. 4.32 with Γ_p by TDNS (black dots). The red curve is the interpolated values of $|\nu|$ versus ζ obtained from the TDNS method. (c) Comparison of the extracted value of Δf_0 with different methods. The red curve is the interpolated value of Γ_p and $|\nu|$ obtained by TDNS. With this interpolated values, the noise of the fitting result is reduced.

Finally, we discuss the case of the extraction of Δf_0 experimentally from the analysis of the harmonics linewidths. When Γ_p and/or $|\nu|$ obtained from TDNS technique is assumed to be known for the resolution of Eqs. 4.32, it gives the same increase of Δf_0 versus ζ (see black dots, white circles and red curve in Fig. 4.29-c). Even when ν is constant, this increase appears, but is somehow less clear (from $\Delta f_0 \approx 10$MHz to $\Delta f_0 \approx 15$ or 20 MHz). This increase of Δf_0 versus ζ is relatively small compared to the one observed when the values of Γ_p or ν are assumed from TDNS technique (from $\Delta f_0 \approx 10$ MHz to $\Delta f_0 \approx 40$ MHz).

We discuss now in more detail the method itself. By this method, the extracted value of Γ_p does not really depend on the nonlinear parameter ν, and a good agreement between TDNS and harmonic analysis methods is found. This statement considers the fact that the fitting procedure is not "always" converging (for example at $\zeta = 1.6$). Indeed, Γ_p is related to the time where the transition $\Delta\phi^2 \sim \tau$ to $\Delta\phi^2 \sim \tau^2$ occurs. This transition is not affected much by the value of ν. As a consequence, it requires that some Δf_i used to solve Eqs. 4.32 are of the order of Γ_p, otherwise, Γ_p has almost no effect on the relationship between Δf_i (i.e. all Δf_i lie in the same "limiting behavior" defined by Eq. 4.19 in section 4.2.4). For example, in the case of Bianchini et al. [78], all harmonic linewidths should lie in the bottom left part of the phase variance (see Fig. 4.27) such that the relationship $\Delta f_n = n^2 \Delta f_1 = n^2 2\Delta f_0$ should hold. Finally, it should be noted that another case limiting the use of harmonic linewidths may appear when, in the auto-oscillating regime with high ν values, the linewidth values Δf_i belong to the "limit behavior" defined by the second equation ($\Delta\phi^2 \sim \tau^2$) of Eq. 4.19 and are in relation such that $\Delta f_n = n\Delta f_1 = n\sqrt{2\Delta f_0 \Gamma_p}$. Other cases may arise (for example all Δf_i belong to the upper right part of the curve in Fig. 4.27-a), but it is important to understand that the value of the FWHM of the fundamental may affect the fitting procedure.

In macrospin simulations, where the harmonic linewidths Δf_n up to $n = 5$ are used,

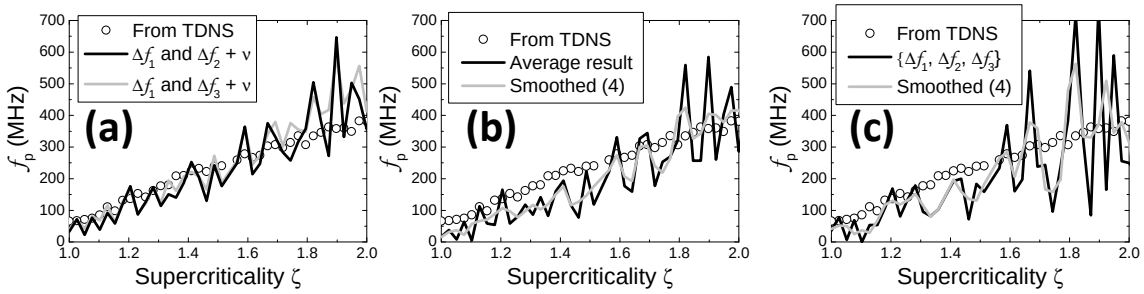

Fig. 4.30: (a) Extraction of Γ_p using Eq. 4.32 and using ν and $\Delta f_1, \Delta f_2$ (black curve) or $\Delta f_1, \Delta f_3$ (gray curve) as input. (b) Comparison between Γ_p obtained from TDNS and from the average of the extraction of Γ_p using the 4 combinations $\Delta f_i, \Delta f_j, \Delta f_k$. The gray curve is obtained from the black curve after a floating average of 4 neighbors. (c) Comparison between Γ_p obtained from TDNS and from Eq. 4.32 with input conditions $\Delta f_1, \Delta f_2, \Delta f_3$. The gray curve is obtained from the black curve after a floating average of 4 neighbors.

the fitting procedure has a better convergence for Γ_p when Δf_1 and Δf_2 (and Δf_3) are considered. In Fig. 4.30, different options were used to fit the value of Γ_p. The first option is to compare the method as if the data originated from experiment, i.e. only Δf_1 and Δf_2 and ν where given parameters. In this case, the result for Γ_p is similar to the one measured by TDNS (see black curve in Fig. 4.30-a). Finally, in case of Fig. 4.30-b, all the results of the combinations $\Delta f_i, \Delta f_j, \Delta f_k$ for $i, j, k < 5$ are averaged (black curve) and smoothed with 4 neighbors (gray curve). In this case, the fitting routine output are the three parameters $\Gamma_p, \nu, \Delta f_0$. Since experimental data are often limited to $n = 3$, we present this case apart in Fig. 4.30-c. Even in macrospin simulations, some scattering in the results is found, but the fitting routine gives the correct value and trend of Γ_p over ζ from 1 to 2. Again, since Kudo et al. [80] gave an easy way of obtaining ν, this complementary technique is shown here in order to obtain an *estimate* of Γ_p, when only the two or three first harmonics are measured in the frequency domain (this has been confirmed in Fig. 4.29-a) with ν obtained from Fig. 4.24.

In contrast to the case of Γ_p, a better fit of ν is obtained when using higher harmonics (assuming $\Delta f_1 < f_p$), or even with high index (i, j, k) difference. Firstly, we again consider cases that can be obtained in experiments, the case where Δf_1 , Δf_2 and Γ_p are given (black dots in Fig. 4.31-a), and the three first harmonics (gray squares in Fig. 4.31-b). The scattering of the fitting result for ν is more pronounced than for Γ_p. Furthermore, the mean value of $|\nu|$ versus ζ (about 3) is smaller than the one obtained from TDNS (about 5). In this case, a third method, such as the one given for experiments (Δf_1 versus I^2/P see Fig. 4.24), would be required to determine which method is the most accurate, the TDNS or the harmonic linewidth analysis. Beside this divergence in the value of $|\nu|$, the harmonic linewidth analysis confirms the decrease of ν versus ζ. Indeed, in the case where all nonlinear parameters are free, $|\nu|$ decreases from $|\nu| \approx 4$ for $\zeta \approx 1.2$ to $|\nu| \approx 1.8$ for $\zeta \approx 2$.

In fact, this decrease of ν with ζ should be associated with an increase of Δf_0 with ζ, as remarked in the section 4.3. This is confirmed by the black dots in Fig. 4.32-b where the trend of Δf_0 is to increase with ζ when all parameters $\Gamma_p, \nu, \Delta f_0$ are fitted from linewidth values only. We also confirmed that with Γ_p, ν obtained from TDNS, an

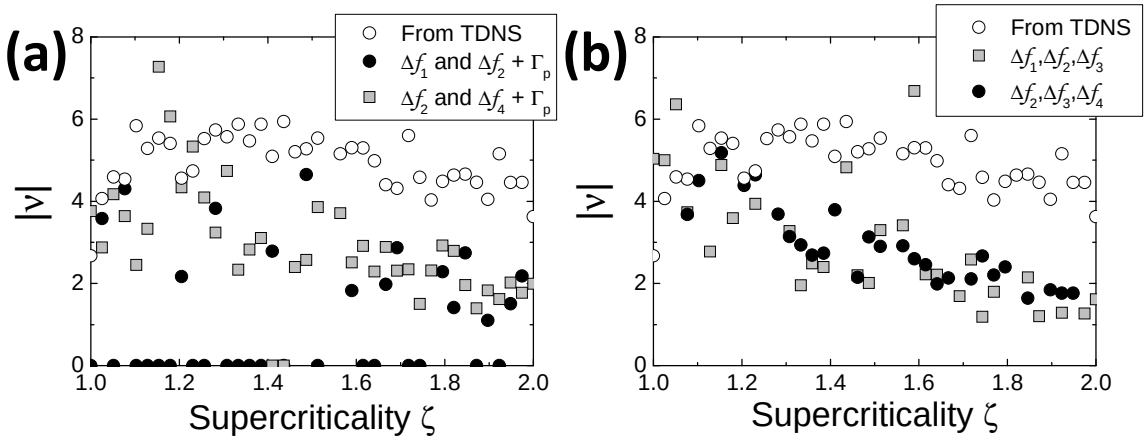

Fig. 4.31: (a) Comparison of ν obtained from TDNS and by solving Eq. 4.32 with Γ_p known. From the fitting procedure $|\nu| \approx 2$, while from TDNS $|\nu| \approx 5$. In both cases, ν decreases with ζ. By using only Δf_1 and Δf_2, the fitting always fail since these values lie in the top right part of Fig. 4.27. (b) $|\nu|$ obtained from a set of linewidth values.

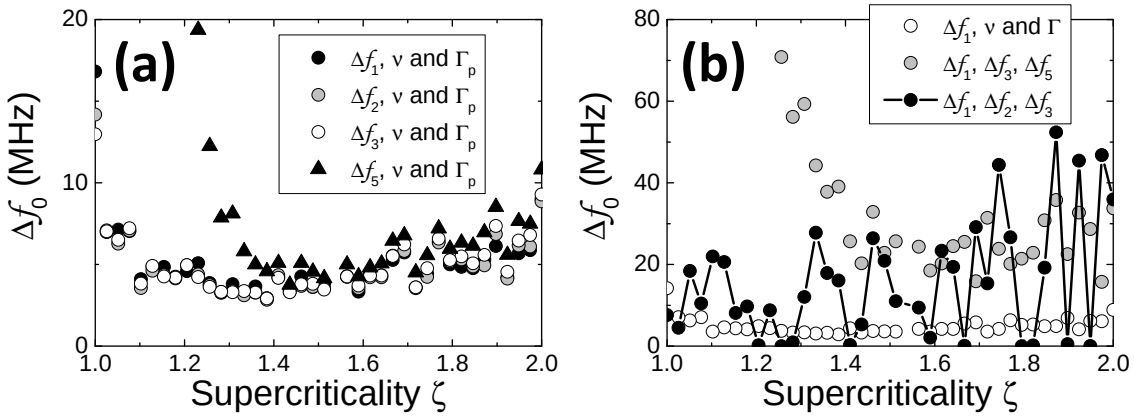

Fig. 4.32: (a) Extraction of Δf_0 using Eq. 4.20 for each harmonic. Below $\zeta = 1.4$, the fifth harmonic linewidth is incorrectly fitted, leading to inconsistent values of Δf_0. (b) Extraction of Δf_0 from the Eqs. 4.32 without fitting parameters (Γ_p, ν). Since this procedure leads to $\nu \approx 2$ instead of $\nu \approx 5$, a large value of Δf_0 is obtained.

increase of Δf_0 is required to obtain Δf_n (see Fig. 4.32-a).

In conclusion, we have provided a general analytical description for the linewidth Δf_n of higher harmonics in a non-isochronous auto-oscillator. Using this analytical description it is possible to determine all nonlinear parameters of a non-isochronous auto-oscillator if the linewidths of at least three generated harmonics are experimentally measured or numerically calculated. This independent study of the STO parameters $\Gamma_p, \nu, \Delta f_0$ from TDNS allows in macrospin simulations[16] and in experiment to confirm the increase of Δf_0 for ζ larger than 1.5.

This result is unexplainable in the sense where this increase of Δf_0 is not seen in usual diffusion problems. Moreover, the role of the non-stationary nature of the stochastic process (the noise) affecting the magnetization dynamics is also uncertain. This problem can be complicated by the fact that around $\zeta \approx 1.5$, the in-plane component of the magnetization in the direction of the applied field (i.e. M_X) can be negative, i.e. the oscillation angle in-plane is $> 90°$. This would result in dissipative terms that strongly vary in amplitude and in sign within the magnetization trajectory and therefore give to the noise this strong "nonstationary" nature.

[16]Up to $\zeta \approx 2.5$ there is no evidence of an out-of plane trajectory.

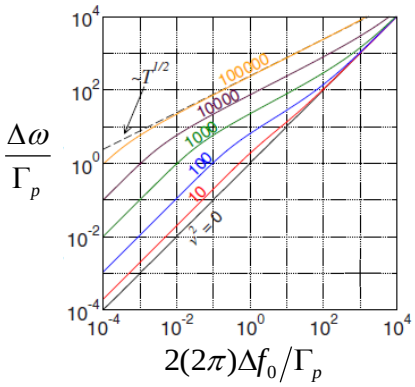

Fig. 4.33: Normalized FWHM $2(2\pi)\Delta f/\Gamma_p$ versus $2(2\pi)\Delta f_0/\Gamma_p$ on a log-log scale for different ν. In the case of large ν, the observed temperature dependence is almost always square root, while it can be a linear dependence for moderate values of ν. From [53].

4.5 Temperature dependence, noise origin and nonlinear parameters

In the previous part we discussed intensively the non-isochronous nature of the STO. It leads to the conclusion that the phase noise, i.e. a substantial linewidth broadening, has two main contributions from the environment: a direct one and one provided by the nonlinear amplitude-phase coupling. Note that we always consider the noise source $f_n(t)$ originating from the thermal fluctuation acting *directly* on the magnetization. The noise $f_n(t)$ that is supposed to affect both the amplitude and the phase of the auto-oscillation is supposed, similarly to the well known Brown model [33] for a magnetic particle, to originate from exchange with the thermal bath. Since the Brown model, like any model based on fluctuation/dissipation theorem, only describes the thermal field acting *at the equilibrium* of the system. Thus the KTS model has to implement a power dependent noise function $f_n(t)$ (see chapter 2). Moreover, this noise function is itself considered "linearly proportional" to the temperature at a given power p_0, as the Brown model has a linear temperature dependent fluctuating field. Finally, in a first approximation, it can be considered that reducing the temperature would also reduce the FWHM, through $\Delta f_0 \propto k_B T$.

Since the phase variance is a nonlinear function of time, the FWHM is itself a nonlinear function of Δf_0 (i.e. the temperature T). Therefore, reducing the temperature by a factor "x" does not necessarily imply a reduction of the FWHM by a factor "x". From both simulations and experiments, a square root [138] or a linear dependence [139] of the FWHM with temperature has been reported. Other exponential dependences of the FWHM with temperature have been considered to originate from mode hopping [138] and will not be discussed here.

In section 4.2.4, we gave the three limit behaviors of the FWHM (at a fixed T) depending on its value compared to Γ_p (Eq. 4.19). Two of these behaviors are directly proportional to Δf_0, and one is proportional to $\sqrt{\Delta f_0}$. Since $\Delta f_0 \propto T$, according to the value of Γ_p with respect with the FWHM value, the square root or the linear dependence with T can be found in the KTS model.

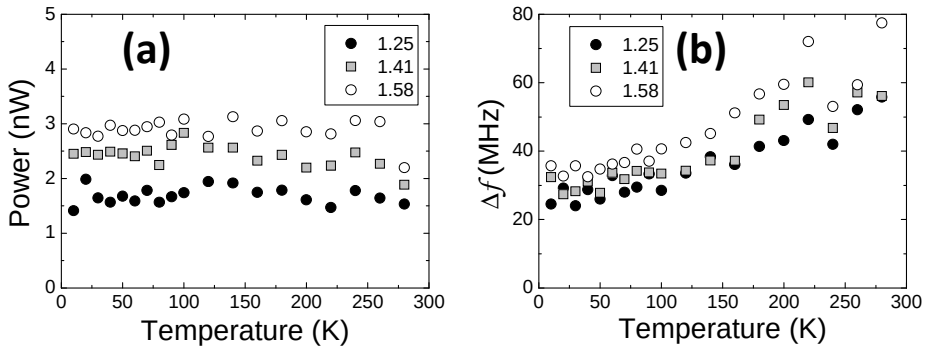

Fig. 4.34: (a) Integrated peak power versus temperature for different ζ. (b) FWHM versus temperature for different ζ. Results from DevC.

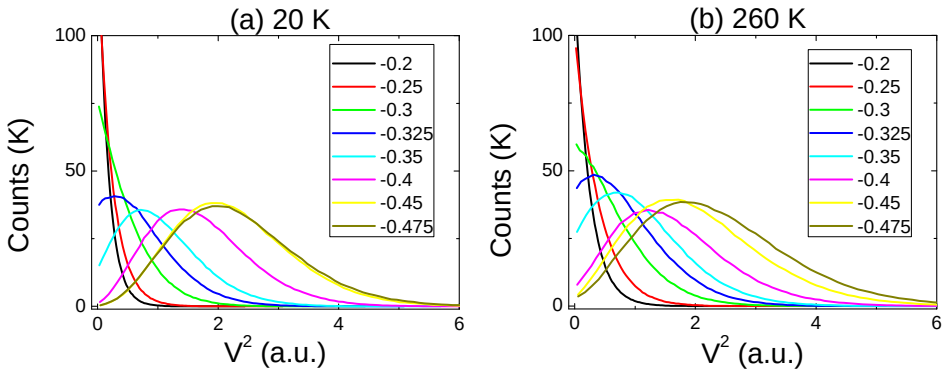

Fig. 4.35: Power distribution for different applied current I for (a) T = 20K and (b) T = 260 K. The power distribution looks critical in both case around $I_c \approx -0.3$ mA (green curve). Results from DevC.

Since the temperature dependence of the FWHM depends on Γ_p, it is convenient to present the normalized FWHM (i.e. $2\pi\Delta f/\Gamma_p$) versus the normalized temperature [53] (i.e. $\Delta f_0/\Gamma_p \propto T/\Gamma_p$). Fig. 4.33 gives this normalized curve for different values of ν. Because the data plot is in log-log scale, the slope informs on the temperature dependence of the FWHM. The square root dependence, in this scale, provides a slope of 1/2 while a linear dependence with temperature provide as slope of 1.

In section 4.1, the temperature dependence of the subcritical linewidth and power for a MTJ-STO has been discussed. Fig. 4.34 shows the experimental FWHM and power dependence versus T for different supercriticalities ζ, for $\zeta > 1$ (Fig. 4.7 showed the same curves for $\zeta < 1$ measured on the same device). While the power remains constant with temperature, indicating the above threshold regime of the STO, a clear linear dependence of the FWHM is seen from 100 K to 300 K, with a saturation of the FWHM from 100 K to 20 K. This saturation of the FWHM is not well understood yet and could be related to temperature-independent noise [140].

From TD measurements, we can estimate from the power distribution that the critical current I_c remains constant and is $I_c \approx -0.3$ mA (see Fig. 4.35). Most of the measurements are reproducible, in the sense where a linear decrease of the FWHM with decreasing temperature is observed for many samples of different size. Fig. 4.36-a

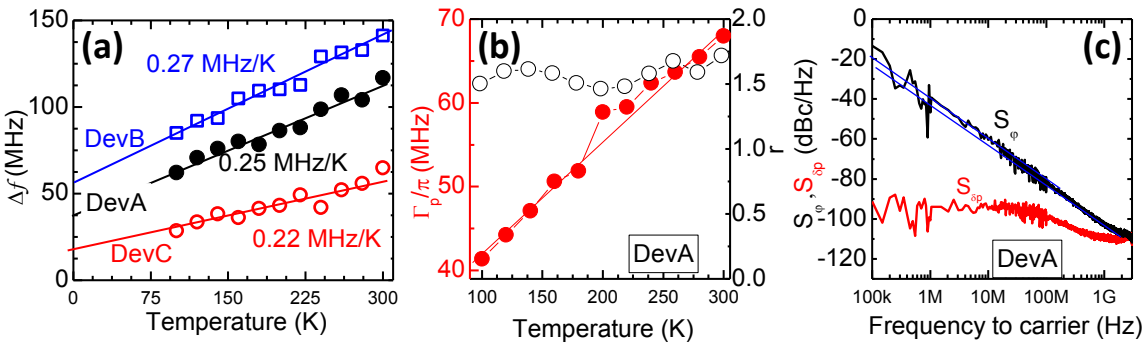

Fig. 4.36: Temperature dependence of: (a) the FWHM emission linewidth for three different devices: DevA: 85 nm diameter ($\mu_0 H_{app}$ = 61mT; $\zeta = 1.4$), DevB: 75 nm ($\mu_0 H_{app}$ = 48 mT; $\zeta = 1.3$) and DevC: 62 nm ($\mu_0 H_{app}$ = 65 mT; $\zeta = 1.4$). (b) The amplitude relaxation rate Γ_p (left axis) and the relative FWHM $r = 2(2\pi)\Delta f/\Gamma_p$ for $\zeta = 1.4$, (right axis) for DevA. (c) Log-log plot of the phase noise S_ϕ and power noise $S_{\delta p}$ at 300 K for DevA. The extracted ν is given in the figure.

shows the FWHM temperature dependence of three samples (DevA, DevB and DevC) of different sizes. All samples exhibit about the same slope: 0.25 MHz/K with a different positive intercept.

We define the normalized FWHM $r = 2(2\pi)\Delta f/\Gamma_p$, which is flat over the temperature range $T = 100 \sim 300$ K (see Fig. 4.36-b). This results from the fact that in experiment a linear increase of Γ_p with temperature is observed similar to Δf. Therefore the ratio r is constant. The direct consequence of this is that the normalized temperature must be constant: the normalized temperature does not change with temperature. If we had to plot the experimental data in a plot similar to Fig. 4.33, all measurement would lie in one point for DevA.

This surprising result makes a direct comparison of the experiments to the theoretical predictions less clear. First we discuss the decrease of Γ_p with the decrease of temperature T. We have shown that Γ_p scales with the linear Gilbert damping rate Γ_G, or eventually with a phenomenological damping rate given by $\Gamma_\omega = \alpha\omega_g$ (see discussion in section 4.2.2 and Fig. 4.18, note that DevC $\neq$ Sample C and DevA $\neq$ Sample A). In fact, for DevA, an increase of the experimental Γ_G (i.e. the measured FWHM when $\zeta = 0$), cannot be related to the damping constant α or the saturation magnetization M_s (see discussion in section 4.1.3). Therefore, we expect from this formulation that $\Gamma_p \propto \Gamma_G$ would increase with the decrease of the temperature. Moreover, the mode frequency does not change significantly (but rather increases due to M_s) such that "Γ_ω" is supposed to increase with decreasing temperature experimentally. Since the critical current ($\zeta = 1$) is monitored by the amplitude/power distribution, we see no clear evidence of a shift of the critical current I_c that could explain the dependence observed (Γ_p depends on ζ).

In conclusion, while the FWHM decrease can be attributed to a decrease of $\Delta f_0 \propto T$, the restoration rate Γ_p, which is the energy exchange with the thermal bath, also decreases with the thermal energy $k_b T$. Finally, we note that in macrospin simulations the ratio r indeed decreases with decreasing temperature (i.e. Γ_p is constant for all effective T simulated) and is in agreement with Fig. 4.33. We recall that the thermal noise input

as a delta correlated fluctuating field from the Brown formulation has been used (see Ref. [33] and Eq. 1.13).

We have tried to understand first the increase of Δf_0 with ζ and then we found that it is not only linear with temperature, but that the exchange rate Γ_p changes with temperature in way that cannot be explained by material parameters in experiment. Several explanation might be given. First the KTS model, similarly to the case discussed by T.J. Silva and M. Keller in Ref. [48], has many simplifications in the form of the noise acting on the magnetization. We have seen from the Brown model that the "whiteness" of the thermal noise may disappear at low temperatures, or that it implies another formulation of the problem. In particular, Rezende proposed to treat the effect of the applied current to the magnetization interacting with a thermal bath as a quantum problem [58]. Since it involves the appearance of a coherent quantum state (i.e. according to the Rezende paper, coherent quantum state exhibit a Poisson distribution of the "power" distribution rather than a Gaussian one) it is hard to identify such a distribution in our measurements (see for example Fig. 4.35) and therefore to state on this solution.

Finally, in order to find a possible explanation of the saturation of the linewidth as well as the positive intercept, we can note that an equivalent fluctuating field originating from spin current fluctuations [140] can overcome the classical thermal field proposed by Brown below a certain temperature. Therefore, one can imagine it to be possible to see such phenomenon in our experiments.

This nontrivial behavior of the STO, observed in the temperature range of 20 K - 300 K and revealed here in the light of TDNS analysis, actually requires more evidence to really conclude on the physical origin of the noise in STOs.

4.6 Flicker noise in degraded junctions

As a final result of this chapter, we show to what extent the KTS theory is general and is expandable to any kind of auto-oscillator. We first discuss the very trivial nature of the system's bifurcation in the KTS model as presented in [54]. Indeed, this model considers only a single mode of the magnetization that turns out to be auto-oscillating upon increasing current. In the next section, we present a study where the auto-oscillating mode does not originate from the "FMR" mode of the magnetization.

In the last section of chapter 3, we have presented the distinction between LTMR and HTMR devices. The HTMR devices are in good agreement with the KTS theory. In the presence of noise, the distribution function of the power is continuous (i.e. with a single mean value $\bar{p}$); there are no "jumps" between the auto-oscillating state and the equilibrium position of the magnetization.

However, it has been shown in [81] that in LTMR devices the auto-oscillating mode appears and then disappears with time close to $\zeta = 1$ and that the auto-oscillating mode does not originate from the "FMR" mode (the lowest frequency mode in the absence of STT). Fig. 4.37 shows the transition between the FMR mode and the auto-oscillating state. Contrary to the HTMR case, there is no smooth transition at $\zeta = 1$. At the time of the study by Houssameddine et al. [115, 81], this has been understood as "stochastic" transitions between the FMR mode and the auto-oscillating mode.

With the knowledge on the IPP-mode acquired from macrospin simulations and the

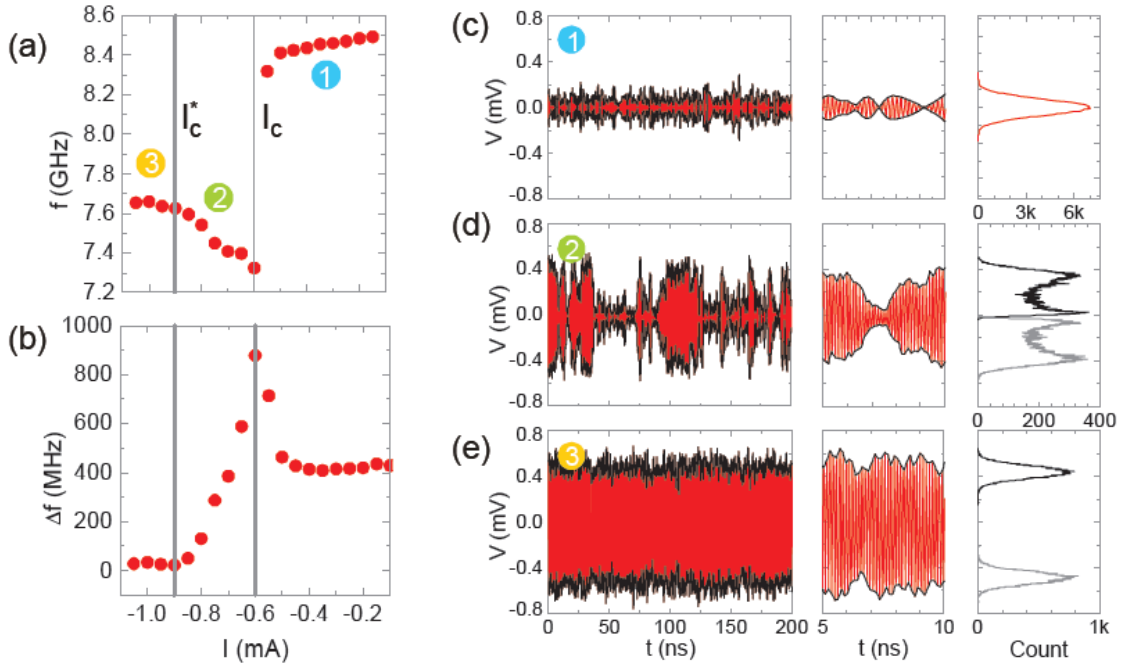

Fig. 4.37: Measurement of an LTMR sample with applied field $H_0 = 575$ Oe. Peak frequency (a) and FWHM (b) dependence versus the applied current I, obtained from frequency domain measurements. (c)-(e) Time traces for three value of current ① in the subthreshold regime, ② in an intermittent regime and ③ in a steady-state of the auto-oscillation. (Left): 200ns long time trace measured (red) with time varying amplitude (black). (Middle) zoom on a 5ns time windows. (Right) amplitude distribution function. ② corresponds to the coexistence of the FMR mode with a auto-oscillating mode. From [81].

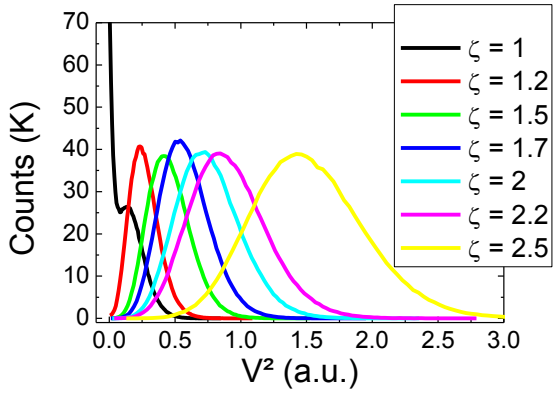

Fig. 4.38: Power distribution of the LTMR device studied in this section. At the threshold $\zeta = 1$ (Black curve), the system "jumps" from steady state $V^2 \approx 0.15$ to static state $V^2 \approx 0$.

studies on HTMR samples, it is clear that this case is nontrivial and is not considered in the KTS model. Yet, the KTS theory is a generic theory aiming to describe any kind of non-isochronous autonomous dynamics, which is independent on how the oscillating state is reached. The LTMR belongs to this class.

Fig. 4.38 shows a typical power distribution from LTMR device. For $\zeta > 1.5$, almost no stochastic transition between the static and the dynamic mode appears such that it is possible to study amplitude and phase noise of the oscillation.

The result is presented in Fig. 4.39-a. Similar to HTMR devices, a relaxation phenomenon qualified by Γ_p is seen both in phase and amplitude noise. While we defined Γ_p from the "linear linewidth" Γ_G in HTMR devices, we cannot consider this in the case of LTMR devices. Nevertheless, as discussed in the general introduction of auto-oscillators, a Γ_p is required to stabilize a nonzero amplitude. Similar to HTMR device, we thus identify a nonlinear contribution to phase noise.

Besides the standard phase and amplitude noise characterization similar to HTMR devices, we also observed an additional $1/f$ slope in the amplitude noise ranging from ≈ 1 MHz to the minimum of the resolution of the method (100 kHz) for LTMR devices. Because of the nonlinear amplitude phase coupling, it up-converts the $1/f$ amplitude noise to a $1/f^3$ phase noise. We can note the similitude with the so called Leeson effect in semiconductor-based oscillators [43].

In order to confirm these trends, we performed, in collaboration with XLIM/CNRS laboratory, two different low frequency measurements. The first one involves a phase noise measurement with the retardation line method, Fig. 4.39-b. This method allows one to use a heterodyne detection of the phase noise for noisy oscillators since the local oscillator is replaced by the signal of the oscillator with a 20 ns delay (details on the method can be found in Ref. [89]). This measurement confirms the trends observed in the phase noise from TDNS. In this case, the flicker frequency noise is observed from 100 Hz to ≈ 500 kHz. We note the difference of the two measurements on the value of the frequency which appear at the transition $1/f^3$ and $1/f^2$.

To further investigate the presence of $1/f$ noise and its origin, we suppose that this "amplitude noise" could originate from low frequency electrical current fluctuations. We will see in chapter 5, dedicated to current modulation, that such effects may indeed generate a "pure" amplitude noise.

To verify the presence of "electrical noise" in our LTMR devices, we performed low frequency noise measurement under bias field whose amplitude is similar to the one applied in the auto-oscillation regime (i.e. with the same field value). Nevertheless, we note no evolution of the low frequency current noise with applied field. This is expected since the magnetoresistance is not supposed to vary much in the saturated AP state of the tunnel junction (Fig. 4.40-a).

Yet, it is well known that the STT induces strong low frequency fluctuations of the magnetoresistance of magnetoresistive devices (spin valves or tunnel junctions), since it allows the magnetization to be pulled away from equilibrium (see for example the low frequency component in Fig. 1.14-b and details in Refs. [141, 142, 143, 144]). Therefore, we measure, for the same field value and for the inverse current polarity $-I$ as the one applied in order to obtain Fig. 4.39-a,b (i.e. $+I$), the electrical low frequency noise of our junctions presented in Fig. 4.40-a,b (therefore in these measurements $\zeta < 0$).

The enhanced presence of flicker current noise due to pinholes in MTJs suggests that

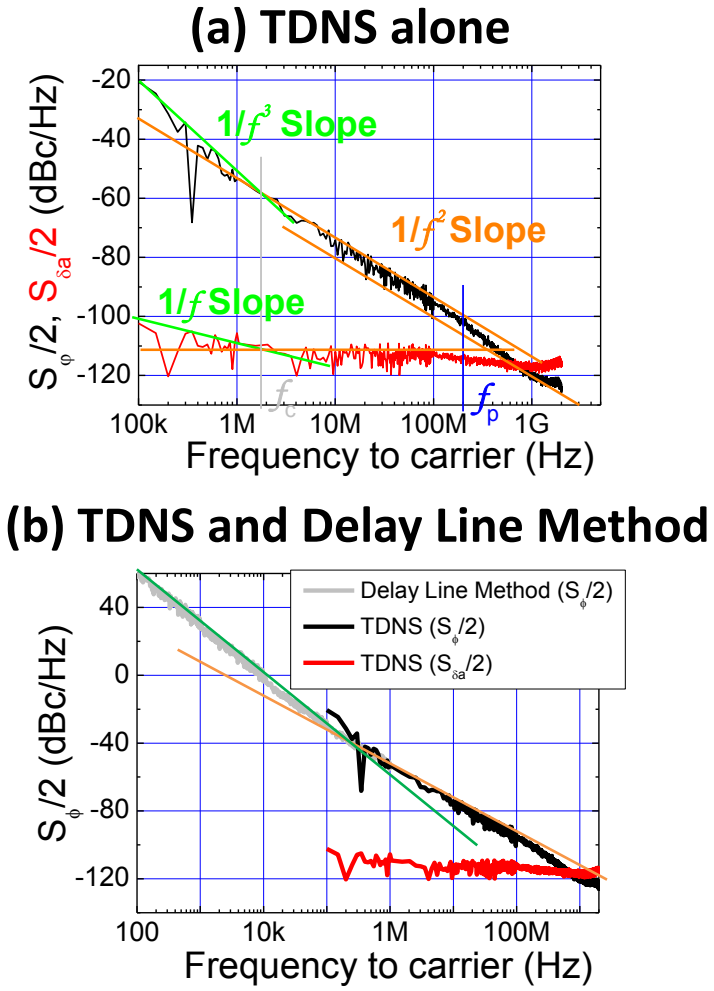

Fig. 4.39: (a) Amplitude and Phase noise obtained from the TDNS method. (b) Comparison between the phase noise obtained from TDNS and the one obtained from delay line method. In all $H_{app} = -600$ Oe.

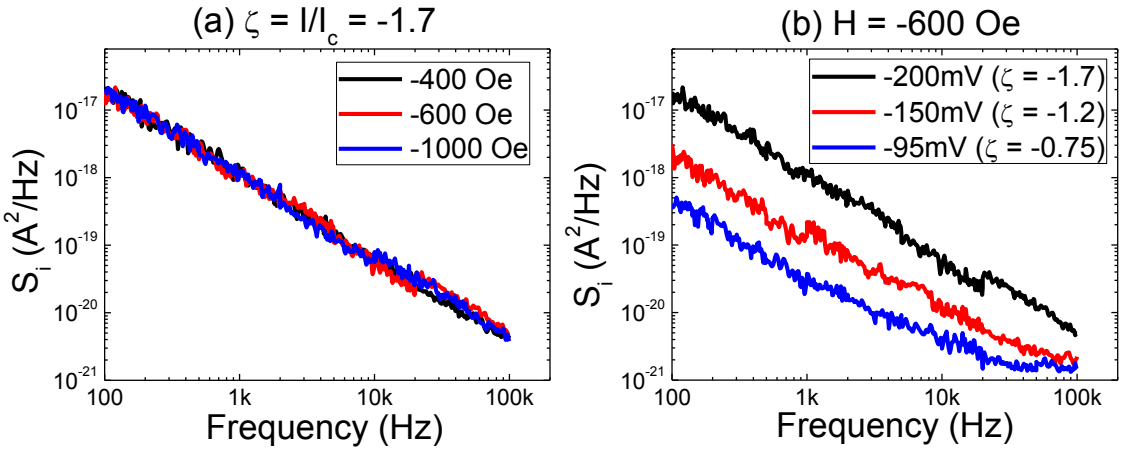

Fig. 4.40: (a) Current noise plot for $\zeta = -1.7$ and different field. (b) Current noise for $H_{app} = -600$ Oe and different ζ.

the enhanced phase noise at low frequency in degraded LTMR junctions, as compared to HTMR devices results from flicker frequency noise. An extended discussion on the value of S_i compared with the measurement of S_ϕ will be done in the next chapter 5 on macrospin simulations in presence of current noise.

Similar $1/f$ frequency noise has been reported by Keller et al. [85] in spin valve nanocontact devices using a low frequency TDNS setup. We have verified that such a setup conserves the amplitude noise contribution of the auto-oscillation and therefore would probably correlate the flicker amplitude noise to the flicker frequency noise.

It should noted that the exact experimental conditions could not be exactly reproduced in the experiment carried out in XLIM/CNRS laboratory with a delay line method and for the TDNS in SPINTEC, since not the same experimental setup has been used (current source, applied field and applied field angle), and that the LTMR may have been degraded between measurements.

Since an extended flicker current noise is expected in degraded junctions compared to those with a high quality barrier [145], and that so far we have not found evidence of such a noise contribution in our high barrier (HTMR) quality device down to the frequencies of $f = 100$ kHz, it would be profitable to conduct more such correlated (delay-line / TDNS technique / low frequency current) measurements in the future to investigate the presence of these noise correlations.

In conclusion, we have shown that the KTS model, which assumes an up-conversion of amplitude noise to the phase noise, is able to explain a similar effect from the Leeson effect in MTJ-based STOs. Indeed, a flicker current noise originating from external parameters (dc current source or tunnel effect) only affects the anti-damping term (the "amplifier") of the oscillator. Similar to what has been shown here, these contributions should be characterized in absence of an auto-oscillating regime of the STO, since this contribution is "extrinsic" of the system. Therefore, in a first approximation, a current modulation would only affect the phase through the nonlinear amplitude phase coupling as predicted by the KTS model. This question will be addressed in the next chapter.

Part III

Non-autonomous regime of non-isochronous STOs

In chapter 4, we have studied in detail the STO in its "free-running" or autonomous regime, i.e. when no sources (except noise) interact with the STO. Despite the tunability of the STO, i.e. the possibility to change its mode frequency ω_g with applied current, the agility of STO, i.e. the speed to change the STO state, has been less studied [146, 147].

The interaction of the STO with an external system is now investigated as a complement to the autonomous regime. Indeed, the use of STOs for a practical application requires the STO to interact with its environment in some deterministic way. The results provide possible routes of optimization of STOs for applications, i.e. to optimize the STOs performances when driven in non-autonomous regimes.

This part describes the effects of the interaction of the STO with an external microwave current source. It is subdivided into two chapters since the effect of the driving signal depends on its frequency f_e. In section 2.2, both modulation and injection locking experiments from the literature were reviewed. While low frequency signals ($f_e < \Gamma_p/2\pi$) would only affect the anti-damping term Γ_-, the higher frequency signals ($f_e \approx f_g$) lead to "synchronization" of the STO to the external microwave source[17]. We will see how both experiments lead to rich dynamics of the STOs in a non-autonomous regime.

[17]It is only a matter of semantics, since there is no distinction between the two, both could be called synchronization or injection locking [41]. We only distinguish the two because of the different information that can be retrieved from each.

Chapter 5

Modulation experiments

In this chapter, we discuss results obtained by modulating the current, using the techniques presented in chapters 3 and 4 on phase and amplitude noise. The advantages are that the study of modulation is not limited to the observation of modulation sidebands in the frequency domain. The use of the TDNS technique allows the direct comparison of the expected time varying phase and amplitude term of the auto-oscillator driven in a non-autonomous regime and the experimental results. We will sspecially focus on two points that can be addressed within the KTS model.

The first one is the non-trivial dependence of the sideband amplitude on the modulating current amplitude that we will explain by a second-order phase/frequency response of the STO to an excitation. We show how this can be used to extract a fundamental parameter of the STO that is the nonlinear damping term Q (see Eq. 2.23 in section 2.2.2.1).

The second point is the modulation frequency dependent phase response of STOs [54] (see section 2.2.2.2) that has been less studied in recent experimental [70, 71] and theoretical [73, 148] works. Since the phase response is of interest for applications, it will be the focus of our study. The modulation speed of STOs is fundamental in STO reader application [149, 150, 151, 152, 153] and in frequency shift keying (FSK) transmission protocols [146, 147].

While the agility, i.e. the speed at which the STO mode frequency can be changed, of vortex-based STOs has been studied (see [147]), in the context of characterizing the STOs as frequency synthesizers, we show here that this agility is exactly Γ_p. We give hereafter a very simple method to check this agility, which is at the same time a complementary method to extract the nonlinear parameter Γ_p, from a "non-autonomous" regime of the STO [154]. In addition to the potential application for the definition of STOs' specifications, as with all methods presented in this work, this technique can be extended to any non-isochronous auto-oscillator, i.e. any voltage control oscillator (VCO).

5.1 Modulation in the KTS model

The explanations in this section are given within the context of the KTS model, neglecting the noise effect which has been discussed in chapter 4. However, the noise is still

present in the system[1]. We start with an introduction of the physical concept underlying this experiment, and we derive the mathematical expressions, as in [54], to express the expected result in terms of time domain measurements. We also give a novel approach to simply explain the origin of nonlinear frequency modulation results obtained experimentally.

5.1.1 Physical picture of the modulation in the frame of an auto-oscillator

Here, we are interested in the effect of the modulation of the anti-damping term $\Gamma_{-}^{I_{\mathrm{DC}}}(p)$ for a given applied current $I_{\mathrm{DC}} = I(t=0)$ that stabilizes the oscillation power at p_0 (see the red curve in Fig. 5.1-d). The idea is that at a certain time (t_1) in the measurement, we modify the input DC current to a slightly higher value as shown in Fig. 5.1-a. As a consequence the anti-damping dissipative term changes. If we consider the physical picture of the compensation of the dissipative terms (see Fig. 2.5 in section 2.1.2), an instantaneous change of I corresponds to an instantaneous change of the anti-damping dissipative term Γ_{-}. In Fig. 5.1-e, this corresponds to going from the red curve to the dashed green curve, while the dissipative damping term Γ_{+} remains unchanged. Therefore, under the condition of $I_{\mathrm{DC}} = I(t_1)$, the only stable dynamical equilibrium state is p_1, while the STO power is still at $p(t_1) = p_0$.

The system power will naturally relax towards this new equilibrium position, or *limit cycle*. Since the system has a limited energy supply (or dissipation) rate, a transient in the power appears, as pictured in Fig. 5.1-b. The transient solution, in the case of the KTS model, is governed by Eq. 2.24, and the transient power and the transient phase evolution is governed by Eq. 2.25 with a time dependent anti-damping term only:

$$\begin{aligned} \frac{dp}{dt} + 2\left[\Gamma_{+}(p) - \Gamma_{-}(p,t)\right] p = 0 \ , \\ \frac{d\phi}{dt} + \omega(p) = 0 \ . \end{aligned} \tag{5.1}$$

Therefore, the power transient leads to a phase (or frequency) transient. This transient is schematically represented in Fig. 5.1-c, in the case of a negative nonlinear amplitude-phase coupling (i.e. $\omega(p)$). The corresponding relaxation constant is given by the characteristic relaxation time to return to the stable state $p(t) = p_1$ (see Fig. 5.1-f). As shown in the Fig. 5.1, when switched back to $I_{\mathrm{DC}} = I_0$ at $t = t_2$ a similar process appears such that the system relaxes towards p_0 and ω_0. This exact protocol has been followed in vortex based STOs [146], where the instantaneous frequency is monitored by means of time domain techniques. However, the experimental protocol used made it impossible to exactly determine the relaxation time of the STO that was supposed to be below 20 ns for a mode frequency of $f_g = 300$ MHz. Based on the same experiment setup, with a

[1]The "only" interaction between noise and modulation experiments that can be seen in frequency domain (e.g. on the FWHM) has already been explained in [71]. This experiment describes how the response to the noise of the STOs are averaged over the whole power range that is covered by current modulation.

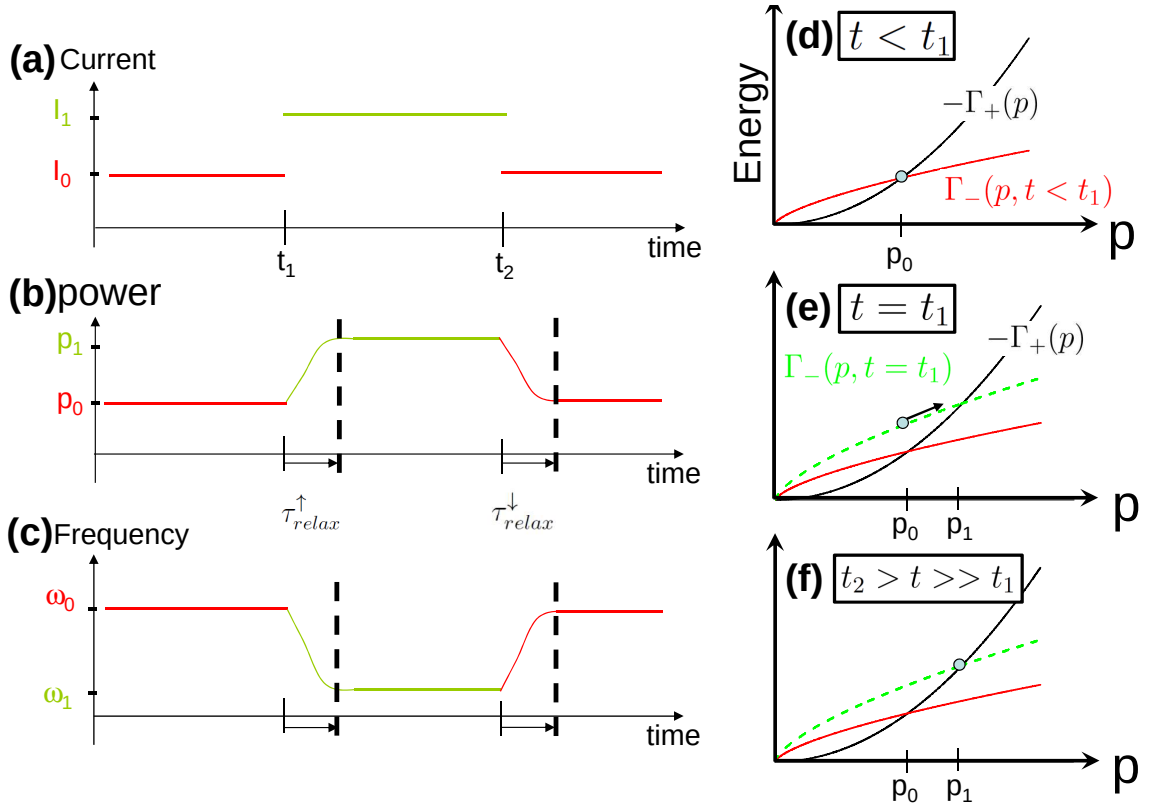

Fig. 5.1: (a) Time varying dc current. At t_1, the DC current is changed from I_0 to a higher value I_1. (b) Consequence on the instantaneous auto-oscillation power p. (c) Consequence on the frequency of a non-isochronous auto-oscillator. (d) Energy supplied (red or green) compared to the energy dissipated (black curve). The compensation of these two energies makes the dynamical equilibrium of the system. (e) When changing the current, the anti-damping term Γ_- instantaneously changes; the oscillation power is still p_0 but now additional energy is given to the system so that the new dynamical equilibrium is at p_1. (f) After a certain time, the system is set to a new dynamical equilibrium p_1.

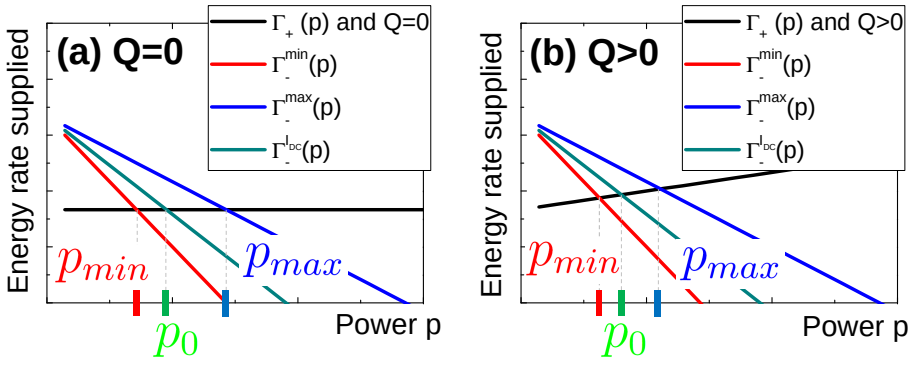

Fig. 5.2: Illustration of the stationary oscillation power due to the compensation of the damping terms $\Gamma_+(p)$ and $\Gamma_-(p)$. For (a) $\Gamma_+(p) = \Gamma_G$ and for (b) $\Gamma_+(p) = \Gamma_G(1 + Qp)$.

complex fit of the data from the frequency domain experiments performed with different modulation frequencies, the authors obtained a relaxation time of about 5 ns [147]. Since we want to define an experimental protocol to determine the relaxation/transient of the system in the gigahertz range, the simplest one is to use a microwave monochromatic signal: a gigahertz sinusoid.

5.1.2 Sinusoid modulation of the anti-damping dissipation in STOs

In the following, we are interested in the effect of the modulation of the anti-damping term $\Gamma_-^{I_{\rm DC}}(p)$ at a given applied current $I_{\rm DC}$. When a modulation current of amplitude $I_{\rm AC}$ and frequency f_M is applied its form is changed to [54]:

$$\Gamma_-^{I_{\rm DC}+I_{\rm AC}}(p) = \sigma I_{\rm DC}(1-p) + \sigma I_{\rm AC}\cos(2\pi f_M t)(1-p)\ . \tag{5.2}$$

If we consider the compensation of the dissipative terms (see Fig. 5.1 and 2.5 in section 2.1.2), this means that the anti-damping dissipative term Γ_- oscillates between two extrema in time (see Fig. 5.2). In Fig. 5.2, if we consider the minimal (resp. maximal) value $\Gamma_-^{\rm min}$ ($\Gamma_-^{\rm max}$) in Eq. 5.2, it leads to minimal (resp. maximal) oscillation power $p_{\rm min}$ (resp. $p_{\rm max}$). Therefore, the STO power oscillates between two "power" states $p_{\rm min}$ and $p_{\rm max}$, while its power without AC oscillating current is p_0 that arises from $\Gamma_-^{I_{\rm DC}}$. Since the value of the nonlinear damping term Q is not known[2], the aforementioned picture is considered in several limit cases: without nonlinear damping $Q = 0$ (see Fig. 5.2-a) and with $Q > 0$ (see Fig. 5.2-b).

It is important to note that there is no simple relation between the time varying applied current $I(t)$ and time varying power $p(t)$, and that this relation depends also on Q (see Eq. 2.27 in section 2.2). Therefore, when applying a modulating current, a simple resolution of the dynamical equations can be found for only two limiting cases.

The first limiting case corresponds to very low modulation frequency f_M ($f_M \ll f_p$) such that a stationary power is found for any time t. Indeed, for very low frequency

[2]it is not the oscillator quality factor Γ_p.

perturbation, we can consider that the time dependent power $p(t)$ is the one that equilibrates the damping and the anti-damping terms for all $t \gg 1/\Gamma_p$: $\Gamma_+(p(t)) = \Gamma_-(p(t),t)$. This equation already led to the definition of the mean power p_0 in the case of the autonomous regime (see Eq. 2.27 in section 2.2.2.1) and gives now the relationship between the stationary power $p(t)$ and the excitation $\epsilon_t = (I_{\mathrm{AC}}/I_{\mathrm{DC}})\cos(2\pi f_M t)$:

$$\begin{aligned} p(t) &= \frac{p_0}{1+\frac{\zeta}{Q+\zeta}\epsilon_t} + \frac{\zeta\epsilon_t}{(Q+\zeta)\left(1+\frac{\zeta}{Q+\zeta}\epsilon_t\right)} \\ &\approx p_0 + \epsilon_t\frac{\zeta}{Q+\zeta}(1-p_0) - \epsilon_t^2\left(\frac{\zeta}{Q+\zeta}\right)^2(1-p_0) + o(\epsilon_t^2) \end{aligned} . \tag{5.3}$$

The power $p(t)$ has a harmonic response to the excitation ϵ_t. Finally, similarly to the time dependent power solution, we can give the approximated time varying frequency response:

$$\omega(p(t),t) \approx \omega_0 + Np_0 + N\epsilon_t\frac{\zeta}{Q+\zeta}(1-p_0) - N\epsilon_t^2\left(\frac{\zeta}{Q+\zeta}\right)^2(1-p_0) + o(\epsilon_t^2). \tag{5.4}$$

The direct consequences of the second order response in ϵ_t^2 are:

1. The mean angular frequency $< \omega((p(t),t) >$ is not equal to $\omega(p_0)$ as already observed experimentally [69, 70].

2. We expect a second harmonic phase (or frequency) response for increasing high modulation depth $I_{\mathrm{AC}}/I_{\mathrm{DC}}$ and low modulation frequencies f_M.

The effect of this second harmonic phase response is that the amplitude of the nth order sidebands are in a nontrivial relationship. This effect has been evidenced in Refs. [69, 70, 148], yet the value of f_p is unknown so that it is not clear whether the condition $f_M \ll f_p$ is fulfilled.

The second limiting case that has a simple analytical solution corresponds to the case of small modulation depth $\epsilon = I_{\mathrm{AC}}/I_{\mathrm{DC}}$ and is valid for all frequencies f_M (below the mode frequency f_g). In this case, the power modulation $\delta p(t)$ is expected to be small so that a linearization of the general oscillator equation 2.24 is possible. In this case we use Eq. 2.33 given in section 2.2.2.2 and derived in [54]:

$$\begin{aligned} \frac{d\delta p}{dt} + 2\Gamma_p\delta p - 2\epsilon\Gamma_-(p_0)p_0\cos(\omega_m t) = 0 \\ \frac{d\phi}{dt} + \omega_g + N\delta p = 0 \end{aligned} ,$$

whose solutions are:

$$
\begin{aligned}
d\delta p(t) &= \epsilon \frac{2\Gamma_-(p_0)p_0}{\sqrt{\omega_m^2 + 4\Gamma_p^2}} \cos(\omega_m t + \psi) \\
&\quad , \\
\phi(t) &= -\omega_g t - \epsilon \frac{N2\Gamma_-(p_0)p_0}{\omega_m \sqrt{\omega_m^2 + 4\Gamma_p^2}} \sin(\omega_m t + \psi) + \phi_0
\end{aligned}
\tag{5.5}
$$

where $\omega_g = \omega_0 + Np_0$ is the mode frequency and $\psi = -\arctan(\omega_M/2\Gamma_p)$. This equation is similar to the solution with noise as discussed in chapter 4. The effect of the white Gaussian noise is that the system is "modulated" with the same strength at all frequencies at the same time. The modulation experiments correspond to an excitation at a given (determined) frequency f_M: the system's response, for small modulation levels, is actually the same as the one with noise. The difference is that the modulation only affects the amplitude, i.e. only modifies the nonlinear contribution to the phase. Modulation experiments are then a means of characterizing Γ_p from the phase. Because we will compare our experiments with the PSD of the frequency of the oscillator, we express the phase response in terms of the oscillator frequency response:

$$
2\pi\nu(t) = \omega(t) \approx \omega_0 + Np_0 + \epsilon \frac{N2\Gamma_-(p_0)p_0}{\sqrt{\omega_M^2 + 4\Gamma_p^2}} \cos(\omega_M t + \Psi) \; . \tag{5.6}
$$

We will solely focus on the amplitude of the prefactor of the cosine of Eq. 5.6. Its contribution to the PSD S_ν of the STO frequency $\nu(t)$ can be written as:

$$
S_\nu(f) \propto A(f_M)\delta(f_M - f) \; , \tag{5.7}
$$

with δ being the Dirac function and $A(f_M)$ the frequency response of the STO. It is convenient to express the frequency response of the STO by the frequency of the excitation:

$$
A(f_M) = \epsilon^2 \frac{(N2\Gamma_-(p_0)p_0)^2}{4\pi^2} \times \frac{1}{f_M^2 + f_p^2} \; . \tag{5.8}
$$

One can figure out the two limiting behaviors of the frequency response of the STO $A(f_M)$ defined by Eq. 5.8. For $f_M \ll f_p$, the response $A(f_M) =$ constant and it corresponds to the first harmonic/order frequency response obtained in Eq. 5.4. For $f_M \gg f_p$, the frequency response of the STO is inversely proportional to the square of f_M. We propose in the following to verify both trends of Eq. 5.8, while in the case $f_M \ll f_p$, we will also be interested in the second order/harmonic frequency response given in Eq. 5.4.

5.2 Experimental protocol

Our modulation experiments are done with a standard analog microwave generator (model Agilent®PSG analog source E8257B). The signal generated is a pure sinusoidal signal. The rejection of the second harmonic of the signal is more than 30 dBc so that it can be neglected. Contrary to the experiment in [146], we use a rather simple experimental

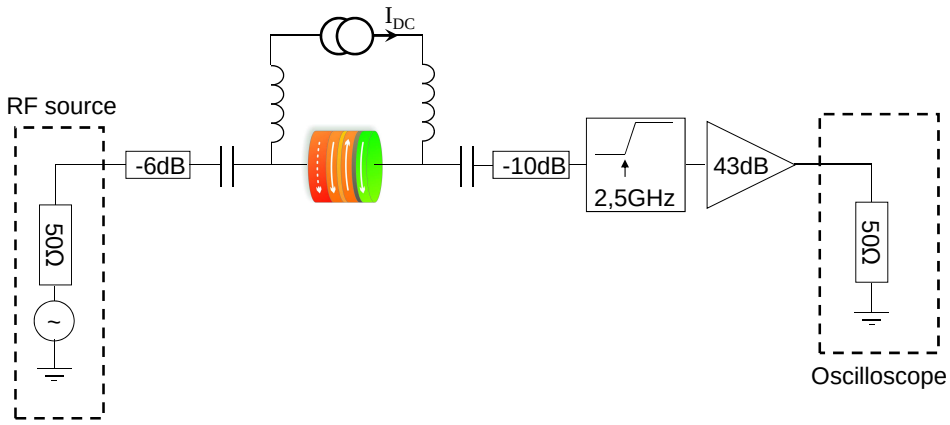

Fig. 5.3: Experimental setup for modulation measurements. This setup provides a reliable measurement of the STO RF generation with the single shot oscilloscope.

protocol that does not involve any complex interferometry setup. Moreover, as discussed in the previous section the estimation of the agility (the phase response in Eq. 5.5) is simple compared to the indirect demonstration made in [147]. The experimental protocol we use in modulation experiments is shown Fig. 5.3. We describe the measurement chain from the left to the right.

The RF source is connected to one port of a transmission device. A 6 dB attenuator is positioned in between the bias-tee and the source. Its purpose is to reduce the standing wave in the left part of the chain due to the strong impedance mismatch between the 50 Ω chain and the $R_{\mathrm{MTJ}} \approx 600$ Ω. The DC current is supplied through two identical bias-tees whose lowest frequency of the high frequency port is $f = 80$ kHz (e.g. from 80 kHz, $S_{21} > -1$ dB). It allows input modulating frequencies down to 90 kHz without further compensation.

The right arm is dedicated to the measurement instrument. Before amplifying the signal by 43 dB in the band of 100 MHz - 14 GHz, we filter out the low frequency component that can arise from the RF source. This filtering technique allows one to amplify at a higher gain without saturating the amplifiers (as observed in Ref. [146]) and is therefore suitable for time domain measurements of spin valve structures. In fact, while the power of the RF source is set between −30 to −20 dBm, a fraction of this signal directly enters the right part of the chain (with 5 to 10 dB of losses due to the impedance mismatch). Therefore, a fraction of power enters the amplifier and risks to "saturate" it as in the case of the experiment of [146]. The high pass filter is a cavity filter with a rejection higher than 50 dBc from DC to 2.5 GHz. Therefore, it does not absorb the modulating signal. That is why a 10 dB attenuator is positioned between the MTJ and the high-pass filter: the backward wave (and therefore the standing wave) can be suppressed. The signal is then measured with the 50 Ω single shot oscilloscope. Time traces are 20 µs long.

The idea of this measurement is to obtain the frequency response of the STO to a microwave excitation of different power P_{mod} and frequency f_M. The frequency response is either defined by Eq. 5.4 or by the first order response Eq. 5.8. We expect the STO to respond to low frequency excitations when $f_M < \Gamma_p/\pi$ and to have a frequency response that becomes attenuated for $f_M > \Gamma_p/\pi$, we thus apply modulation frequencies f_M over

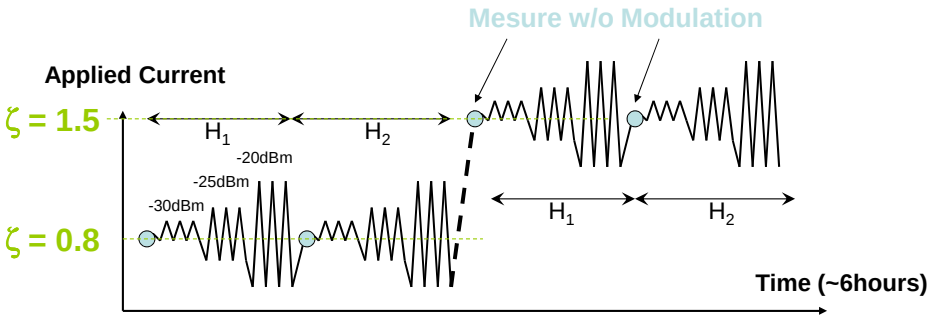

Fig. 5.4: Experimental protocol principle. Before injecting microwave current to the structure, a time trace is acquired under H_{mod} and under constant current (ζ varies from 0.8 to 1.5). Then P_{mod} gradually increases. For each P_{mod}, f_M is varied from 100 kHz to 2 GHz.

several decades. Therefore, hundreds of time traces are acquired for each applied source power P_{mod}, applied DC current I_{DC} and applied field H_{app}. The oscilloscope requires at least 2 seconds to acquire and save the 20 µs time trace, while the RF source needs a certain delay to adjust its frequency. Therefore, the experiment lasts several minutes with I_{DC} near the current breakdown[3] with a microwave stress of different intensities: the device does not keep its main characteristics during the whole measurement.

To take into account this possible effect on the measurement, we used a specific measurement protocol, shown in Fig. 5.4. The overall measurement time is about 6 hours. First, the DC current I_{DC} and the external field H_1 are applied and a time trace without any modulating current is acquired. Second, the RF source is set to the lowest power value ($P_{mod} = -30$ dBm) and its frequency is swept from $f_M = 100$ kHz to $f_M = 2$ GHz with an adaptive frequency step to obtain several measurements on each frequency decade. The source power is increased (up to $P_{mod} = -20$ dBm) before the field is changed to H_2 and the previous steps reproduced. Finally, the current I_{DC} is increased until the voltage breakdown of the (HTMR) sample that occurred when $\zeta = 1.5$ under the maximum modulation strength for the device presented here. Since we only present this method as a tool to extract Γ_p and to highlight the main features of the nonlinear compensation of the dissipative terms, we only present a detailed the study on the modulation results for $H_{app} = H_1 = -490$ Oe.

5.3 Modulation Experiments

The results are presented in two forms. The first manner to represent the effect of the modulation current on the STO is the spectrogram. We have explained in section 3.2.3.2 that spectrograms are inadequate to provide enough precision to characterize all timescales of the phase/frequency fluctuations of oscillator output. When applying the microwave modulating current, we expect that the frequency modulation depth is high (i.e. the STO changes significantly its mode frequency) so that during slow modulation

[3]HTMR samples exhibit a breakdown time apparently given by the E model (i.e. the junctions break according to a statistical model based on energy bonds). The DC voltage breakdown varies among samples from 0.3V to 0.5V. The critical current I_C corresponds to critical voltage $V_C \approx 0.25 \sim 0.35$ V.

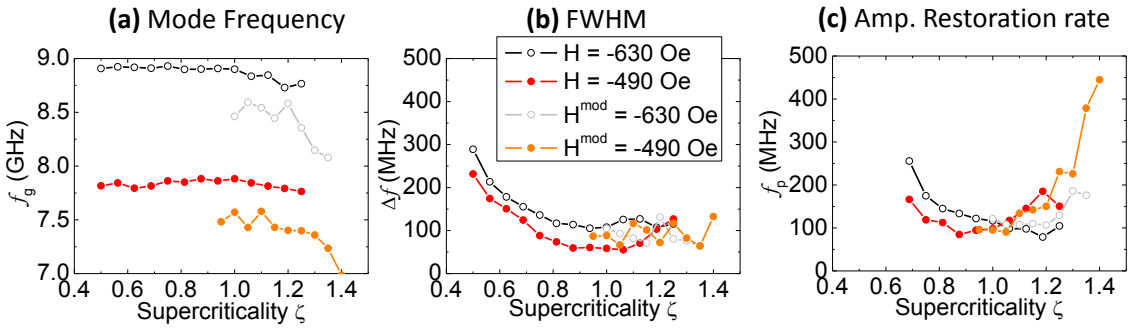

Fig. 5.5: (a) Mode frequency, (b) FWHM and (c) $f_p = \Gamma_p/\pi$ versus supercriticality ζ for different fields. The first characterization of the sample has been realized for $0.4 < \zeta < 1.2$ (black circles and red dots) and then the protocol described in section 5.2 has been applied for $0.6 < \zeta < 1.5$ (gray circles and gray dots, labeled H^{mod}). Our reference measurements are the orange curves. However, degradation occurs during the experiment.

frequency f_M, the STO frequency modulation is observable with spectrograms. The second way to represent the effect of modulation is the amplitude and phase noise plots. Here, we will use the frequency noise plot S_ν that has been defined in section 3.2.1. We will use them to directly quantify and qualify the frequency response $A(f_M)$ of the STO over the microwave modulating excitation.

The main characteristics of the STO devices that we used for the study are given in Fig. 5.5. The sample exhibits a clear redshift and a linear decrease of the linewidth below the threshold. It is assumed that this circular device of 62nm of diameter exhibits a typical IPP mode. It is worth noting that the main characteristics of the STO slightly changes during the modulation experiment where the mode frequency slightly decreases for both fields studied. Many effects, such as heating of the sample, heating of the electromagnet that provides the applied field, or slight sample conditioning[4] can be the origin of this changes. Our reference frequency f_g, FWHM Δf and restoration rate Γ_p will be those of the autonomous STO measured during the modulation experiment (orange curves labeled H^{mod}, when P_{mod} is set to 0 in Fig. 5.5) since they are measured just before the modulation experiment starts at a given ζ (see Fig. 5.4).

We have divided the experimental results into three sections. The first section gives the qualitative features that can be obtained from frequency modulation both in sub- and super-critical regimes. The last two sections give the quantitative results that can be obtained from experiments using the full frequency response Eq. 5.4 at low frequency modulation and the results that can be compared to the frequency response $A(f_M)$ in Eq. 5.8.

[4]Prior to the first dynamical measurement, the TMR was 63% and the RA= 1.7Ω.µm^2 that end in TMR= 83% and RA= 1.8Ω.µm^2. This increase of both TMR and RA sometimes happens in HTMR samples. We suppose the sample exhibits a redshift when increasing $\zeta > 1$, and that the FWHM also increases from $\zeta > 1$.

5.3.1 STO Spectrogram under low frequency modulation

We first illustrate the general features induced by applying a modulation frequency of 500 kHz that allows one to understand the basic concept of frequency modulation over some periods of oscillation of the AC source. Secondly, we illustrate the information that can be obtained from time domain experiments at low modulation frequency 100 kHz. In this case, we can extract the time varying frequency and linewidth with precision.

Fig. 5.6-a,b show typical spectrograms obtained in the below-threshold ($\zeta = 0.9$) and above-threshold ($\zeta = 1.25$) regimes with the highest modulation depth ($P_{mod} = -20$ dBm) and a relatively low modulation frequency ($f_M = 500$ kHz). In Fig. 5.6-c,d with the same timescale, we report the integral of the PSD peak computed on every segment that has been used to create the spectrogram. The segments are 82 ns long and the overlap between each segment is 50%.

We can see in the sub-threshold regime ($\zeta < 1$) that the output power is modulated while the mode frequency is constant over the time. In the above critical regime ($\zeta > 1.2$), the signature of the frequency modulation of an IPP mode is clear. Indeed the downward frequency shift (redshift) in the spectrogram is observed together with an increase of the integrated power of the peak (i.e. higher value of the applied current in Fig. 5.6-d). It is important to note that the increase of power is directly associated with the increase of the instantaneous current that is applied to the STO. Indeed, as explained in the previous chapter, the power measured in watts is proportional to the resistance variation times the square of the applied current. From the power measurement, it is however difficult to evaluate the effective microwave current felt by the STO, i.e. the absolute value of I_{AC}.

In order to further analyze the sub- and the super-critical regimes during the modulation of the DC current applied to the STO, spectrograms using larger time windows have been used. For this, we reduced the modulation frequency f_M down to 100 kHz in order to have a better appreciation of the STO characteristics. In fact, a specific post treatment has been performed on the 20 µs time traces. First, sliding windows of 65536 points (i.e. ≈ 1.310 µs long) with 10% of overlap have been selected. Each window has been cut into 16 non-overlapping time traces whose PSDs have been calculated and averaged. The resulting PSD has a spectral resolution of ~ 12 MHz (82 ns), which is enough to have a rough estimation of the FWHM Δf by a Lorentzian fit (the FWHM is supposed to be 4 times higher than this resolution).

In Fig. 5.7 we report the time varying frequency, FWHM and power of the STO under current modulation of frequency $f_M = 100$ kHz and different power in the above (left panel) and the below (right panel) threshold regime. All values have been obtained from Lorentzian fits as described above.

In the below threshold regime ($\zeta = 0.9$) the time evolution of the frequency, the FWHM and the power under modulation are what is expected from the KTS model. Namely, the frequency is almost constant during the modulation, while the linewidth is substantially affected. Once again, the peak power is modulated mainly by the current conversion effect ($P_{peak} \approx \Delta R_{dyn} I^2$, where ΔR_{dyn} is the AC resistance generated by the magnetization dynamics and I the applied current to the MTJ) while the power variation is surprisingly high for $P_{mod} = -20$ dBm. The measurement time spent between each measurement may explain the downward shift of the frequency along the modulation

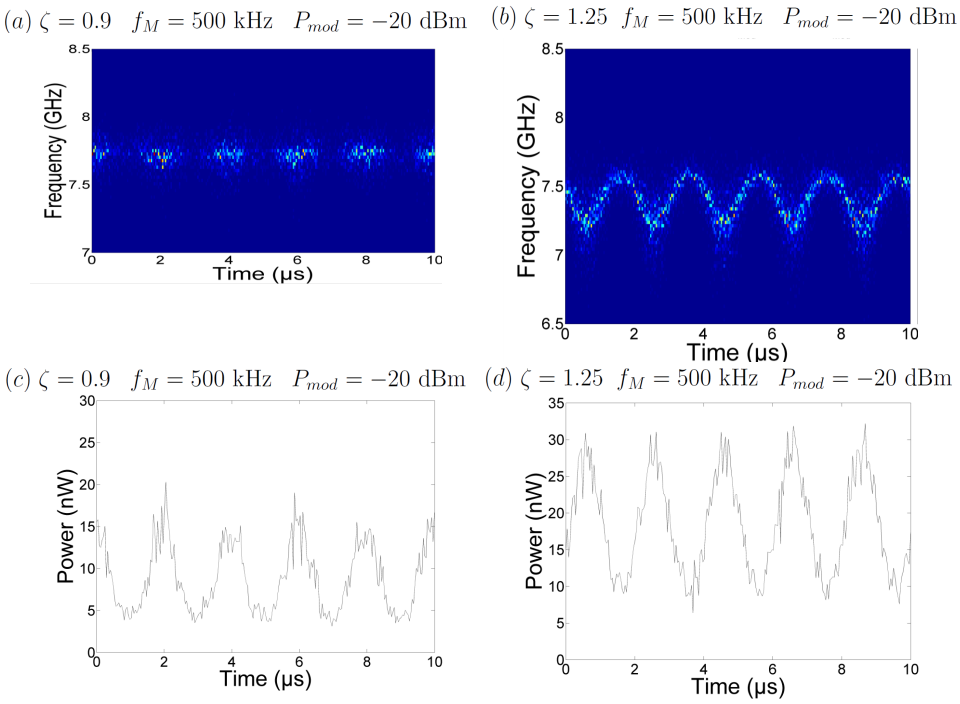

Fig. 5.6: (a) and (b) Spectrograms obtained on a 10µs segment in the sub-threshold ($\zeta = 0.9$) and supercritical ($\zeta = 1.25$) regime while a modulating current ($f_M = 500$ kHz and $P_{mod} = -20$ dBm) is applied to the STO (linear scale, a.u.). (c) and (d) give the corresponding integrated power calculated as the integral below the spectra used to plot the spectrograms. The PSD segments are 82 ns long and the overlap between each segment is 50%. In (a) and (c), only the output power is modulated while the mode frequency is constant over time. While in (b) and (d) it appears that the highest power corresponds to the lowest mode frequency, as expected from an IPP mode with a redshift.

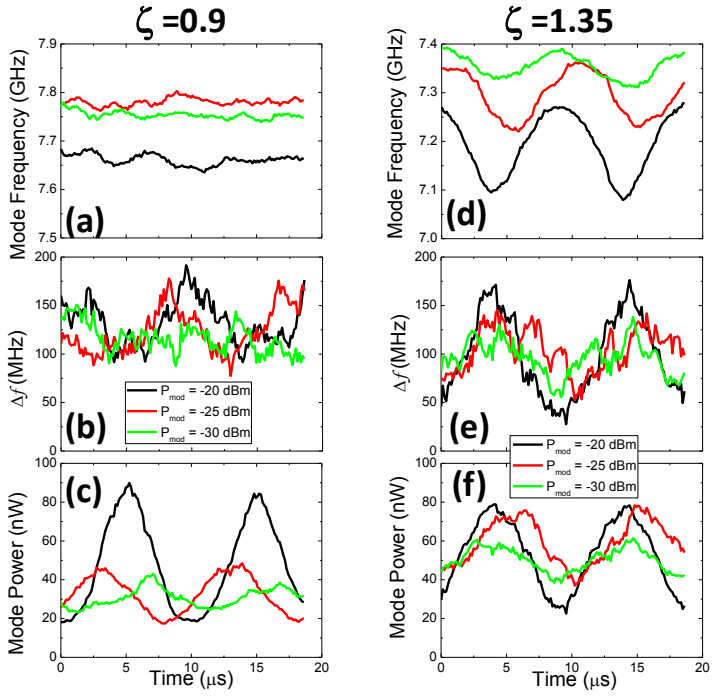

Fig. 5.7: Time varying frequency (a) and (d), time varying FWHM (b) and (e) and time varying power (c) and (f) extracted from time traces with different modulation depths P_{mod} (see labels) when $f_M = 100$ kHz. Left panel sub-critical regime ($\zeta = 0.9$) and right panel super-critical regime ($\zeta = 1.35$).

measurements. Indeed, since 10 minutes separate each measurement, we can consider that it is an effect of sample heating (increasing of temperature, sample conditioning) or setup drift (i.e. applied field). Ideally for $P_{mod} = -25$ dBm, the difference between the FWHM at the highest applied current (i.e. the highest peak power measured), $\Delta f_{min} \approx 100$MHz, and the FWHM at the lowest applied current (i.e. the lowest peak power measured) $\Delta f_{max} \approx 160$ MHz, makes a current modulation of about $10 \sim 20\%$ of the applied DC current, i.e. $I_{\mathrm{AC}} \approx 0.04 \sim 0.08$ mA. If we now compare with the deembedding (see section 3.1.4), $P_{mod} = -25$ dBm corresponds to $I_{\mathrm{AC}} \approx 0.08$ mA. Therefore, the linear decrease of the FWHM in the sub-threshold regime can be used to retrieve the modulating current applied to the MTJ.

In the above threshold regime ($\zeta = 1.35$), the minimum of the frequency is observed with the maximum of power, for all P_{mod} applied. It is also noted that the frequency excursion (the difference between the minimal and maximal frequency value) that occurs during the measurement increases with increasing P_{mod}. Moreover, as expected with an increase of Δf with ζ (all HTMR sample exhibits such behavior that is not clear in Fig. 5.5-b because of the aging), the FWHM increases when the frequency is minimal, i.e. when the applied current is maximal. In addition, we see from the shape of the time varying mode frequency $f_g(t)$ that the frequency response of the STO is not purely sinusoidal, indicating the second harmonic response of the STO to the modulating current predicted by Eq. 5.4. However, the average frequency of the mode seems to decrease with the increasing modulation depth P_{mod} in a manner not expected from the KTS model Eq. 5.4. Moreover, the maximum peak power reached when $P_{mod} = -25$ dBm and $P_{mod} = -20$ dBm indicates further irreversible effects during the measurement. The irreversible changes of the sample can be supposedly attributed to stress effects during the long experiments that are not observed during a 20 µs time trace.

5.3.2 Frequency response roll-off

Spectrograms are limited to very low frequency modulation. A more quantitative analysis can be done using the Time domain Spectroscopy Technique (see Chapter 3) to retrieve the frequency PSD S_ν of the STO as shown in Fig. 5.8. Its advantages over spectrograms have been described in Chapter 3, their main interests are that it is possible to retrieve simply both amplitude and phase (frequency) noise. It is clear from Fig. 5.8 that there is a roll-off in the frequency response $A(f_M)$ of the STO above a certain value, as indicated by the dashed blue lines that are guides for the eyes of the measured $A(f_M)$. As written in Eq. 5.8, this roll-off frequency is $\Gamma_p/\pi \approx 100$ MHz (compare to the value of Γ_p in the autonomous regime Fig. 5.5-b). A similar response in the amplitude noise $S_{\delta a}$ is observed (not shown) where an additional modulation (due to electrical modulation) is also present. The total amplitude modulation has been taken into account in recent modulation experiments [70, 73].

If we consider only the low frequency regime ($f_M \ll \Gamma_p/\pi$), we see that the STO response is independent of f_M. In this region, the frequency response $A(f_M)$ between Fig. 5.8-c and Fig. 5.8-b increases by 5 dB, when the modulation power P_{mod} is increased by 5 dB. It is important to note that $A(f_M)$ is proportional to ϵ^2 (see Eq. 5.8). An increase of 5 dB of P_{mod} indeed corresponds to an increase of $A(f_M)$ of 5dB (since in linear scale, $P_{mod} \propto \epsilon^2$). The relative increase of 3 ± 1 dB of the frequency response between

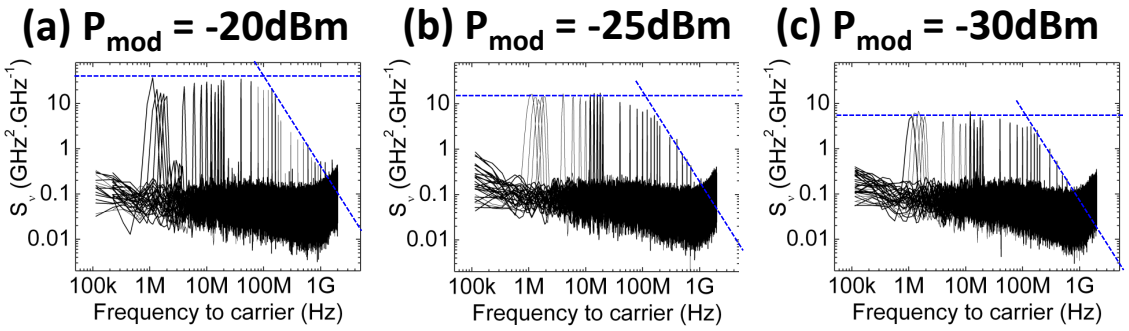

Fig. 5.8: PSD of the frequency noise obtained for all modulation experiments using the ZCM for (a) $P_{mod} = -20$dBm, (b) $P_{mod} = -25$dBm and (c) $P_{mod} = -30$dBm. The dotted blue lines indicate the roll-off of the frequency response. It is worth to note the second order frequency response when $P_{mod} = -20$dBm (small peaks around $f =\sim 5$MHz for example). The change in slope appears for $\Gamma_p/\pi \approx 100$MHz. In this case $\zeta = 1.25$.

Fig. 5.8-b and Fig. 5.8-a is however not expected, even in the case of second order power dependence of the mode frequency Eq. 5.4. Since there is no clear evidence of sample degradation during this part of experiment, this discrepancy may be attributed to the large modulation depth such that the oscillation power returns to zero when the applied instantaneous current is close to its minimum, i.e. at this modulation depth the system is no longer in the auto-oscillating regime. Because $P_{mod} = -20$ dBm represents almost 20% of the DC current $I_{\mathrm{DC}} = 0.52$ mA, this scenario is probable (from deembedding, $I_{\mathrm{AC}} \approx 0.15$ mA). Yet, even when $\zeta = 1.35$ (not shown here), this phenomenon occurs, but in this case the conditioning of the sample is also probable.

Finally, we note that Γ_p/π is not the maximum modulation frequency that the system can respond to. Indeed, if the frequency response for $f_M = 1$GHz is not visible for the lowest modulation depth P_{mod}, a clear frequency response of the STO appears at $f_M = 1$ GHz when $P_{mod} = -20$ dBm. The STO can work virtually at all modulation frequencies, but the specification (the conversion factor frequency/milliampere) is only constant below Γ_p at about 3 MHz/µA.

5.3.3 Nonlinear damping Q extracted from modulation experiments

We have discussed the possibility of the second order frequency response for low modulation frequency. As shown in Fig. 5.9, the frequency response PSD of the STO reveals a second order frequency response for any $f_M < f_p$. If we now consider the ratio $r = a_1/a_2$ between the frequency response a_1 at f_M and a_2 at $2f_M$, we have from Eq. 5.4:

$$r = \frac{\left(\epsilon N \frac{\zeta}{\zeta+Q}(1-p_0)\right)^2}{\left(\frac{1}{2}\epsilon^2 N \left(\frac{\zeta}{\zeta+Q}\right)^2 (1-p_0)\right)^2} = \frac{4(\zeta+Q)^2}{\epsilon^2\zeta^2} , \tag{5.9}$$

which finally gives:

$$Q = \zeta \times (\epsilon \times \sqrt{r}/2 - 1) . \tag{5.10}$$

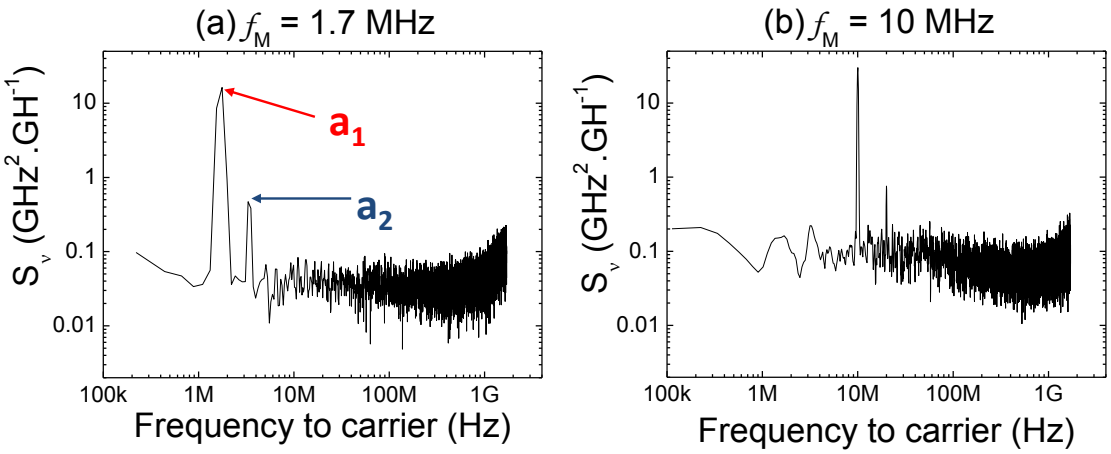

Fig. 5.9: PSD of the frequency noise obtained for $P_{mod} = -20$ dBm, (a) $f_M = 1.7$ MHz and (b) $f_M = 10$ MHz. From these plots it is easy to see the second order frequency response. The ratio a_1/a_2 can be calculated for any $2f_M < f_p$. Above this value, the analysis is more tedious. $\zeta = 1.25$.

From Fig. 5.9, we have $r \approx 40 \sim 100$. Since $\epsilon = I_{\rm AC}/I_{\rm DC} \approx 0.15/.5 \approx 0.3$, $Q \approx -0.2 \sim 0.6$ with a mean value of 0.2 for 1 MHz $< f_M <$ 30 MHz from 11 different frequencies. In the KTS model, Q was estimated to be $0 \leq Q \leq 3$ for an IPP mode [54].

In order to measure the value of Q with more accuracy, it would require a more systematic study that the one presented here. In particular, one should focus on the exact determination of ϵ which considerable influences the extracted value of Q. Also, MTJ-based STOs are very sensitive to current stresses which affect the quality of the insulator barrier. Therefore, it would be worth to try these modulation experiments on GMR-based STOs that are more robust to current stresses. In addition, this method of extraction of Q based on Eq. 5.9 should be confirmed in macrospin simulations on magnetic configurations where the value of Q can be calculated almost analytically (for example, by identification of p_0 obtained from the renormalization of the macrospin trajectory in p-variable (e.g. Fig. 4.15-b) with Eq. 2.27).

5.3.4 Conclusion on modulation experiments

We have experimentally verified the effect of a time varying spin transfer torque term on the dynamics of the magnetization. We find a good agreement between theory and experiments, where Γ_p is the key parameter that sets the timescale of the transient state of the STO. Indeed, we showed that a relaxation phenomenon exists when the state of the STO is changed. While it has helped to understand the physical concepts underlying the modulation of the STO's frequency, we have also addressed one of the most important characteristics of the STOs that: agility.

Indeed, besides potential applications in frequency synthesizers, STOs are proposed to be a part of the next generation read heads of hard drive disks. The basic idea is to measure the bit transition in the media by measuring the frequency change of an STO that is positioned above the magnetic bits. Based on the KTS model, it has been predicted

that high data transfer rates can be achieved by this technique [149, 150, 153, 155, 156] Recently, experimental proofs have shown the possibility of using STOs with a field pulse of 1 ns [151, 152, 157], i.e. a reading rate of 1 Gbit/s, with a carrier frequency of only 3 GHz.

The telecommunication and read head applications motivate the interest of both theoretical and experimental investigations to understand how to increase the amplitude restoration rate Γ_p. In the following we present two aspects where the restoration rate of the auto-oscillation is primarily involved. The section related to the noise in current could have been given in section 4.6 on phase noise originating from noise current. However, we show it here since the noise in current is related to the modulation aspects discussed above, except that it corresponds to small modulation amplitudes, and as a white frequency noise, white frequency current noise acts on the STO within the same strength at all frequencies.

Finally we investigate a simple RF design widely used by RF engineers, where a modulating current is generated in order to "instantaneously" compensate the noise in frequency (coming from thermal fluctuations). Such a design is called a phase locked loop (PLL), where an input parameter (such as the input DC current to the STO) is used to "control" the phase of an auto-oscillator. We only focus on the interpretation of the PLL and we will not focus on its detailed study (i.e. a parametric study of the stability of the PLL).

5.4 Perspective: noise in current and cyclostationary processes

We have mentioned in section 4.6 the possible presence of flicker, i.e. $1/f$, current noise in some of our devices that would generate a flicker amplitude noise, which ,due to the nonlinear amplitude coupling, results in a flicker frequency noise. To first verify that a noise in current leads to phase noise, we investigate the effect of current noise on the magnetization dynamics from macrospin simulations. From the modulation experiments presented in section 5.3, it is clear that it would induce a noise in Γ_- that will affect in first place the amplitude of the auto-oscillation. From the KTS theory, we can therefore describe the magnetization subject to a current noise by the equations:

$$\begin{aligned} \frac{d\delta p}{dt} + 2\Gamma_p \delta p &= 2\sqrt{p(t)}\xi(t) \\ &, \\ \frac{d\Phi}{dt} + \omega_0 + N\delta p_0 + N\delta p &= 0 \end{aligned} \tag{5.11}$$

where $\xi(t)$ is real and delta correlated whose diffusion constant is given by current fluctuations. Since $2\sqrt{p(t)}\xi(t)$ would be non-stationary, we approximate $2\sqrt{p(t)}\xi(t) \approx 2\sqrt{p_0}\xi(t)$ under the assumption of small power fluctuations. We see that there is no direct noise contribution of the phase, in contrast to the phenomenological noise term $f_n(t)$ in KTS theory.

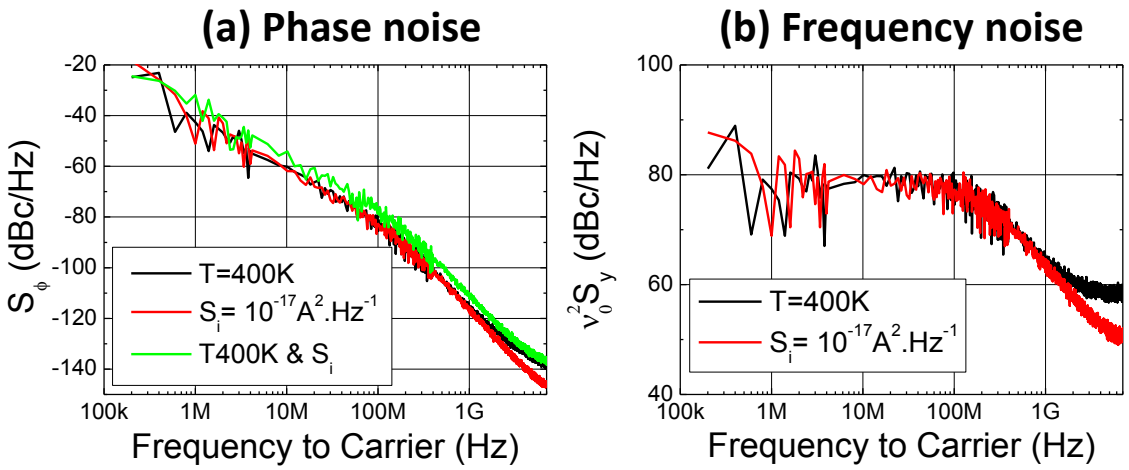

Fig. 5.10: (a) PSD of phase noise for three different cases: (i) thermal fluctuating field (black curve), (ii) current noise of strength S_i (red curve) and (ii) thermal fluctuating field and current noise (green curve). (b) PSD of frequency noise for case (i) and (ii). Simulations have been performed by F. Garcia with the same material parameters as those used in chapter 4.

The results of macrospin simulations are presented in Fig. 5.10, where we show three different situations: (i) a thermal noise field has been considered (black curves), (ii) only white frequency current noise has been considered (red curves) and (ii) when both noise contributions are present (green curve).

The effect of the current noise in Eq. 5.11 as compared to the effect of the thermal noise in Eq. 2.35 is clearly seen in Fig. 5.10-a,b as we will discuss now. In Fig. 5.10-b we show the frequency noise plots where the slopes can be better estimated. It is clear that in the presence of the current noise alone (red curves), there is no "linear" contribution to the phase or frequency noise, while when considering the temperature noise only, this linear noise contribution exists (black curves). Moreover, the two independent nonlinear contributions to phase noise are additive (green curve is 3 dB above the two others in Fig. 5.10-a), as expected from KTS model with two independent noise sources.

Since we work with MTJs, we may consider that the shot noise could lead to such a white noise contribution in current, and therefore shot noise may be the origin of the linewidth broadening we observe experimentally. However, the results from temperature dependent experiments do not seem to be in agreement with this statement, at least in HTMR. Indeed, we have observed, at least in the region T = 100 - 300 K for HTMR devices, a linear decrease of the noise Δf_0 (accompanied with a decrease of FWHM Δf, see Fig. 4.36 in section 4.5). Nevertheless, the noise current can contribute to the linewidth broadening below T = 100 K. To confirm this, one should observe an increase of $|\nu|$ extracted from TDNS upon decreasing the temperature while the FWHM Δf of the STO remains constant. However, the "electrical background" found in experiments so far for both the phase and the amplitude noise make it difficult to identify such a contribution.

Nonetheless, the current noise measured so far in our LTMR-MTJs seems to be about $S_i \approx 10^{-21}$ A^2.Hz^{-1} (see noise floor at high frequencies in Fig. 4.40 section 4.6). It is worth noting that in LTMR MTJs, we did not observe any temperature variation

of the FWHM $\Delta f \approx 10 \sim 30$ MHz (from 20 K to 300 K). Moreover, in the case of macrospin simulations, when $S_i \approx 10^{-21}$ A^2.Hz^{-1}, we observed a $\Delta f \approx 20$ MHz (not shown here), that is the value observed in LTMR devices. Finally, in LTMR devices, the FWHM exhibit a plateau in its value (from $\zeta = 1.2 \sim 1.8$) that only starts to increase for very high current densities ($\zeta > 1.8$). Once again, more temperature dependent measurements in MTJs based STO would help to answer to this question.

Finally, this approach of "current noise" involves the notion of cyclostationary noise sources [158] in STOs. Indeed, in the case where the MTJ-based STO is driven by voltage, we have seen that the electrical current that flows in the MTJ is proportional to the angle formed by the pinned and free layer (see Eq. 1.4). In addition, the shot noise in tunnel junctions, is proportional to the amount of current flowing through the structure. In simulations of Fig. 5.10 we only assumed a constant current noise amplitude that did not vary along the trajectory.

Considering that we have just seen how the current noise may affect the dynamics of the STO, and that the DC current naturally fluctuates with the magnetization dynamics (see Eq. 1.4), we can consider that the current noise (shot noise) will have different amplitudes along the trajectory. This noise therefore depends on the closed-loop trajectory: it is called a cyclostationary process (a process that is stationary with "a cycle" of the oscillator). In general, the study of these noise contributions to the oscillator phase noise is a tricky question that requires advanced modeling software tools, but can still be integrated in the LLGS equation coupled to transport models.

5.5 Perspective: PLLs

The final perspective section of this chapter on modulation is the phase locked loop (PLL) that can be achieved in STOs. Typically, PLLs are used to "control" the phase of a noisy oscillator using a less noisy oscillator that oscillates at lower frequency.

In Fig. 5.11 the block diagram (from SIMULINK®) of a simulated PLL for a STO, designed by M. Zarudniev, is given. The block diagram labeled "STO" resolves the KTS equations 2.35 for an instantaneous input that is the DC current. The outputs of the block are the total phase and the total power, as well as the total (real) signal. The total phase is divided by 10 by an ideal frequency divider. The output of this divider is compared (by a phase comparator) to an ideal cosine signal whose frequency is 10 times smaller than the mode frequency f_g of the noisy STO. Finally, the output of the phase comparator is filtered (the cut-off frequency is below Γ_p/π and especially below the mode frequency divided by 10) and fed back to the input port of the STO model. The results of the STO controled by this PLL are shown in Fig. 5.12 and are compared with the "free-running STO" outputs, i.e. when the PLL state is OFF. In Fig. 5.12-a, we see that the PLL transforms a 140 MHz linewidth signal to a Dirac peak (the "pure" signal the STO is compared to).

We can see that the effect on phase noise is straightforward: no phase correction is done above the low-pass filter cut-off frequency $f_c = 100$ MHz. For $f < f_c$, the phase noise of the STO has a slope $1/f^0$ instead of the slope $1/f^2$: the phase noise is canceled (compare the black (PLL ON) and gray (PLL OFF) curves in Fig. 5.12-b). This is a

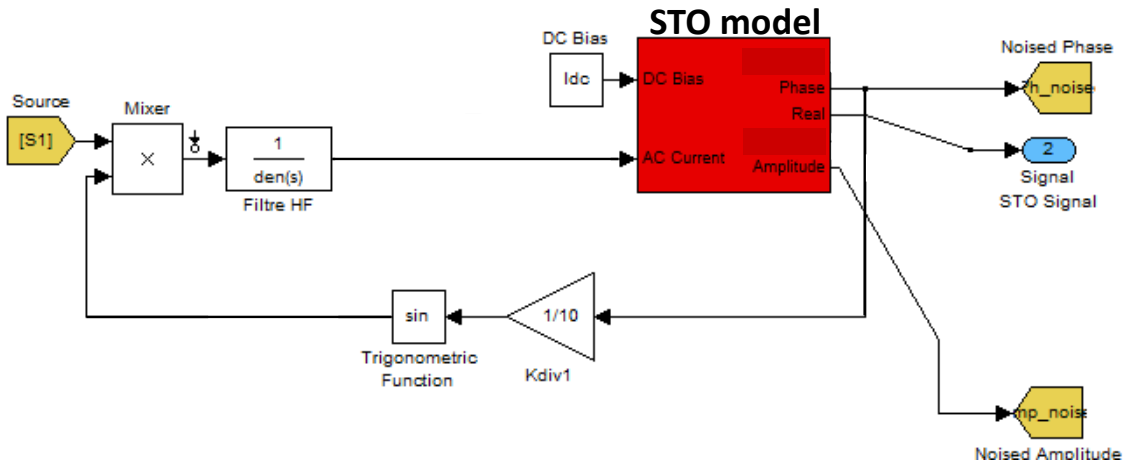

Fig. 5.11: Phase locked loop (PLL) block diagram designed by M. Zarudniev (CEA-LETI) using SIMULINK®. The red block diagram is the STO modeled using a KTS equation (power / phase). Parameters are $N = -4 \times 10^{10}$, $Q = 1$, $\sigma = \Gamma_G = \pi 0.3 \times 10^9$, $\omega_0 = 2\pi 10^9$ rad.s^{-1}, $p_0 \approx 0.33$ ($\zeta = 2$) and $T \approx 300$ K. The free running STO is defined by: $f_g \approx 7.87$ GHz, $\Delta f \approx 140$MHz and $f_p \approx 300$MHz. The filter is a second order low-pass filter with a cut-off frequency $f_c = 100$ MHz. The ideal signal is generated by the same STO model, without noise contribution in phase and amplitude. The division factor is 10.

general feature of PLLs: the phase noise is canceled below its cut-off frequency (f_c). We can understand that in the case case of a PLL, the perturbing current is used to stabilize the auto-oscillation. We can see that the decrease of phase noise is associated with a similar decrease of amplitude noise (compare red (PLL ON) and blue (PLL OFF) curves in Fig. 5.12-b). This effect can be simply understood by the fact that decreasing the phase noise in the region $f < f_c < f_p$ is equivalent to decreasing the nonlinear contribution to the phase noise, i.e. decreasing the amplitude noise of the STO.

Usually, the frequency division is higher than 10, since the oscillator to control is phase compared (after division) to 10 MHz or 100 MHz stable oscillators. To have a better efficiency, the retro-acting current frequency should be below Γ_p/π (it is the case here since $f_c < f_p$). When dividing by 100 (such that the reference oscillator has now a frequency of ≈ 80 MHz) and adapting consequently the low-pass filter cut-off frequency to $f_c = 10$ MHz, the shape of the corrected phase noise is similar to the one presented in Fig. 5.12-b, but the correction now starts around $f \approx f_c = 10$ MHz (in the case of Fig. 5.12-b we have identified this frequency to be around 100 MHz). It makes the phase noise to be around -60 dBc/Hz at 1 MHz with a division by a factor 100, while it is -80 dBc/Hz at 1 MHz with a division by a factor of 10. We note that the corresponding measurement has been done in Ref. [86] with a vortex-based STO and no frequency division in the PLL. The large decrease of linewidth observed in their experiment can be attributed to the control of the phase deviation of the vortex-based STO.

The PLL results presented here are a toy model and cannot serve as a real demonstration of a PLL design since, for example, no delays have been taken into account. Preliminary results show that short delays strongly influence the stability of the PLL and would require more detailed studies.

All RF VCOs that are used in telecommunications (i.e., commercially) are phase

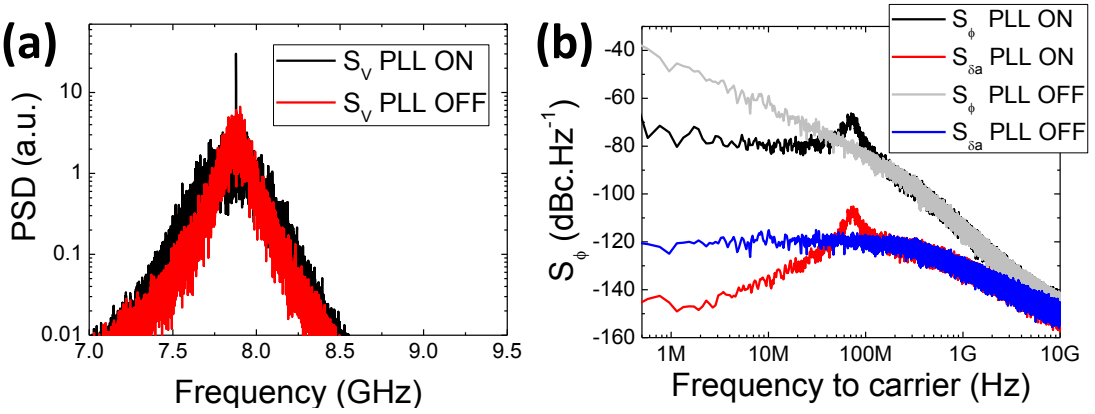

Fig. 5.12: (a) Comparison of the signal PSD of the resulting signal with PLL state ON and OFF. (b) Comparison of phase and amplitude noise with PLL state ON and OFF.

controlled by advanced PLL designs [159]. What will make the choice of a design of PLL+VCO for practical use over another PLL+VCO's design is the cost in space of the PLL+VCO on the chip, the price of the device and finally the ratio power consumption over phase noise specifications. In the case of STOs, the study of practical design PLL+STO, versus nonlinear parameters would be useful to understand what in STOs should be improved in priority (Γ_p, $|\nu|$, Δf_0).

Finally, we see that the PLL acts as if the STO were phase locked to another oscillator (with a lower frequency). In the next chapter, we study in more detail the direct "phase to phase" synchronization phenomenon, which is the forcing of the phase of the STO to an external phase signal: the injection locking experiment.

Chapter 6

Synchronization

Synchronization or mutual phase locking of several hundreds of STOs has been imagined to increase the total emitted power [160, 161] and to reduce the intrinsic (high) phase noise present in a single STO. It is a general assumption that a network formed of N quasilinear oscillators, each under the influence of their own internal noise, oscillating coherently, would reduce the phase noise factor of the total network output by a factor of about N [162]. In the case of STOs interacting with each other, the analysis of only two interacting STOs can already become rather complex when coupled via their generated AC current [163]. Therefore, the study of the phase coherence of an STO interacting with an external signal is of crucial importance to determine the behavior of an STO interacting in a more complex network.

A brief review of injection locking experiments has been given in section 2.2. One recent experimental result of STOs is the fractional synchronization [164, 165, 166]. In these experiments, an external force can synchronize the STO frequency f_g to any frequency f_e that respects the condition $f_e = \frac{p}{q} f_g$ with p, q integers. It is virtually possible to synchronize the STO at all frequencies f_e.

The fractional synchronization is explained through the symmetries of the trajectory over one period ($q = 1$) or several ($q > 1$) periods with respect to the symmetry of the excitation force acting on $\vec{M}$ [164]. Here we focus our study on the "fractional" synchronization for varying p and constant $q = 1$. We first highlight the symmetry of the STT on a macrospin trajectory of an in-plane precession mode, in order to give insight into the non-trivial synchronization conditions for $p > 1$. Afterwards, we present a model that has been developed by Zarudniev et al. [167]. This model aims to give mathematical arguments of this synchronization condition that is related to the ellipticity of the macrospin trajectory.

The experimental confirmation of the fractional synchronization and further aspects of the synchronized state are then demonstrated for three cases: (i) the IPP mode of HTMR MTJ devices, (ii) the non-trivial mode of LTMR devices and (iii) the vortex mode of the out-of-plane polarizer structure [168, 169].

To analyze the experimental results in the case of the IPP mode, we conduct macrospin simulations in the presence of noise to understand how the effect of a microwave current compares to external (thermal) noise. From macrospin simulations, we give the main features of this non-autonomous regime with the additional presence of noise where the nonlinear parameters (Γ_p and ν) play an important role, to highlight the features

of the autonomous regime that can be used to describe the non-autonomous regime, which are relevant for applications. As further experimental proof, we extract the time varying phase of the LTMR device in the phase locked regime that we compare with the predicted features of the non-autonomous regime of a non-isochronous auto-oscillator (from macrospin simulations).

6.1 Macrospin description of the fractional synchronization for the IPP mode

This section presents the conditions of fractional synchronization to an RF current (with $q = 1$) using macrospin simulations for the IPP mode with a polarizer that is collinear to the free layer (FL) magnetization equilibrium position. We first make general comments on the form and on the symmetries of the STT along one period of the trajectory in the presence of a microwave current. Then we show the effect of the microwave current on the macrospin trajectory. To interpret the role of the ellipticity on this fractional synchronization, a model developed by M. Zarudniev et al. [167] is presented. This model allows the possibility to use a simplified phase state representation (i.e. with the amplitude and the phase of an oscillator) of the magnetization under the influence of both DC and AC currents.

6.1.1 Symmetry of the "microwave" STT term

First, we investigate the three components of the trajectory of the magnetization. Fig. 6.1 shows the magnetization components M_X, M_Y and M_Z, with the associated STT term calculated from macrospin simulations. In such a representation, the X-component of the STT term oscillates twice as fast as than the mode frequency f_g. Moreover, at the turning point of the in-plane trajectory of the magnetization, i.e. when $M_Z = 0$, M_Y =max, the STT is the most important for the magnetization dynamics. Indeed, it can be shown that the energy provided by STT is mainly positive (i.e. the anti-damping term plays the most important role) at the turning points, when considering the transient state under DC current before the switching [170] or before the limit cycle is reached. Therefore the "symmetry" condition[1] on STT_X should be satisfied, especially at the point of $M_Z = 0$ (the red circles in Fig. 6.1-d).

We now apply the alternating current at frequency f_e at the vicinity $f_e \approx pf_g$, with $p = 1, 2, 3, 4$, and we consider again the STT term component along one period of the trajectory. Fig. 6.2 shows that when f_e is an even multiple of f_g the symmetry is satisfied. When f_e is an odd multiple of f_g, however, this symmetry condition is not satisfied.

This simple interpretation in terms of the STT symmetry along the magnetization trajectory is confirmed by more detailed simulations of the mode frequency as a function of the frequency of the microwave source f_e, as shown in Fig. 6.3-a. As it can be seen, no or very weak locking occurs when the microwave frequency f_e is located at the vicinity of f_g and $3f_g$, while the STO frequency locks to the external signal over a certain range of frequencies when f_e is at the vicinity of $2f_g$ and $4f_g$.

[1] Symmetry means two cycles of STT_X along one period.

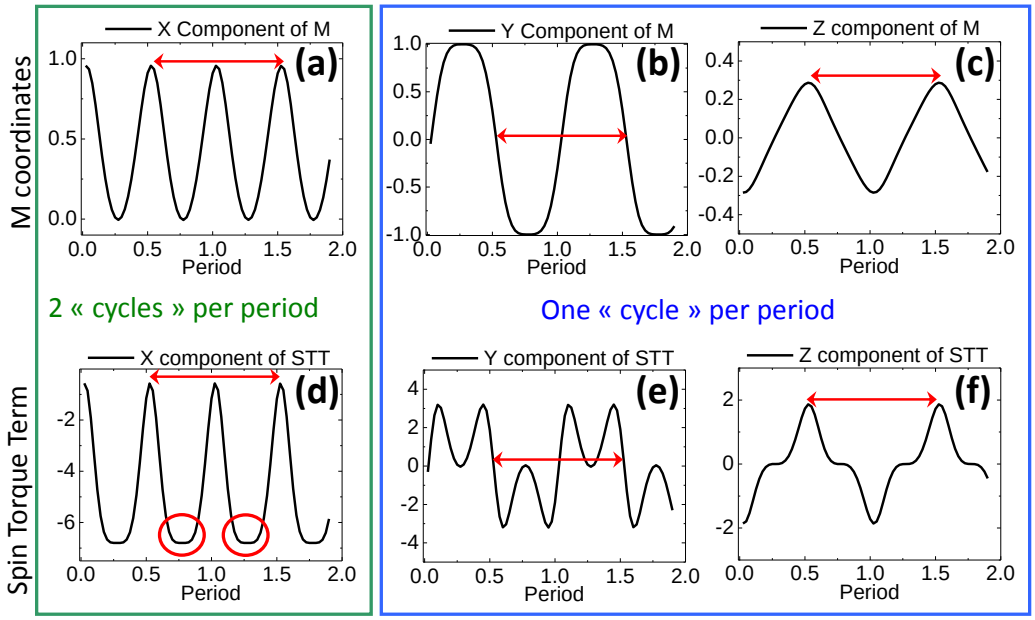

Fig. 6.1: Analysis of a simulated trajectory with DC current without alternating current. Projection of the magnetization on the Cartesian coordinates; along (a) X on (b) Y and (c) Z. The M_x component makes two cycles in one period of oscillation (therefore its frequency is $2f_g$). Decomposition of the STT (a_j) term on the Cartesian coordinates; along (d) X on (e) Y and (f) Z. The X component of the STT term makes two cycles in the period of oscillation.

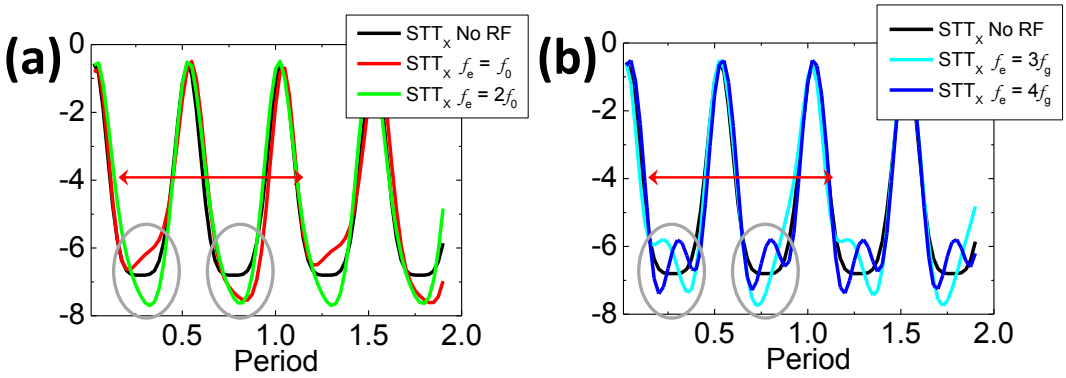

Fig. 6.2: (a) Simulation of STT_X in presence of an alternative current when $f_e = f_g$ and $f_e = 2f_g$. The symmetry condition (the gray circle) is only satisfied when $f_e = 2f_g$. (b) STT_X in presence of an alternative current when $f_e = 3f_g$ and $f_e = 4f_g$. The symmetry condition (the gray circle) is only satisfied when $f_e = 4f_g$.

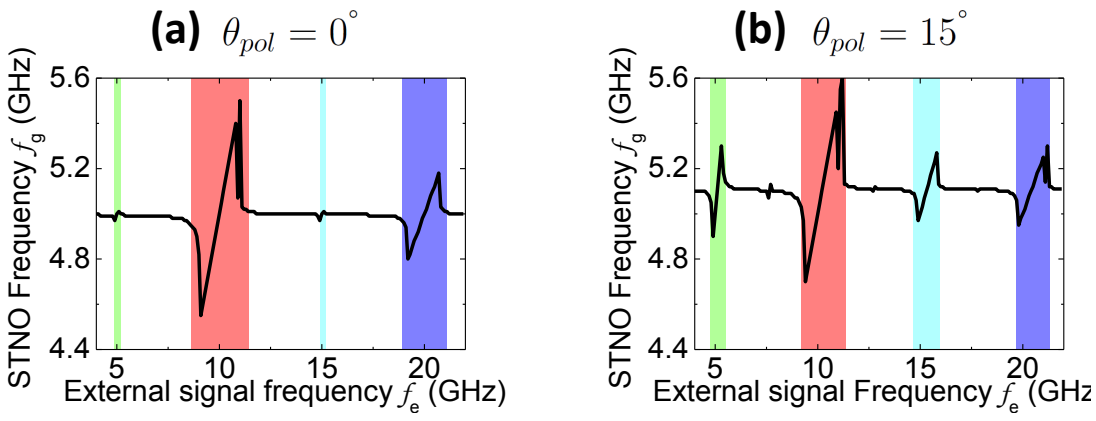

Fig. 6.3: (a) Simulation of the STO mode frequency f_g versus source frequency for $\theta_{pol} = 0^\circ$. (b) STO mode frequency f_g versus source frequency for $\theta_{pol} = 15^\circ$. The same DC and AC currents are applied in both cases ($I_{\mathrm{DC}}/I_{\mathrm{AC}} = 0.6$). Dashed areas represent the locking bands.

When breaking this symmetry condition the odd synchronization condition can be recovered. Such symmetry breaking may happen, for example, by tilting the polarizer direction with an in-plane angle θ_{pol} with respect to the equilibrium direction of the magnetization of the FL. This is explicitly shown in Fig. 6.3-b, where the same current is applied in the case of $\theta_{pol} = 15^\circ$ and of $\theta_{pol} = 0^\circ$. Such a small angle does not affect much the critical current nor the mode frequency f_g (about 5 GHz).

6.1.2 Ellipticity dependent fractional synchronization

We present now a fractional synchronization model directly derived from the LLGS equation derived by Zarudniev et al. [167] for the IPP trajectory.

In a similar fashion to Eq. 2.13, the LLGS in cartesian coordinates and SI units is considered, with an arbitrary in-plane polarizer angle θ_p, an applied field H_0 (collinear to the magnetization equilibrium direction, the X-axis) and no anisotropy. Only the projection of the IPP trajectory on the (Y,Z) plane is considered:

$$\begin{aligned}\begin{pmatrix}\dot{m}_y\\ \dot{m}_z\end{pmatrix} =& -\gamma_0\begin{bmatrix}-(H_0+M_s m_x)m_z\\ H_0 m_y\end{bmatrix}\\ &+\alpha\gamma_0\begin{bmatrix}-H_0 m_x m_y + M_s m_y m_z^2\\ -H_0 m_x m_z - M_s(m_x^2+m_y^2)m_z\end{bmatrix}\\ &+\sigma I(t)\cos(\theta_p)\begin{bmatrix}m_x m_y\\ m_x m_z\end{bmatrix}+\sigma I(t)\sin(\theta_p)\begin{bmatrix}-(m_z^2+m_x^2)\\ m_y m_z\end{bmatrix}\end{aligned} \quad . \tag{6.1}$$

In the *linear* regime, solving this equation would lead to the usual FMR mode and criticality lines, by considering the solution to be oscillating ($\propto e^{i\omega t}$). Since we want to solve it in the nonlinear auto-oscillating state for the IPP mode, we consider the ellipticity of the solution such that:

$$\begin{cases} m_y(t) \approx \frac{r}{2}e^{i\Phi(t)} + \frac{r}{2}e^{-i\Phi(t)} = r\cos(\Phi(t)) \\ m_z(t) \approx \frac{a-1}{2a}e^{i\Phi(t)} + \frac{a+1}{2a}e^{-i\Phi(t)} = \frac{r}{a}\sin(\Phi(t)) \end{cases} , \tag{6.2}$$

with $a \approx \sqrt{\frac{H_0+Ms}{H_0}}$ the amplitude normalization coefficient. If we consider now the complex signal $A = m_y(t) + im_z(t) = r(t)e^{i\Phi(t)}$, in the presence of the oscillating current ($I(t) = I_{\mathrm{DC}} + I_{\mathrm{AC}} \sin \Phi_e$), Eq. 6.1 can be linearized, around a limit circle. This leads to:

$$\begin{cases} \dot{r} = k_d(1 + k_q r^2)r + \sigma I_{\mathrm{DC}} \cos(\theta_p)(1 - k_s r^2)r \\ \quad + k_1 r \sin(\Phi_e - \Phi) + k_2 r^3 \sin(\Phi_e - 2\Phi) + n_p(t) \\ \dot{\Phi} = \omega_0 + N r^2 + \frac{k_1}{r}\sigma I_{\mathrm{DC}} \sin(\Phi_e - \Phi) + n_\Phi(t) \end{cases} . \tag{6.3}$$

Here k_d, k_q are damping terms found by identification with a real macrospin trajectory. The mode frequency is $\omega_0 = |\gamma_0|\sqrt{H_0(H_0 + M_s)}$, $N = -\gamma_0^2 \frac{(a^2-1)H_0 M_s}{8a^2\omega_0}$ and $k_s = \frac{a^2+1}{4a^2}$ (see details in Ref. [167, 171]). $n_p(t)$ and $n_{\Phi(t)}(t)$ are noise terms affecting respectively amplitude and phase of the oscillation. The prefactors of the synchronization terms at f and $2f$ are:

$$\begin{cases} k_1 = -\sigma \frac{I_{\mathrm{AC}}}{2} \sin(\theta_p) \\ k_2 = \sigma \frac{I_{\mathrm{AC}}}{2} \frac{a^2-1}{4a^2} \cos(\theta_p) \end{cases} . \tag{6.4}$$

In fact, one can show that the equation Eq. 6.3 is similar to the one given in the KTS model. In the model presented here, the term k_d and k_q cannot be obtained analytically, while this is possible in the KTS model from the canonical transformation of the system. Therefore, we can consider Zarudniev's model as phenomenological compared to the theoretical KTS model. Nevertheless, we now have a term that can explain directly the synchronization of the magnetization to a signal frequency $f_e = 2f_g$. We have previously mentioned that in Ref. [49], the KTS theory in its simplest form (i.e. Eq. 2.24 in section 2.2.2.1) intentionally eliminates the term that "describes the second order parametric excitation of the spin waves" ($V_h c^*$ and $V_J c^*$ in Ref. [49]). We did therefore not use the KTS formalism in order to qualitatively explain the fractional synchronization here, but it can be probably achieved through the KTS theory.

Finally, from the above expressions 6.4 (neglecting noise) one can write an explicit expression of the locking range $\Delta\omega_1$ at the vicinity $f_e \approx f_g$ and the locking range $\Delta\omega_2$ at the vicinity $f_e \approx 2f_g$ from the stability conditions of Eq. 6.3:

$$\Delta\omega_1 = k_1\sqrt{1 + \left(\frac{N}{k_s\sigma I_{\mathrm{DC}} \cos(\theta) - k_d k_q}\right)^2} \quad \Delta\omega_2 = \frac{N k_2 r_{eq}^2}{k_s\sigma I_{\mathrm{DC}} \cos(\theta) - k_d k_q + k_2} . \tag{6.5}$$

Here r_{eq} is the amplitude in the stationary autonomous regime. This result is very interesting for the following reasons:

1. It gives the θ_p dependence on the synchronization bands (see Fig. 6.4);
2. It confirms that the locking band for $f_e \approx f_g$ is enhanced by the nonlinearity of the system as predicted in Ref. [54];
3. That for $\theta_p = 0$ no synchronization is expected for $f_e \approx f_g$ as predicted in Ref. [66] and shown in section 6.1.1;
4. The synchronization is expected for $f_e \approx 2f_g$ (shown in section 6.1.1);

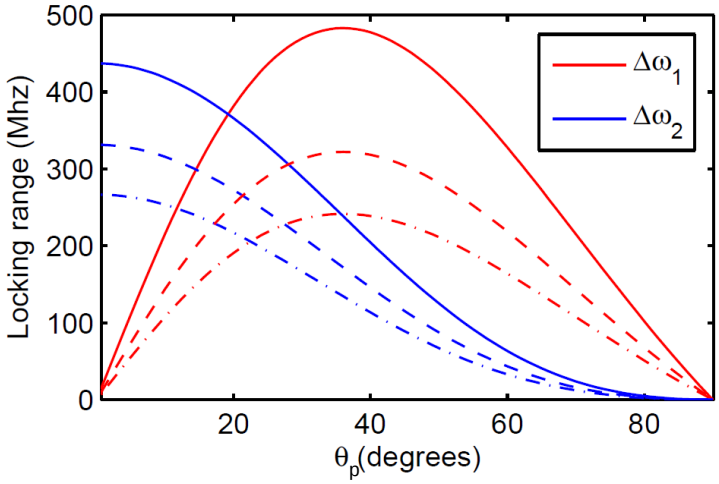

Fig. 6.4: Calculated locking ranges $\Delta\omega_1$ (red) and $\Delta\omega_2$ (blue) from Eq. 6.5 for a fixed I_{DC} and variable θ_p for $I_{\mathrm{DC}}/I_{\mathrm{AC}} = 0.5$ (solid lines), $I_{\mathrm{DC}}/I_{\mathrm{AC}} = 0.33$ (dashed lines) and $I_{\mathrm{DC}}/I_{\mathrm{AC}} = 0.25$ (dashed dotted lines). From [167].

5. The locking condition $f_e \approx 2f_g$ is only possible because of the nonlinearity in frequency ($N \neq 0$).

The last point means that the locking condition at the vicinity $f_e \approx 2f_g$ requires that $N \neq 0$. In fact, it is straightforward to see from Eq. 6.3 that this synchronization only occurs due to amplitude synchronization that stabilizes the phase indirectly through the amplitude phase coupling (N). Finally, the locking bands are calculated in Fig. 6.4 for different ratios $I_{\mathrm{AC}}/I_{\mathrm{DC}}$. For $\theta_p \approx 15^{\circ}$, the locking band $\Delta\omega_1$ is about the same order as $\Delta\omega_2$ as shown in Fig. 6.3.

6.2 Experimental verification

Experimentally, we have confirmed the feasibility of synchronization at $2f_g$ in MTJs on HTMR [166] and LTMR devices at room temperature. Another experimental result obtained for an STO based on a perpendicular polarizer will be shown in section 6.3.4.4 to highlight specific features of the non-isochronous auto-oscillators in a non-autonomous regime. As for the autonomous case in Chapter 4, we discuss first the experimental cases that we can qualitatively compare to macrospin simulations. We focus on the demonstration of the locking condition $f_e \approx 2f_g$ in HTMR IPP mode and LTMR, where we give the locking bands as well as the measurements of the mode linewidth in the locked state, which are possible since the source frequency signal does not perturb the STO signal extraction when $f_e \approx 2f_g$.

6.2.1 HTMR devices

Our experiments were performed by injecting first a DC current I_{DC} into the device to induce a self-sustained oscillation and by tuning the in-plane magnetic field H so that the free running STNO frequency is $f_g^{HTMR} \approx 5.0$ GHz with $\theta_p \approx 5^{\circ}$ in the case of

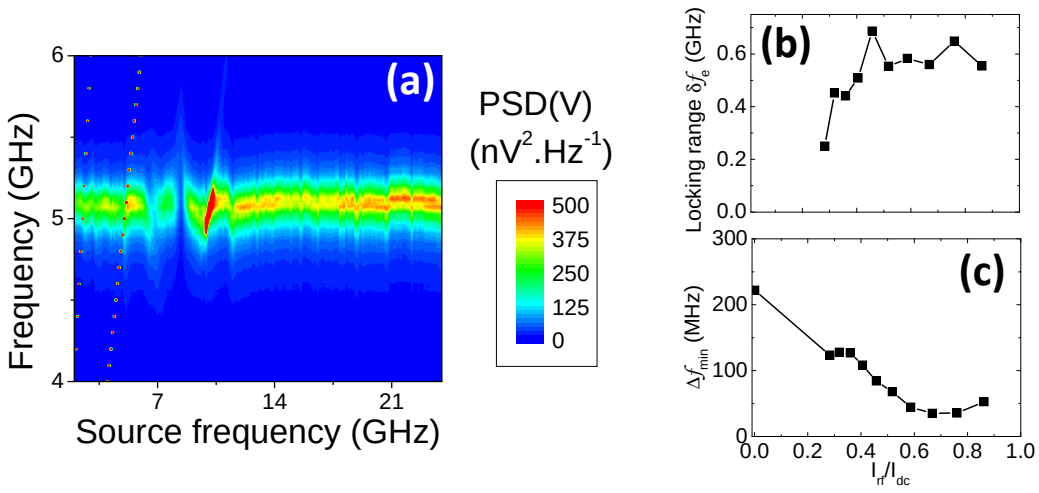

Fig. 6.5: (a) Experimental PSD map (linear scale) of the STO frequency f versus the source frequency f_e for $I_{\mathrm{RF}}/I_{\mathrm{DC}} = 0.37$. Red dots are artifacts of the measurement. (b) Injection locking range δf_e and (c) minimum linewidth Δf_{min} as a function of $I_{\mathrm{RF}}/I_{\mathrm{DC}}$.

HTMR. The HTMR sample is a nanopillar of 85 nm diameter with oscillations that are stabilized at a bias field of $H_{app} = 90$ Oe (applied along the easy axis) and a DC current of $I_{\mathrm{DC}} = 0.6$ mA. At this current the resistance value in the antiparallel state is 415 Ω and the magneto-resistance is 50%.

Then a microwave current of varying frequency f_e and amplitude I_{RF} was added, in a similar manner that the one described in Fig. 5.4. The amplitude I_{RF} of the driving RF current was estimated as in Ref. [172] from the measured power levels of the RF signal source, taking into account reflections and the capacitance between the STO top and bottom electrodes. The frequency f_g and the linewidth Δf of the externally driven STO were extracted using a Lorentzian fit of the voltage PSD.

Synchronization at $f_e \approx 2f_g$

Fig. 6.5-a shows the power spectral density (PSD) map of the output voltage for the STO frequency f versus the driving frequency f_e. It is clear from Fig. 6.5-a that the frequency f of the driven STO follows the driving frequency f_e only in the vicinity of the point $f_e = 2f_g$, while very weak or even no locking is observed near the points $f_e = f_g$ or $f_e = 3f_g$. The red dots at $f_e = f_g$ are an artifact of the measurement and are due to the signal of the driving source that cannot be suppressed. The disappearance of the generated power between 6 GHz and 8 GHz might be related to the presence of a secondary oscillation peak in the STO power spectrum (see details in [166]).

Locking range and linewidth in synchronized state

When the amplitude of the driving signal increases from $I_{\mathrm{RF}}/I_{\mathrm{DC}} = 0.25$ (Fig. 6.6-a) to $I_{\mathrm{RF}}/I_{\mathrm{DC}} = 0.57$ (Fig. 6.6-c), the width of the injection locking frequency range δf_e increases (full lines), while the linewidth of the driven STO oscillation (gray dots) varies inside the injection-locking range δf_e, and reaches a minimum value Δf_{min} at its center.

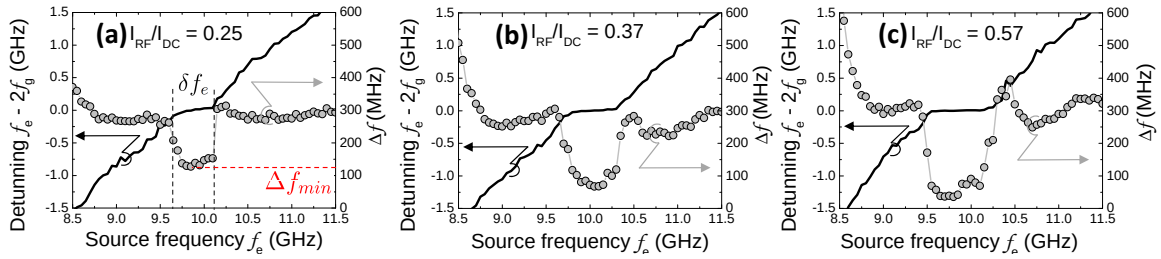

Fig. 6.6: Experimental detuning defined as $f_e - 2f_g$ (solid lines) and FWHM Δf versus source frequency f_e for (a) $I_{\mathrm{RF}}/I_{\mathrm{DC}} = 0.25$, (b) $I_{\mathrm{RF}}/I_{\mathrm{DC}} = 0.37$ and (c) $I_{\mathrm{RF}}/I_{\mathrm{DC}} = 0.57$.

Here we defined δf_e as the interval inside which the oscillation linewidth is reduced to half of the difference between the free-running and the minimum value. With the further increase of the driving amplitude I_{RF} the injection locking range continues to increase, reaching $\delta f_e = 0.6$ GHz at $I_{\mathrm{RF}}/I_{\mathrm{DC}} = 0.8$ (Fig. 6.5-b), while the minimum STO linewidth Δf_{min} continues to decrease (Fig. 6.5-c). Note, however, that even at reasonably large amplitudes of the driving signal $I_{\mathrm{RF}}/I_{\mathrm{DC}} = 0.57$ (Fig. 6.6-c), when the frequency f of the driven STO is locked to $f_e/2$, the minimum STO linewidth Δf_{min} remains rather large (about 35 MHz). This corresponds to an improvement by a factor of 7 as compared to the linewidth of the free running STO, but it is still much larger than the linewidth of the generator of the microwave driving signal (of the order of several Hz). These results indicate that despite a clear "frequency locking", the oscillation phase is not stationary and evolves in time, thus a "true" phase-locked state is not obtained. Such a behavior of the driven STO can be attributed to the influence of noise [161, 42]. The external microwave driving signal has to compete with noise, which results in phase slips and, thus, in fluctuations of the STO phase.

In conclusion, on HTMR devices that exhibit an IPP mode of the magnetization of the free layer, we have confirmed that the synchronization at the vicinity $f_e \approx 2f_g$ is favored as predicted from macrospin simulations and the phenomenological model from Zarudniev. This is an important condition to consider when phase locking several oscillators. We have also seen that the noise acting on the magnetization plays an important role in the synchronized regime. This will be investigated within macrospin simulations in section 6.3. In the following, we present similar experimental results obtained from LTMR devices.

6.2.2 LTMR devices

We proved in section 4.6 that LTMR devices exhibit nonlinear amplitude phase coupling N and that the amplitude restoration rate Γ_p is similar to HTMR devices. Thus, we consider LTMR samples as non-isochronous auto-oscillators.

The "only" disadvantage of LTMR samples is the constant degradation process that happens during the measurement when applying an additional microwave current bias. In the case of LTMR, $f_g^{\mathrm{LTMR}} \approx 7.0$ GHz, which varied during the experiment because of the gradual degradation of the junction during the experiment. Therefore, the locking

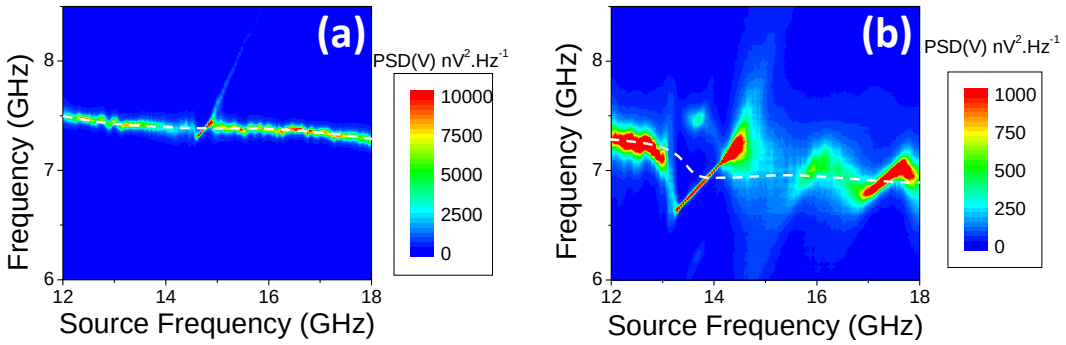

Fig. 6.7: Experimental PSD map (linear scale) of the STO frequency f versus the source frequency f_e for (a) $I_{\mathrm{RF}}/I_{\mathrm{DC}} = 0.24$ and (b) $I_{\mathrm{RF}}/I_{\mathrm{DC}} = 0.32$. The dashed white line represents the STO frequency that decreases due to the continuous degradation happening in the experiment.

band δf_e and minimum FWHM Δf_{min} are not studied as a function of the ratio $I_{\mathrm{RF}}/I_{\mathrm{DC}}$. The LTMR device is a nanopillar of 115 nm in diameter with oscillations that are stabilized at a bias field of $H_{app} \approx 385$ Oe (applied along the easy axis) and a DC current of $I_{\mathrm{DC}} = 1.2$ mA at the initial state of the LTMR ($\zeta \approx 1.5$ and $\Gamma_p \sim 100$ MHz from time domain measurements at the initial state of the device).

Fig. 6.7 shows two PSD maps of the STO frequency versus the source frequency for two different ratios $I_{\mathrm{RF}}/I_{\mathrm{DC}}$. The white dashed line represents the continuous degradation process of the barrier, which tends to decrease the STO frequency during the experiment. It is clear from Fig. 6.7 that fractional synchronization at the vicinity $f_e \approx 2f_g$ can be obtained, and even at the vicinity of $f_e \approx 5/2f_g = 17.5$ GHz for the higher ratio of $I_{\mathrm{RF}}/I_{\mathrm{DC}}$.

The corresponding detuning and Δf_{min} obtained from the PSD maps are shown in Fig. 6.8 at the vicinity $f_e \approx 2f_g$ (Fig. 6.8-a,b) and $f_e \approx 5/2f_g$ (Fig. 6.8-c). In the latter, we did not observe pure phase locking, but rather the same "frequency locking" as for the case of HTMR. In contrast for $f_e \approx 2f_g$ and for $I_{\mathrm{RF}}/I_{\mathrm{DC}} = 0.32$, Δf_{min} is equal to the resolution bandwidth of the spectrum analyzer, we can thus consider a limited effect of noise (i.e. a limited number of phase slips as defined later), reaching the "phase locked" state.

In order to understand these experimental results on the linewidth in the synchronized state we give first a quantitative approach based on macrospin simulations and then a qualitative approach of the synchronization effect. For this, we review the "classical" picture of synchronization effect in auto-oscillators. While synchronization is in any cases given by the nonlinear properties of auto-oscillators [173], we describe the phase dynamics in the synchronized regime with an Adlerian picture (i.e. only the phase is considered). It will allow us to explain some qualitative results obtained from pure phase synchronization in the LTMR devices. Finally, the role of amplitude in the synchronization is investigated by means of macrospin simulations. The description is given as a future perspective for more systematic studies of synchronization in STOs.

The structure of the next section is the following:

- Comparison of experimental frequency domain data with macrospin simulations in

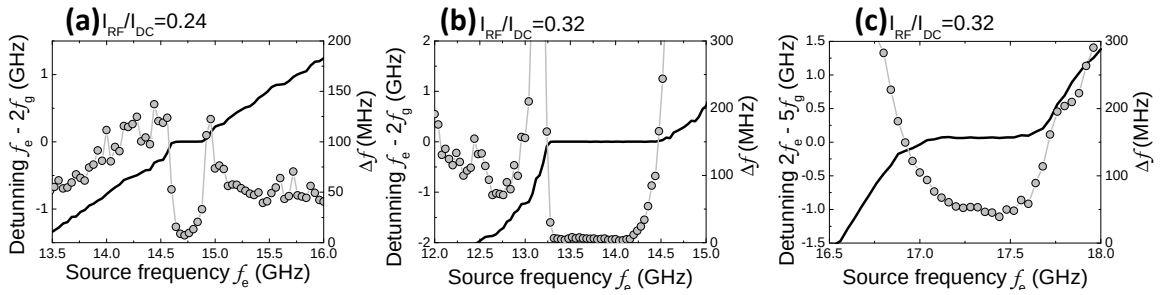

Fig. 6.8: Experimental detuning defined as $f_e - 2f_g$ (solid lines) and FWHM Δf versus source frequency f_e for (a) $I_{\mathrm{RF}}/I_{\mathrm{DC}} = 0.24$, (b) $I_{\mathrm{RF}}/I_{\mathrm{DC}} = 0.32$. (c) Detuning defined as $2f_e - 5f_g$ (solid lines) and FWHM Δf versus source frequency f_e for $I_{\mathrm{RF}}/I_{\mathrm{DC}} = 0.32$ at the vicinity $f_e \approx 5/2f_g$.

presence of noise (section 6.3.1).

- Introduction of phase synchronization in quasi-linear oscillators and how it compares with macrospin simulations (section 6.3.2).
- Qualitative description of the phase synchronization in the presence of noise for macrospin simulations and LTMR devices (section 6.3.3).
- Emphasis of the rich non-Adlerian synchronization dynamics in the case of STO from macrospin simulations (section 6.3.4).
- Qualitative effect of the synchronization on the amplitude of the auto-oscillation (in section 6.3.4).

6.3 Synchronization in auto-oscillators

6.3.1 Macrospin simulations

In order to elucidate the role of noise in the injection locking process we performed macrospin simulations using fluctuating fields in the form of Eq. 1.13 with effective temperatures T = 0 K, 50 K, and 400 K. The total current I acting on the STO was the sum of the DC current I_{DC} and the sinusoidal variable current I_{RF} that represents the injected RF driving signal of the frequency f_e.

The magnitudes of the bias current I_{DC} ($\zeta \approx 1.4$) and the bias magnetic field H (applied along the easy axis) were chosen to make the STNO free running frequency equal to $f_g = 5$ GHz. We also calculated the mismatch $f_e - 2f$ of the STO frequency and the STO linewidth Δf at $T = 400$ K for different values of the ratio $I_{\mathrm{RF}}/I_{\mathrm{DC}}$. These results are presented in Fig. 6.9-a and 6.9-b respectively.

It should be noted that the variation of Δf across the injection locking range is qualitatively similar to that observed in the experiment (see Figs. 6.6-a,b,c) with a gradual reduction from the free-running value towards a minimum value at the center. The role of the noise is further illustrated by Fig. 6.9-d where the minimum linewidth as a function of the ratio $I_{\mathrm{RF}}/I_{\mathrm{DC}}$ is shown for two different effective temperatures.

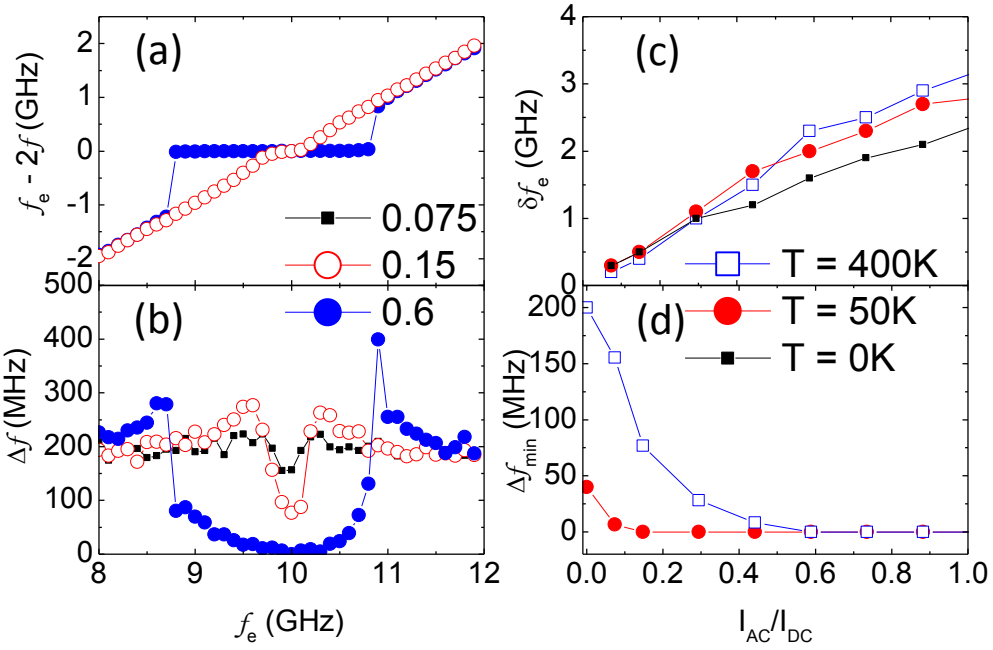

Fig. 6.9: (a) Simulated frequency detuning $f_e - 2f_g$ and (b) linewidth versus the driving frequency f_e for different ratios $I_{\mathrm{RF}}/I_{\mathrm{DC}} = 0.075$, 0.15, 0.6 with $I_{\mathrm{DC}} = 15$ mA and $T = 400$ K. (c) Simulated synchronization range δf_e for $T = 0$ K, 50 K, 400 K and (d) minimum linewidth Δf_{min} versus $I_{\mathrm{RF}}/I_{\mathrm{DC}}$ for $T = 50$ K, 400 K.

Clearly for $I_{\mathrm{RF}}/I_{\mathrm{DC}} < 0.5$ Δf_{min} is higher at $T = 400$ K than at $T = 50$ K, while for $I_{\mathrm{RF}}/I_{\mathrm{DC}} > 0.5$ the linewidth at both temperatures is below the numerical resolution. While the effective temperature, and therefore the noise, has a strong influence on the phase noise characteristics of the injection-locked state, the injection-locking range δf_e is only moderately affected by temperature, as shown in Fig. 6.9-c. The numerically obtained increase of the δf_e with increasing temperature has been previously reported in Ref. [174]. In the simulations for $T \neq 0$, δf_e in Fig. 6.9 has been defined as in the experiment on the HTMR device (Fig. 6.6), while for $T = 0$ K (with $\Delta f = 0$), δf_e corresponds to the range where $f_e - 2f$ is zero, similar to the definition in Ref. [154] where the experiments have been conducted at $T = 4.2$ K.

It should also be noted that our numerical results demonstrate only qualitative agreement with the experiment. For example, in the numerical modeling at $T = 400$ K we need $I_{\mathrm{RF}}/I_{\mathrm{DC}} \approx 0.25$ to achieve $\delta f_e = 0.6$ GHz (see Fig. 6.9-c), while in the experiment the same result is obtained only at $I_{\mathrm{RF}}/I_{\mathrm{DC}} = 0.7$ (see Fig. 6.5-b). A similar picture is seen in the behavior of the minimum STO linewidth: the reduction of Δf_{min} by a factor of 7 in numerical modeling takes place at $I_{\mathrm{RF}}/I_{\mathrm{DC}} = 0.3$ (Fig. 6.9-d), while the ratio of $I_{\mathrm{RF}}/I_{\mathrm{DC}} = 0.7$ is needed for a similar effect in the experiment in the HTMR device (Fig. 6.5-c). This discrepancy might be explained by a possible overestimate of the RF current in our microwave measurements and by the fact that in the experiment our STO is driven by the bias current that is just above the critical value. The critical value of the bias current ($I_c = 0.55$ mA) was estimated from the variation of the linewidth with the bias current.

We have found a qualitative agreement between macrospin simulations and HTMR experiments for the locking band and linewidths inside the locking band. To give insights into the underlying process of the STO dynamics in the presence of noise and the external forcing signal, we now give general aspects of phase synchronization in auto-oscillators.

6.3.2 Phase synchronization phenomenon in quasi-linear oscillators

We would like to stress here that the forthcoming descriptions are well defined and described in literature [41]. This is referred to as Adlerian synchronization [173]. We define the phase of the oscillator $\phi(t)$ (whose free running frequency is ω_g), while $\phi_e(t)$ is the phase of the forcing signal whose frequency is ω_e. Even though no equation will be used in the following description, we give the Adler equation, which governs the quasi-linear (isochronous) oscillator phase in the synchronized regime:

$$\frac{d\psi}{dt} = \Delta\omega_0 + B\sin\psi \ , \tag{6.6}$$

where $\psi = \phi - \phi_e$, $\Delta\omega_0 = \omega_g - \omega_e$ the frequency mismatch between the natural free-running oscillator frequency ω_g and the forcing signal ω_e and B a constant proportional to the external source signal. Because of the synchronization condition, $\sin(\psi) \approx \psi$ is used to solve the nonlinear equation 6.6. Contrary to the autonomous case where the phase was free, the phase is stable in time in this case due to synchronization. When $\sin\psi \approx \psi$, Eq. 6.6 is similar to the equation that governs the amplitude in an autonomous auto-oscillator. We will see at the end of this section that the synchronization of STOs is non-Adlerian, because of the presence of amplitude-phase coupling. Nevertheless, the following picture can be applied to understand the basic concepts of synchronization phenomenon.

We first introduce the notion of synchronization without noise. The free running oscillator has the frequency f_g. We consider first the external signal with the frequency $f_e = f_g$. The initial phase difference between the oscillator and the external signal is ϕ^{init} (just when external signal is turned on). The action of the external force on the oscillator depends on this phase difference. Naturally, the system (oscillator + external force) will minimize its energy by choosing the phase difference ϕ^0 that minimizes the interaction energy, which can be represented by a potential as shown in Fig. 6.10-b, toward a stable equilibrium. After a transient, the phase difference evolves from ϕ^{init} to ϕ^0. Usually, this phase difference ϕ^0 is $\pi/2$ in the case of an isochronous (or quasilinear) auto-oscillator, but in the case of STOs, an additional phase shift occurs due to nonlinearities (see [54]).

If a frequency mismatch $\Delta\omega_0$ is now present, i.e. $f_e \neq f_g$, in the same representation as in Fig. 6.10-a (see Fig. 6.11), we have an additional effect of the external force that tries to push/pull the oscillator (red arrows in Fig. 6.11). It shifts the two equilibrium points (the stable one and the saddle one), and the stable equilibrium point has as a consequence an additional phase shift $\Delta\phi$ compared to the zero frequency mismatch case, such that the total phase shift is finally $\Delta\phi + \phi^0$. This additional phase shift due to frequency mismatch is well established in the Adler model [42, 173]. In this model, Eq. 6.6, this shift is $\Delta\phi = -\Delta\omega_0/B$, while ϕ^0 is not accounted for.

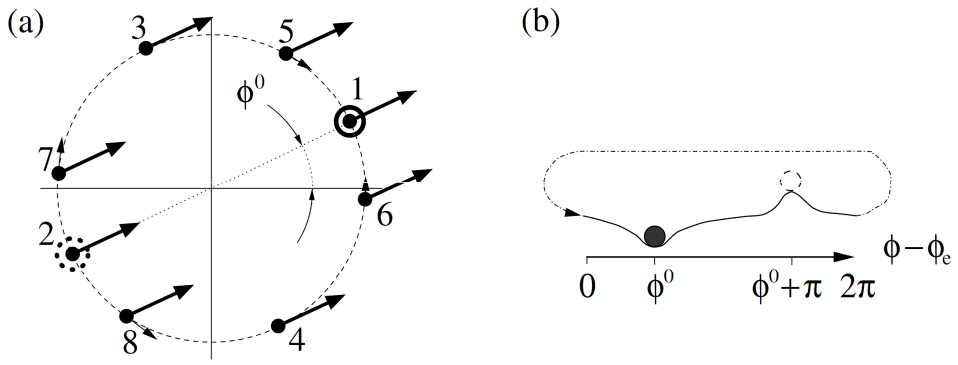

Fig. 6.10: (a) In the phase plane, the action of the external force is the same. However, since the external source does not affect the amplitude in isochronous oscillators, depending on the phase shift (point 1 to 8), the effect of the force on the oscillator will be of different strength (the oscillator can only move on the dashed circle). Point 1 and 2 are the two equilibrium points. However, point 2 is unstable. This is represented in an equivalent energy landscape versus the phase difference in (b). From [41].

More interestingly, this frequency difference makes the previously mentioned potential tilted (represented now in Fig. 6.11-b). In consequence the saddle equilibrium is not π shifted from the stable equilibrium (see Fig. 6.11). Without noise, the oscillator stays at a constant phase difference with respect to the external source, while its frequency is the one of the external source f_e. When the stationary points of the phase potential 1 and 2 merge, i.e. $\Delta\phi = \pi/2$, the stationary points disappear; phase slips occur (even without noise). In this case, the detuning frequency is no longer zero (see Fig. 6.12) and the synchronized state is lost.

The situations described above can be represented within Adler model, which gives the locking range as a function of the external force ϵ (or B in Eq. 6.6). This is called an Arnold tongue, as illustrated in Fig. 6.12-a, by the gray shaded area, which corresponds to the locking range. It is now instructive to look at the phase difference versus time for various points indicated by $1, 2, ...5$ at constant ϵ. This is shown in Fig. 6.12-b for the 6 different points (solution to Adler equation) and compared to macrospin simulation for an STO in Fig. 6.12-c for a source frequency at the vicinity of $f_e \approx 2f_g$. Note that in this case the phase difference is $\phi - \phi_e/2$. From this, we can distinguish three main different dynamical synchronized states:

- The case ①, $\Delta\phi = 0$ and the phase potential is almost symmetric, in the sense that upward $(+2\pi)$ or downward (-2π) phase difference jumps are equally probable in the presence of noise. In Fig. 6.12, it corresponds to the point marked "1". This case can be observed when the potential is 2π periodic (see the Fig. 6.10-b), i.e. the forcing frequency is the same as the STO frequency.

- The case ②, marked as "2" in Fig. 6.12-a is when the frequency mismatch is non-zero (or non-negligible). It leads to a constant offset in the phase difference. In the macrospin simulation presented in Fig. 6.12-c, instead of point marked as "1", only points similar to "2" as been presumably represented. Indeed, due to the nonlinear

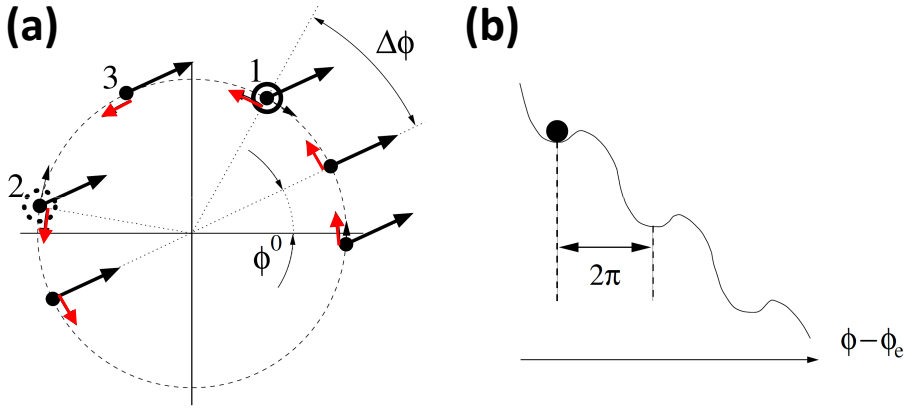

Fig. 6.11: (a) Since the external signal always wants to push/pull the oscillator to its own frequency, the phase "feels" an additional effect (in red arrows). Since the external force also wants to have a phase difference of ϕ^0 with the oscillator, the compensation of both occurs with an additional phase difference $\Delta\phi$. The equilibrium points (points 1 and 2) occur now with a phase difference less than π. Without further perturbations, the system stabilizes in a local minimum (b). From [41].

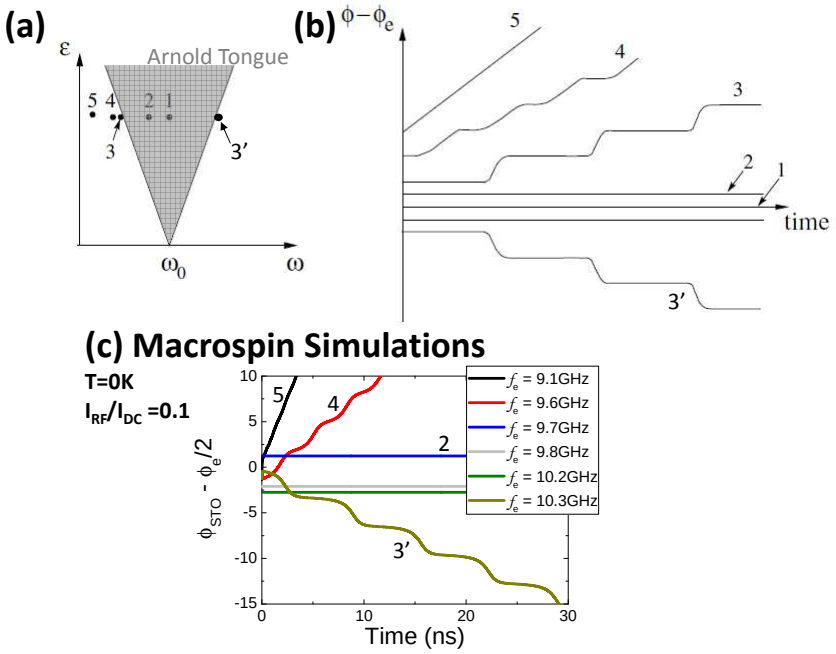

Fig. 6.12: (a) Different points at a constant force strength are shown on an Arnold tongue. The dashed area, the Arnold Tongue, represents the "locked" state of the oscillator. In (b) we represent the phase difference $\phi - \phi_e$ versus time for each state. State 1 and 2 are phase-locked, State 3 and 3' are found at the boundary of the Arnold tongue, and 4 and 5, far away from it. (c) $\phi_{\mathrm{STO}} - \phi_e$ obtained from a macrospin simulation with a zero effective temperature ($T = 0$ K) and different source frequency f_e. Each state found in (a) and (b) can be reproduced, indicating or not the synchronized state of the STO. (a) and (b) from [41].

amplitude-phase coupling, an additional phase offset between STO and the signal source is present (which is not considered in the Adler model). Nevertheless, we can see that the phase offset depends on the frequency mismatch (see Fig. 6.12-c). In this case ②, the potential is inclined (since $f_e \neq f_g$, see the Fig. 6.11). Depending on the condition $f_g > f_e$ or $f_g < f_e$, only downward or upward phase jumps will occur in the presence of noise. When increasing the frequency difference $f_e - f_g$, the "barrier" seen by the phase difference decreases, leading to more and more phase slips under a constant phase perturbation.

- For the case ③, there are no stationary or equilibrium points for the phase difference. This case is obtained from the points marked by "3", "3' " and "4" in Fig. 6.12-a. The evolution of the phase difference at a given time differs according to the position of the phase difference in the phase potential. The phase difference evolves slowly near the (former) stable equilibrium and sharply just after the (former) saddle equilibrium. This case that occurs at the vicinity of the Arnold tongue corresponds to a unsynchronized state.

While the Adlerian picture assumes that the amplitude of the auto-oscillation is not changed by the application of the external signal, we can see that these pictures for isochronous (quasi-linear) oscillators give very good insights on what is happening in STOs.

Now that these three main cases have been described, we are now able to "classify" the phase slips we observe in our macrospin simulations in the presence of noise.

6.3.3 Synchronization of a macrospin mode and a LTMR device; Phase Slips

For HTMR devices, no time domain data have been acquired so that unfortunately the experimental phase cannot be analyzed in this experiment. However, macrospin simulations with an alternative current allows such a study. Therefore, we present an analysis of the synchronized state in the presence of noise for an STO from macrospin simulation that we compare with to KTS model.

We first analyze in detail the phenomenon that occurs to the phase in the "Arnold tongue", i.e. in the "locking band" as defined in Fig. 6.13-a,b for $I_{\mathrm{RF}}/I_{\mathrm{DC}} = 0.6$, where we reported the three cases discussed previously from an Adlerian picture. In each case ①, ② and ③, we have extracted the phase mismatch $\phi_{\mathrm{STO}}(t) - \phi_e(t)/2$ between the STO ($\phi_{\mathrm{STO}}(t)$ obtained from the Analytic Signal see section 3.2.3.2) and the signal source divided by two ($\phi_e(t)/2$) presented in Fig. 6.13-c.

The first case ① is in the center of the synchronization window (i.e. $f_e \approx 2f_g$, with f_g the STO free-running frequency), where the oscillation peak is a Dirac function in the frequency domain (i.e. the mode has a single frequency). In this case, phase jumps occur upward or downward by $\pm\pi$ as expected from a symmetric phase potential (and π periodic)[2].

[2]Because we use the locking condition $f_e \approx 2f_g$, the phase potential is π periodic and not 2π as discussed in the previous section.

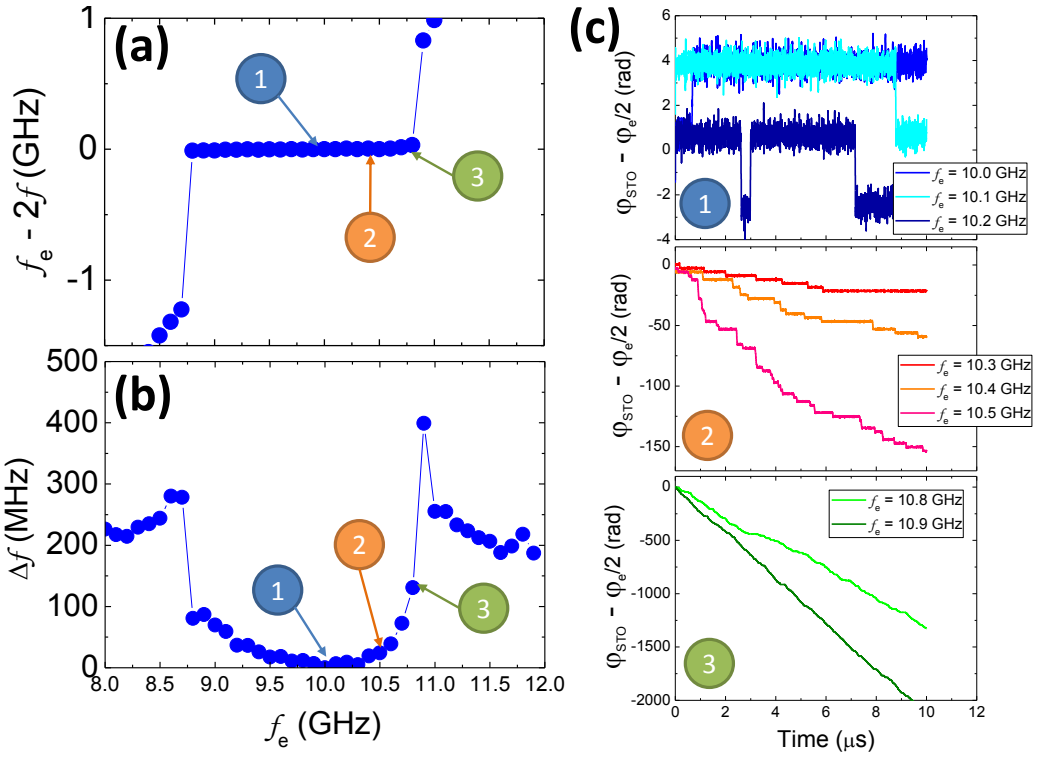

Fig. 6.13: Simulations. (a) Detuning and (b) FWHM versus f_e for $I_{\mathrm{RF}}/I_{\mathrm{DC}} = 0.6$ for $T = 400$ K. Three different cases are represented. (c) Phase difference $\phi_{\mathrm{STO}}(t) - \phi_e(t)/2$ for the three different cases. Case ①: some phase slips occur, phase slips might be reversible. Case ②: many phase slips occur and are not reversible. Case ③: the phase difference is such that a linear component clearly appears, inducing non-zero detuning. The case $f_e = 10.9$ GHz is no longer "locked" to the microwave current.

The second case ② occurs when Δf is larger than the frequency resolution of the simulated spectrum, but small compared to the free running linewidth of the STO. The source frequency f_e is close to, but smaller, than the 0 K locking border. In this case, only downward $(-\pi)$ phase jumps are observable after a random time. The higher the frequency mismatch, the larger the number of phase slips occurring during the 10 μs time trace.

Unfortunately, because case ③ cannot be investigated by Adlerian dynamics in STOs , no qualitative picture can be given. The last case ③ in the Adlerian picture, and especially the cases labeled 3 and 3', corresponds to the ones where the source frequency f_e is close to the boundary of the synchronization range. In macrospin simulations, this would correspond to a frequency applied just near the boundary of the 0 K locking band but still inside the 400 K locking band (See Fig. 6.9-c). In this case many phase slips occur, but the overall picture is rather complicated, since in this region the synchronization is hysteretic [165]. However, only a qualitative agreement can be found with the Adlerian case ③; the phase differences look like the curves 3 or 3' in Fig. 6.12-b and within the oscillator phase fluctuations, the effective barrier seems to be zero.

To further investigate experimentally the spectral purity of the "phase locked" state (cases ① and ②), we have performed time domain measurements in the case of the LTMR device when synchronized to the external signal (at the same time as the measurements

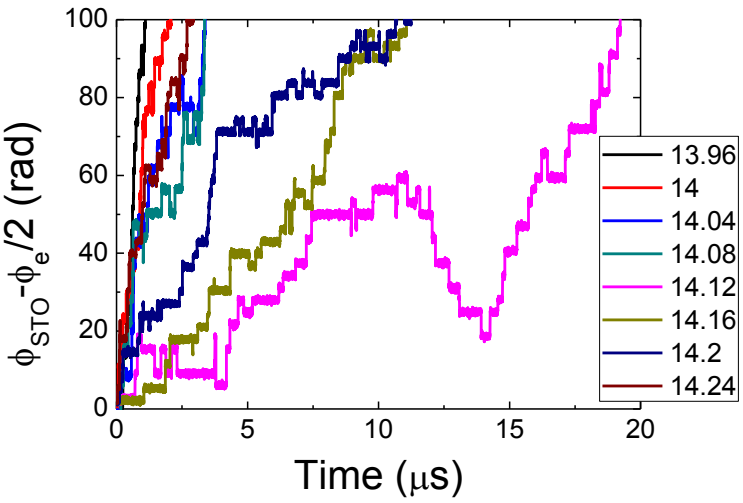

Fig. 6.14: Experiments. Phase difference $\phi_{\mathrm{STO}} - \phi_e/2$ measured on a LTMR sample for different source frequency f_e.

shown in section 6.2.2). To do so, we used a 1 GHz analog filter around $f_c = 7$ GHz in order to remove the source signal peak. The phase has been extracted by the usual method (described in chapters 3 and 4), but the unwrapping frequency is half that the microwave source $f_e/2$. We show the phase difference $\phi_{\mathrm{STO}} - \phi_e$ obtained in the LTMR device in Fig. 6.14.

It is clear from the Fig. 6.14 that the phase is never stationary in the sense where phase slips (upward and downward) always occur in the supposed region ① ($f_e = 14.2$GHz). Because of the almost equal probability to obtain upward and downward jumps, we can suppose that the phase potential is symmetric. For lower frequencies, we indeed see almost only upward jumps, as explained by an inclined phase potential (when $f_e < 2f_g$). Because the device is not stable, the signal lost its integrity when $2f_e > f_g$, and we do not obtain the expected result. Since the device is not stable, the peak observed on the spectrum analyzer even for $f_e = 14.2$ GHz is broader than the one when $f_e = 13.8$ GHz (see Fig. 6.15, the sidebands in the red curve are discussed in the next section 6.3.4).

This fact somehow limits the conclusions that can be drawn from these measurements, since the sample did not conserve its integrity during the measurement. However, this first study should encourage to measure the synchronized state both in frequency and time domain.

It is more than probable that a systematic study of the locked STO to an external signal provides further information on the nonlinear parameters/dynamics of the autonomous state. Indeed, to get the nonautonomous behavior of the STO, it is required that the STO phase, ϕ_{STO} is "locked" to the source phase ϕ_e. It is clear from the chapter 4 and 5 that the frequency of the auto-oscillation in the autonomous regime is given by the amplitude, through the nonlinear amplitude-phase coupling. Therefore, one can imagine that the amplitude of the STO is somehow "locked" to the external force as a necessary condition since STO is non-isochronous. Actually, we previously highlighted the fact that, for the case of the injection locking $f_e \approx 2f_g$, the synchronization occurs through

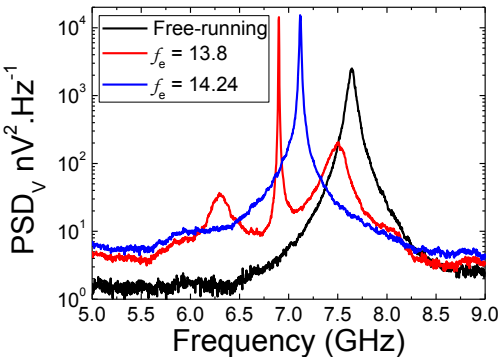

Fig. 6.15: Experiments (LTMR Device). Comparison of the PSD for different source frequency f_e. The blue curve has a larger FWHM, while the red curve has a linewidth similar to the one of the resolution bandwidth of the spectrum analyzer.

the amplitude (see Eq. 6.3 in section 6.1.2). While the solution of the STO in presence of external forcing signal can be found elsewhere [54, 59], we give in the next section the solution of the synchronization in presence of noise in STOs in order to highlight features of the dynamics of the STOs that could be found in locking experiments.

6.3.4 Non-Adlerian dynamics and its consequence on the emitted spectrum

6.3.4.1 Mathematical description

We focus now on the mathematical description of the cases ① and ②. We want to study the synchronized solution (in both phase and amplitude); we therefore assume the existence of this solution. Then, in the synchronized state, the instantaneous power takes the form: $p(t) = p_0 + \delta p_0 + \delta p(t)$ while the instantaneous phase mismatch is: $\psi(t) = \phi_{\mathrm{STO}}(t) - \omega_e t + \psi_0$. p_0 is the free running power (in absence of the synchronizing signal) and δp_0 is the amplitude shift induced by the synchronization condition and ψ_0, the phase shift between the source and the STO that is induced by the synchronization condition. Under the assumption $\sin(\psi - \psi_0) \approx \psi - \psi_0$, the phase difference fluctuations $\psi(t)$ and power fluctuations $\delta p(t) \ll 1$ are solutions of:

$$\begin{aligned}\begin{pmatrix} \frac{d\delta p}{dt} \\ \frac{d\psi}{dt} \end{pmatrix} = &\begin{bmatrix} -2\Gamma_p & -2p_0 F\sin(\psi_0) \\ N & -F\cos(\psi_0) \end{bmatrix} \begin{pmatrix} \delta p \\ \psi \end{pmatrix} \\ &+ \begin{pmatrix} 2\delta p_0 \Gamma_p + 2p_0 F\cos(\psi_0) + 2\sqrt{p_0}\Re f_n(t) \\ -\Delta\omega_0 - F\sin(\psi_0) + \frac{1}{\sqrt{p_0}}\Im f_n(t) \end{pmatrix}.\end{aligned} \tag{6.7}$$

This equation has been written in [42] with $N = 0$ (isochronous case in 1968) and in [59, 174] with $N \neq 0$ (non-isochronous case in 2010). Without noise, the stationary solutions $(\delta p_0, \psi_0)$ are:

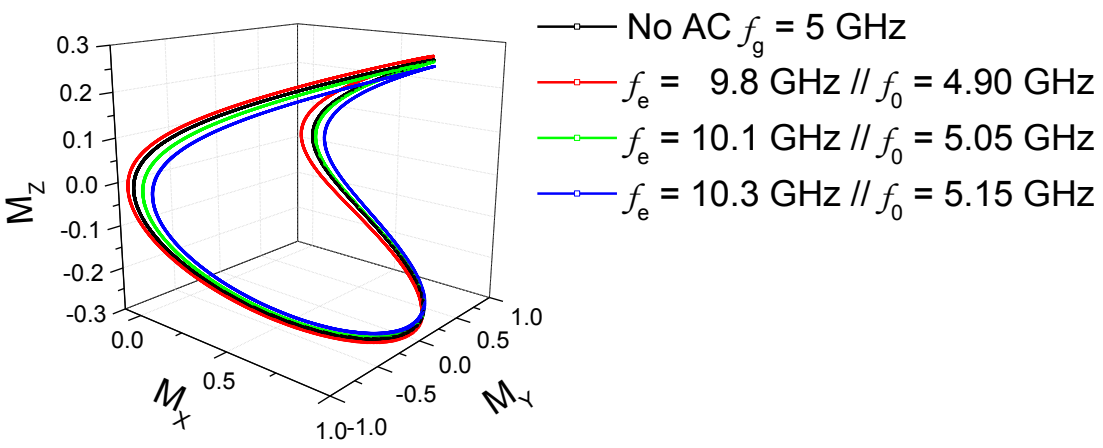

Fig. 6.16: Macrospin trajectories obtained from the resolution of LLGS at 0 K and different frequencies of the external microwave current. The free-running frequency is f_g and becomes $f_0 = f_e/2$ when synchronized in all cases.

$$\psi_0 = \arctan(\nu) - \arcsin\left(\frac{\Delta\omega_0}{\Delta\nu_0}\right) , \tag{6.8}$$

$$\delta p_0 = p_0 \frac{\nu\Delta\omega_0 + \sqrt{\Delta\nu_0^2 - \Delta\omega_0^2}}{(1+\nu^2)\Gamma_p} , \tag{6.9}$$

where $\Delta\nu_0^2 = \sqrt{1+\nu^2}F$ is the nonlinearity-enhanced frequency interval of phase locking. It is interesting to note that δp_0 is proportional to ν times the frequency mismatch. Therefore, if one wants to lock the system to a frequency f_e smaller than f_g, it has to reduce (increase) the total power $p_0 + \delta p_0$ in the case of $\nu > 0$ ($\nu < 0$). This is illustrated in Fig. 6.16 with $\nu < 0$ in the case of the IPP mode. The free-running trajectory is in black, with the frequency f_g. If the system oscillates at a frequency higher (lower) than f_g, it should be below (above) the black trajectory. If one wants to synchronize the system with $f_e > 2f_g$ (green and blue trajectories), the system has to decrease p_0, i.e. the "average" solid angle formed by the trajectory. If the system is now synchronized with $f_e < 2f_g$ (red trajectory), the power needs to be increased, i.e. the "average" solid angle increases. For macrospin simulations, this effect has been first observed in Ref. [175].

We can interpret this amplitude/power stabilization on a specific orbit as a necessary condition for the phase synchronization. In the non-isochronous case, if the amplitude was free, the phase also would be free, because of the amplitude/phase coupling. Therefore, we can anticipate that a control of amplitude would control the phase, in an *amplitude locked loop* for example [176, 177].

6.3.4.2 Sideband appearance in the emitted spectrum

The linearized system Eq. 6.7 has two eigenvalues, which correspond to two time constants. The first λ_1 describes how a small perturbation δp or $\delta\psi$ is attenuated towards

the power/phase equilibrium state (the locked state). The second eigenvalue λ_2 is the beat frequency, or oscillating transient response, and is higher than the first (see details in Ref. [59]).

Finally, in the presence of noise the solutions δp (or equivalently δa) and $\psi(t)$ expressed by their autocorrelation functions are given by:

$$\Gamma_{\psi}(\tau) \propto e^{-\lambda_1 \tau}[1 + \cos(\lambda_2 \tau)] \,, \tag{6.10}$$

$$\Gamma_{\delta a}(\tau) \propto e^{-\lambda_1 \tau}[1 + \cos(\lambda_2 \tau)] \,, \tag{6.11}$$

with:

$$\lambda_1 = \Gamma_p \;\text{ and }\; \lambda_2 \approx \Gamma_p \sqrt{\mu/\mu_{cr} - 1} \,, \tag{6.12}$$

with $\mu = I_{\mathrm{RF}}/I_{\mathrm{DC}}$ the modulation depth and μ_{cr} a critical modulation depth from which the non-Adlerian regime Eq. 6.10 starts ($\mu > \mu_{cr}$). The amplitude and phase noise in the synchronized regime (when $f_e \approx 2f_g$, case ①) is given in Fig. 6.17 for different applied RF current at $T = 50$ K (in order to have the minimum of phase slips). In Fig. 6.17, the phase slips stop when $I_{\mathrm{RF}} > 15$ (a.u.) and the phase becomes stationary (in the sense of a stochastic process) and ergodic in the timespan calculated here: the solution is defined by Eq. 6.10. When $I_{\mathrm{AC}} < 15$, phase slips occur so that no solution can be given. However, between two phase slips, the system can be considered stationary and the solutions 6.10 and 6.11 are valid in those time windows.

Even in the frequency log-scale Fig. 6.17-c, we can see that λ_2 increases with I_{AC} as expected [59]. The direct consequence of this beat frequency is that sidebands appear in the synchronized regime near the peak at a frequency given by λ_2 (see Fig. 6.18-c). Those sides bands have been reported in macrospin simulations [178] and micromagnetic simulations [174, 179]. We also report them for LTMR device, as shown in Fig. 6.18-e. The stability of the LTMR device did not allow however to make a systematic study on them. Nevertheless, we note that the sideband frequency is about 500 MHz, higher than the $f_p = \Gamma_p/\pi$ value for this sample (about 200 MHz).

6.3.4.3 Effect on the low frequency noise of STOs

More interestingly, the low frequency (below $f < 1$ GHz) component of the signal PSD in Figs. 6.18-a,c is similar to the one of the amplitude noise in the autonomous regime. When the STOs are in non-autonomous regime (Figs. 6.18-b,e), the low frequency component of the PSDs is reduced similarly to the reduction of the amplitude noise in this regime (compare black and green curves in Fig. 6.17-c). It is not surprising since, as noted in section 4.4, the zero frequency signal present in m_x is equivalent to the amplitude relaxation toward the mean value of m_x (see Eq. 4.26). Therefore, the low frequency noise (often confused with a low frequency $1/f$ noise) is indeed due to the relaxation of the m_x component toward its average. Moreover, this increase of low frequency noise due to the effect of the spin transfer torque onto the magnetization is used to determine the enhancement of high frequency noise in GMR/TMR reader in hard disk drives [141, 142, 143, 144]. In our case, we can use this low frequency component to extract Γ_p with

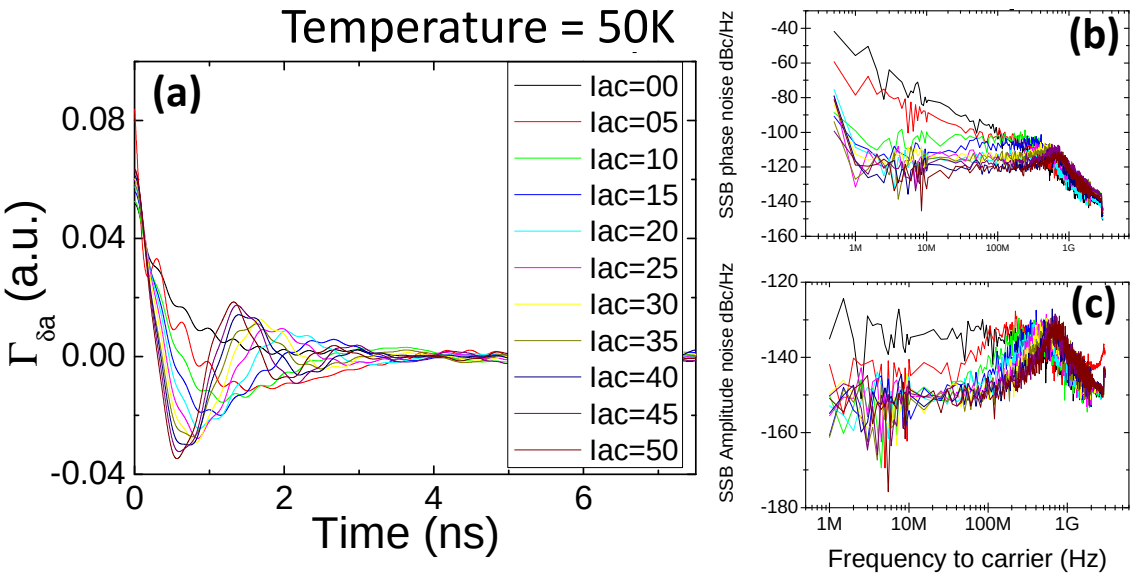

Fig. 6.17: Macrospin simulations. (a) Autocorrelation function $\Gamma_{\delta a}$ of amplitude fluctuation $\delta a(t)$ in the synchronized state for different applied microwave currents I_{AC} (note that $I_{\mathrm{DC}} = 68 \times 10^{12}$ A/m^2). From $I_{\mathrm{AC}} > 15 \times 10^{12}$ A/m^2, the beat frequency can be seen in $\Gamma_{\delta a}$. We can also notice that the period of the oscillation decreases with increasing I_{AC} (i.e. λ_2 increases). Corresponding phase noise plot (b) and amplitude noise plot (c). The peak frequency (or λ_2) increases with I_{AC} and is higher than $\Gamma_p/\pi \approx 200$ MHz. The temperature is 50 K.

a simple measurement in the frequency domain of the free running oscillation[3]. In the synchronized regime, m_x is necessarily stabilized (around $p_0 + \delta p_0$), and thus reduces the noise component on m_x. A straightforward reduction by a factor of 10 of this low frequency noise component in the "locked" regime has been observed in the LTMR device as shown in Fig. 6.18-d,e.

6.3.4.4 Stabilization of the MR signal under synchronization

Since the mean value of m_x (projected on the polarizer direction) gives the mean value of the resistance in magnetoresistive devices, we can suppose that the injected signal changes the value of the resistance of the magnetoresistive device through the shift of mode power δp_0. To verify the resistance dependence of the STO versus the frequency mismatch $f_e - p/q f_g$ in the synchronized state, we performed synchronization experiments on the perpendicular-polarizer structure (see Fig. 6.19 and Ref. [81, 168] for details). As we have already explained, the continuous degradation of the LTMR device (associated with a decrease of the total MR) has prevented such an analysis on LTMR synchronization experiments.

For the sake of clarity, we do not present the whole study of this sample and state diagrams that can be found elsewhere [169], but we focus on the single experimental

[3]The amplitude roll-off observed in the experiments can originate from this low frequency component of the extracted electrical signal. Therefore, it justifies the fact that the experimental amplitude roll-off indeed originate from the amplitude relaxation toward the mean power

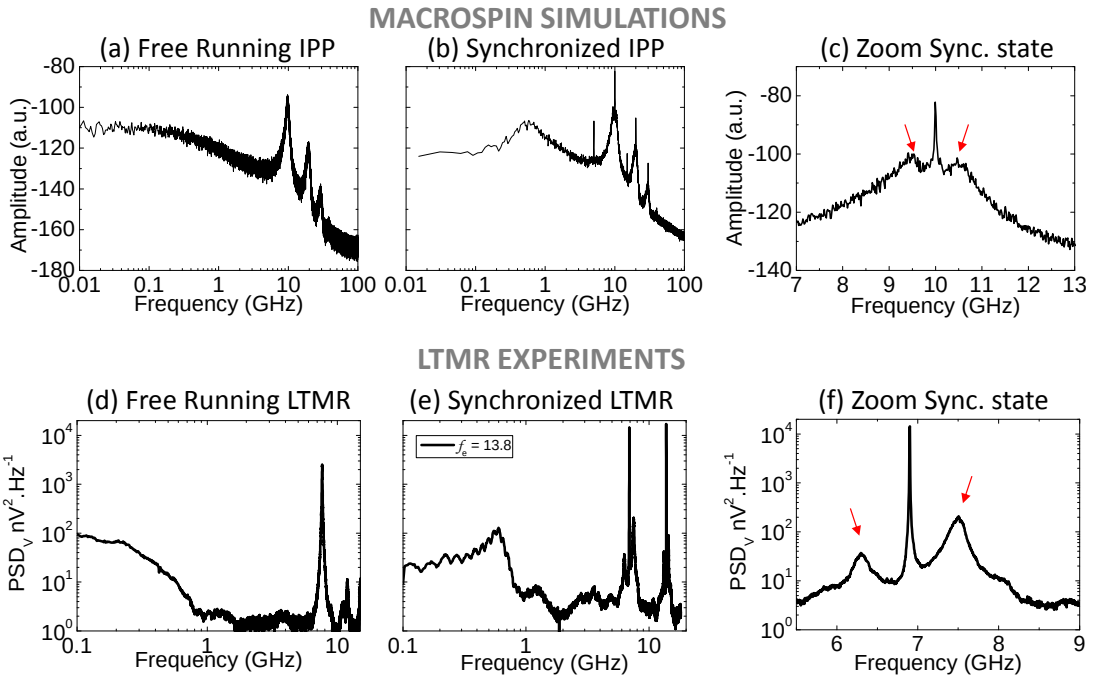

Fig. 6.18: Top panels: Macrospin simulations.(a) PSD of m_x for the free-running IPP mode (See Fig. 1.14 in Chapter 1). (b) PSD of m_x in the synchronized state ($I_{\mathrm{RF}}/I_{\mathrm{DC}} = 0.6$) with $f_e = 10$ GHz. (c) PSD of m_x where side-bands are indicated by red arrows. Effective temperature: 400 K. Bottom panels: LTMR experiments PSD of the free running LTMR-STO (d) and the STO locked to an external signal of $f_e = 13.8$ GHz (e). The free-running frequency is originally $f_g \approx 7.8$ GHz but is reduced because of the conditioning process of the sample. Figure (e) shows explicitly the effect of synchronization on the low frequency spectrum of the signal compared to Figure (d) while Figure (f) shows the two (asymmetric) side-bands.

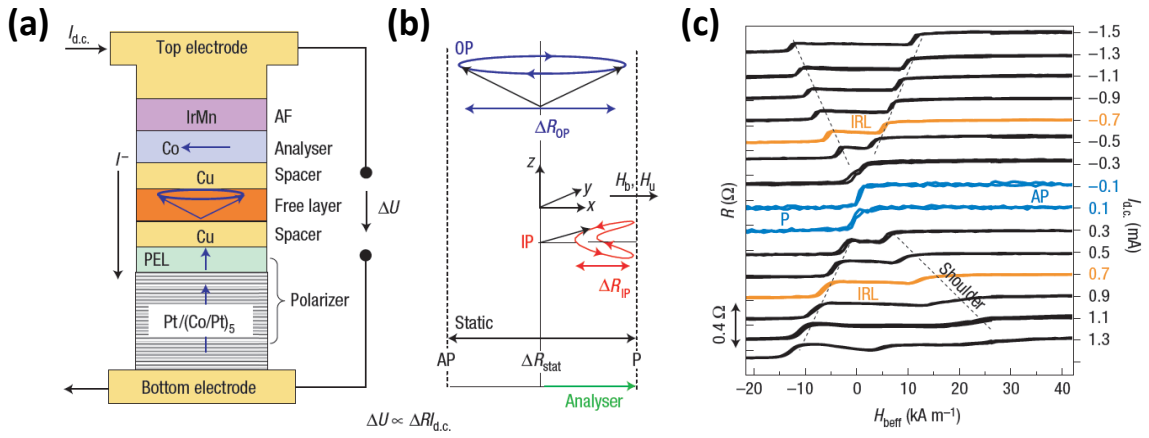

Fig. 6.19: (a) Stack of the perpendicular polarizer structure. While the perpendicular polarizer induces an out-of-plane auto-oscillation of the free layer (Py), the analyzer (the top magnetic layer) allows one to retrieve the GMR signal. (b) Output of an OPP mode compared to an IPP mode. The signal of the OP mode oscillates between the AP and the P resistance state. When oscillating, the mean resistance is in between the AP and the P resistance state. (c) Experimental evidence of the Intermediate Resistance Level (IRL). From [168].

graph given in Fig. 6.20. In this figure, the resistance measured inside the locking band is proportional to the injected frequency. It is straightforward from the Fig. 6.20 that when $f_e \approx f_g$, the resistance (in the synchronized state) is equal to the mean resistance state outside the locking band.

This simple evidence proves that not only the non-isochronous property can be verified easily, but that many effects of the nonlinear nature of the STO can lead to deterministic behaviors of the oscillator.

6.3.4.5 Conclusion

In conclusion, we have found a general good agreement of the non-autonomous regime observed experimentally in STOs compared to what is expected from the theoretical models. Of course, the magnetization dynamics driven by an external microwave current or field can be subject to even more complicated pictures in the presence of noise [180], as for example the chaos [181]. Nonetheless, for small perturbation around the limit cycle defined by the synchronized state $(p_0 + \delta p_0, f_e)$, the non-autonomous dynamics can be related to the autonomous dynamics defined by the nonlinear parameters ν and Γ_p.

In addition, we have shown the importance of the noise in the stability of the synchronized regime. The relatively weak phase coherence found in our best "synchronized state" (see upward and downward phase jumps in Fig. 6.14) are most likely problematic for exhibiting the long term stability of networks of STOs. Further experimental evidence from TDNS analyses would be of importance to determine the real possibilities of STOs as a component of complex RF architectures.

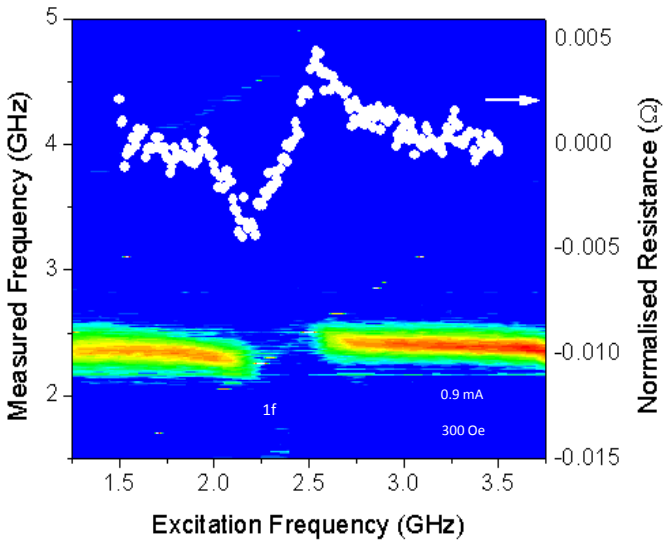

Fig. 6.20: PSD map of the measured STO spectra as a function of the applied source frequency f_e in linear scale. The superimposed white dots (same X-axis) show the normalized resistance value as a function of the source frequency f_e. Measurements by A. Jenkins.

6.4 Perspectives of synchronization in STOs

This section describes further possible studies to be realized for synchronization experiments in STOs. This is not an exhaustive list of what can be realized in the future but it is written as a perspective for studies initiated by this thesis work.

The first case is a simulation study on coupled layers to demonstrate the potential improvements that can be reached for STOs. It is shown how the extraction of the nonlinear parameters (Γ_p, ν) can help to the study of such a complex system.

The second case summarize some aspects on STOs networks.

6.4.1 Perspective: Oscillator Formalism toward Applications

In the previous sections dedicated to synchronization, we have investigated the reduction of the phase noise by "external" forces and/or external coupling between two individual oscillators. Another possibility for accomplishing this involves coupling layers inside the magnetic stack. Here we present a macrospin simulation that indicates the linewidth can be reduced in coupled systems.

Prior to the begin of my thesis, it has been demonstrated by macrospin simulations that the reciprocal effect of the STT onto the polarizer leads to a "self-synchronization" inside the multilayered magnetic device [182]. The "reciprocal effect of the STT" can be easily understood with the simple introduction of STT in section 1.2.1. Indeed, within a certain electron flow direction, the STT onto the free layer acts as an anti-damping that leads to an increase in the angle between the free and polarizer layers. Conversely, the reciprocal STT onto the magnetization of the polarizer acts as a damping term and leads to a decrease in the angle between the polarizer layer with respect with the free layer magnetization, destabilizing the FL. It turns out that a dynamical coupling can occur when the mode frequencies of each magnetization cross. Such a crossing occurs in a MR device formed by a "normal" free layer and a Synthetic Anti-ferromagnetic (SAF) trilayer, as shown in Fig. 6.21-a. The geometry is reported in Fig. 6.21-b.

This coupling gives rise to two interesting features. First, when sweeping the field, there are no abrupt jumps of the frequency of the free layer, whereas a dynamical coupling supported by the dipolar fields in the same structure occurs with abrupt jumps [183]. This difference is supposed to originate from the different nature of the dynamical coupling. The coupling occurs through non-conservative quantities (damping and anti-damping) in the case of reciprocal STT, while it occurs through a conservative interaction in the case of dipolar fields. The qualitative difference between the two couplings is shown in Fig. 6.21-a.

The second feature of this dynamical coupling is that it is accompanied with a substantial linewidth reduction (see Fig. 6.22). We use the time domain noise spectroscopy developed in Part II to analyze the evolution of the nonlinear parameters inside and outside the "self-locking" range. It can be shown that a combined effect of the reduction of $|\nu|$ and the increase of Γ_p are responsible of this FWHM reduction [184].

It is clear that the dynamic STT interaction between the magnetic layers of the STO leads to the formation of a collective auto-oscillation mode that involves magnetization of both the free and fixed magnetic layers. The observed linewidth reduction is related to the coupling-induced reduction of the effective nonlinear coefficient ν that describes

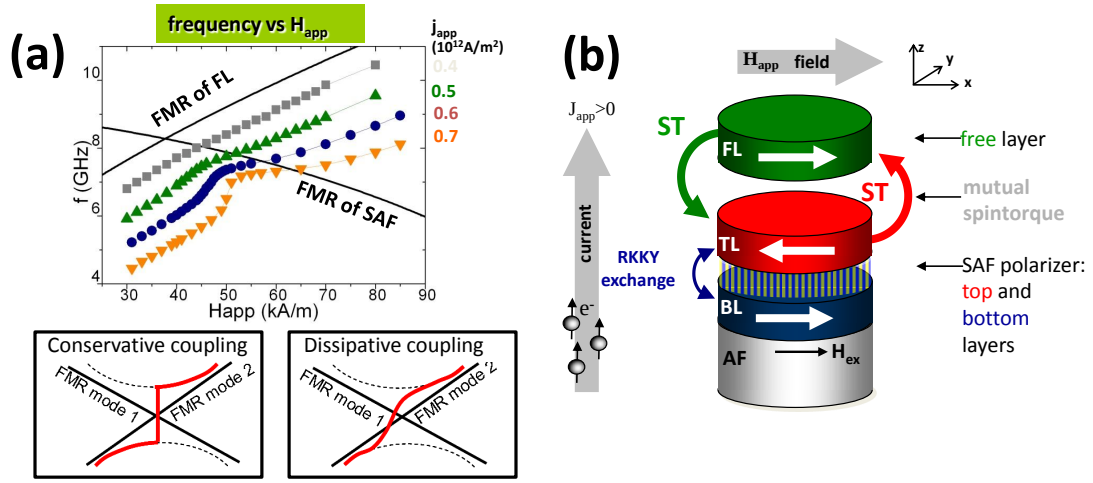

Fig. 6.21: (a) Simulated mode frequency versus applied field. When the auto-oscillation of the free layer "crosses" the FMR-SAF, a dynamical coupling appears from Ref. [184]. The schematics represent the qualitative difference between conservative and dissipative coupling. (b) Geometry of the simulated structure.

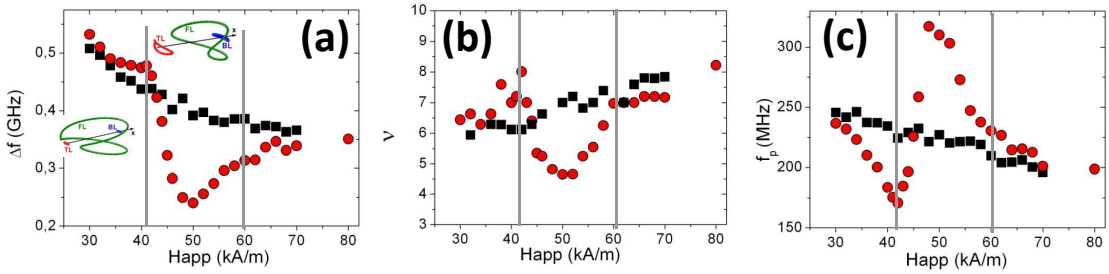

Fig. 6.22: Simulated (a) FWHM of the free layer with (red dots) and without (black squares) coupling via mutual STT. (b) ν and (c) Γ_p extracted from the analysis of the time trace with and without dynamical coupling. The vertical gray line represents the "self-locking" range. $J_{app} = 50.10^{11}$ A/m^2. Simulations from D. Gusakova.

nonlinear amplitude-phase coupling in STOs. Besides revealing the important role of the dynamic coupling between the STO layers in tailoring the phase noise properties of an STO, this numerical study also provides a theoretical evaluation of the nonlinear parameters of ν and Γ_p that cannot be accurately evaluated analytically, especially in the case of coupled magnetic layers. Although in this study we only considered the interlayer STT coupling via the spin polarized current, we believe that the obtained results can be generalized to other types of dynamic interlayer interactions (i.e. dipolar interaction). We believe such studies on complex STO structures would lead to the definition of the problem in a simpler way using the KTS model formalism (Γ_p, ν).

It should also be mentioned that a recent experimental study [185] reveals a strong reduction in the generation linewidth in the case when vortex oscillations in the polarizing and free layer of a spin valve structure are coupled via dipolar fields. Thus, our analysis suggests that the control of coupling between the magnetic layers of an STO could provide an important tool to improve the microwave performance characteristics of STOs.

6.4.2 Perspective: Mutual phase locking and RF-devices

The final goal of proving and improving electrical synchronization is to reach mutual phase locking of several STOs. This mutual phase locking may appear through magnetostatic or dipolar fields and/or electrical current. Due to the KTS model, or advanced phenomenological STO descriptions such as Eq. 6.3, it is possible to study and produce robust STO networks from the amplitude/phase models that correctly describe the STO in its autonomous state. As a perspective part, we would like to cite two studies on the electrical mutual phase locking of STOs.

Based on the amplitude/phase equations of the STOs from the KTS model, Tiberkevitch et al. [68] studied the dynamics of an array of 10 STOs serially connected. In their paper, the authors show that by inducing an external phase shift through a RLC resonant circuit, the cooperative dynamics of all the 10 different STOs can occur. The paper also proves the use of a linearized amplitude/phase model as a powerful tool for the network analysis. They indeed first obtained their result for interconnected STOs with the amplitude/phase model that they finally checked with LLGS macrospin simulations.

Finally, based the Eq. 6.3, Zarudniev et al. [167] studied the one-to-one and all-to-all interconnection scheme for a network of 10 different in-plane STOs. The fractional synchronization ($p = 2$ and $q = 1$) is considered and improves considering synchronization in the network. Once again, the comparison of the model to LLGS macrospin simulations showed the equivalence of the two approaches (LLGS and amplitude/phase model taking into account the fractional synchronization). The study of the phase noise shows a reduction of the phase noise by a factor N, with N the number of interconnected STOs [167].

These models offer now the possibility to build and study even more complex topologies of STO networks [186]. The bridge provided by the KTS model that transforms the complex LLGS equation into an oscillator equation should allow one to conceive robust RF sources based on STO networks.

However it should be mentioned that these models are all based on simplifications of the real physical system. One of the difficulties in realizing STOs is that nominally identical STOs (from a fabrication point of view) are not the same because of the dispersion of the nano-structuration of the devices. This leads to a dispersion of anisotropies, internal fields and critical currents, and therefore a disperison in ν, Γ_p, ω_0, Q, and so on. This dispersion has not been taken into account in models. In this case, the phenomenological approach is preferred (such as KTS approach), where one can feed models with real experimental data (ν, Γ_p, f_g, Q, ...).

Part IV

Conclusion

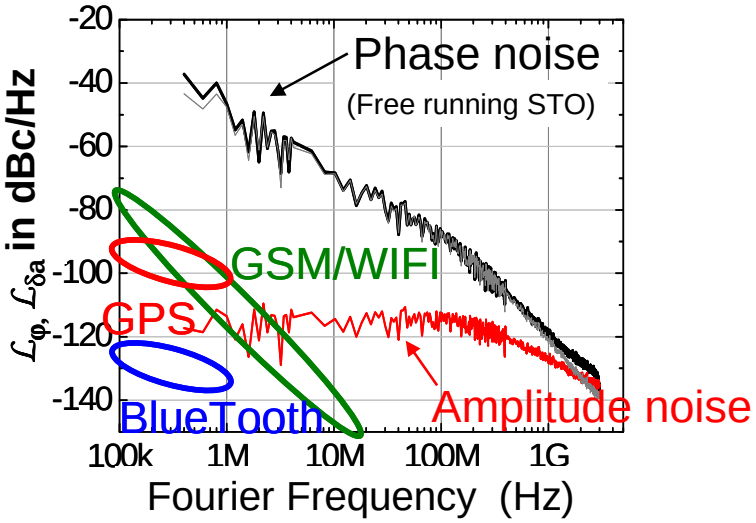

Fig. 6.23: Comparison of the phase noise of the free running STO (from macrospin simulation) to the telecommunication standards specifications (from Table 3.1).

We have developed a tool that can accurately measure the phase and the amplitude noise of a STO. The intensive comparison of experiments and simulations to model predictions, i.e. the KTS theory, found a general good agreement. Concerning the phase noise in STOs, the key point that has been demonstrated is the relative enhancement of the phase noise due to a nonlinear amplitude phase coupling of the STO, due to the non-isochronous nature of STOs.

For the moment, the relative high phase noise prevents any applications in telecommunications (see Fig. 6.23). The PLL can be an approach to reduce the phase noise as shown in this work and experimentally elsewhere [86]. The final design performance with respect to power consumption, agility, robustness,..., will define the potential use of STO in transceivers. The second approach, involving the mutual synchronization of STOs, should take the symmetry into account and might be realized via fractional synchronization principles. Simulations indicate the feasibility of such a network. Both approaches will require more characterization of real STO devices to determine the input parameters for models, such as the KTS model and subsequent development to it.

Indeed, we have seen that the characterization of the autonomous regime can well explain the response of the non-autonomous properties of the STOs (modulation, synchronization). Not only the models can be used to verify the experimental data, but the models can also estimate the best uses of the STO for telecommunication applications. Therefore, a greater interconnection between STO experimentation and RF designers should be engaged for the sake of the development of STO technology, but also in order to locate the potential applications for STOs.

A promising application of STOs is the "STO reader" that seems to benefit from the high modulation speed (Γ_p) and the high "susceptibility" to a shift in STO state (ν). Since read heads are nowadays already using ultra-low RA MTJs as the main component

of the read head, the integration of MgO-based STO would be easier.

However, MgO-based STOs working at high bias current can potentially exhibit some unwanted effects, for example, long term aging (element diffusion, polarizer stability, AF pinning stability,...) or even barrier destruction such that their practical uses may not be possible. This is a material question that needs to be solved on the long run in parallel to RF and signal treatment problems.

Another new route to explore comes from the recent observation that spin transfer torque can be generated inside a ferromagnetic material near a material with a large Rashba spin orbit coupling or large spin hall effect [187]. These spin transfer torques are able to drive the magnetization of the ferromagnetic layer into the nonlinear regime. Potentially, with a magnetoresistive device to sense these dynamics (as shown in [188]) the breakdown of the MgO barrier can be avoided such that it allows one to study the nonlinear dynamical effects at higher spin transfer torque amplitudes.

In all those perspectives for new applications routes, the study of the nonlinear dynamics of the magnetization is required and with this theoretical and experimental concepts that have been provided by this thesis will be of interest.

Bibliography

[1] Etienne Trémolet De Lacheisserie. *Magnétisme*. EDP Sciences, 2000.

[2] S. F. Matar, A. Houari, and M. A. Belkhir. Ab initio studies of magnetic properties of cobalt and tetracobalt nitride Co4N. *Physical Review B*, 75(245109), 2007.

[3] M. Julière. Tunneling between ferromagnetic films. *Physics Letters A*, 54:225, 1975.

[4] John C. Slonczewski. Conductance and exchange coupling of two ferromagnets separated by a tunneling barrier. *Physical Review B*, 39(10):6995, 1989.

[5] John G. Simmons. Generalized Formula for the Electric Tunnel Effect between Similar Electrodes Separated by a Thin Insulating Film. *Journal of Applied Physics*, 34(6):1793 – 1803, 1963.

[6] W. F. Brinkman, R. C. Dynes, and J. M. Rowell. Tunneling Conductance of Asymmetrical Barriers. *Journal of Applied Physics*, 41(5):1915 – 1921, 1970.

[7] F. Montaigne, C. Tiusan, and M. Hehn. Angular dependence of tunnel magneto-resistance in magnetic tunnel junctions and specific aspects in spin-filtering devices. *Journal of Applied Physics*, 108(063912), 2010.

[8] William H Butler. Tunneling magnetoresistance from a symmetry filtering effect. *Science and Technology of Advanced Materials*, 9(014106), 2008.

[9] W. Butler, X.-G. Zhang, T. C. Schulthess, and J. MacLaren. Spin-dependent tunneling conductance of Fe|MgO|Fe sandwiches. *Physical Review B*, 63(054416), January 2001.

[10] X. Zhang and W. H. Butler. Large magnetoresistance in bcc Co / MgO / Co and FeCo / MgO / FeCo tunnel junctions. *Physical Review B*, 70(172407), 2004.

[11] S. Ikeda, J. Hayakawa, Y. Ashizawa, Y. M. Lee, K. Miura, H. Hasegawa, M. Tsunoda, F. Matsukura, and H. Ohno. Tunnel magnetoresistance of 604% at 300K by suppression of Ta diffusion in CoFeB/MgO/CoFeB pseudo spin-valves annealed at high temperature. *Applied Physics Letters*, 93(082508), 2008.

[12] M. N. Baibich, J. M. Broto, Albert Fert, F. Nguyen Van Dau, F. Petroff, P. Eitenne, G. Creuzet, A. Friederich, and J. Chazelas. Giant Magnetoresistance of (001)Fe/(001)Cr Magnetic Superlattices. *Physical Review Letters*, 61(21): 2472–2475, 1988.

[13] G. Binasch, P. Grünberg, F. Saurenbach, and W. Zinn. Enhanced magnetoresistance in layered magnetic structures. *Physical Review B(R)*, 39(7): 4828–4830, 1989.

[14] J. C. Slonczewski. Current-driven excitation of magnetic multilayers. *Journal of Magnetism and Magnetic Materials*, 159:L1–L7, 1996.

[15] L. Berger. Emission of spin waves by a magnetic multilayer traversed by a current. *Physical Review B*, 54(13):9353–9358, 1996.

[16] M. Tsoi, A. G. M. Jansen, J. Bass, W.-C. Chiang, M. Seck, V. Tsoi, and P. Wyder. Excitation of a Magnetic Multilayer by an Electric Current. *Physical Review Letters*, 80(19):4281–4284, 1998.

[17] E. B. Myers, D. C. Ralph, J. A. Katine, R. N. Louie, and R. A. Buhrman. Current-Induced Switching of Domains in Magnetic Multilayer Devices. *Science*, 285:867, 1999.

[18] J. A. Katine, F. J. Albert, R. A. Buhrman, E. B. Myers, and D. C. Ralph. Current-Driven Magnetization Reversal and Spin-Wave Excitations in Co/Cu/Co Pillars. *Physical Review Letters*, 84(14):3149–3152, 2000.

[19] G. D. Fuchs, N. C. Emley, I. N. Krivorotov, P. M. Braganca, E. M. Ryan, S. I. Kiselev, J. C. Sankey, D.C. Ralph, and R. A. Buhrman. Spin-transfer effects in nanoscale magnetic tunnel junctions. *Applied Physics Letters*, 85(7):1205, 2004.

[20] M. Hosomi, H. Yamagishi, T. Yamamoto, K. Bessho, Y. Higo, K. Yamane, H. Yamada, M. Shoji, H. Hachino, C. Fukumoto, H. Nagao, and H. Kano. A Novel Nonvolatile Memory with Spin Torque Transfer Magnetization Switching : Spin-RAM. *IEEE International Electron Devices Meeting*, pages 459 – 462, 2005.

[21] M. Durlam, D. Addie, J. Akerman, B. Butcher, P. Brown, J. Chan, M. Deherrera, B. N. Engel, B. Feil, G. Grynkewich, J. Janesky, M. Johnson, K. Kyler, J. Molla, J. Martin, K. Nagel, J. Ren, N. D. Rizzo, T. Rodriguez, L. Savtchenko, J. Salter, J. M. Slaughter, J. J. Sun, M. Lien, K. Papworth, P. Shah, W. Qin, R. Williams, L. Wise, and S. Tehrani. A 0.18pm 4Mb Toggling MRAM. In *IEEE International Electron Devices Meeting*, pages 995–997, 2003.

[22] Jim Hutchby and Mike Garner. Assessment of the Potential & Maturity of Selected Emerging Research Memory Technologies Workshop & ERD/ERM Working Group Meeting (April 6-7, 2010), 2010.

[23] Y. Tserkovnyak, A. Brataas, G. E. W. Bauer, and B. I. Halperin. Nonlocal magnetization dynamics in ferromagnetic heterostructures. *Reviews of Modern Physics*, 77(1375), 2005.

[24] S. S. P. Parkin and D. Mauri. Spin engineering: Direct determination of the RKKY far-field range function in ruthenium. *Physical Review B(R)*, 44(13), 1991.

[25] T. Katayama, S. Yuasa, J. Velev, M. Ye. Zhuravlev, S. S. Jaswal, and E. Y. Tsymbal. Interlayer exchange coupling in Fe / MgO / Fe magnetic tunnel junctions. *Applied Physics Letters*, 89(112503), 2006.

[26] C. Baraduc, M. Chshiev, and U. Ebels. *Nanomagnetism and Spintronics: Fabrication, Materials, Characterization and Applications*, Chapter 8, pages 173–192. World Scientific, 2008.

[27] J. C. Sankey, Y.-T. Cui, J. Z. Sun, J. C. Slonczewski, R. A. Buhrman, and D. C. Ralph. Measurement of the spin-transfer-torque vector in magnetic tunnel junctions. *Nature Physics*, 4(1):67–71, November 2007.

[28] I. Theodonis, N. Kioussis, A. Kalitsov, M. Chshiev, and W. H. Butler. Anomalous Bias Dependence of Spin Torque in Magnetic Tunnel Junctions. *Physical Review Letters*, 97(237205), 2006.

[29] S.-C. Oh, S.-Y. Park, A. Manchon, M. Chshiev, J.-H. Han, H.W. Lee, J.-E. Lee, K.T. Nam, Y. Jo, Y.-C. Kong, B. Dieny, and K.-J. Lee. Bias-voltage dependence of perpendicular spin-transfer torque in asymmetric MgO-based magnetic tunnel junctions. *Nature Physics*, 5(12):898–902, 2009.

[30] Y. Zhou, J. Persson, and J. Akerman. Intrinsic phase shift between a spin torque oscillator and an alternating current. *Journal of applied Physics*, 101(09A510), 2007.

[31] Z. Yang, S. Zhang, and Y. C. Li. Chaotic Dynamics of Spin-Valve Oscillators. *Physical Review Letters*, 99(13), September 2007.

[32] M. L. Schneider, M. R. Pufall, W. H Rippard, S. E. Russek, and J. A. Katine. Thermal effects on the critical current of spin torque switching in spin valve nanopillars. *Applied Physics Letters*, 90(092504), 2007.

[33] W. F. Brown. Thermal Fluctuations of a Single-Domain Particle. *Physcial Review*, 130(5):1677–1686, 1963.

[34] J. Xiao, A. Zangwill, and M. D. Stiles. Macrospin models of spin transfer dynamics. *Physical Review B*, 72(014446), 2005.

[35] Z. Diao, Z. Li, S. Wang, Y. Ding, A. Panchula, E. Chen, L.-C. Wang, and Y. Huai. Spin-transfer torque switching in magnetic tunnel junctions and spin-transfer torque random access. *Journal of Physics: Condensed Matter*, 19(165209), 2007.

[36] D. Ravelosona, S. Mangin, Y. Lemaho, J. A. Katine, B. D. Terris, and E. E. Fullerton. Domain Wall Creation in Nanostructures Driven by a Spin-Polarized Current. *Physical Review Letters*, 96(186604), 2006.

[37] J. Z. Sun, R. P. Robertazzi, J. Nowak, P. L. Trouilloud, G. Hu, D. W. Abraham, M. C. Gaidis, S. L. Brown, E. J. O'Sullivan, W. J. Gallagher, and D. C. Worledge. Effect of subvolume excitation and spin-torque efficiency on magnetic switching. *Physical Review B*, 84(064413), 2011.

[38] J.-V. Kim, Q. Mistral, C. Chappert, V. S Tiberkevich, and A. N. Slavin. Line Shape Distortion in a Nonlinear Auto-Oscillator Near Generation Threshold: Application to Spin-Torque Nano-Oscillators. *Physical Review Letters*, 100(167201), April 2008.

[39] S. I. Kiselev, J.C. Sankey, I.N. Krivorotov, N.C. Emley, R.J. Schoelkopf, R.A. Buhrman, and D.C. Ralph. Microwave oscillations of a nanomagnet driven by a spin-polarized current. *Nature*, 425:380–383, 2003.

[40] K.-J. Lee, A. Deac, O. Redon, J.-P. Nozières, and B. Dieny. Excitations of incoherent spin-waves due to spin-transfer torque. *Nature Materials*, 3:877–881, 2004.

[41] A. Pikovsky, M. Rosenblum, and J. Kurths. *Synchronization. A universal concept in nonlinear sciences*, volume 12. Cambridge University Press, Cambridge, 2001.

[42] Kaneyuki Kurokawa. Noise in Synchronized Oscillators. *IEEE TRANSACTIONS ON MICROWAVE THEORY AND TECHNIQUES*, MTT-16(4):234–240, 1968.

[43] D. B. Leeson. Simple Model of Feedback Oscillator Noise Spectrum. *Proceedings Letters of the IEEE*, 54(2):329–330, 1966.

[44] Enrico Rubiola. A generalization of the Leeson effect. *arXiv:1004.5539v1*, 2010.

[45] S. Petit, N. De Mestier, C. Baraduc, C. Thirion, Y. Liu, M. Li, P. Wang, and B. Dieny. Influence of spin-transfer torque on thermally activated ferromagnetic resonance excitations in magnetic tunnel junctions. *Physical Review B*, 78(184420), 2008.

[46] S. Petit, C. Baraduc, C. Thirion, U. Ebels, Y. Liu, M. Li, P. Wang, and B. Dieny. Spin-Torque Influence on the High-Frequency Magnetization Fluctuations in Magnetic Tunnel Junctions. *Physical Review Letters*, 98(077203), February 2007.

[47] Sébastien PETIT-WATELOT. *Influence du couple de transfert de spin sur les fluctuations magnétiques thermiquement activées dans les jonctions tunnel magnétiques*. PhD thesis, CEA/SPINTEC, 2007.

[48] T. J. Silva and M. W. Keller. Theory of Thermally Induced Phase Noise in Spin Torque Oscillators for a High-Symmetry Case. *IEEE Transactions on Magnetics*, 46(9):3555–3573, 2010.

[49] A. N. Slavin and V. S Tiberkevich. Excitation of Spin Waves by Spin-Polarized Current in Magnetic. *IEEE Transations on Magnetics*, 44(7):1916–1927, 2008.

[50] Joo-von Kim. Stochastic theory of spin-transfer oscillator linewidths. *Physical Review B*, 73(174412), 2006.

[51] V. S. Tiberkevich, A. N. Slavin, and J.-V. Kim. Microwave power generated by a spin-torque oscillator in the presence of noise. *Applied Physics Letters*, 91(192506), 2007.

[52] J.-V. Kim, V. S. Tiberkevich, and A. N. Slavin. Generation Linewidth of an Auto-Oscillator with a Nonlinear Frequency Shift: Spin-Torque Nano-Oscillator. *Physical Review Letters*, 100(017207), January 2008.

[53] V. S. Tiberkevich, A. N. Slavin, and J.-V. Kim. Temperature dependence of nonlinear auto-oscillator linewidths: Application to spin-torque nano-oscillators. *Physical Review B*, 78(092401), September 2008.

[54] A. N. Slavin and V. S. Tiberkevich. Nonlinear Auto-Oscillator Theory of Microwave Generation by Spin-Polarized Current. *IEEE Transactions on Magnetics*, 45(4): 1875–1918, 2009.

[55] S. Rezende, F. de Aguiar, and A. Azevedo. Magnon excitation by spin-polarized direct currents in magnetic nanostructures. *Physical Review B*, 73(094402), 2006.

[56] S. Rezende, F. de Aguiar, R. Rodríguez-Suárez, and A. Azevedo. Mode Locking of Spin Waves Excited by Direct Currents in Microwave Nano-oscillators. *Physical Review Letters*, 98(087202), February 2007.

[57] R. Rodríguez-Suárez, A. Matos-Abiague, A. Azevedo, and S. Rezende. Frequency shift of spin waves in tunnel-junction spin-transfer nano-oscillators. *Physical Review B*, 82(132410), October 2010.

[58] Sergio M. Rezende. Quantum coherence in spin-torque nano-oscillators. *Physical Review B*, 81(092401), 2010.

[59] Y. Zhou, V. S. Tiberkevich, G. Consolo, E. Iacocca, B. Azzerboni, A. N. Slavin, and J. Å kerman. Oscillatory transient regime in the forced dynamics of a nonlinear auto oscillator. *Physical Review B*, 82(012408), 2010.

[60] A. N. Slavin and P. Kabos. Approximate Theory of Microwave Generation in a Current-Driven Magnetic Nanocontact Magnetized in an Arbitrary Direction. *IEEE Transactions on Magnetics*, 41(4):1264–1273, 2005.

[61] A. N. Slavin and V. S. Tiberkevich. Theory of mutual phase locking of spin-torque nanosized oscillators. *Physical review B*, 74(104401), 2006.

[62] F. B. Mancoff, N. D. Rizzo, B. N. Engel, and S. Tehrani. Phase-locking in double-point-contact spin-transfer devices. *Nature*, 437(September):393–395, 2005.

[63] S. Kaka, M. R. Pufall, W. H. Rippard, T. J. Silva, S. E. Russek, and J. A. Katine. Mutual phase-locking of microwave spin torque nano-oscillators. *Nature*, 437(September):389–392, September 2005.

[64] W. Rippard, M. Pufall, S. Kaka, T. Silva, S. Russek, and J. Katine. Injection Locking and Phase Control of Spin Transfer Nano-oscillators. *Physical Review Letters*, 95(067203), August 2005.

[65] B. Georges, J. Grollier, M. Darques, V. Cros, C. Deranlot, B. Marcilhac, G. Faini, and A. Fert. Coupling Efficiency for Phase Locking of a Spin Transfer Nano-Oscillator to a Microwave Current. *Physical Review Letters*, 101(017201), July 2008.

[66] A. N. Slavin and V. S. Tiberkevich. Nonlinear self-phase-locking effect in an array of current-driven magnetic nanocontacts. *Physical Review B*, 72(092407), 2005.

[67] S. Bonetti. *Magnetization Dynamics in Nano-Contact Spin Torque Oscillators*. PhD thesis, KTH, 2010.

[68] V. S. Tiberkevich, A. N. Slavin, E. Bankowski, and G. Gerhart. Phase-locking and frustration in an array of nonlinear spin-torque nano-oscillators. *Applied Physics Letters*, 95(262505), 2009.

[69] M. R. Pufall, W. H. Rippard, S. Kaka, T. J. Silva, and S. E. Russek. Frequency modulation of spin-transfer oscillators. *Applied Physics Letters*, 86(082506), 2005.

[70] P. K. Muduli, Ye. Pogoryelov, S. Bonetti, G. Consolo, Fred Mancoff, and Johan Å kerman. Nonlinear frequency and amplitude modulation of a nanocontact-based spin-torque oscillator. *Physical Review B(R)*, 81(140408), April 2010.

[71] Ye. Pogoryelov, P. K. Muduli, S. Bonetti, Fred Mancoff, and Johan Akerman. Spin-torque oscillator linewidth narrowing under current modulation. *Applied Physics Letters*, 98(192506), 2011.

[72] Ye. Pogoryelov, P. K. Muduli, S. Bonetti, E. Iacocca, F. Mancoff, and J. Akerman. Frequency modulation of spin torque oscillator pairs. *Applied Physics Letters*, 98(192501), 2011.

[73] G. Consolo, V. Puliafito, G. Finocchio, L. Lopez-diaz, R. Zivieri, L. Giovannini, F. Nizzoli, G. Valenti, and B. Azzerboni. Combined Frequency-Amplitude Nonlinear Modulation : Theory and Applications. *IEEE Transactions on Magnetics*, 46(9):3629–3634, 2010.

[74] K. Kudo, T. Nagasawa, R. Sato, and K. Mizushima. Amplitude-phase coupling in a spin-torque nano-oscillator. *Journal of Applied Physics*, 105(07D105), 2009.

[75] Q. Mistral, J.-V. Kim, T. Devolder, P. Crozat, C. Chappert, J. A. Katine, M. J. Carey, and K. Ito. Current-driven microwave oscillations in current perpendicular-to-plane spin-valve nanopillars. *Applied Physics Letters*, 88(192507), 2006.

[76] M. Quinsat, D. Gusakova, J. F. Sierra, J. P. Michel, D. Houssameddine, B. Delaet, M.-C. Cyrille, U. Ebels, B. Dieny, L. D. Buda-Prejbeanu, J. A. Katine, D. Mauri, A. Zeltser, M. Prigent, J.-C. Nallatamby, and R. Sommet. Amplitude and phase noise of magnetic tunnel junction oscillators. *Applied Physics Letters*, 97(182507), 2010.

[77] T. Nagasawa, K. Mizushima, H. Suto, K. Kudo, and R. Sato. Amplitude Noise in Spin-Torque Oscillators. *Applied Physics Express*, 4(063005), May 2011.

[78] L. Bianchini, S. Cornelissen, J.-V. Kim, T. Devolder, W. van Roy, L. Lagae, and C. Chappert. Direct experimental measurement of phase-amplitude coupling in spin torque oscillators. *Applied Physics Letters*, 97(032502), 2010.

[79] C. Boone, J. Katine, J. Childress, J. Zhu, X. Cheng, and I. Krivorotov. Experimental test of an analytical theory of spin-torque-oscillator dynamics. *Physical Review B(R)*, 79(140404), April 2009.

[80] K. Kudo, T. Nagasawa, R. Sato, and K. Mizushima. Measurement of nonlinear frequency shift coefficient in spin-torque oscillators based on MgO tunnel junctions. *Applied Physics Letters*, 95(022507), 2009.

[81] Dimitri Houssameddine. *Dynamique de l'aimantation de nano-oscillateurs micro-ondes à transfert de spin*. PhD thesis, UMR SPINTEC, 2009.

[82] M. David Pozar. *Microwave engineering*. Jhon Wiley & Sons, 2005.

[83] P. Villard, U. Ebels, D. Houssameddine, J. A. Katine, D. Mauri, B. Delaet, P. Vincent, M.-C. Cyrille, B. Viala, J.-P. Michel, J. Prouvée, and F. Badets. A GHz Spintronic-Based RF Oscillator. *IEEE Journal of Solid-State Circuits*, 45(1):214–223, 2010.

[84] Agilent. Spectrum Analysis Basics, 2005.

[85] M. W. Keller, M. R. Pufall, W. H. Rippard, and T. J. Silva. Nonwhite frequency noise in spin torque oscillators and its effect on spectral linewidth. *Physical Review B*, 82(054416), 2010.

[86] M. W. Keller, A. B. Kos, T. J. Silva, W. H. Rippard, and M. R. Pufall. Time domain measurement of phase noise in a spin torque oscillator. *Applied Physics Letters*, 94(193105), 2009.

[87] E. S. Ferre-Pikal, J. R. Vig, J. C. Camparo, L. S. Cutler, L. Maleki, W. J. Riley, S. R. Stein, C. Thomas, F. L. Walls, and J. D. White. DRAFT REVISION OF IEEE STD 1139-1988 STANDARD DEFINITIONS OF PHYSICAL QUANTITIES FOR FUNDAMENTAL FREQUENCY AND TIME METROLOGY - RANDOM INSTABILITIES. *1997 IEEE International RFrequency Control Symposium*, pages 338–357, 1997.

[88] François Vernotte. Stabilité temporelle et fréquentielle des oscillateurs : modèles. *Technique de l'ingénieur*, R 680.

[89] A. L. Lance, W. D. Seal, and F. Labaar. Phase Noise Analysis and AM Noise Measurements in the Frequency Domain. *International Journal of Infrared and Millimeter Waves*, 11(4):239 – 289, February 1984.

[90] PN9000 Automated Phase Noise Measurement System Application Note. Aeroflex Application Note 1, 2012.

[91] K. Mizushima, K. Kudo, and R. Sato. Phase and amplitude noise spectra in spin-transfer nano-oscillators. *Journal of Applied Physics*, 101(113903), 2007.

[92] Alper Demir and Alberto Sangiovanni-Vincentelli. *Analysis and Simulation of Noise in Nonlinear Electronic Circuits and Systems*. Kluwer Academic Publishers, 1998.

[93] James A. Barnes. Models for the Interpretation of Frequency Stability Measurements. *National Bureau of Standard*, 1976.

[94] J. Rutman. Characterization of phase and frequency instabilities in precision frequency sources: Fifteen years of progress. *Proceedings of the IEEE*, 66(9): 1048–1075, 1978.

[95] Agilent. Data sheet Agilent E8257D PSG (Analog), 2012.

[96] B. Picinbono. On instantaneous amplitude and phase of signals. *IEEE Transactions on Signal Processing*, 45(3):552–560, March 1997.

[97] Tektronix. DPO70000C/D Series User Manual, 2012.

[98] Tektronix. DSA/DPO70000B Specifications and Performance. 2012.

[99] S. Yuasa, T. Nagahama, A. Fukushima, Y. Suzuki, and K. Ando. Giant room-temperature magnetoresistance in single-crystal Fe/MgO/Fe magnetic tunnel junctions. *Nature materials*, 3(12):868–71, December 2004.

[100] K. Tsunekawa, D. D. Djayaprawira, M. Nagai, H. Maehara, S. Yamagata, N. Watanabe, S. Yuasa, Y. Suzuki, and K. Ando. Giant tunneling magnetoresistance effect in low-resistance CoFeB/ MgO (001)/ CoFeB magnetic tunnel junctions for read-head applications. *Applied Physics Letters*, 87(072503), 2005.

[101] A. Zaleski, J. Wrona, M. Czapkiewicz, W. Skowronski, J. Kanak, and T. Stobiecki. The study of conductance in magnetic tunnel junctions with a thin MgO barrier : The effect of Ar pressure on tunnel magnetoresistance and resistance area product. *Journal of Applied Physics*, 111(033903), 2012.

[102] Jérémy Alvarez-Hérault. *Mémoire magnétique à écriture par courant polarisé en spin assistée thermiquement*. PhD thesis, SPINTEC, 2010.

[103] H. Maehara, K. Nishimura, Y. Nagamine, K. Tsunekawa, T. Seki, H. Kubota, A. Fukushima, K. Yakushiji, K. Ando, and S. Yuasa. Tunnel Magnetoresistance above 170% and Resistance-Area Product of 1 $(\mu m)^2$ Attained by In situ Annealing of Ultra-Thin MgO Tunnel Barrier. *Applied Physics Express*, 4(033002), 2011.

[104] J. Akerman, R. Escudero, C. Leighton, S. Kim, D. A. Rabson, R. W. Dave, J. M. Slaughter, and I. K. Schuller. Criteria for ferromagnetic-insulator-ferromagnetic tunneling. *Journal of Magnetism and Magnetic Materials*, 240:86–91, 2002.

[105] B. Oliver, Q. He, X. Tang, and J. Nowak. Dielectric breakdown in magnetic tunnel junctions having an ultrathin barrier. *Journal of Applied Physics*, 91(7):4348, 2002.

[106] J. Das, R. Degraeve, P. Roussel, G. Groeseneken, G. Borghs, and J. De Boeck. Area scaling and voltage dependence of time-to-breakdown in magnetic tunnel junctions. *Journal of Applied Physics*, 91(10):7712, 2002.

[107] B. Oliver, Q. He, X. Tang, and J. Nowak. Tunneling criteria and breakdown for low resistive magnetic tunnel junctions. *Journal of Applied Physics*, 94(3):1783, 2003.

[108] C. Shang, Y. Chen, and K.-S. Moon. Kinetics of pinhole nucleation and growth in magnetic tunnel junctions. *Journal of Applied Physics*, 93(10):7017, 2003.

[109] Z.-S. Zhang and D. A. Rabson. Electrical and thermal modeling of the non-Ohmic differential conductance in a tunnel junction containing a pinhole. *Journal of Applied Physics*, 95(2):557, 2004.

[110] K. Hosotani, Y. Asao, M. Nagamine, T. Ueda, H. Aikawa, N. Shimomura, S. Ikegawa, T. Kajiyama, S. Takahashi, A. Nitayama, and H. Yoda. Effect of interface buffer layer on the reliability of ultra-thin MgO magnetic tunnel junctions for spin transfer switching MRAM. In *IEEE International Reliability Physics Symposium Proceedings*, pages 650–651. IEEE, 2007.

[111] B. Oliver, G. Tuttle, Q. He, X. Tang, and J. Nowak. Two breakdown mechanisms in ultrathin alumina barrier magnetic tunnel junctions. *Journal of Applied Physics*, 95(3):1315, 2004.

[112] Q. Chen, T. Min, T. Torng, C. Horng, D. Tang, and P. Wang. Study of dielectric breakdown distributions in magnetic tunneling junction with MgO barrier. *Journal of Applied Physics*, 105(07C931), 2009.

[113] H. Xi, S. Franzen, J. Guzman, and S. Mao. Degradation of magnetic tunneling junctions caused by pinhole formation and growth. *Journal of Magnetism and Magnetic Materials*, 319:60–63, December 2007.

[114] D. Houssameddine, S. H. Florez, J .A. Katine, J.-P. Michel, U. Ebels, D. Mauri, O. Ozatay, B. Delaet, B. Viala, L Folks, B. D. Terris, and M.-C. Cyrille. Spin transfer induced coherent microwave emission with large power from nanoscale MgO tunnel junctions. *Applied Physics Letters*, 93(022505), 2008.

[115] D. Houssameddine, U. Ebels, B. Dieny, K. Garello, J.-P. Michel, B. Delaet, B. Viala, M.-C. Cyrille, J. A. Katine, and D. Mauri. Temporal Coherence of MgO Based Magnetic Tunnel Junction Spin Torque Oscillators. *Physical Review Letters*, 102(257202), June 2009.

[116] R. Matsumoto, A. Fukushima, K. Yakushiji, S. Yakata, T. Nagahama, H. Kubota, T. Katayama, Y. Suzuki, K. Ando, S. Yuasa, B. Georges, V. Cros, J. Grollier, and A. Fert. Spin-torque-induced switching and precession in fully epitaxial Fe / MgO / Fe magnetic tunnel junctions. *Physical Review B*, 80(174405), 2009.

[117] G. C. Han, E. L. Tan, B. Y. Zong, Y. K. Zheng, S. G. Tan, and L. Wang. Abnormal increase in ferromagnetic resonance amplitude just before the breakdown in tunnel magnetoresistive heads. *Journal of Applied Physics*, 103(07F518), 2008.

[118] T. Devolder, L. Bianchini, J.-V. Kim, P. Crozat, C. Chappert, S. Cornelissen, M. Op De Beeck, and L. Lagae. Auto-oscillation and narrow spectral lines in spin-torque oscillators based on MgO magnetic tunnel junctions. *Journal Of applied Physics*, 106(103921), 2009.

[119] A. V. Nazarov, H. M. Olson, H. Cho, K. Nikolaev, Z. Gao, S. Stokes, and B. B. Pant. Spin transfer stimulated microwave emission in MgO magnetic tunnel junctions. *Applied Physics Letters*, 88(162504), 2006.

[120] A. V. Nazarov, K. Nikolaev, Z. Gao, H. Cho, and D. Song. Microwave generation in MgO magnetic tunnel junctions due to spin transfer effects (invited). *Journal of Applied Physics*, 103(07A503), 2008.

[121] M. Al-mahdawi, M. Doi, S. Hashimoto, H.N. Fuke, H. Iwasaki, and M. Sahashi. Frequency Modulation of a Nano-Oxide Layer-Based Spin-Torque Oscillator With FeCo Nanocontacts. *IEEE Transactions on Magnetics*, 47(10):3380–3382, 2011.

[122] Tetsuya Nakamura, Hiroaki Suzuki, Yoshihito Okutomi, Masaaki Doi, Hiromi Niu Fuke, Hitoshi Iwasaki, and Masashi Sahashi. Feature of Current-Induced Microwave Oscillation in Nano-Contacts Magneto-Resistive Devices After High-Temperature Annealing. *IEEE Transacations on Magnetics*, 46(6):2212–2215, 2010.

[123] M. Doi, H. Endo, K. Shirafuji, S. Kawasaki, M. Sahashi, N. H. Fuke, H. Iwasaki, and H. Imamura. Spin-transfer-induced microwave oscillations in spin valves with ferromagnetic nano-contacts in oxide spacer layer. *Journal of Physics D: Applied Physics*, 44(092001), 2011.

[124] J.-G. Zhu. Pinholes and spin transfer effect in magnetic tunnel junction heads. *Journal of Applied Physics*, 97(10N703), 2005.

[125] Yisong Zhang, Zongzhi Zhang, Yaowen Liu, Zhixiong Kang, B. Ma, and Q. Y. Jin. Micromagnetic study of hotspot and thermal effects on spin-transfer switching in magnetic tunnel junctions. *Journal of Applied Physics*, 101(10):103905, 2007.

[126] N. Strelkov, A. Vedyayev, N. Ryzhanova, D. Gusakova, L. D. Buda-Prejbeanu, M. Chshiev, S. Amara, N. De Mestier, C. Baraduc, and B. Dieny. Spin-current vortices in current-perpendicular-to-plane nanoconstricted spin valves. *Physcial Review B*, 84(024416), 2011.

[127] I. N. Krivorotov, N. C. Emley, R. A. Buhrman, and D. C. Ralph. Time-domain studies of very-large-angle magnetization dynamics excited by spin transfer torques. *Physical Review B*, 77(054440), February 2008.

[128] I. N. Krivorotov, N. C. Emley, A. G. F. Garcia, J. C. Sankey, S. I. Kiselev, D. C. Ralph, and R. A. Buhrman. Temperature Dependence of Spin-Transfer-Induced Switching of Nanomagnets. *Physical Review Letters*, 93(166603), October 2004.

[129] C. E. Patton and C. H. Wilts. Temperature Dependence of the Ferromagnetic Resonance Linewidth in Thin NiFe Films. *Journal of Applied Physics*, 38(9):3537, 1967.

[130] M. Diaz De Sihues, P. J. Silva, and J. R. Fermin. Effect of temperature on the ferromagnetic resonance of Ni50Fe50 thin films. *Physica B*, 354:361–364, 2004.

[131] J. F. Sierra, V. V. Pryadun, F. G. Aliev, S. E. Russek, M. García-Hernández, E. Snoeck, and V. V. Meltushko. Temperature dependent dynamic and static magnetic response in magnetic tunnel junctions with Permalloy layers. *Applied Physics Letters*, 93(172510), 2008.

[132] H. Yu, R. Huber, T. Schwarze, F. Brandl, T. Rapp, P. Berberich, G. Duerr, and D. Grundler. High propagating velocity of spin waves and temperature dependent damping in a CoFeB thin film. *Applied Physics Letters*, 100(262412), 2012.

[133] P. K. Muduli, O. G. Heinonen, and J. Akerman. Intrinsic frequency doubling in a magnetic tunnel junction-based spin torque oscillator. *Journal of Applied Physics*, 110(076102), 2011.

[134] B. Georges, J. Grollier, V. Cros, A. Fert, A. Fukushima, H. Kubota, K. Yakushijin, S. Yuasa, and K. Ando. Origin of the spectral linewidth in nonlinear spin-transfer oscillators based on MgO tunnel junctions. *Physical Review B(R)*, 80(060404), August 2009.

[135] Vasil Tiberkevich. Private communication. 2010.

[136] Vasil Tiberkevich. Private Communication. 2012.

[137] A. Demir, A. Mehrotra, and J. Roychowdhury. Phase noise in oscillators: a unifying theory and numerical methods for characterization. *IEEE Transactions on Circuits and Systems I: Fundamental Theory and Applications*, 47(5):655–674, May 2000.

[138] J. C. Sankey, I. N. Krivorotov, S. I. Kiselev, P. M. Braganca, N. C. Emley, R. A. Buhrman, and D. C. Ralph. Mechanisms limiting the coherence time of spontaneous magnetic oscillations driven by dc spin-polarized currents. *Physical Review B*, 72(224427), December 2005.

[139] M. L. Schneider, W. H. Rippard, M. R. Pufall, T. Cecil, T. J. Silva, and S. E. Russek. Temperature dependence of spin-torque-driven self-oscillations. *Physical Review B*, 80(144412), 2009.

[140] J. Foros, A. Brataas, G. E. W. Bauer, and Y. Tserkovnyak. Noise and dissipation in magnetoelectronic nanostructures. *Physical Review B*, 79(214407), 2009.

[141] N. Smith, J. A. Katine, J.y R. Childress, and M. J. Carey. Thermal and Spin-Torque Noise in CPP (TMR and/or GMR) Read Sensors. *IEEE Transactions on Magnetics*, 42(2):114–119, 2006.

[142] L. Wang, G. Han, Y. Zheng, and B. Liu. Simulation and Stability Analysis of Current and Transverse Field Effects on Spin Transfer Noise. *IEEE Transactions On Magnetics*, 43(6):2313–2315, 2007.

[143] S. Maat, N. Smith, M .J. Carey, and J. R. Childress. Suppression of spin torque noise in current perpendicular to the plane spin- valves by addition of Dy cap layers. *Applied Physics Letters*, 93(103506), 2008.

[144] N. Smith, M. J. Carey, and J. R. Childress. Measurement of Gilbert damping parameters in nanoscale CPP-GMR spin valves. *Physical Review B*, 81(184431), 2010.

[145] Selma Amara. *Degradation Processes in MRAM*. PhD thesis, 2012.

[146] M. Manfrini, T. Devolder, J.-V. Kim, P. Crozat, N. Zerounian, C. Chappert, W. Van Roy, L. Lagae, G. Hrkac, and T. Schrefl. Agility of vortex-based nanocontact spin torque oscillators. *Applied Physics Letters*, 95(192507), 2009.

[147] M. Manfrini, T. Devolder, J.-V. Kim, P. Crozat, C. Chappert, W. Van Roy, and L. Lagae. Frequency shift keying in vortex-based spin torque oscillators. *Journal of Applied Physics*, 109(083940), 2011.

[148] G. Consolo and V. Puliafito. Analytical and Micromagnetic Study of Nonlinear Amplitude Modulation in Spintronic Modulators. *IEEE Transactions on Magnetics*, 46(6):2063–2066, June 2010.

[149] K. Mizushima, K. Kudo, T. Nagasawa, and R. Sato. High-data-transfer-rate read heads composed of spin-torque oscillators. *Journal of Physics: Conference Series*, 266(012060), January 2011.

[150] K. Mizushima, K. Kudo, T. Nagasawa, and R. Sato. Signal-to-noise ratios in high-signal-transfer-rate read heads composed of spin-torque oscillators. *Journal of Applied Physics*, 107(063904), 2010.

[151] T. Nagasawa, H. Suto, K. Kudo, K. Mizushima, and R. Sato. Frequency transition of spin-torque oscillator under the magnetic-field pulse in nanosecond range. *Journal of Applied Physics*, 109(07C907), 2011.

[152] T. Nagasawa, H. Suto, K. Kudo, T. Yang, K. Mizushima, and R. Sato. Delay detection of frequency modulation signal from a spin-torque oscillator under a nanosecond-pulsed magnetic field. *Journal of Applied Physics*, 111(07C908), 2012.

[153] K. Kudo, T. Nagasawa, K. Mizushima, H. Suto, and R. Sato. Numerical Simulation on Temporal Response of Spin-Torque Oscillator to Magnetic Pulses. *Applied Physics Express*, 3(043002), April 2010.

[154] S. Urazhdin, V. S. Tiberkevich, and A. N. Slavin. Parametric Excitation of a Magnetic Nanocontact by a Microwave Field. *Physical Review Letters*, 105(237204), December 2010.

[155] Rie Sato and Koichi Mizushima. SIGNAL REPRODUCING METHOD, MAGNETIC HEAD AND MAGNETIC RECORDING AND REPRODUCING APPARATUS, US Patent, US 2011/0013304, 2008.

[156] R. Sato, K. Kudo, T. Nagasawa, H. Suto, and K. Mizushima. Simulations and Experiments Toward High-Data-Transfer-Rate Readers Composed of a Spin-Torque Oscillator. *IEEE Transactions on magnetics*, 48(5):1758–1764, 2012.

[157] H. Suto, T. Nagasawa, K. Kudo, K. Mizushima, and R. Sato. Real-Time Measurement of Temporal Response of a Spin-Torque Oscillator to Magnetic Pulses. *Applied Physics Express*, 4(013003), January 2011.

[158] A. Hajimiri and T. H. Lee. A General Theory of Phase Noise in Electrical Oscillators. *IEEE Journal of Solid-State Circuits*, 33(2):179–195, 1998.

[159] Keliu Shu and Edgard Sanchez-Sinencio. *CMOS PLL Synthesizers: Analysis and Design*. Springer Science, 2005.

[160] J. Grollier, V. Cros, and A. Fert. Synchronization of spin-transfer oscillators driven by stimulated microwave currents. *Physical Review B(R)*, 73(060409), 2006.

[161] B. Georges, J. Grollier, V. Cros, and A. Fert. Impact of the electrical connection of spin transfer nano-oscillators on their synchronization: an analytical study. *Applied Physics Letters*, 92(232504), 2008.

[162] H.C. Chang, X. Cao, U. K. Mishra, and R. A. York. Phase Noise in Coupled Oscillators: Theory and Experiment. *IEEE Transactions on Microwave Theory and Techniques*, 45(5):604–615, 1997.

[163] E. Iacocca and J. Akerman. Destabilization of serially connected spin-torque oscillators via non-Adlerian dynamics. *Journal Of Applied Physics*, 110(130910), 2011.

[164] S. Urazhdin, P. Tabor, V. S. Tiberkevich, and A. N. Slavin. Fractional Synchronization of Spin-Torque Nano-Oscillators. *Physical Review Letters*, 105(104101), August 2010.

[165] P. Tabor, V. S. Tiberkevich, A. N. Slavin, and S. Urazhdin. Hysteretic synchronization of nonlinear spin-torque oscillators. *Physical Review B(R)*, 82(020407), July 2010.

[166] M. Quinsat, J. F. Sierra, I. Firastrau, V. Tiberkevich, A. Slavin, D. Gusakova, L. D. Buda-Prejbeanu, M. Zarudniev, J.-P. Michel, U. Ebels, B. Dieny, M.-C. Cyrille, J. A. Katine, D. Mauri, and A. Zeltser. Injection locking of tunnel junction oscillators to a microwave current. *Applied Physics Letters*, 98(182503), 2011.

[167] M. Zarudniev, P. Villard, M. Quinsat, U. Ebeles, and E. Colinet. Spin torque oscillator modelling and application to the coupling by a radiofrequency current. *To be submitted*, 2012.

[168] D. Houssameddine, U. Ebels, B. Delaët, B. Rodmacq, I. Firastrau, F. Ponthenier, M. Brunet, C. Thirion, J.-P. Michel, L. D. Prejbeanu-Buda, M.-C. Cyrille, O. Redon, and B. Dieny. Spin-torque oscillator using a perpendicular polarizer and a planar free layer. *Nature materials*, 6(6):441–7, June 2007.

[169] A. S. Jenkins, J. F. Sierra, M. Quinsat, B. Rodmacq, B. Delaet, B. Dieny, M.-C. Cyrille, and U. Ebels. Full Phase Diagram of Spin Torque Oscillators with Perpendicular Polariser. *To be submitted*, 2012.

[170] Thomas Dunn and Alex Kamenev. Swing switching of spin-torque valves. arXiv:1207, 2012.

[171] M. Zarudniev. *Frequency control of non-linear oscillators.* PhD thesis, 2012.

[172] R. Lehndorff, D. E. Bürgler, C. M. Schneider, and Z. Celinski. Injection locking of the gyrotropic vortex motion in a nanopillar. *Applied Physics Letters*, 97(142503), 2010.

[173] Robert Adler. Locking Phenomena in Oscillators. *PROCEEDINGS OF THE IEEE*, 61(10):1380–1385, 1973.

[174] M. D'Aquino, C. Serpico, R. Bonin, G. Bertotti, and I. Mayergoyz. Micromagnetic analysis of injection locking in spin-transfer nano-oscillators. *Physical Review B*, 82(064415), August 2010.

[175] S. H. Florez, J. A. Katine, M. Carey, L. Folks, O. Ozatay, and B. D. Terris. Effects of radio-frequency current on spin-transfer-torque-induced dynamics. *Physical Review B*, 78(184403), 2008.

[176] D. Houssameddine, M. Quinsat, B. Delaet, M.-C. Cyrille, and U. Ebels. Magnetoresistive radiofrequency oscillator and method for generating an oscillating signal, EU Patent, WO 2011/107475 A1, 2011.

[177] D. Houssameddine, M. Quinsat, B. Delaet, M.-C. Cyrille, and U. Ebels. Magnetoresistive radiofrequency oscillator and method for generating an oscillating signal, EU Patent, WO 2011/107473 A1, 2011.

[178] M. Zarudniev, E. Colinet, P. Villard, U. Ebels, M. Quinsat, and G. Scorletti. Synchronization of a spintorque oscillator array by a radiofrequency current. *Mechatronics*, pages 10–13, August 2011.

[179] M. Aquino, C. Serpico, G. Bertotti, R. Bonin, and I. D. Mayergoyz. Analysis of thermally induced magnetization dynamics in spin-transfer. *Physica B: Physics of Condensed Matter*, 407(9):1389–1393, 2012.

[180] D. Li, Y. Zhou, C. Zhou, and B. Hu. Fractional locking of spin-torque oscillator by injected ac current. *Physical Review B*, 83(174424), May 2011.

[181] Yan Zhou. *Spin momentum transfer effects for spintronic device applications.* PhD thesis, KTH, 2009.

[182] D. Gusakova, D. Houssameddine, U. Ebels, B. Dieny, M.-C. Cyrille, and B. Delaët. Spin-polarized current-induced excitations in a coupled magnetic layer system. *Physical Review B*, 79(104406), 2009.

[183] K. Kudo, T. Nagasawa, H. Suto, T. Yang, K. Mizushima, K. Kudo, T. Nagasawa, H. Suto, T. Yang, and Koichi Mizushima. Influence of dynamical dipolar coupling on spin-torque-induced excitations in a magnetic tunnel junction nanopillar. *Journal of Applied Physics*, 111(07C906), 2012.

[184] D. Gusakova, M. Quinsat, J. F. Sierra, U. Ebels, B. Dieny, L. D. Buda-Prejbeanu, M.-C. Cyrille, V. Tiberkevich, and A. N. Slavin. Linewidth reduction in a spin-torque nano-oscillator caused by non-conservative current-induced coupling between magnetic layers. *Applied Physics Letters*, 99(052501), 2011.

[185] N. Locatelli, V. V. Naletov, J. Grollier, G. De Loubens, V. Cros, C. Deranlot, C. Ulysse, G. Faini, O. Klein, and A. Fert. Dynamics of two coupled vortices in a spin valve nanopillar excited by spin transfer torque. *Applied Physics Letters*, 98(062501), 2011.

[186] M. Zarudniev, A. Korniienko, G. Scorletti, and P. Villard. Subsystem Output Feedback Control for Large-Scale Systems: Interconnection Matrix Design. In *CDC2012 (submitted)*, 2012.

[187] V. E. Demidov, S. Urazhdin, E. R. J. Edwards, M. D. Stiles, R. D. Mcmichael, and S. O. Demokritov. Control of Magnetic Fluctuations by Spin Current. *Physical Review Letters*, 107(107204), 2011.

[188] L. Liu, C.-F. Pai, Y. Li, H. W. Tseng, D. C. Ralph, and R. A. Buhrman. Spin-Torque Switching with the Giant Spin Hall Effect of Tantalum. *Science*, 336(May):555, 2012.